

Computer Modelling and Applications in Metallurgical Research and Industry

Edited by

D. N. Sah

R. Vijayaraghavan

P. R. Roy



**Indian Academy of Sciences
Bangalore 560 080**

Computer Modelling and Applications in Metallurgical Research and Industry

Proceedings of the Symposium on Computer Modelling and Applications in Metallurgical Research and Industry organised by the Materials Science Committee of the Board of Research in Nuclear Sciences, Department of Atomic Energy at BARC, Bombay on March 14-15, 1985.

**A collection of reprints of the papers published in
Bulletin of Materials Science (Vol. 8, No. 2, May 1986,
pp. 91-264)**

Edited by

D. N. Sah

R. Vijayaraghavan

P. R. Roy



**Indian Academy of Sciences
Bangalore 560 080**

© 1986 by the Indian Academy of Sciences

Reprinted from the Bulletin of Materials Science
Volume 8, pp. 91-264, 1986

Edited by D. N. Sah, R. Vijayaraghavan and P. R. Roy for the
Indian Academy of Sciences and printed by Macmillan India
Press, Madras 600 041

CONTENTS

Proceedings of the symposium on COMAMRI

Foreword	91
Computer models for fuel element behaviour	<i>J R Matthews</i> 93
Computer calculations of phase diagrams	<i>A K Mallik</i> 107
Computer-aided design of rolling mills	<i>K G Pandey</i> 123
Computer modelling application in life prediction of high temperature components	<i>V M Radhakrishnan</i> 133
Computer applications in the field of furnace design	<i>V S Pakala</i> 147
Computer simulation of defects and radiation damage	<i>K Krishan, B Purniah and S Srinivasan</i> 155
Some fundamental considerations to precede image analysis	<i>Dieter Vollath</i> 169
Computer-aided roll pass design for continuous billet mill	<i>Ashok Kumar, Sudhaker Jha and V Ramaswamy</i> 183
Computer-aided composition-treatment-structure-property correlation studies in steels	<i>K Vijayaraju and E S Dwarakadasa</i> 193
Computer simulation of pressure sintering	<i>N Ramakrishnan, T Balakrishna Bhat and V S Arunachalam</i> 199
Computer simulation of serrated yielding	<i>K Neelakantan</i> 209
An absolute method for the determination of surface tension of liquids using pendent drop profiles	<i>S Ramesh Babu</i> 217
Personal computer-based CAMAC system for data acquisition	<i>S K Kataria, V S Ramamurthy, V G Gaonkar and Surendra Kumar</i> 225
Image analysis system for quantitative metallography	<i>V K Chadda, D G Joshi, S N Murthy, S V Kulgod, C Baburao, D K Bhattacharya and Baldev Raj</i> 231
Modern computer assisted methods in metallurgy	<i>G W Jenkinson and T Kelly</i> 239
Computer simulation of dislocation-carbon interaction in nickel	<i>B Purniah and S Srinivasan</i> 247
Water reactor fuel performance code PROFESS and its application for predicting the behaviour of the fuel elements of D-Com blind problem	<i>D N Sah, D Venkatesh and E Ramadasan</i> 253

A very faint, large watermark-like image of a classical building with four prominent columns and a triangular pediment occupies the center of the page.

Digitized by the Internet Archive
in 2018 with funding from
Public.Resource.Org

<https://archive.org/details/computermodeling00unse>

Proceedings of the symposium on COMAMRI

FOREWORD

Computer modelling has many important applications in several areas of metallurgical research and industries, e.g. on-line control of metallurgical processes, design of components, plants and furnaces, prediction of materials behaviour under conditions which are difficult to be simulated by experiment, phase diagram calculations, simulation of radiation damage in materials, on-line data acquisition and data processing etc. Research in these areas has acquired impetus recently in our country by virtue of increased availability of computers and due to a need to modernize the industries by utilizing the potential of digital computers. However, there was no forum where the work done in this area could be presented and discussed. In view of this, a need was felt to organize a symposium to review the state-of-art of the developments made in the field of computer utilization in metallurgy and to provide an opportunity for a close interaction between the scientists and engineers working in this field. Therefore, the Materials Science Committee of the Board of Research in Nuclear Sciences, Department of Atomic Energy organized a two-day National Symposium on "Computer Modelling and Applications in Metallurgical Research and Industry (COMAMRI)" at BARC Bombay on 14–15 March 1985. The symposium was spread over five technical sessions dealing with computer modelling and applications in the areas of nuclear fuel element behaviour, phase diagrams and phase stability, iron and steel industry, design and performance, simulation studies, image analysis and data processing. About 200 delegates from India and abroad participated in the symposium. A panel discussion held at the close of the symposium identified several important areas for future work and made suggestions for better interaction between the scientific workers in this field. Some of the points noted during panel discussion emphasized the need for (a) development of application-oriented computer models for on-line control of chemical and metallurgical processes, (b) development of sensors for high temperature use for the measurement of parameters such as pressure, temperature, flow rate etc. (c) holding short term courses on computer modelling techniques, (d) setting up of a National Code Centre, and (e) assisting the industries in intelligent use of computers.

The National Organising Committee decided to publish the symposium proceedings as a special issue of the Bulletin of Materials Science with a view to provide a wide circulation of the technical information contained in the invited talks and contributed papers presented at the symposium. Out of a total of 25 technical presentations made at the symposium, 17 are included in this volume. These papers cover a wide range of applications of computer modelling in metallurgy and materials science. To our knowledge, this is the first published document in our country containing a collection of papers on this topic and we are confident that it will be very useful to the scientists and engineers working in this field.

We wish to express our thanks to Prof. R. Vijayaraghavan of TIFR and Shri D. N. Sah, the Convener of Symposium on COMAMRI, for their strenuous efforts in reviewing and editing of the papers contained in this volume.

C. N. R. Rao
Editor of Publications
Indian Academy of Sciences

P. R. Roy
Chairman, Materials Science Committee
B.R.N.S., B.A.R.C.

Computer models for fuel element behaviour

J R MATTHEWS

Theoretical Physics Division, AERE Harwell, UK

Abstract. Over the past 20 years computer modelling of fuel performance has developed into a well-established procedure, which has been valuable in the understanding and the improvement of fuel rod behaviour. The range of computer models presently applied to cylindrical ceramic fuels is reviewed. A critical appraisal is made of the numerical techniques used for mechanical and thermal analysis. The necessity for benchmark calculations is emphasized and various approaches for model validation are discussed. A number of special topics are chosen for deeper discussion. These include: improved description of cladding deformation and the estimation of failure; the analysis of stress concentrations in the cladding; fission gas analysis; and chemical modelling. Finally some speculation is made on the future of fuel rod modelling.

Keywords. Computer modelling; nuclear fuels; oxide fuels; deformation; failure; heat transfer; fission products; fission gases.

1. Introduction

This paper will give a very personal view of the subject of fuel element computer modelling. It will look critically at the development of computer programs for the simulation of the behaviour of cylindrical fuel rods containing ceramic fuel under normal and accident conditions. On this basis particulate fuels, metal fuels and cermet fuels will not be considered. To limit the scope somewhat, the behaviour of individual fuel rods will be discussed and the subject of rod-to-rod interactions or fuel rod interactions with other structural components will not be covered.

The development of computer models for fuel performance has its origins in the mid-1960s when, at a number of centres, heat transfer and fuel rod mechanics calculations were coupled for the first time. The best known of these early models is CYGRO, which laid out the structure that future models followed (Freidrich 1965). During the next five years there was an explosion of activity when almost every research centre in the USA, Japan and Western Europe produced its own fuel performance model; for a list of the models of this period see Matthews (1972). Some of the names of the computer codes written at that time are still used, such as SATURN, COMETHE, LIFE and CYGRO, but the methods used within them have in general been greatly improved.

During the 1970s there was a growing interest in reactor safety and many of the codes were extended for use in accident calculations. There was also an interest in producing more detailed codes that permitted the study of microstructural processes within the fuel and its cladding. More recently the decline of nuclear power plant ordering in the USA has limited the number of active centres in that country. Interest has remained strong in Western Europe and Japan and there have also been encouraging developments in Eastern Europe, Latin America and India. For recent reviews of water reactor fuel element modelling for performance and safety studies see Gittus (1982, 1984).

The content of fuel behaviour codes varies enormously and they range from very simple empirical models with the minimum of computational framework to complex detailed calculations including many physical and chemical sub-models. The simpler codes tend to be aimed at the fuel of a single reactor type, or even a single fuel variant within that type. The more physically based codes are often applied to a wide range of fuels. This is not surprising as most power reactors use fuel of similar configuration: i.e. a cylindrical metal cladding tube filled with cylindrical UO_2 or $(\text{U}, \text{Pu})\text{O}_2$ pellets. This is the case for fast breeder reactors, the UK advanced gas cooled reactor, the pressurised water reactor, the boiling water reactor and the various heavy water reactors.

2. Range of fuel behaviour codes

It would be impossible in this short paper to list all the current fuel codes and not much would be gained without a reasonably detailed assessment of each. However it is worth looking at the range of models and classifying them with a few selected examples. Most models attempt to represent a fuel rod by assembling a series of transverse slices or zones and connecting them loosely by pin pressure, axial loading conditions and the coolant heat transfer (see figure 1). This is often referred to as the $1\frac{1}{2}$ -dimensional approximation. A number of codes use two-dimensional finite-element analyses to investigate specific aspects of behaviour such as clad interaction with pellet "hour-glassing" or local stress concentrations near cracks, e.g. SAFENR (Chhatre *et al* 1983) or MIPAC (Ichikawa *et al* 1980). The modelling of whole pin behaviour however is wasteful because the local stress concentrations occur on a scale that is too small to be usefully covered. Often such calculations are done by coupling with a $1\frac{1}{2}$ -dimensional code.

The $1\frac{1}{2}$ -dimensional codes fall into a number of types. There are simple performance codes that do not have complicated mechanics models, but concentrate on temperature calculation and the development of fuel restructuring and fission gas release, e.g. the US fast reactor code SIEX (Dutt and Baker 1975) and the UK thermal reactor code MINIPAT (Hughes *et al* 1982). Such simple codes are also often used to supply the starting conditions for accident analysis codes, i.e. FRAPCON (Berna *et al* 1980). Then there are detailed performance codes that include descriptions of the deformation of both the fuel and cladding by creep and plastic flow, as well as thermal and restructuring calculations, e.g. the UK code FRUMP (Wilmore and Matthews 1979), the Argentinian code BACO (Harriague *et al* 1980) and the Indian code PROFESS (Sah and Venkatesh 1984). These codes also have some limited transient capability. The most complex are extremely versatile, e.g. URANUS (Preusser and Lassmann 1983) which can be applied to oxide or carbide fuel, water or fast breeder reactors, transient or steady state, and in deterministic or probabilistic modes. Similarly the US LIFE-4 code (Stephen *et al* 1977) has been issued in transient, water reactor and carbide versions in addition to the fast breeder performance form it was originally written in. The COMETHE code (van Vliet and Meulemeester 1980) should also be mentioned as it has been widely used for analysis of performance and mild transients on water reactor and fast breeder fuel both in its country of origin and by EPRI in the USA.

In going to the field of safety analysis the range of codes is bridged by the TRAFIC code (Matthews 1984), which has the complete range fuel performance models, but also special modules for analysis of accident conditions. These include models for sodium boiling, molten fuel motion within the fuel pin, fuel ejection from the pin and a

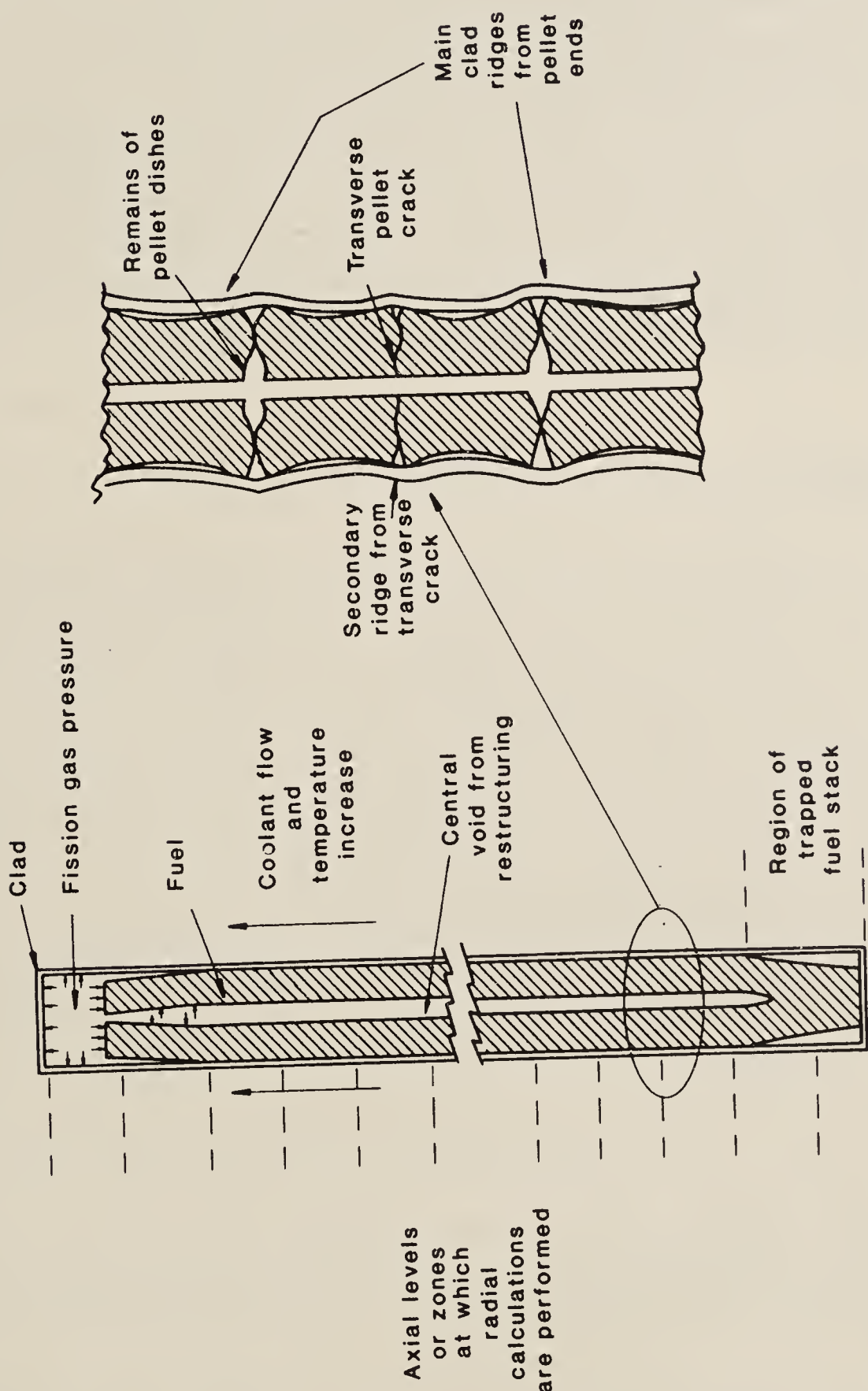


Figure 1. Schematic illustration of how a series of one-dimensional calculations (in the radial direction) are coupled, via coolant heat transfer axial loading and pin internal pressure. Causes of axial stress concentrations are also shown; the stack-trapping effect and clad ridging from pellet hour-glassing.

transient fission gas model (Matthews *et al* 1985). More specific accident models concentrate on the aspects of behaviour which are inherent in the type of fuel being studied. The fuel pin modelling within these codes is often simplified, as the main objective of the calculation is the blockage of coolant channels, the thermo-hydraulic problem and changes in the fuel rod configuration. For water reactors the most comprehensive code is FRAP-T6 (Seifken 1983). On the fast breeder reactor side the French Physura code (Melis 1982) and the US code SAS-4A (Wider *et al* 1982) probably have the widest range of models. Most of the fast reactor models have recently been compared on a common test problem (Cacciabue *et al* 1982).

In addition to the whole pin models there are separate models that deal with a specific aspect of fuel rod behaviour. Many of these models can be coupled to whole pin models, although they are uneconomic for routine use. One example is fission gas behaviour analysis with codes such as GRASS and FASTGRASS (Rest 1979). Another is the detailed deformation analysis of Zircaloy and 316 stainless steel using the MATMOD programs (Schmidt and Miller 1981; Miller and Sherby 1977).

3. The philosophy of fuel behaviour modelling

Fuel rod behaviour modelling is one of the first examples of a complex physical system being simulated on the computer. For this reason it is worth examining the philosophy of modelling laying down some general principles to guide more effective future work.

First of all let us consider why such computer codes need to be constructed, rather than simpler calculations on specific aspects of behaviour such as temperature, fission gas release or cladding deformation. The reason is one of self-consistency. All aspects of the fuel behaviour are intimately connected. Take the example of fuel temperature. Fuel temperature is very sensitive to the size and condition of the fuel-cladding interface. Changes in the fuel temperature cause changes in the fuel size from thermal expansion and hence the size of the fuel-cladding gap and its heat transfer coefficient. Similarly release of fission gas from the fuel, which is sensitive to fuel temperature, alters the purity of the rod-filling gas, which changes the gas heat transfer coefficient and hence the fuel temperatures. Such interconnections make some sort of comprehensive fuel-rod model essential to the understanding of its behaviour. On a wider front whole pin models are also required to study the interactions with the coolant thermal and hydraulic behaviour. For the fast breeder reactor this is extended for safety analyses to calculation of the interactions with the reactivity of the reactor core.

The applications of fuel behaviour computer models are varied and it is essential to construct a model with appropriate characteristics. The following guidelines are worth adopting.

- (i) The accuracy of the calculation should be sufficient. Methods should be chosen to give adequate accuracy, but the use of error control which is more stringent than necessary is inefficient.
- (ii) The code should use sub-models which have consistent levels of approximation. It is no use coupling a sophisticated fission gas model or detailed finite-element model to a code which is basically incompatible.
- (iii) No short-cuts should be taken on stability. The adding of extra models without proper coupling to avoid instabilities has led to problems in many codes.

- (iv) The code should be constructed in modular form to make the addition of sub-models easy. This is not a trivial problem when stability is to be maintained.
- (v) The main methods used in the code and all the sub-models should be verified (benchmarked) against standard or closed-form solutions. There has been at least one case of a major fuel-model being found to be at fault after several years of application.
- (vi) All the controlling processes should be identified and included in the code. This is not so easy and is the key to effective modelling.
- (vii) Computer codes should be identified by their materials properties, data-sets as well as their sub-models. Confusion often occurs because the data-set used was not clearly identified.
- (viii) If empirical correlations are used as sub-models care should be taken that the correct assumptions were used when making them. This is an easily forgotten problem, e.g. when correlating gap conductance against fuel relocation the same models for fuel expansion and cracking should be used in making the correlations as in the code in which it is to be used; otherwise the effect could be included twice.

When constructing models, a decision has to be made on the degree of mechanistic detail which should be included in the code. Some codes are phenomenological but the processes identified are described by empirical correlations of the macroscopic processes. In this case the code itself can be calibrated by means of free parameters in the models. In practice this approach has not been very successful. The models can give a good description of the fuel-rod behaviour within the range of the data-base, but outside the deviations can be unsatisfactory. Such codes add little to the understanding of the system. A more satisfactory approach is to restrict empirical correlation to processes that can be evaluated by separate experiment. If the code then gives bad predictions it means that some controlling process or interaction has been omitted. Fuel behaviour codes for design purposes or for use as part of a larger thermo-hydraulics or accident code, do not need detailed physically based sub-models. Codes used for experiment interpretation should be based on sub-models with a sound physical basis. Detailed modelling is very valuable in determining what the controlling processes are, and ensuring that simpler models have identified ranges of application.

4. Methods for thermal and mechanical calculations

The number of numerical methods for solving the basic heat transfer and fuel rod mechanics problems is almost as many as there are fuel codes. These, however, break down into three basic techniques on closer examination. Numerical approximations are required because most of the properties controlling behaviour are sensitive to temperature and to other physical variables which are functions of position. The three techniques are: (i) the finite difference approximation, where the differential equations for the system are approximated by difference expansions; (ii) the finite element approximation, where trial functions representing the variables being calculated are made to fit the differential equations of the system approximately over limited regions and then the whole system is made self-consistent; and (iii) the use of analytical or semi-analytical solutions to represent the behaviour over rings of the material which are then made self-consistent over the whole system. There are a host of variations on these

methods by taking different orders of difference approximation, integration techniques, orders of trial function and the choice of variables to represent the system. Currently there is a move towards the use of finite element methods because of the ease with which the variation in properties over the system can be accommodated. Finite element methods tend to be simpler to formulate, but care has to be taken when interpolating values from the solutions as the values taken from the trial functions can sometimes be misleading at positions other than integration points.

The heat transfer problem within the fuel pin presents few problems, even taking account of transients, apart from where melting takes place. Care has to be taken to ensure that enthalpy is conserved when fixing the position of the melting front (Matthews 1979).

The description of the mechanical behaviour of the fuel rod is a much more difficult problem. One of the main difficulties arises from the very large variation in creep properties in the fuel, because of the sensitivity of creep to temperature. The creep strength of the fuel can vary typically by 10 orders of magnitude in a highly rated fuel design, in going from the cooler outer fuel regions dominated by irradiation creep to the hot plastic centre. This caused many problems in early models. One standard solution to the problem was to partition the fuel, above a somewhat arbitrary temperature, into a plastic zone where all shear stresses are relaxed. Despite this, the time-steps taken by the codes were often unacceptably small. One method of overcoming this problem was to extrapolate the total strains calculated by the codes to the next time-step and then solve for the stresses at the end of the time-step to enable a better estimate of the creep strain to be obtained (Jankus and Weeks 1970). This method works well for many cases and especially where the strain increment is controlled by a change in temperature or a swelling increment which is a weak function of the stress in the system. The method, however, breaks down in some circumstances and particularly for the case of the creep of the cladding tube by fission gas pressure (Nimo and Ogawra 1980). The only sound solution is to use a method which has a strong implicit component and is guaranteed stable. The Crank-Nicholson or Euler backward approximations are adequate for most applications, but the problem of dealing with nonlinearities in the response of the system has to be faced.

The simplest method of linearising the problem is to use the Newton-Raphson approximation. Many workers have avoided implicit solutions and the use of the Newton-Raphson method because they interfered with the modular nature of the code and were complicated to implement. Recent work has shown that this need not be the case (Matthews 1983) and the TRAFIC code is fully modular and uses a fully implicit method of solution. One aspect to be careful of is the treatment of fuel hot-pressing and stress-dependent fuel swelling. Some codes take care to deal with the problem of fuel creep, but then find there are stability problems when a new fuel densification or swelling model is added to the code. The same criteria should be applied to the calculation of fuel volume changes as those used to implement creep deformation.

There are many other problems associated with the fuel-rods mechanics calculation, and it is worth quickly listing a few. Fuel strains are often large, even if cladding strains are small, and care must be taken to make the deformation account for finite strains. In some cases the plastic strains in the fuel or clad are very large compared with the level of elastic strain in the system. Some finite element techniques become inaccurate in this situation and an additional degree of freedom should be introduced into the solution to avoid this (Hermann 1965). Fuel cracking is an important factor in determining the

fuel-cladding gap and reducing the fuel-cladding mechanical interaction (FCMI). Some models calculate no FCMI prior to the closure of the cracks. This will underestimate the cladding strains and as will be seen below the cracks play an important role in fuel-rod failure. Some codes neglect transverse cracks, lying normal to the axial direction; in doing so they will underestimate fuel relocation and miss important effects on fuel stack axial-loading (see figure 1).

Finally the interaction between the thermal and mechanical calculations must not be forgotten. In most codes the thermal calculation is performed first for a time-step followed by the mechanics, with iterations if necessary. This can result, when the fuel-cladding gap is small, in an oscillating instability. This problem is only encountered occasionally and can be countered by introducing some form of numerical damping into the calculation. A more rigorous approach would be to couple the thermal and mechanical calculations; a possibility that we will return to in the discussion on future developments.

5. Special topics

In this section we discuss recent developments and requirements in a few selected areas of interest.

5.1 Improved models for cladding deformation and failure

The deformation and rupture of fuel-rod cladding presents perhaps the greatest challenge to fuel behaviour modelling. Up to now cladding deformation has been included in codes by simple correlations on creep and plastic deformation, supplemented by corrections for radiation hardening and empirical representation of irradiation creep, the growth of Zircaloy or void swelling of steels in fast breeder reactors. In fact the dimensional changes that a metal alloy will undergo under an applied stress and a simultaneous exposure to fast neutron damage are extremely complex. Figure 2 illustrates this. Some of the effects have been recently reviewed by Bullough (1984). Irradiation changes the dislocation structure, alters the distribution of both the major and minor constituents of the alloy and produces a range of embrittling effects. Added to this is the effect of the presence of fission products adjacent to the cladding inner surface.

To make sense of these interactions new techniques are required. Simple semi-empirical models can be constructed, which are based on the actual physical processes taking place. In this way several processes like irradiation creep, dislocation structure evolution, growth, void swelling and thermal creep can all be interlinked (Bullough *et al* 1981). The model can then be used as the basis of an empirical correlation, but with the minimum of free variables. This should increase the ability of modelling to reproduce the observed behaviour of fuel-rods and remove some of the present discrepancies.

5.2 Stress concentration and failure

Failure of thermal reactor fuel rods is often dominated by local stress concentrations. There are two main sources; the ends of pellets (see figure 1) and the regions of cladding

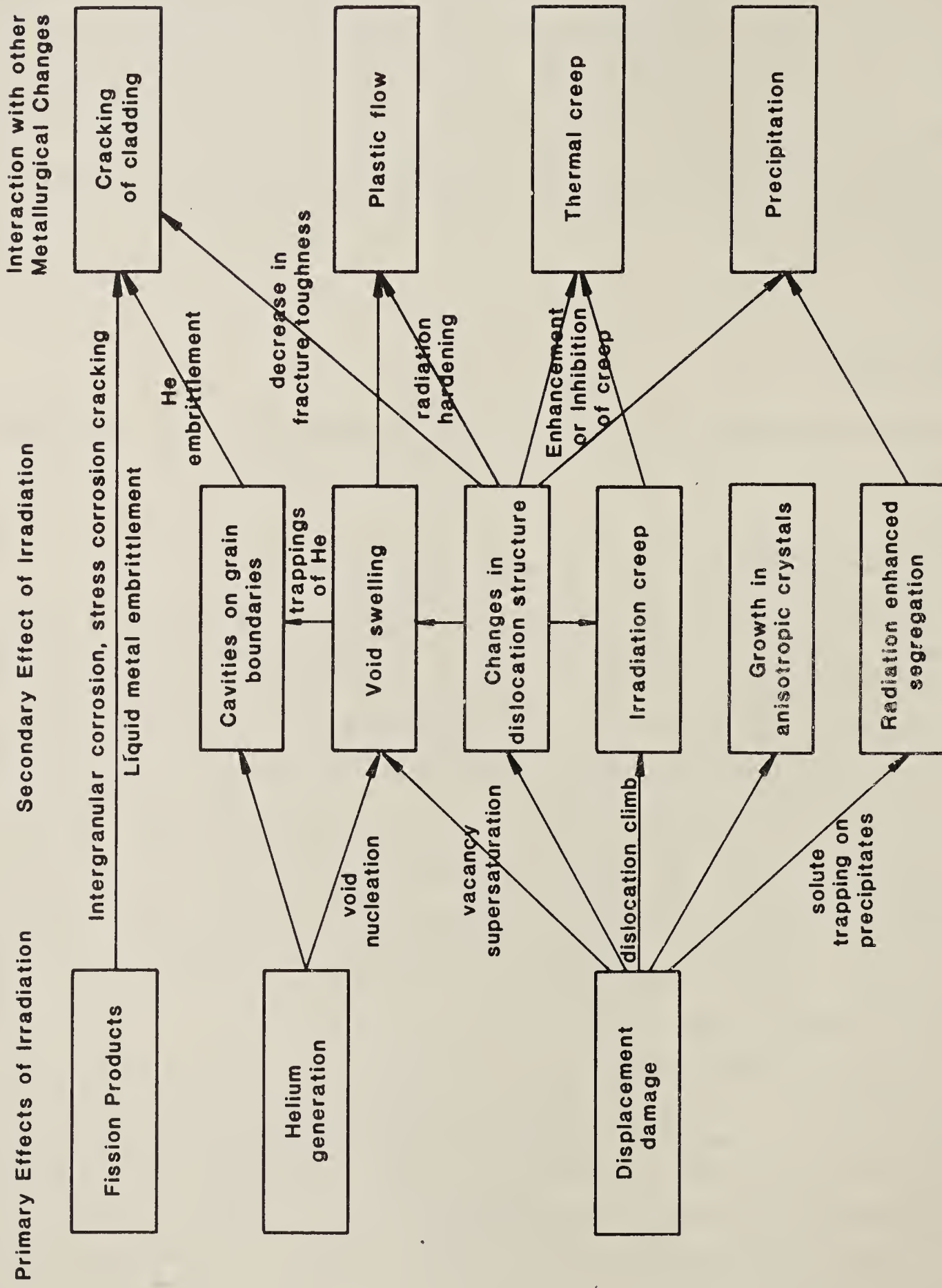


Figure 2. Illustration of the effects of radiation damage and how they interact with the metallurgical characteristics of engineering alloys.

adjacent to radial cracks in fuel pellets (see figure 3). The most widely used model for stress concentrations over cracks is that of Gittus (Gittus *et al* 1970; Gittus 1972). Although found useful in practice this model has several deficiencies. The stress equilibrium conditions in the cladding shell are not soundly based. To do this properly is difficult and complicated and much of the elegance of Gittus' solutions is lost (Tromans and Matthews 1984). The treatment neglects bending moments in the cladding, which are often dominant (Nakatsuka 1981). The solutions to the friction problem should have a stuck region and a sliding region, in order to satisfy cyclic boundary conditions (figure 3). The stress concentration extends only over the region of the cladding over the crack and where sliding takes place (figure 4). The extent of the sliding region is sensitive to the external coolant pressure. The size of the stress concentration on the cladding inner surface is greatly underestimated by the thin shell model, as the through wall stress gradients are large. Only rigorous two-dimensional calculations are able to fix the inner stress accurately. The stress concentration is over-

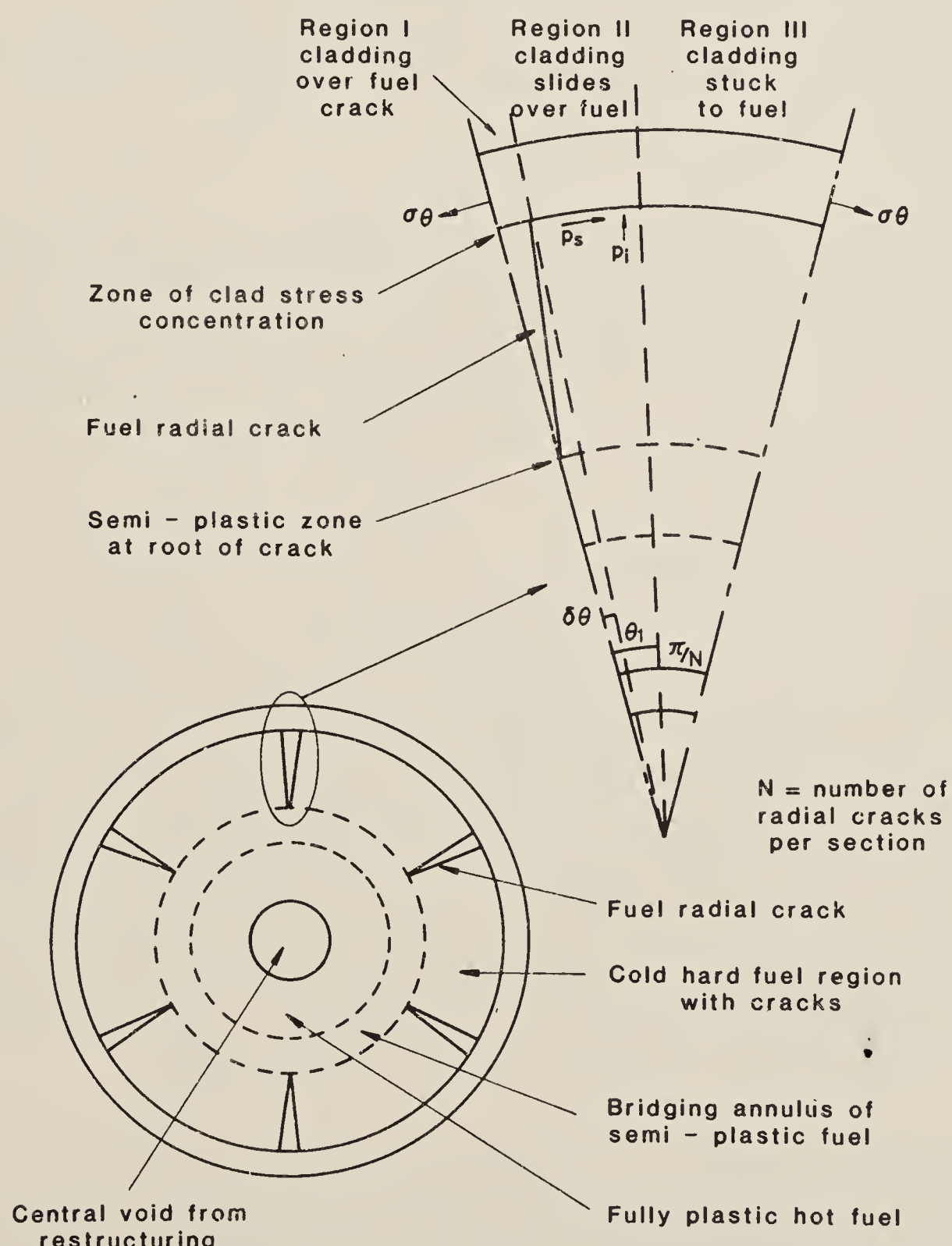


Figure 3. Schematic illustration of the relationship between fuel radial cracking, fuel structural zones and stress concentrations in cladding.

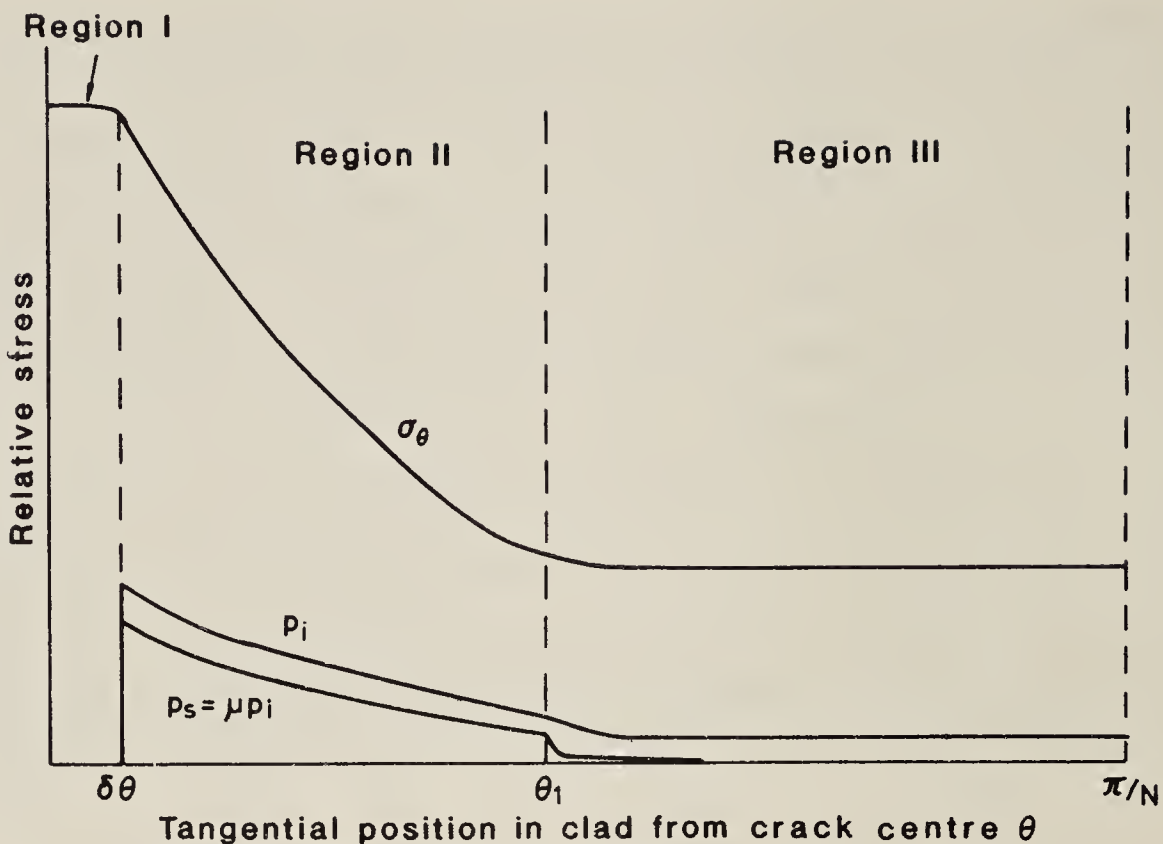


Figure 4. Schematic illustration of clad mean hoop stress, normal pressure and shear traction, vary with angular position, when sliding and sticking occur between fuel and cladding.

estimated, however, because the reaction of the fuel is neglected. Even if the fuel adjacent to the cladding is hard, the fuel at the crack roots may be plastic and reduce the load on the cladding (Stephen *et al* 1979). The stress concentration at the cladding does not arise from the radial displacement of the fuel, but from the relative opening of the cracks, which occurs from thermal expansion on power increases and from differential swelling (Tromans and Matthews 1984). Finally the simple shell model does not include other sources of internal stress in the cladding, such as thermal stresses, which will be important when nonlinear deformation is taking place.

Many of these remarks also apply to simple analyses of cladding interactions with the pellet ends. The lesson is that this is an example where simple one-dimensional calculations are inadequate. Guidelines for the effect of clad-ridging from pellet interactions or stress concentrations over cracks, should be carried out with the appropriate two-dimensional finite-element model of the fuel and clad together.

These aspects of local cladding stress concentrations are not so important in fast reactor fuel because: the coolant pressure is low; the cladding is relatively thick and strong; the fuel is more highly rated and softer with many more radial and transverse cracks; and stress corrosion cracking has not yet been recognized as a problem. The main problem with strain concentrations in fast reactor cladding arises from local temperature perturbations or hot-spots. These occur because of the high surface heat fluxes on fast reactor fuel-rods and because of the problem with fast neutron induced swelling of the cladding causing distortions of the fuel bundle.

5.3 Fission gas behaviour

Fission gas swelling and release are important processes in determining fuel pin behaviour both under normal and accident conditions. Swelling is an important factor in FCMI and can also cushion rapid clad loading in overpower transient conditions.

Fission gas release is also important as many fuel designs have limited plenum volumes to accommodate fission gases. Fast reactor fuel normally releases a high proportion of its fission gas inventory during normal high rating operation and many aspects of fuel behaviour in accidents are controlled by the retained gas in the fuel after melting (Wood *et al* 1984).

The processes involved in a complete description of fission gas behaviour are many and their interactions are complex (see figure 5). A recent review describes how these processes are handled in the OGRES and NEFIG models which form part of the TRAFIC code (Matthews and Wood 1984). There are, however, some indications that there may be some deficiencies in our understanding of fission gas behaviour in transients. Experiments both in the laboratory (Zimmermann 1984) and in-pile (Sontheimer *et al* 1984) give higher gas releases than anticipated. This was also evident in the DCOM blind problem that was reviewed at the Bowness-on-Windermere Conference in 1984. Current mechanistic fission gas models predict that on mild temperature transients most of the gas would be trapped in small bubbles and fission gas release would be small. There are several rival explanations of this discrepancy: the bubbles may become over-stuffed with gas and reject gas atoms, leaving a higher concentration in solution (Brearley *et al* 1984); grain boundary sweeping may be more important than previously thought (van Vliet and Billaux 1984); or the amount of gas held on the grain boundaries may be higher than previously thought. All of these explanations have their deficiencies. The observation of the growth of a coarse bubble population after high temperature annealing, suggests that what were previously thought to be small bubbles were in fact vacancy clusters which disappear before they trap gas (Matthews *et al* 1985). Hopefully these questions will be resolved in the next few years, as several experimental programmes are being conducted at present to provide more microstructural information.

5.4 Chemical modelling

Perhaps the most neglected aspect of fuel behaviour modelling has been fuel chemistry. Models so far have at most simple descriptions of oxygen redistribution within the fuel or simple calculations of caesium and plutonium migration. Chemical effects are very important in determining fuel-rod failure and better estimates of the fuel-cladding gap inventory of fission products and their chemical state are required. This is not a trivial problem as the number of chemical species and compounds involved is large. Among the problems are: calculations of the amounts of free iodine and tellurium as a function of linear rating and burn-up; good definition of the oxygen potential to the fuel-cladding interface, which is particularly important for stainless steel clad rods; definition of the location and chemical state of caesium throughout the fuel rod; and good description of oxygen and plutonium redistribution during irradiation.

6. Future developments

This paper has looked at a range of important topics in the subject of fuel behaviour modelling, but there are insufficient space to discuss many other aspects that are just as important. For example we have neglected to discuss fuel restructuring processes and the behaviour of fuel rods during extreme accident conditions. To finish the paper it is worth briefly commenting on possible future trends.

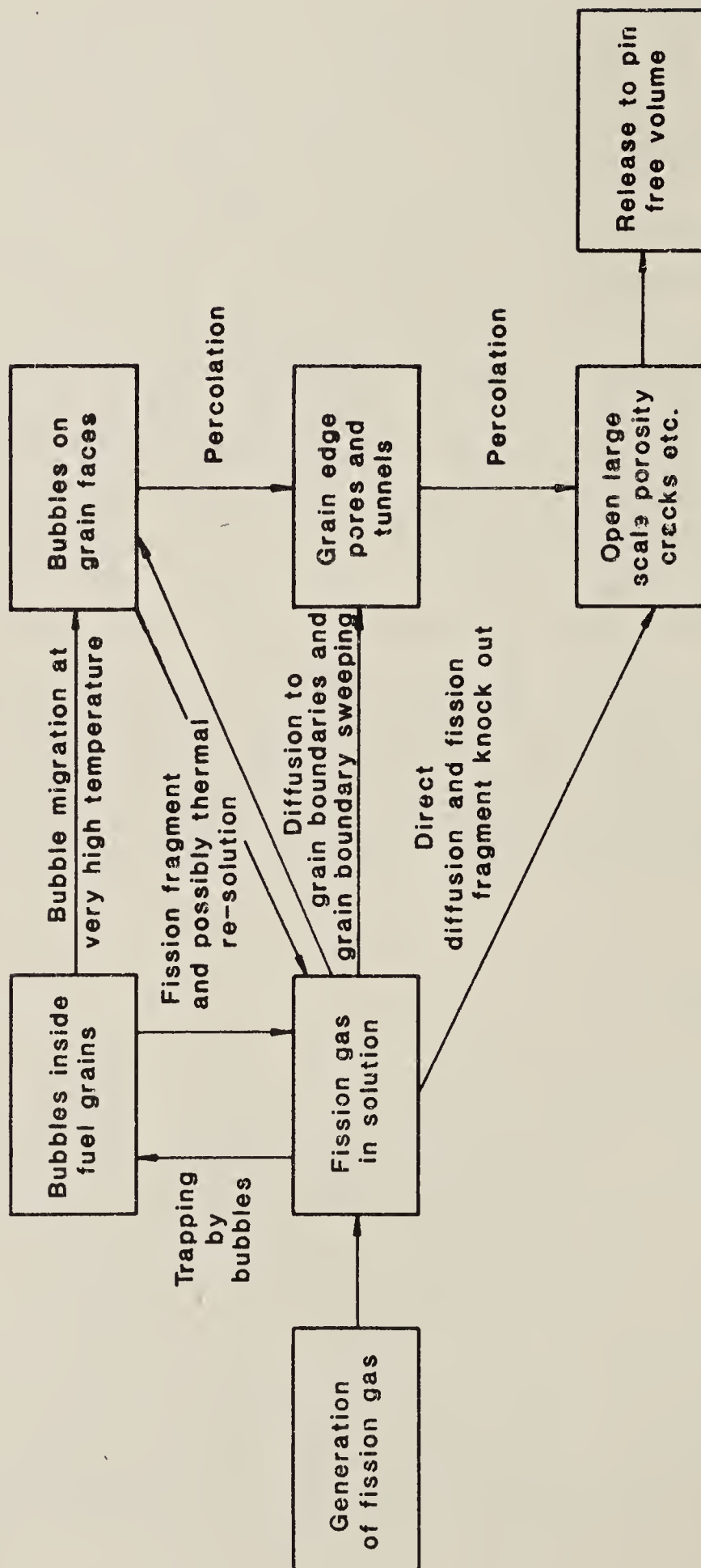


Figure 5. Illustration of the interactions between the various mechanisms governing fission gas release and swelling.

The most important new development is the introduction of the supercomputers (Duff 1984), which have recently increased the computing power available to fuel rod modellers by two orders of magnitude. This will enable calculations that were previously too expensive and long-running to be tackled. Two- and three-dimensional models of fuel behaviour will be introduced in cluster behaviour or even whole-core models. The basic $1\frac{1}{2}$ -dimensional fuel pin code will still have an important place in modelling, but it will be more frequently supplemented by two-dimensional finite-element calculation to study stress concentrations and non axysymmetric effects. In particular it will be possible to couple the mechanics and thermal calculation directly for the whole fuel rod. This will remove the remaining sources of instability in the code and with proper vectorization of the calculation could be achieved with little cost penalty. It will then be possible to have improved treatments of coolant boiling, molten fuel motion and complex axial loadings coupled to the code. The TRAFIC code is being rewritten in this form at the moment for use on the Harwell CRAY computer.

References

- Berna G A *et al* 1980 FRAPCON-2. A computer code for the calculation of steady-state thermo-mechanical behaviour of oxide fuel rods NUREG/CR-1845
- Brearley I R *et al* 1984 *Eur. Appl. Rept., Nucl. Sci. Technol.* **5** 1159
- Bullough R 1984 in *Proc. Conf. on dislocations and properties and real materials*, London (Royal Society, Metals Society)
- Bullough R *et al* 1981 *J. Nucl. Mater.* **103**, **104** 1263
- Cacciabue P C *et al* 1982 Comparative analysis of a hypothetical 0·15/sec transient overpower accident in an irradiated LMFBR core using different computer models. Commission of the European Communities Report EUR 8018EN
- Chatre A G 1983 *Trans. 7th Int. Conf. on Structural Mechanics in Reactor Technology*, Chicago, paper C3/6
- Duff I S 1984 in *Proc. Conf. on Vector and Parallel Processors in Computation and Science II*, Oxford, UK
- Dutt D S and Baker R B 1975 SIEX, A correlation code for the prediction of LMFBR fuel performance, Hanford Report HEDL-TME 74-55
- Freidrich C M 1965 CYGRO Stress analysis of the growth of concentric cylinders, Bettis Atomic Power Labs. Report WAPD-TM-514
- Gittus J H *et al* 1970 *Nucl. Appl. Technol.* **9** 40
- Gittus J H 1972 *Nucl. Eng. Des.* **18** 69
- Gittus J H 1982 International experience and status of fuel element performance and modelling for water reactors, Springfields Nuclear Power Development Labs. Report ND-R 604(S)
- Gittus J H 1984 Proc. Specialists Meeting on Water Reactor Fuel Element Performance Computer Modelling, Bowness-on-Windermere, UK, IAEA report IWGFPT/19, p. 15
- Harriague S *et al* 1980 *Nucl. Eng. Des.* **56** 83
- Hermann L R 1965 *A.I.A.A. July 3*, 1896
- Hughes H *et al* 1982 Fuel rod behaviour during transients Part 1. Description of codes, Springfields Report ND-R-702(S)
- Ichikawa M *et al* 1980 Proc. Specialists Meeting on Fuel Element Performance Computer Modelling, Blackpool, UK, IAEA Report IWGFPT 7 p. 216
- Jankus V Z and Weeks R W 1970 LIFE 1 - A Fortran IV computer code for the prediction of fast reactor fuel element behaviour. Argonne Report ANL 7736
- Matthews J R 1972 *Adv. Nucl. Sci. Technol.* **6** 67
- Matthews J R 1979 *Trans. 5th Int. Conf. on Structural Mechanics in Reactor Technology*, Berlin, paper D7/1
- Matthews J R 1983 *J. Nucl. Eng. Des.* (to be published)
- Matthews J R 1984 The basis of the TRAFIC fuel performance code, Harwell Report AERE-R. 10818 (rev.)
- Matthews J R *et al* 1985 *The application of the TRAFIC fuel performance code to steady and transient conditions*, BNW Conf. on Nuclear Fuel performance, Stratford-upon-Avon, UK
- Matthews J R and Wood M H 1984 *Eur. Appl. Res. Rept., Nucl. Sci. Technol.* **5** 1685

- Melis J C et al 1982 *PHYSURA – A code for the interpretation of safety experiments*, Int. Topical Meeting on LMFBR Safety and Related Design and Operational Aspects, Lyon, France p. II-45
- Miller A K and Sherby O D 1977 *Development of the Materials Code MATMOD (constitutive equations for Zircaloy)* EPR NP 567
- Nakatsuka M 1981 *Nucl. Eng. Des.* **65** 197
- Nimo H and Ogawa S 1980 Proc. Specialists Meeting on fuel element performance computer modelling, Blackpool, UK, IAEA Report IWGFPT/7 paper 29
- Preusser T and Lassmann K 1983 *Trans. 7th Int. Conf. on Structural Mechanics in Reactor Technology, Chicago, paper C4/3*
- Rest J 1979 in *Proc. 2nd Int. Seminar on Mathematical/Mechanical Modelling of Reactor Fuel Elements* (Berlin: Bundersanstalt fur Materialprufung)
- Sah D N and Venkatesh D 1984 Proc. Specialists Meeting on Water Reactor Fuel Element Performance Computer Modelling. Bowness-on-Windermere, UK, IAEA Report IWGFPT/19 p. 237
- Schmidt C G and Miller A K 1981 *Res. Mechanica* **3** 109, 175
- Seifken L J 1983 *Trans. 7th Int. Conf. on Structural Mechanics in Reactor Technology, Chicago paper C3/1*.
- Sontheimer F et al 1984 *J. Nucl. Mater.* **124** 33
- Stephen J D et al 1977 *The LIFE code system for analysis of oxide fuel pin thermal/structural behaviour*. Trans. Advanced LMFBR Fuels Topical Meeting, Tucson, Arizona
- Stephen J D et al 1979 Proc. Specialists Meeting on Theoretical Modelling of LMFBR Fuel Pin Behaviour, Fontenay-aux-Roses, France, IAEA Report IWGFR/31, p. 139
- Tromans N J and Matthews J R 1984 (unpublished work)
- Van Vliet J and Billaux M 1984 Proc. Specialists Meeting on Water Reactor Fuel Element Performance Computer Modelling, Bowness-on-Windermere UK, IAEA Report IWGFPT/19 p. 151
- Van Vliet J and de Meulemeester E 1980 *Nucl. Eng. Des.* **56** 71
- Wider H U et al 1982 *Status and validation of the SAS4A accident analysis code system*. Int. Topical Meeting on LMFBR Safety and Related Design and Operational Aspects, Lyon, France p. II-13
- Wilmore D and Matthews J R 1979 *FRUMP – A physically based fuel model*. Proc. Conf. on Fast Breeder Reactor Fuel, Monterey, California, p. 665
- Wood M H et al 1984 *Eur. Appl. Res. Rept., Nucl. Sci. Technol.* **5** 1515
- Zimmermann H 1984 *Eur. Appl. Res. Rept., Nucl. Sci. Technol.* **5** 1349

Computer calculations of phase diagrams

A K MALLIK

Indian Institute of Technology, Bombay 400 076, India

Abstract. The thermodynamic route of establishing phase diagrams is a relatively recent activity, considering that till about the fifties most phase diagrams were determined by the measurement of certain physical property or quantitative microscopy using light optics or x-ray diffraction. The thermodynamic formalism used by Kaufman and Bernstein is explained and illustrated with examples of the development of hypothetical binary phase diagrams. The calculation of ternary phase diagrams can begin with the binary phase diagram data as a first approximation. However, to calculate a reasonably accurate ternary phase diagram a certain amount of ternary solution data is necessary. Various empirical equations have been proposed in the literature to express ternary thermodynamic data.

Calculation of simple ternary isothermal sections is illustrated with the examples of Mo-V-W and Cd-Sn-Pb systems. The numerical techniques which involve the differentiation of thermodynamic parameters with respect to composition get more involved with the number of components becoming 3 or more. A simpler approach has been applied recently to find the minimum position on the Gibbs free energy surface.

Keywords. Phase diagrams; solution models; binary diagrams; lattice stability; ternary diagrams; miscibility gap; hill climbing technique.

1. Introduction

A phase diagram represents the domains of stable phases under a given condition of composition and pressure. Till the fifties, phase diagrams were approached mainly through experimental measurements which did not involve thermodynamics, using either direct phase estimation methods or indirect methods. The indirect methods involve measurement of a physical property or rather a change thereof like dilation, resistivity etc or thermal analysis. The thermodynamics of phase equilibria represented, till about the fifties, a parallel activity with few bridges or connections with the former approach. As the stable state of a phase is associated with the minimum of free energy, it should be possible to link up thermodynamics with phase diagram, provided of course that an adequate representation of thermodynamic data is available. The reason why this link-up got going only after the fifties is perhaps due to the lack of communication between the physical chemists and physical metallurgists.

The relatively slow progress of the thermodynamic route to phase diagram has also been caused by the lack of data even for binary systems, not to speak of ternary systems. On the contrary, by the use of a physical property, phase diagrams can be determined directly. A natural consequence has been that “the number of systems for which phase diagrams have been determined is much greater than that for which the thermodynamic properties of solution phases are known” (Ansara 1979).

The situation has changed considerably during the last twenty five years and more and more phase diagrams are being generated from thermodynamic data. Not only does it provide considerable saving of labour but the exercise gives a deeper insight to the systematics of phase diagrams. The calculations have become feasible with the

availability of computers and appropriate numerical methods. Further, with the availability of sophisticated instruments, it has become possible to generate more precise and reliable thermodynamic data. Some of the early usage of thermodynamic data for the calculation of phase diagrams were by Wagner (1954), White *et al* (1977) and Hardy (1953). Extensive contributions have been made subsequently by Kubaschewski and Barin (1974), Kaufman and Bernstein (1970), Hillert (1970), Gaye and Lupis (1975), Chart *et al* (1975) and Pelton and Thompson (1975) on the calculation of phase diagrams. To conserve space, the mathematical formalism used in the present paper will be that of Kaufman and Bernstein, except where mentioned otherwise.

2. Phase equilibrium

At a given temperature and pressure, the maximum number of coexisting phases in a system formed by m components is equal to $(m + 1)$ phases according to the phase rule. If there are j phases in the system, the partial free energy of a given component is the same for each phase under equilibrium conditions (figure 1). The condition can be expressed by a set of nonlinear equations such as

$$\bar{G}_i^{(1)} = \bar{G}_i^{(2)} = \bar{G}_i^{(j)}, \quad (1)$$

for $i = 1$ to m th element and 1 to j th phase. The equilibrium for a system is represented by the condition that the molar free energy is minimum.

3. Solution models

For an alloy system $A-B$, in which X represents the atom fraction of B and which exhibits two competing phases α and β , the free energies of each phase may be represented by the following equations

$$G^\alpha = (1 - X)G_A^\alpha + XG_B^\alpha + RT [X \ln X + (1 - X) \ln (1 - X)] + {}^E G^\alpha, \quad (2)$$

$$G^\beta = (1 - X)G_A^\beta + XG_B^\beta + RT [X \ln X + (1 - X) \ln (1 - X)] + {}^E G^\beta. \quad (3)$$

In (2) and (3) G_A^α and G_A^β are the free energies of the α and β modifications of the element A , while G_B^α and G_B^β are the free energies of the α and β modifications of the element B .

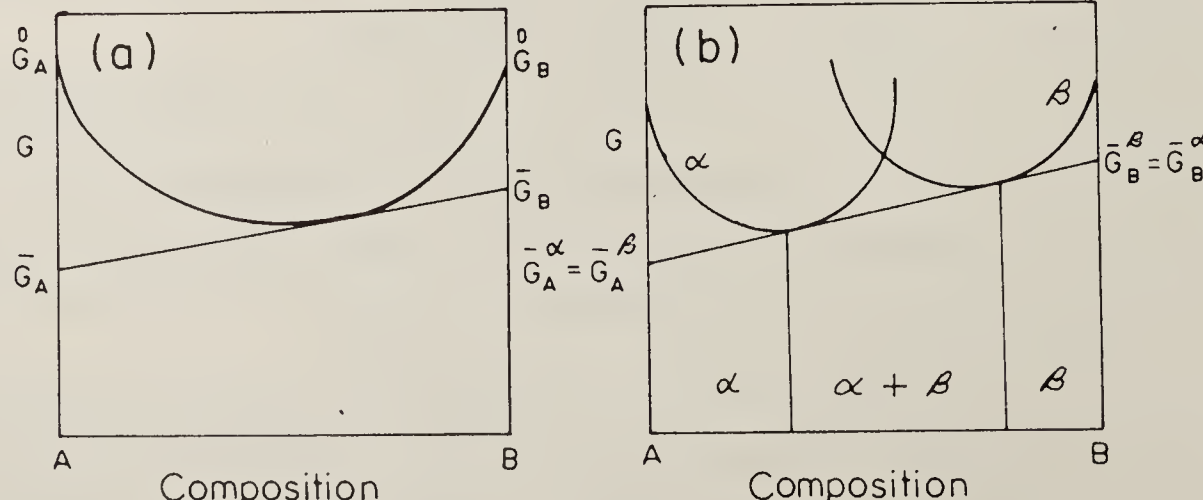


Figure 1. Common tangent construction to define equilibrium between two phases.

The excess free energies of mixing of the α and β phases are expressed as ${}^E G^\alpha$ and ${}^E G^\beta$ and X is the atom fraction of B .

The partial molar free energies of A and B in an alloy containing X atom fraction B are G_A and G_B respectively and are defined as

$$\bar{G}_A = G - X \frac{\partial G}{\partial X}, \quad (4)$$

$$\bar{G}_B = G + (1 - X) \frac{\partial G}{\partial X}. \quad (5)$$

By differentiating G^α and G^β in (2) and (3) with respect to X , one can obtain the expressions for \bar{G}_A^α , \bar{G}_A^β , \bar{G}_B^α and \bar{G}_B^β i.e. the partial free energy terms. Further applying the concept of equality of chemical potentials as defined in (1), the following general equations can be obtained.

$$\Delta G_A^{\alpha \rightarrow \beta} + RT \ln \left(\frac{1 - X_\beta}{1 - X_\alpha} \right) = \left({}^E G^\alpha - X \frac{\partial {}^E G^\alpha}{\partial X} \right) - \left({}^E G^\beta - X \frac{\partial {}^E G^\beta}{\partial X} \right), \quad (6)$$

$$\Delta G_B^{\alpha \rightarrow \beta} + RT \ln \frac{X_\beta}{X_\alpha} = \left({}^E G^\alpha + (1 - X) \frac{\partial {}^E G^\alpha}{\partial X} \right) - \left({}^E G^\beta + (1 - X) \frac{\partial {}^E G^\beta}{\partial X} \right). \quad (7)$$

When ${}^E G = 0$, the solution is said to be ideal and the above equations can be considered simplified. Unfortunately, the ideal solution model is too simplistic and few solutions whether liquid or solid conform to it. A wide range of solution models have been suggested in the literature. However, in the present paper only the regular solution model will be used, which postulates that the ${}^E G$ term is equal to the enthalpy of mixing ΔH_m . For the regular solution model

$${}^E G^\alpha = E_\alpha X (1 - X), \quad (8)$$

$${}^E G^\beta = E_\beta X (1 - X), \quad (9)$$

where E_α and E_β are the interaction parameters for the α and β phases respectively. Equations (6) and (7) can now be simplified as

$$\Delta G_A^{\alpha \rightarrow \beta} + RT \ln \left(\frac{1 - X_\beta}{1 - X_\alpha} \right) = E_\alpha X_\alpha^2 - E_\beta X_\beta^2, \quad (10)$$

$$\Delta G_B^{\alpha \rightarrow \beta} + RT \ln \frac{X_\beta}{X_\alpha} = E_\alpha (1 - X_\alpha)^2 - E_\beta (1 - X_\beta)^2. \quad (11)$$

4. Numerical methods

Once the phase stability parameters $\Delta G_A^{\alpha \rightarrow \beta}$, $\Delta G_B^{\alpha \rightarrow \beta}$ and the interaction parameters E_α and E_β are estimated with some confidence, (10) and (11) can be solved by appropriate iterative procedures to obtain values for X_α and X_β , which make it possible to locate $\alpha|\alpha + \beta|\beta$ phase boundaries. Rudman (1969) used a trial and error method by assigning arbitrary values to the unknown X_α and X_β , so that the whole range of composition is covered. The values are then selected which best fit the equations. Kaufman and Bernstein (1970) used a method based on the Newton-Raphson iteration technique,

which will be briefly described here. This method involves selecting a couple of approximate equilibrium values for X_α and X_β as a starting point, from which more precise solutions are obtained using approximation computed as under

$$X_{\beta(n+1)} = X_{\beta(n)} - \frac{1}{(X_{\beta n}, X_{\alpha n})} \begin{vmatrix} F(X_{\beta n}, X_{\alpha n}) & F_{X\alpha}(X_{\beta n}, X_{\alpha n}) \\ G(X_{\beta n}, X_{\alpha n}) & G_{X\alpha}(X_{\beta n}, X_{\alpha n}) \end{vmatrix} \quad (12)$$

$$= X_{\beta(n)} - \frac{\Delta X_{\beta(n)}}{J(X_{\beta n}, X_{\alpha n})}$$

$$X_{\alpha(n+1)} = X_{\alpha(n)} - \frac{1}{J(X_{\beta n}, X_{\alpha n})} \begin{vmatrix} F_{X\beta}(X_{\beta n}, X_{\alpha n}) & F(X_{\beta n}, X_{\alpha n}) \\ G_{X\beta}(X_{\beta n}, X_{\alpha n}) & G(X_{\beta n}, X_{\alpha n}) \end{vmatrix} \quad (13)$$

$$= X_{\alpha(n)} - \frac{\Delta X_\alpha(n)}{J(X_{\beta n}, X_{\alpha n})},$$

where $F(X_\beta, X_\alpha) = 0, G(X_\beta, X_\alpha) = 0$, (14)

and the Jacobian

$$J(X_\beta, X_\alpha) = \begin{vmatrix} F'_{X\beta}(X_\beta, X_\alpha) & F'_{X\alpha}(X_\beta, X_\alpha) \\ G'_{X\beta}(X_\beta, X_\alpha) & G'_{X\alpha}(X_\beta, X_\alpha) \end{vmatrix}. \quad (15)$$

It can be seen that differentiation of thermodynamic properties with respect to the atomic fraction is involved and this becomes more difficult and involved as the number of components increases. They also have to be repeated for all expressions relating the free energy and atom fraction.

5. Binary diagrams

The utility of the Newton-Raphson iterative technique can be illustrated with the development of hypothetical binary phase diagrams reported by Balakrishna and Mallik (1979, 1980) and which are shown in figure 2. To begin with, simple isomorphous phase diagram is calculated when the solution is considered ideal. As the interaction parameters E_L and E_α are increased for the purpose of computation, the solidification range is enlarged and a solid state miscibility gap appears. Between the values of 4250 and 4500 cal/mol for the interaction parameters, an invariant peritectic reaction appears. By further raising the interaction parameter magnitude, a monotectic type reaction can be brought out.

The scope of the calculation can be illustrated further to deal with components exhibiting allotropy. Figure 3 shows the development of phase diagrams involving three phases, liquid (L) and solid phases (α) and (β), with varying combinations of the interaction parameters E_L , E_α and E_β . With small positive values of the interaction parameters, the equilibrium between L/β and β/α phases correspond to azeotropic minima. Increase of the value for E_α leads to the development of a miscibility gap in the α region. A further increase of E_α leads to the formation of an eutectoid reaction.

By suitably varying the relative magnitudes of the interaction parameters a wide range of phase diagrams can be generated. In real systems, however, the solid state interaction parameter will be greater than that of the liquid state. Further, by the very

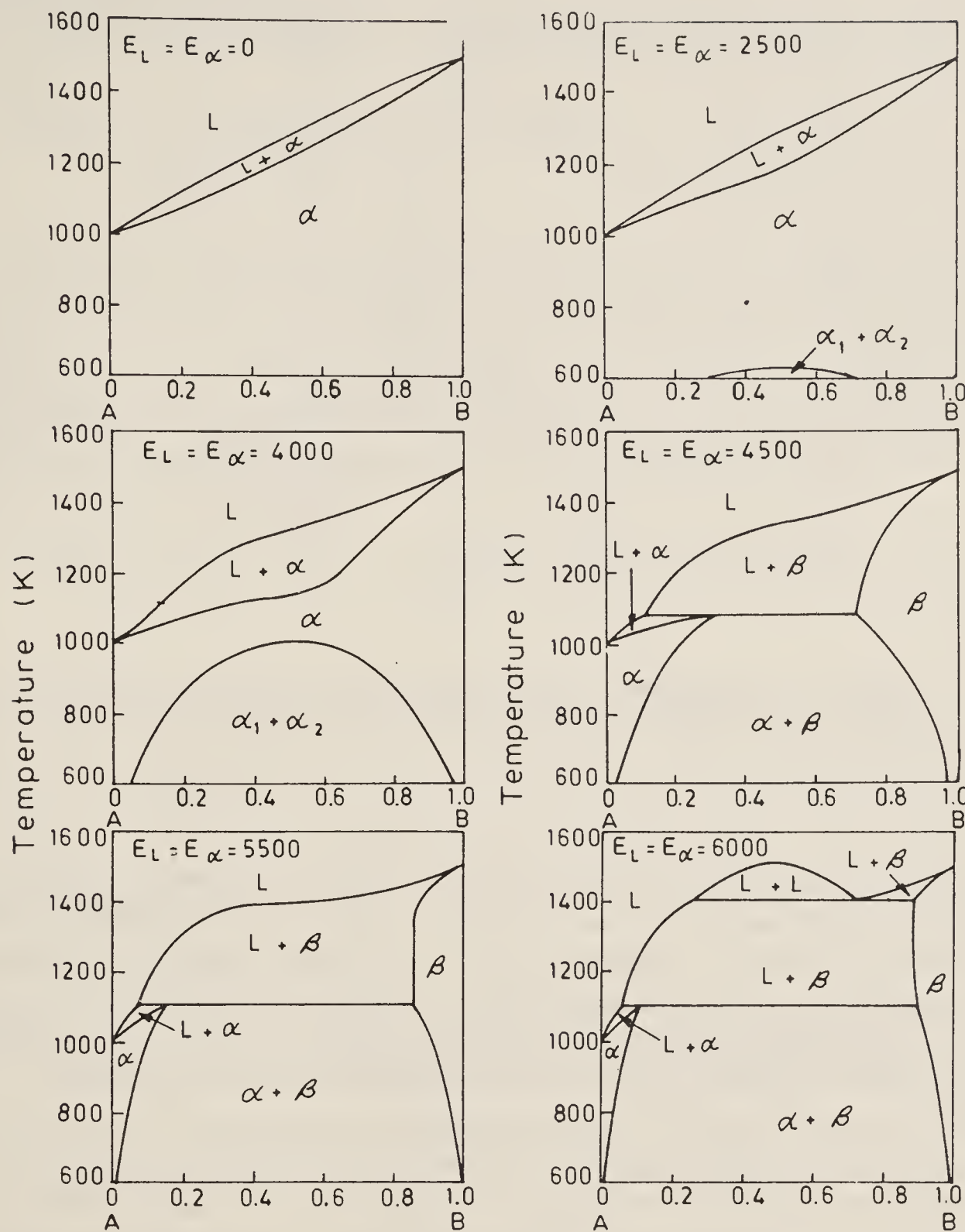


Figure 2. Development of peritectic and monotectic reactions with use of highly positive interaction parameters (cal/mol) (Balakrishna and Mallik 1979).

nature of formalism, the miscibility gaps so obtained are symmetrical. To deal with intermediate phases, in addition to the terminal phases, additional data are needed. Since there are many phase diagrams for which limited or very little thermodynamic data are available, it is quite possible to apply (10) and (11) in reverse, wherein the interaction parameters can be calculated using known values of X_α , X_β at the phase boundaries. The computed interaction parameters can be compared and averaged with available thermodynamic data to replot the phase diagram with more reliability (Appendix 1).

6. Lattice stability

To be able to determine the form of the free energy-composition curves, two important data are needed, which are the lattice stability and the free energy of mixing. While the

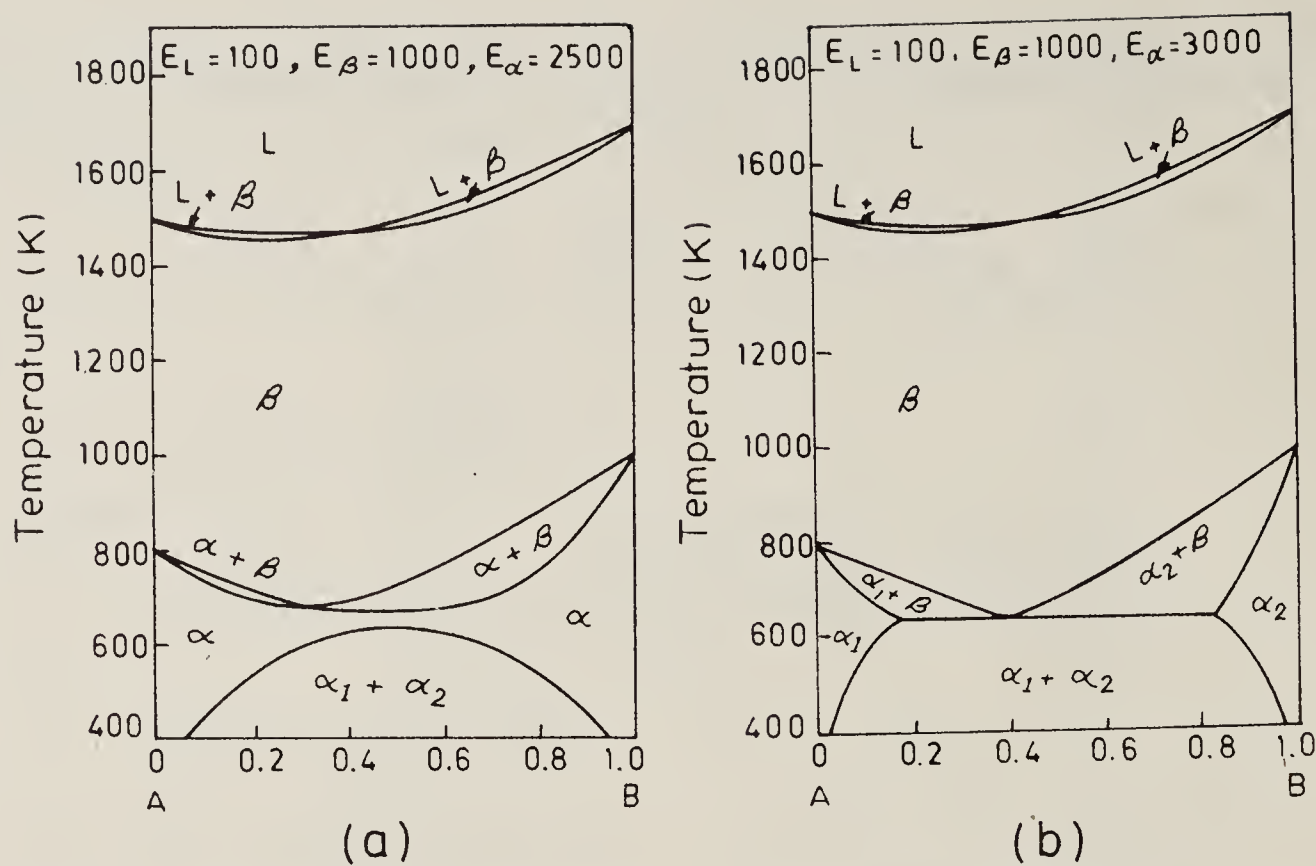


Figure 3. Development of phase diagrams with allotropy of both the components (interaction parameters in cal/mol) (Balakrishna and Mallik 1980).

relative shape of the curves is controlled by the latter, the former i.e. the lattice stability value controls the relative position of the free energy curves. Kaufman and Bernstein (1970) estimated the phase stability values for a number of elements, mainly transition metals, for different structural forms which are liquid, fcc, bcc and cph structures. The regular solution phase diagrams of 72 binary refractory metal systems were computed using the lattice stability values and computed interaction parameters.

While it would be ideal to obtain quantitative information on the lattice stability values from first principle formalism, such calculations are extremely difficult. If a metal exhibits polymorphism at atmospheric pressure, the free energy difference can be estimated from the measurements of the latent heat of transformation, heat of fusion and the volume changes attending the transformations. In cases where no polymorphism is displayed at one atmosphere, phase transformations at high pressures can be studied. The T-P diagram can be used with thermodynamic and volumetric data pertaining to one atmosphere to obtain the lattice stability expressions for various polymorphs. The analysis of phase diagram can enable the estimation of phase stability. For example, the lattice stability of hcp, fcc and bcc forms of Zn has been estimated through individual analysis of Al-Zn, Cu-Zn and Ag-Zn phase diagrams. Kaufman and Nesor (1978) and Kaufman (1978) published an extensive range of lattice stability values for a wide range of elements on coupled phase diagrams and thermochemical data.

7. Empirical equations for solutions

For the calculation of phase diagrams it is necessary to express the thermodynamic properties of multicomponent phases as analytical functions of composition. If no ternary data are available, the following representation for the excess integral free

energy may be used (Kohler 1960)

$$\begin{aligned} {}^E G = & (1 - X_A)^2 {}^E G(BC) + (1 - X_B)^2 {}^E G(CA) + (1 - X_C)^2 {}^E G(AB) \\ & + \sum_{\substack{n \geq 1 \\ m \geq 1 \\ k \geq 1}} \phi_{nmk} X_A^n X_B^m X_C^k. \end{aligned} \quad (16)$$

The three binary terms in (16) gives an exact representation of ${}^E G$ in the ternary system, if the ternary solution as well as all three binary solutions are regular and the ternary terms can be set to zero. An expression for the partial property ${}^E G_A$ corresponding to (16) may be derived by differentiation. Several other empirical equations have been proposed for expressing the thermodynamic properties of ternary systems which are shown in figure 4. Toop (1965) expressed the excess free energy of mixing for a ternary system by the following equation

$${}^E G = \left[\frac{X_B}{1 - X_A} {}^E G_{(AB)} + \frac{X_C}{1 - X_A} {}^E G_{(AC)} \right] X_A + [(1 - X_A)^2 {}^E G_{(BC)}] X_B / X_C \quad (17)$$

The equations given by Toop (1965) and Kohler (1960) have also been used with an additional term of the form $X_A X_B X_C (AX_A + BX_B + CX_C + D)$ to represent experimental data, the coefficients A, B, C and D being calculated from a least square analysis. Pelton and Bale (1977) represented the integral molar excess free energy E at any constant temperature for the ternary system (Bi-Cd-Zn) by a general polynomial expansion as given below

$${}^E G = \sum \phi_{nmk} X_{\text{Zn}}^n X_{\text{Cd}}^m X_{\text{Bi}}^k, \quad (18)$$

where the ϕ_{nmk} are constant coefficients. Any number of terms necessary to adequately represent the system may be included. Expressions for the partial molar excess free

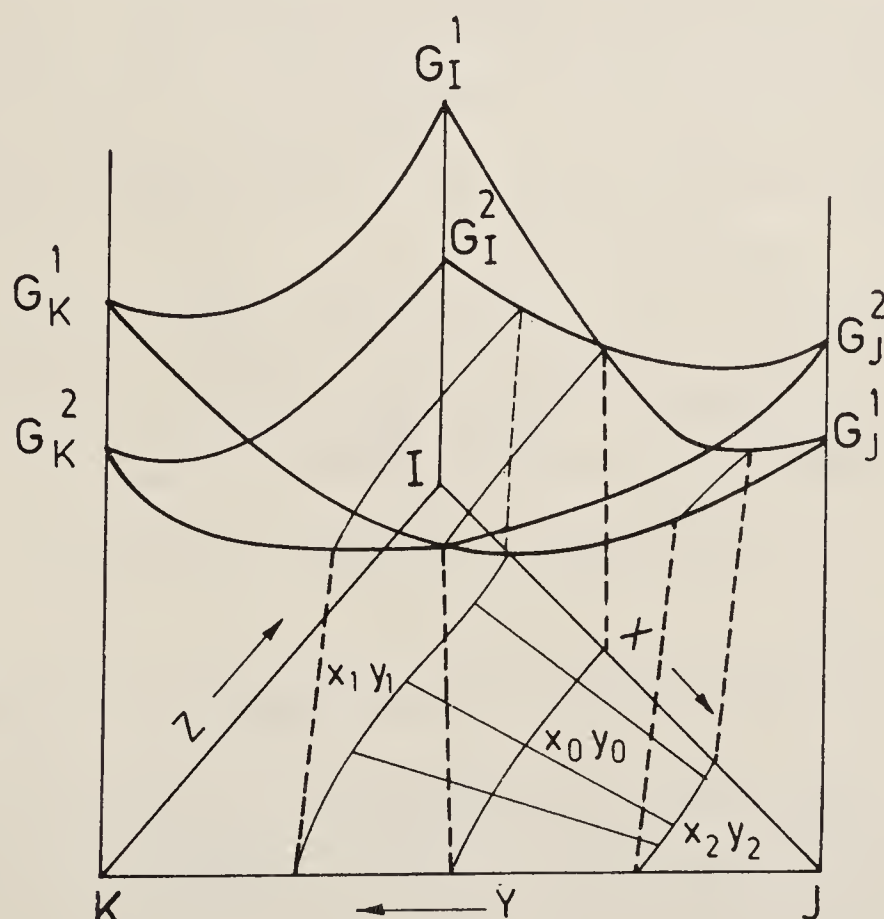


Figure 4. Free energy surfaces of competing phases in ternary system and application of the common tangent principle.

energy may be obtained by differentiation of (18). Using the above formalism Pelton and Bale (1977) calculated the phase diagrams for the Bi-Cd-Zn, Bi-Cd-Sn and Fe-Cr-Ni-O systems.

8. Ternary diagrams

The formalism reported for the binary system can be extended to the ternary system. The integral free energy of a single phase solution with 3 components can be expressed as (Kaufman and Bernstein 1970)

$$G[X, Y, T] = ZG_i + XG_j + YG_k + RT(Z \ln Z + X \ln X + Y \ln Y) + XZE_{ij} + YZE_{ik} + XYE_{jk}, \quad (19)$$

where X, Y, Z are atomic fraction of elements J, K and I respectively, G_i, G_j, G_k the free energies of the pure element I, J, K and E_{ij}, E_{ik} and E_{jk} are the binary interaction parameters.

The partial free energies of I, J, K in a given phase are

$$\begin{aligned} \bar{G}_i &= G - X \frac{\partial G}{\partial X} - Y \frac{\partial G}{\partial Y}, \\ \bar{G}_j &= G + (1 - X) \frac{\partial G}{\partial X} - Y \frac{\partial G}{\partial Y}, \\ \bar{G}_k &= G - X \frac{\partial G}{\partial X} + (1 - Y) \frac{\partial G}{\partial Y}. \end{aligned} \quad (20)$$

The equilibria between two phases, liquid (L) and solid (S) can be shown schematically by the common tangent plane in figure 4, which shows the locus of points (X_1, Y_1) and (X_2, Y_2) corresponding to possible tangent points of a plane tangent to the two free energy surfaces $G^1[X, Y, T]$ and $G^2[X, Y, T]$. As with the binary diagrams and equations (10) and (11), similar equations can be written for the ternary case as

$$\begin{aligned} A_i &= \Delta G_i^{1 \rightarrow 2} + RT \ln(Z_2/Z_1) + (E_{ij}^2 X_2^2 - E_{ij}^1 X_1^2) + (E_{ik}^2 Y_2^2 - E_{ik}^1 Y_1^2) + (\Delta E^2 X_2 Y_2 - \Delta E^1 X_1 Y_1) = 0, \\ A_j &= \Delta G_j^{1 \rightarrow 2} + RT \ln(X_2/X_1) + [E_{ij}^2 (1 - X_2)^2 - E_{ij}^1 (1 - X_1)^2] + (E_{ik}^2 Y_2^2 - E_{ik}^1 Y_1^2) - [\Delta E^2 Y_2 (1 - X_2) - \Delta E^1 Y_1 (1 - X_1)] = 0, \\ A_k &= \Delta G_k^{1 \rightarrow 2} + RT \ln(Y_2/Y_1) + (E_{ij}^2 X_2^2 - E_{ij}^1 X_1^2) + [E_{ik}^2 (1 - Y_2)^2 - E_{ik}^1 (1 - Y_1)^2] - [\Delta E^2 X_2 (1 - Y_2) - \Delta E^1 X_1 (1 - Y_1)] = 0, \end{aligned} \quad (21)$$

where $\Delta E = E_{ij} + E_{ik} - E_{jk}$. (22)

Equation (21) is solved numerically by the Newton-Raphson iteration technique (Appendix 2).

For starting the iteration one has to choose the initial value of X_1 for the independent variable and then choose the starting values of X_2^0, Y_1^0, Y_2^0 . As shown in figure 5 the two binary edges IJ and JK define limits of X_1, Y_1 and X_2, Y_2 . The iteration is continued until it converges on a solution of X_2, Y_1, Y_2 . The value of X_1 is then changed slightly and the procedure is repeated using previous solutions found for X_1 . The correctors

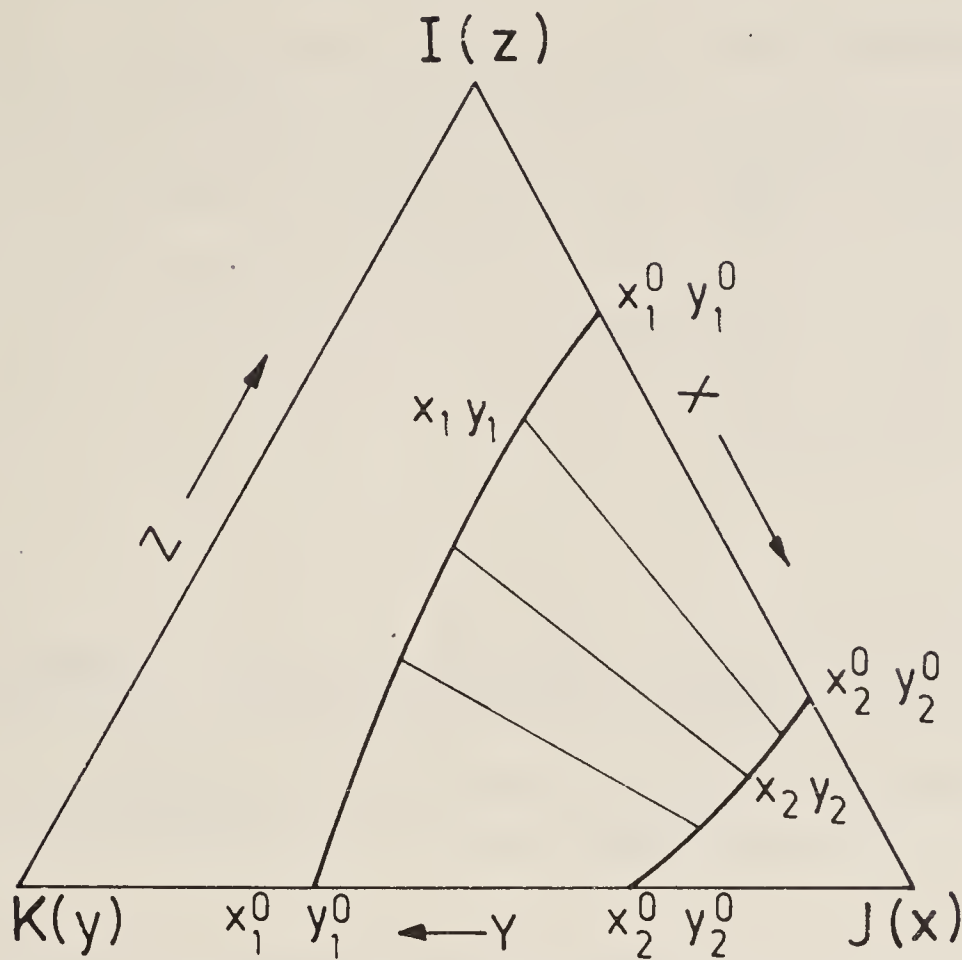


Figure 5. Computation of phase boundaries and tie lines with isothermal ternary sections from IJ edge to the JK edge.

$\Delta X_2, \Delta Y_1, \Delta Y_2$ in the determinant form are

$$\begin{aligned}
 J \Delta X_2 &= \left| \begin{array}{c} -A_i \frac{\partial A_i}{\partial Y_1} \frac{\partial A_i}{\partial Y_2} \\ -A_j \frac{\partial A_j}{\partial Y_1} \frac{\partial A_j}{\partial Y_2} \\ -A_k \frac{\partial A_k}{\partial Y_1} \frac{\partial A_k}{\partial Y_2} \end{array} \right|, \\
 J \Delta Y_1 &= \left| \begin{array}{c} \frac{\partial A_i}{\partial X_2} - A_i \frac{\partial A_i}{\partial Y_2} \\ \frac{\partial A_j}{\partial X_2} - A_j \frac{\partial A_j}{\partial Y_2} \\ \frac{\partial A_k}{\partial X_2} - A_k \frac{\partial A_k}{\partial Y_2} \end{array} \right|, \\
 J \Delta Y_2 &= \left| \begin{array}{c} \frac{\partial A_i}{\partial X_2} \frac{\partial A_i}{\partial Y_1} - A_i \\ \frac{\partial A_j}{\partial X_2} \frac{\partial A_j}{\partial Y_1} - A_j \\ \frac{\partial A_k}{\partial X_2} \frac{\partial A_k}{\partial Y_1} - A_k \end{array} \right|, \tag{23}
 \end{aligned}$$

where J , the Jacobian determinant is

$$J = \begin{vmatrix} \frac{\partial A_i}{\partial X_2} & \frac{\partial A_i}{\partial Y_1} & \frac{\partial A_i}{\partial Y_2} \\ \frac{\partial A_j}{\partial X_2} & \frac{\partial A_j}{\partial Y_1} & \frac{\partial A_j}{\partial Y_2} \\ \frac{\partial A_k}{\partial X_2} & \frac{\partial A_k}{\partial Y_1} & \frac{\partial A_k}{\partial Y_2} \end{vmatrix}. \quad (24)$$

8.1 Calculated phase diagrams

Figure 6 shows the calculated isothermal section for the Mo-V-W system by Bhansali and Mallik (1984) using the above approach, for which experimental diagram is not available. All the binaries are of the isomorphous type with complete solid solubility. Both ideal and regular solution models have been used. It may be noted that while the

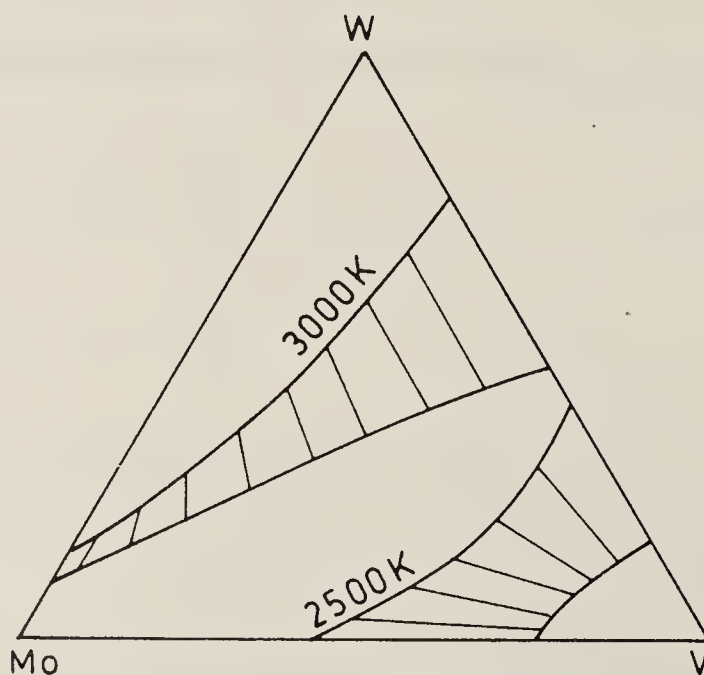


Figure 6. Calculated isothermal sections for the Mo-V-W ternary phase diagram (Bhansali and Mallik 1984).

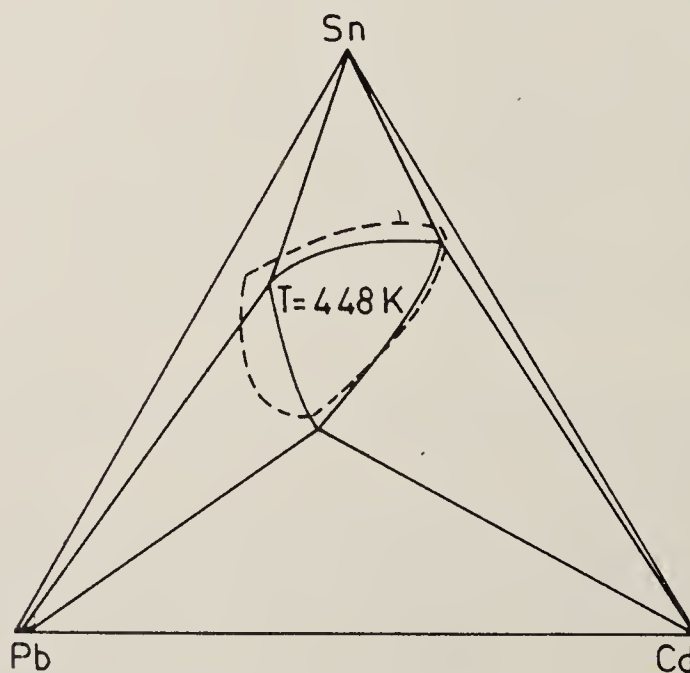


Figure 7. Calculated isothermal sections for the Cd-Pb-Sn ternary phase diagram (Bhansali and Mallik 1984) --- experimental.

ideal solution model produces almost straight liquidus and solidus lines, the regular solution model produces more realistic contours which are naturally curved.

Figure 7 shows the calculated liquidus projections for the ternary system Cd-Pb-Sn, (Bhansali and Mallik 1984) which shows one eutectic reaction at each of the binary edges. The figure also shows experimental lines obtained by thermal analysis and the match between experimental and computed lines is rather satisfactory. This is so considering that only binary phase diagram data have been used in the calculation of this diagram. Two alternatives are available. The first is to use calculated binary interaction parameters. The second is to use interaction parameters which are manipulated to produce the best fit with the binary diagram. In the above ternary phase diagrams the second alternative has been used. It is further possible to introduce ternary interaction parameters. This is where some measurements of thermodynamic data in the ternary region can be extremely useful.

8.2 Ternary miscibility gap

The magnitudes of the interaction parameters indicate the extent of solubility or immiscibility. Positive interaction parameter represents repulsive interaction between the two atomic species in solution. If the binary interaction parameter exceeds $2RT$ a miscibility gap is expected, which may or may not extend to the other binary edge depending on the magnitude of the other binary interaction parameter. The problem of defining the phase boundaries is similar to the two solution phase situation. The schematic free energy surface is shown in figure 8, which shows the occurrence of miscibility gaps on IJ and IK binary edges. Equation (21) can be used with the modification that $\Delta G_i^{1 \rightarrow 2} = 0$, $E_{ij}^1 = E_{ij}^2 = E_{ij}$. In case only one binary shows the miscibility gap the upward convexity of the free energy surface will gradually disappear as one moves from one binary edge to the other.

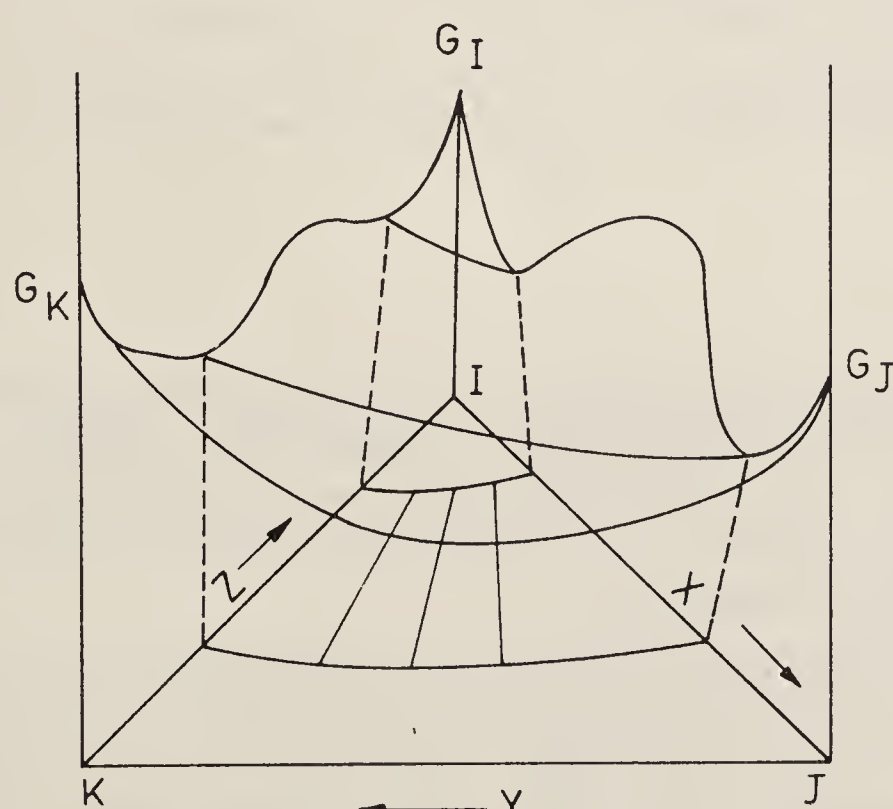


Figure 8. Schematic representation of the free energy surface for miscibility gaps at two binary edges.

9. Hill climbing technique

It has been pointed out that the differentiation of thermodynamic properties with respect to atomic fraction becomes more difficult and cumbersome as the number of components increases beyond three. The problem becomes even more difficult if there are small erroneous inflexions in the free energy curve determined from experimental observations. Nelder and Mead (1965) suggested a simplex approach which finds the minimum positions on the Gibbs free energy surface by hill climbing computational technique. In this method, the free energy of a multicomponent system is calculated at a certain number of coordinates, usually 10. The point which has the highest value of free energy is replaced by another one. The procedure is iterated until a minimum value is obtained. This technique has been used by Counsell *et al* (1971) to calculate the miscibility gap in the liquid Cd-Pb-Zn and Cd-Pb-Sn-Zn systems. The method can also be used when tables of discrete values of thermodynamic data are used in place of analytical expressions. The minimization of free energy has been tested for two-phase separation in binary, ternary and quaternary mixtures. The procedure can be used to minimize a function of m variables by comparison of the values of this function at $m + 1$ points, followed by replacement of the point corresponding to the highest value of the function by another point. The process is continued by reflection, contraction and expansion upto the point when a minimum value is obtained.

10. Higher order phase diagrams

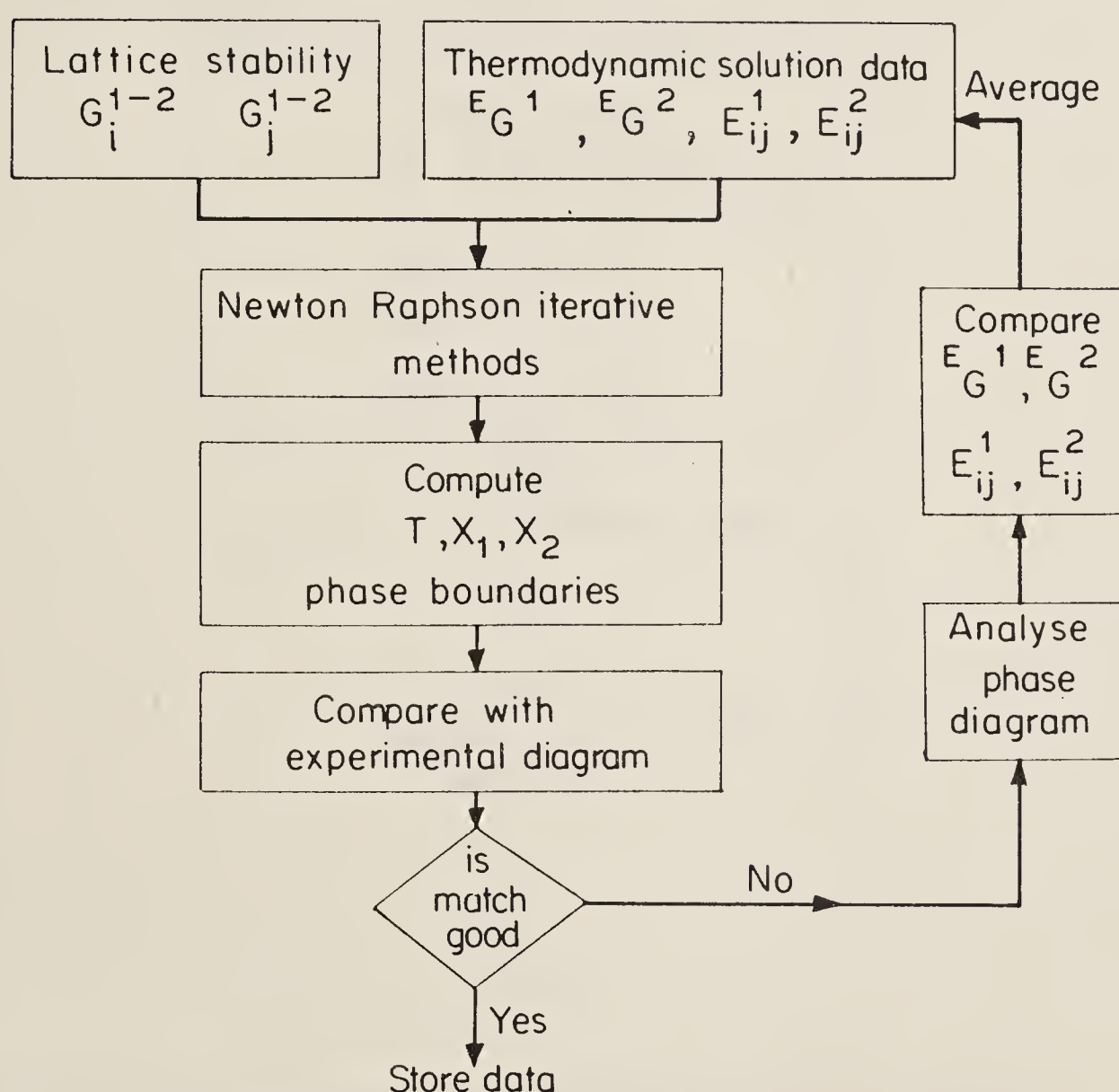
A quaternary phase diagram is usually represented as a regular tetrahedron, where the four equilateral triangular surfaces represent the 4 ternary diagrams and the six edges represent 6 binary diagrams at a given temperature. The lattice simplex method has been used (Ansara 1979) to express mathematically liquidus or solidus volumes in higher order systems. In principle, the method (Scheffe 1958; Gorman and Hinman 1962) involves constructing mathematical models, commonly polynomials, which correlate the property and composition of test alloys. To calculate the coefficients of the equations, the properties are measured according to a definite distribution within a simple lattice. Relatively few quaternary systems have been investigated in detail.

11. Conclusions

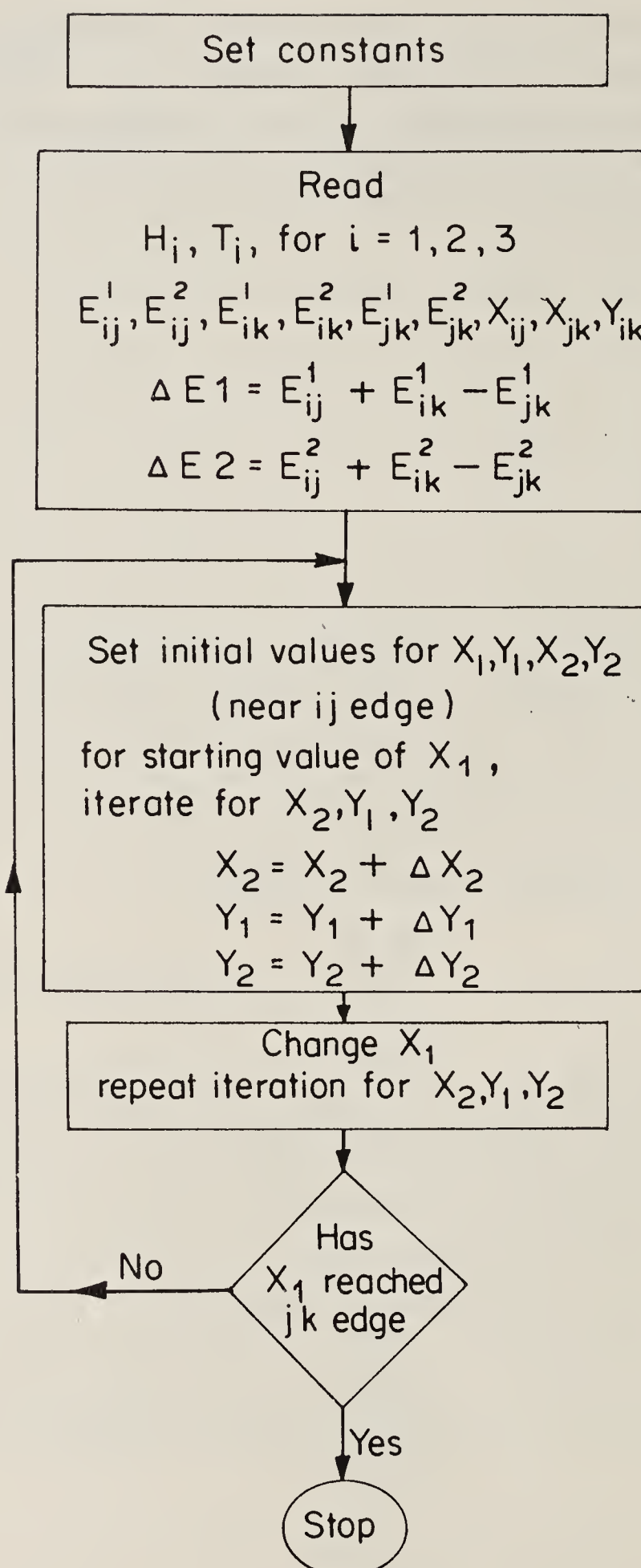
The calculation of binary phase diagrams has been actively pursued in the last 25 years. While adequate description exists for the terminal phases (bcc, fcc and hcp forms), phase diagrams with several intermediate phases can only be attempted with some experimental data about their stability. The regular solution model, notwithstanding its limitations has been used quite extensively.

For the calculation of ternary phase diagrams the starting point can be the binary system data. Analytical series expansions have been developed for representing the thermodynamic data of ternary and higher order solutions as a function of composition. A major uncertainty relates to the extension of the binary intermediate phases into the ternary regions. Asymmetrical miscibility gaps also cannot be determined without some data.

Such computational techniques which use the differentiation of thermodynamic parameters with respect to composition become more difficult beyond ternary diagrams. Thus, use of other minimization techniques, which do not involve differentiation may be more attractive. As yet, the calculation of quarternary phase diagrams has been attempted on a limited scale only.



Appendix 1. Flow diagram for coupling of thermodynamic data with phase diagram data for the generation of averaged phase diagram.



Appendix 2. Flow diagram for the iterative calculation of phase boundaries in ternary diagram isothermal sections.

References

- Ansara I 1979 *Int. Metall. Rev.* **23** 8 20
 Balakrishna S S and Mallik A K 1979 ICMS-77 Varanasi, Indian Inst. of Met, Varanasi p. 107
 Balakrishna S S and Mallik A K 1980 *Trans. Indian Inst. Met.* **33** 155
 Bhansali A and Mallik A K 1985 (Communicated)
 Counsell J F, Lees E B and Spencer P J 1971 *Met. Sci. J.* **5** 210
 Chart T G, Counsell J F, Jones G P, Slough W and Spencer J P 1975 *Int. Metall. Rev.* **20** 57

- Gaye H and Lupis C H P 1975 *Metall. Trans.* **4** 685
Gorman L W and Hinman J E 1962 *Technometrics* **4** 463
Hardy H K 1953 *Acta Metall.* **1** 202
Hillert M 1970 *Phase transformations* (Ohio: Am. Soc. for Metals)
Kohler F 1960 *Monatsh. Chem.* **91** 738
Kaufman L and Bernstein H 1970 *Computer calculations of phase diagrams* (New York: Academic Press)
Kubaschewski O and Barin I 1974 *Pure Appl. Chem.* **38** 469
Kaufman L and Nesor H 1978 CALPHAD (*Computer coupling of phase diagrams and thermochemistry*) **2** 81
Kaufman L 1978 CALPHAD (*Computer coupling of phase diagrams and thermochemistry*) **2** 117
Nelder J A and Mead R 1965 *Comput. J.* **7** 308
Pelton A D and Bale C W 1977 CALPHAD (*Computer coupling of phase diagrams and thermochemistry*) **1** 253
Pelton A D and Thompson W T 1975 *Prog. Solid State Chem.* **10** 119
Rudman P S 1969 *Advances in materials research* (New York: Interscience) Vol. 4
Scheffe H 1958 *J. R. Stat. Soc. B* **20** 344
Toop G W 1965 *Trans. Metall. Soc. AIME*, **233** 850
Wagner C 1954 *Acta Metall.* **2** 242
White J L, Orr R L and Hultgren R 1977 *Acta Metall.* **5** 747

Computer-aided design of rolling mills

K G PANDEY

MECON (India) Limited, Ranchi 834 002, India

Abstract. Computers have been used for design of rolling mills since 1960s. Easy access to high speed digital computers has facilitated use of more accurate rolling theories for design work and comprehensive computer simulations have been developed for all types of mills. These simulations include optimization of roll pass sequence, calculation of roll force, torque and temperature and detailed time studies for productivity calculations. These aspects of mill simulation are examined with specific examples.

In the design of rolling mills equipment, computer-aided design has been widely used. The available software, which covers both steady state and dynamic analysis of items such as mill stands, drive systems, manipulators, cooling beds, roll cooling, and automatic gauge control systems, is reviewed with special reference to the nature of analysis and range of applications.

Computer drafting is being increasingly used by rolling mills designers for both interactive and non-interactive applications. The integration of computer graphics with the design software holds promise for improving the productivity and creativity of designers and is an active area of development in rolling mills design organizations. A specific application where such integration has been achieved is discussed.

Keywords. Computer-aided design; rolling mills; computer drafting; computer simulation

1. Introduction

Mathematical modelling and computer simulation are being widely used today both for design and control of rolling mills. Many of the complex phenomena involved in the rolling process can be understood and quantified only with the help of computer models. Computer simulation is also used to accurately predict the effect of variations in rolling process on the mill design and for optimization studies.

The earliest attempt to develop a mathematical model of the rolling process dates back to the pioneering works of Siebel (1924) and von Karman (1925). By the end of the 1950s substantial theoretical work had been done and many design methods developed. Much of the impetus for this work came from designers and builders of rolling mills. Before undertaking the detailed design of a mill it is a normal practice to compute rolling schedules to properly size the mill for a specific application. The rolling schedule shows the nature and magnitude of forces, torques and power parameters required to reduce metal of a given stock size to the final finish size. These parameters depend on the size of the mill, the reduction pattern adopted and the other conditions of rolling such as temperature, speed, tension, roll coolant etc. It is usual to evaluate several alternatives in terms of their suitability for customer requirements.

The high volume of work involved together with the complexity of various calculations has led to the widespread use of computer methods in almost every phase of rolling mills design. The present day applications of computer-aided design (CAD) may be broadly grouped into (i) simulation models for specific types of mills and (ii) programs for detailed analysis and design of individual equipment. In most of the

leading design organizations dealing with rolling mills, computer drafting is being gradually integrated with the design software.

2. Mill simulation

In the design of a new rolling mill the starting point is a mill simulation program for the specific type of mill i.e. slabbing and blooming mill, billet, bar and section mill, rod mill, plate mill, hot strip mill, single stand reversing and non-reversing cold mill, fully continuous tandem cold mill and skin pass mill. Broadly speaking all mill simulation programs consist of three parts for: (a) calculating the pass sequence (b) computing the roll separating force, torque and power required and (c) a time study for evaluating the productivity. Temperature calculations are also an integral part of (a) and (b) above in the simulation of hot rolling mills. These calculations constitute interacting loops that are intimately related to each other. A straight forward calculation is not possible but for purposes of discussion the four calculations will be treated separately.

2.1 Roll pass sequence

The various factors to be considered in the calculation of a roll pass sequence are pass geometry, roll bite, temperature and other rollability conditions, metal spread, technological limitations of reduction per pass and overall reduction, limitations arising out of mill parameters such as roll force limit and torque limit, and the requirements of mill productivity. In general the calculation of a roll pass sequence aims at maximizing the productivity of the mill without violating any of the constraints due to technology or equipment. Clearly the calculations relating to roll force, torque and power, along with temperature and productivity calculations are implicit in any scheme for computing the roll pass sequence. The resultant complexity makes this an ideal situation for the use of CAD. A few illustrative applications are discussed in detail.

2.1a Single stand cold mill: A cold reducing mill offers two major simplifications: temperature effects can be largely ignored and the metal spread is also negligible. Programs have been developed in which it is necessary only to define the various constraints of roll-bite angle, permissible reduction per pass and total roll force limit, mill speed, torque and power limit and available tension. The optimal reduction pattern that requires minimum number of passes is then automatically calculated. As a first step the rollability conditions are checked. The maximum draft which does not violate the constraints of bite angle and material reduction limits is then computed. With this value of draft the roll force calculation loop is referenced and the values of roll force and torque obtained are checked against the specified constraints. If any of the constraints is violated the draft is reduced and the calculation repeated. With properly defined gradients, a feasible solution is easily found.

2.1b Dimensioning of shaped passes: The need for accurate calculation of roll pass sequence is greater for shaped passes in that the roll grooves have to be cut according to these dimensions and any error in the grooves reflects on the quality of the finished product. The calculations are also more complex because the additional factors of metal spread and temperature assume an important role. As an illustration of the general

approach, the dimensioning of intermediate ovals with the entry and delivery squares defined will be considered. To start the iteration, some reasonable dimensions of the intermediate oval are assumed (table 1). With these assumed dimensions, the various constraints are checked. If any of the conditions is violated a gradient is computed. This gradient is used to calculate the next trial value. The iterative procedure is not prone to oscillation and normally converges within 4 to 6 trials.

2.2 Roll force models

The many roll force models available today may be grouped under one of two broad heads: models based on measured field data of specific energy consumption vs elongation and analytical models based on resistance to deformation vs temperature (for hot rolling) or yield strength vs reduction (for cold rolling). Used with care, both approaches give acceptable results.

The analytical models are, however, better in some ways. They can be used to calculate the roll force and torque only from the geometrical and physical data about the rolls and the rolled material. They are thus more general in nature and may be used more readily to examine the effect of extending the existing regimes of rolling practice.

Analytical models of the rolling process are of course extremely complex. The physical phenomenon is essentially one of inhomogenous compression of a material with variable yield stress moving within the roll bite with a frictional drag that varies in nature, magnitude and direction. The associated mathematics is further complicated by the geometry of a rectilinear work piece passing through a roll gap bounded by two curvilinear roll surfaces.

The many analytic models reported in the literature vary widely in terms of level of detail, complexity and accuracy.

The model that one adopts for simulation is dictated by the end use for which the simulation is developed. Three discrete levels of modelling can be identified. When the modelling is aimed at understanding and quantifying the physical phenomenon involved in rolling, a very high level of detail such as is offered by Orowan (1943) is required. At this level, physical assumptions are almost totally avoided and mathematical approximations are also not made. For purposes of day-to-day design, the simulations need to accurately reflect only the main features of the rolling process and they need to consider only the most important factors. Such models may include many physical assumptions valid for specific design regimes. Mathematical approximations may or may not be required depending on the mathematical complexity of individual design loops and the sensitivity of the whole model to the particular design variable.

Table 1. Iterations for dimensioning of an oval groove

Iteration no.	Oval width (mm)	Oval height (mm)	Norm of error vector
1	52.5	12.00	15.04
2	30.99	13.92	2.59
3	30.16	15.34	0.16
4	30.48	15.23	0.001

Input square: 21 mm. Delivery square: 16.2 mm

Lastly a model that is to be used for process control has to be sufficiently simple to ensure that the computation time adequately meets the control requirements. Such a model must of necessity include all reasonable physical approximations and many mathematical approximations as well.

As an illustration of the above, one may consider a problem that is of fundamental importance in the simulation of rolling process. In any rolling mill, material of large stock size A₁ enters at a low speed V₁ and is reduced to a smaller size A₂ leaving at a higher speed V₂. The deformation is carried out by rolls rotating with a peripheral speed, V, V₁ < V < V₂. A basic question that is important for all calculations is the location of the neutral plane where the metal velocity is equal to the peripheral velocity of the rolls. For a precise determination of the neutral plane it is necessary to integrate the rolling equation:

$$df/d\phi = D s \cos \phi (\tan \phi \pm \mu)$$

where f is the horizontal force per unit width, s the normal roll pressure, D the roll diameter, ϕ the angular coordinate of arc of contact and μ the coefficient of friction as shown in Figure 1 below, with full consideration of sticking/slipping friction, roll flattening etc. This requires numerical integration of a nonlinear variable parameter differential equation and the results allow for a precise understanding of metal behaviour in the roll bite.

For most design calculations, however, such complexity is not required and the use of a simplified closed form equation such as that given by Sims (1954) is generally acceptable:

$$\phi_n = \sqrt{\frac{h_2}{R'}} \tan \left[\left\{ \frac{\pi}{4} \ln(1-r) + (R'/h_2)^{\frac{1}{2}} \arctan \left(\frac{r}{1-r} \right)^{\frac{1}{2}} \right\} / 2(R'/h_2)^{\frac{1}{2}} \right].$$

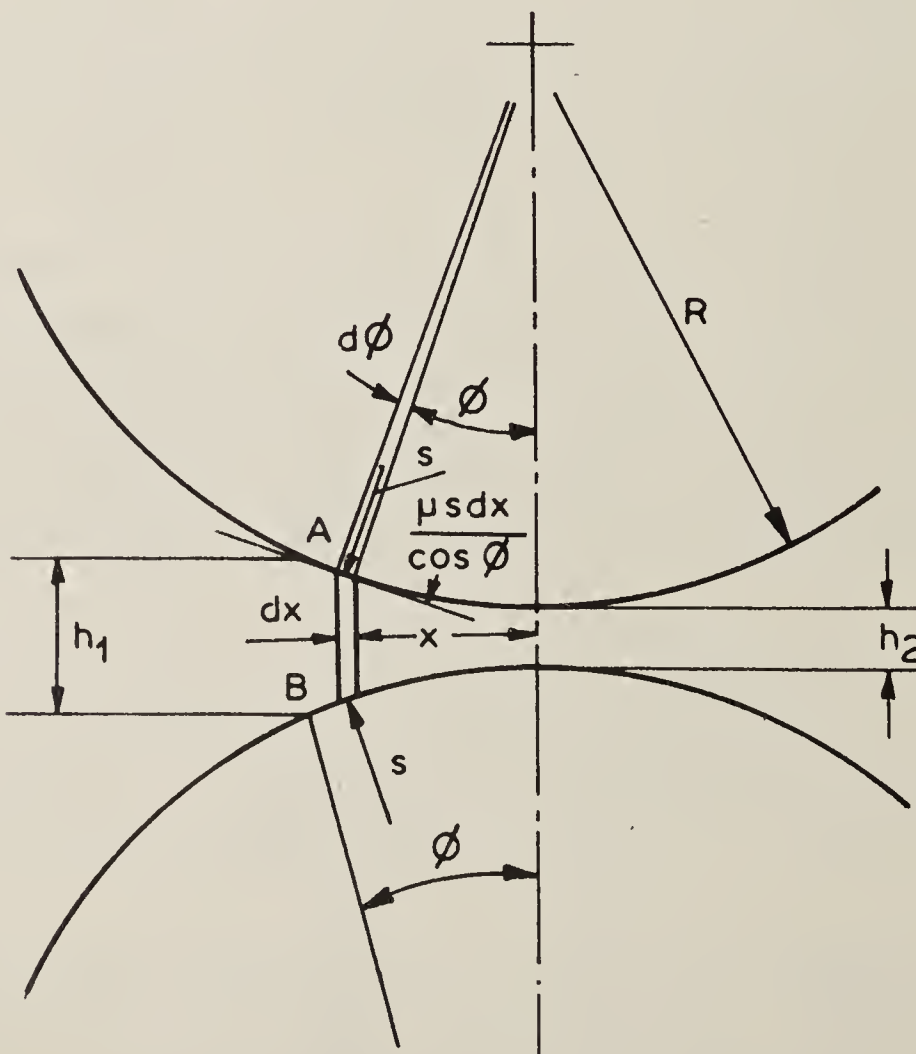


Figure 1. Deformation in roll gap.

For purposes of on-line computer control even the above equation is not acceptable because of the computation time required, and a polynomial approximation of the type

$$\phi_n = a + bx + cx^2; x = \left(\frac{h_1}{R}\right)^{\frac{1}{2}} \left[\left(\frac{1-r}{r}\right)^{\frac{1}{2}} - \left(\frac{1-r}{\sqrt{r}}\right) \right]; r = 1 - h_2/h_1$$

which is sufficiently accurate may be used.

At the second level, which is of greater interest to design organizations, the calculation of roll force is generally straightforward; a notable exception being the estimation of roll flattening. As expressed by Hitchcock (1935), the extent of roll flattening depends both on the undeformed roll diameter and the roll force:

$$R' = f(r, P)$$

where R is the deformed roll radius, r , the undeformed radius and P , the roll separating force. Since the roll separating force is itself dependent on the contact arc, an iterative solution is called for.

Tension is an important technological parameter, particularly in cold rolling. For the results of simulation to be meaningful, the model used must take proper account of this factor. Further, in the process of optimizing the pass sequence, the iterative process must continually seek to maintain optimum levels of tension.

2.3 Temperature calculations

Temperature calculations constitute an essential part of all hot mill simulations. These calculations are required for estimating the force and power parameters of the process because they are mutually related to the temperature. Proper analysis of temperature conditions is also necessary for determining the thermal stresses in the rolls and for designing the roll cooling systems. Additionally, proper control of temperature is important from the viewpoint of the physical and mechanical properties of the metal and dimensional tolerance of the rolled product. Numerous temperature models have been reported in the literature. They are mostly quite detailed in concept but usually involve the "matching" of certain coefficients with experimental data which somewhat limits the predictive value of these models for design purposes.

For temperature calculations it is common practice to divide the roll into different zones as shown in figure 2. Within the roll gap, the heat transfer mechanism consists of heat generation in the strip through plastic deformation and conductive heat transfer between the rolls and the metal. Outside the contact area, both the strip and rolls loose heat through radiation, convection and to the cooling water.

The heat transfer mechanism in the roll gap is perhaps the most complex. In a model proposed by Bryant and Heselton (1982), the roll gap heat transfer to the rolls has been analyzed in terms of multiple line sources. Cernis' solution for line sources is used in conjunction with the method of superposition to calculate the steady state roll temperature distribution with depth at any angle. Similarly, a discrete model of the temperature distribution in the strip is also developed considering unsteady state heat transfer to the rolls. The two equations are solved simultaneously with the boundary condition being that the surface temperatures of roll and strip are equal along the contact arc. The heat transfer mechanism in other zones may be analyzed reasonably well with well-established finite difference methods.

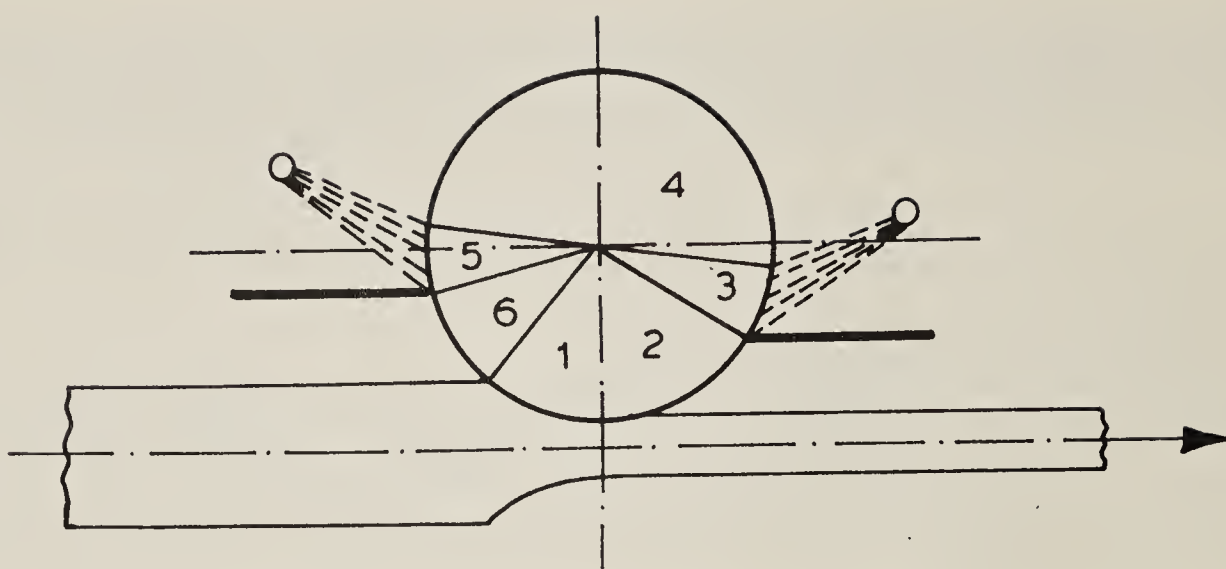


Figure 2. Heat transfer zones of a work roll.

2.4 Productivity calculations

In order to obtain an accurate estimate of mill productivity, all mill simulation models incorporate realistic time studies. These time studies include gap time between pieces, material feeding time, acceleration time, run time at top speed, deceleration time, tail-out time and reversal time. Motor heating is always estimated as an integral part of the mill simulation and the motor characteristics of torque vs speed are fully taken into account. As an illustration of the extent to which detailed analysis is undertaken let us consider the acceleration of a tandem cold mill train. A program that is used for this analysis takes into consideration the variation in inertia of the input and delivery coils, the inertia of the drive trains, the rolling power in each stand and the torque vs speed characteristic of all individual motors. If one of the motors is in current limit at any point of time the acceleration rate is accordingly reduced. Similarly in the simulation of primary mills, the torque vs speed characteristic of the main drive motor is fully taken into account. If the motor goes into current limit after having accelerated beyond the base speed, the acceleration ramp is immediately reduced to a level consistent with the available torque and the combined inertia of the drive train and work piece.

3. Equipment design program

The mill simulations discussed above are required in order to properly size the rolling mills for specific requirements. For the detailed design of individual equipment they are of immense value as a starting point in that they serve to define the nature and magnitude of forces and stresses acting on the system. A different set of "equipment design" programs is required for the routine analysis and design of individual equipment such as mill housings, screwdown systems, drive systems, manipulators, roller tables, cooling beds and winding/unwinding reels. Both static and dynamic analysis are required. In addition, general purpose packages such as STRUDL II are also used as and when required for specific problems. Some of the more important programs in this category are discussed below.

In the ultimate analysis, the detailed design of individual equipment does influence the nature and magnitude of forces developed. Polukhin (1975) attempted to integrate these effects and obtained some rather interesting results but for most design purposes the prevalent method is to isolate the two. The results obtained are sufficiently accurate.

3.1 Analysis of mill stand stresses and deformation

The basic working element in the rolling mill is of course the mill stand which houses the rolls.

The roll separating force required to deform the metal acts on the rolls to cause stresses and deformations in the rolls, bearings, chocks, screws and the housing itself. As a result of elastic deformations in these elements, the effective (active) roll gap varies with the roll separating force.

Large variations in the active roll gap not only result in non-uniform dimensions of the rolled product and variations in interstand tension but they adversely affect the output of the mill and life of rolls. Roll force variations may be as high as 10–15 % of the nominal value and it is therefore important to increase the stand stiffness to as high a value as possible within the constraints of mill size. Proper understanding of mill stand stresses and deformations makes it possible to evaluate the effects of various factors on the stiffness of the stand and optimize the design of the mill housing. The models used for these studies are based on frame analysis and they fully take into account the deflections of the rolls, bearings, chocks, screws and also the compression of the working fluid in case of hydraulic mills.

Dynamic analysis of the mill housing is also required for the design and optimization of automatic gauge control systems as described later. For these purposes it is generally sufficient to use a second order model for the mill housing.

3.2 Torque amplification studies

In much the same way that the mill stand serves to exert the forces required for deforming the metal, the mill spindles must be properly designed to transmit the torque from the motor to the rolls. The sharp increase in operating speeds of mills during the 1960s led to several premature failures of the mill drive components which could not be explained by the conventional steady state analysis used in mill design upto that time. This drew attention to the phenomenon of transient torsional vibrations in mill drive systems. Transient oscillations can produce mechanical torques many times greater than the electrical ratings and resonant or near resonant conditions can lead to fatigue failures. Because of the large number of masses and gears in their drive trains the hot strip mills are particularly susceptible to high torque amplifications, and the first attempt at such analysis was with respect to these mills. In most cases these drives are subjected to linearly varying torques only and the drive systems may be modelled as a linear oscillatory system with proper representation of the inertias, torsional stiffness, damping action in the bearings and the applied torques. In the primary (reversing) mills such as the blooming and slabbing mills, nonlinear effects such as backlash become important and linear models no longer suffice.

In either case, for adequately describing the physical system, the mathematical model has to be of high order. The overall drive system consists of two subsystems i.e. the electrical drive and control system and the mechanical system. In earlier studies relating to hot strip mills the mechanical system only was analyzed but for the reversing primary mills, the interactions of the two subsystems become important and a more elaborate model as shown in figure 3, is required.

The solution of the associated differential equations has become possible only after the development of computer programs. In addition to solving the natural frequencies and normal modes, these programs also determine the transient response to several

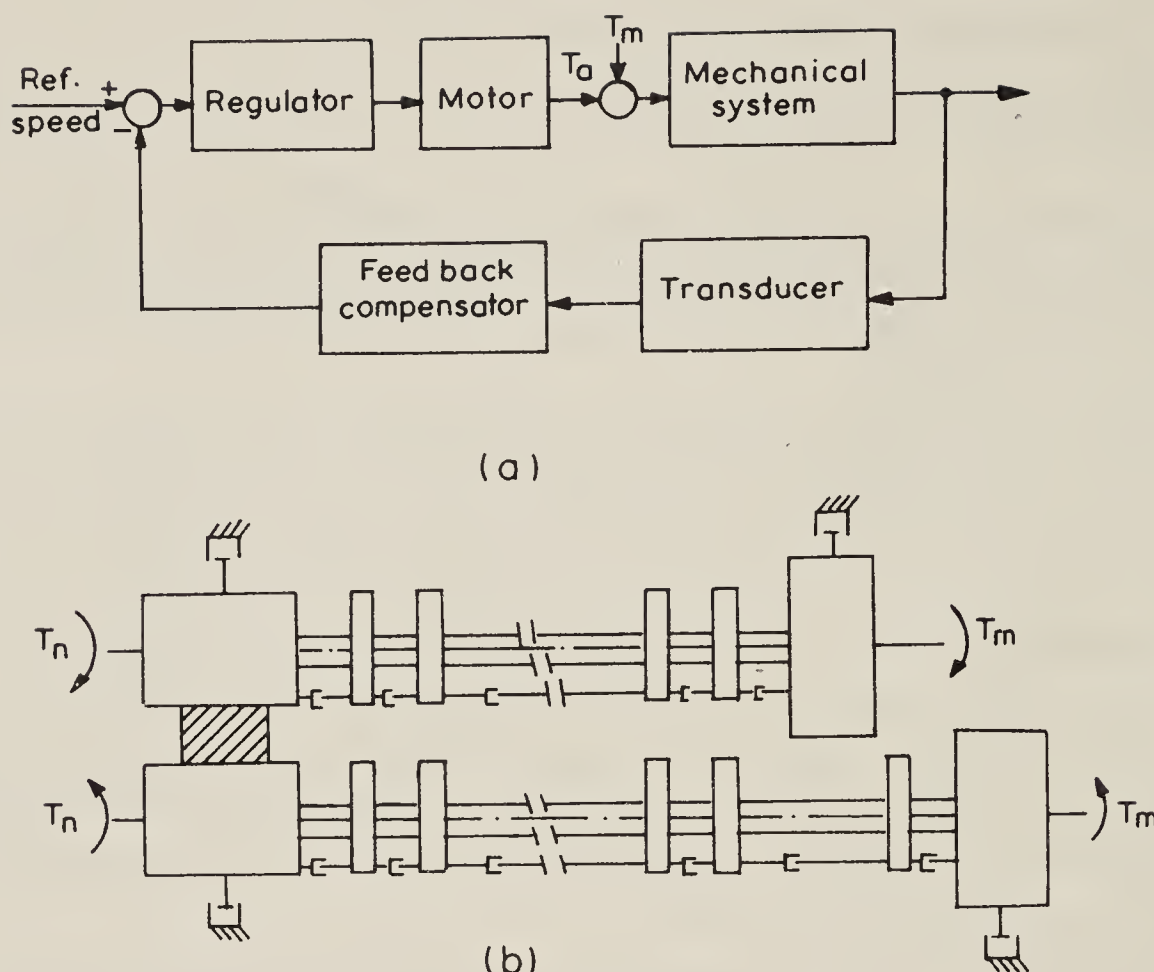


Figure 3. Mathematical models used for dynamic analysis and synthesis. (a) Block diagram of drive system and (b) Lumped parameter model for torque amplification studies.

types of inputs to represent as far as possible all types of disturbances such as ramming of bar, slipping in the role bite, nonuniform section, nonuniform reduction etc.

Computer studies of the large hot strip mills have occasionally led to changes in the proposed design to limit torque amplification to acceptable values. For the reversing mills the computer studies are reported to have led to substantial improvements in the optimization of the speed regulation compensator.

3.3 AGC system response studies

The influence of mill stand rigidity on the dimensional tolerances of the rolled product has been referred to earlier. In order to meet increasingly more stringent demands on dimensional tolerance automatic gauge control (AGC) systems have been developed to compensate for these variations. For proper control these systems are required to have a response time of about 20–30 m sec and a frequency response that is flat upto about 10–15 Hz. Except in case of smaller rolling mills these systems are generally controlled by a microprocessor or a computer.

The design and optimization of AGC systems is generally based on detailed computer models that include all parts of the system i.e. the physical plant, the sensors, the controllers and the actuators. For purposes of illustration, a computer model of a single stand hydraulic AGC system will be considered. A schematic of the same is shown in figure 4. The transfer function of each component is carefully determined and the computer simulation is used both for time domain analysis and frequency domain analysis. Such a model makes it possible to analyze the response to a step or other disturbance in incoming strip thickness, material hardness, roll separating force, tension, speed, etc either with or without AGC. For design optimization the general form of the compensator transfer function may be preselected and the different coefficients varied within a specified range. Clearly the validity of these simulations depends on the

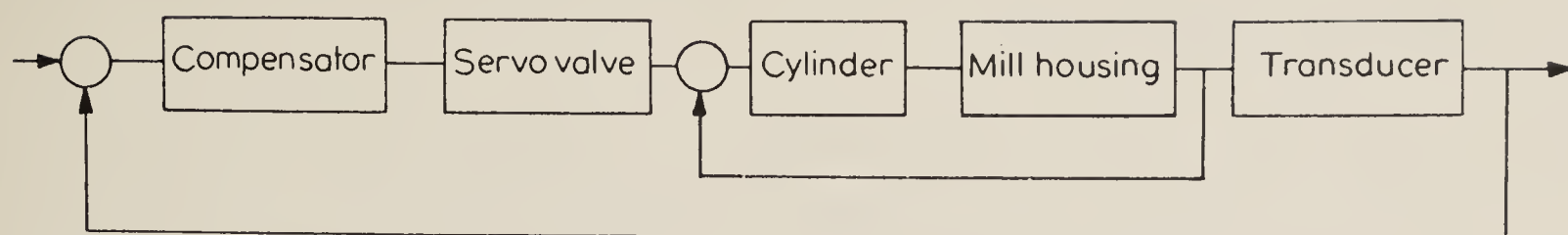


Figure 4. Block diagram of AGC system model.

accurate modelling of individual components such as mill stand, cylinder, load cell and servo valve, and also on the use of an accurate roll force model.

4. Graphics applications

The mathematical models and simulations described so far have played an important role in transforming rolling mills design from the domain of empiricism to an analytical level. Since the engineer works in graphic as well as mathematical terms, the results of analysis needed to be translated into graphic form. Besides the tedium of such work, the likelihood of error and the noncreative expenditure of time required, served as major disincentives for the widespread use of these techniques. New developments in "computer graphics" have finally allowed the design engineers to overcome these problems and communicate with the computer in a truly natural form.

The term computer graphics is very broad and includes numerous peripheral devices such as xy plotters, printers and drafting machines and graphic display screens. The most rudimentary application of computer graphics is for plotting the computed results as graphs, bar charts, etc. Examples of such applications include the plotting of transient response of drive systems, plotting the locus of linkages, plotting the profile of gear teeth, etc.

4.1 Roll groove drawings

At a somewhat more advanced level, computer graphics may be used for generating schematics and mechanical drawings of predefined shape. The graphic display screen is not essential for these applications but it may be used if available.

A popular application at this level is the generation of roll groove drawings. The geometry of these drawings is more or less fixed and all the dimensions may be obtained from the programs that calculate the pass dimensions as discussed earlier. The program developed in the present author's establishment (MECON) consists of the following parts:

- (i) selection of a standard scale factor,
- (ii) calculation of all coordinates for the main drawing and for all dimension lines,
- (iii) selecting a position for the drawing on the plotter and drawing of boundary lines and name plate,
- (iv) plotting the groove drawing,
- (v) plotting the dimension lines and inserting the dimensions and
- (vi) plotting of all textual information.

The data used for generating the groove drawings can also be used for generating roll drawings. This feature has been implemented by some mill builders and is under development at MECON.

4.2 Hydraulic schematic circuits

One of the earliest applications requiring the use of an interactive graphics terminal is the generation of schematics made up of items in a predefined menu. An example of such application is the interactive graphics software presently under development at MECON for hydraulic schematic circuits required in rolling mills design. User-defined keys have been associated with all standard element symbols such as tank, pump, filter, accumulator, check valve, servo valve etc. Working on an interactive graphics terminal, the designer can develop a complete schematic consisting of any arbitrary combination of these elements.

The elements can be individually rotated and scaled with conversational commands. Moreover the drawing as a whole can also be scaled for viewing on the screen or drawing on the plotter. Care has been taken to facilitate editing functions such as deletion and insertion of individual elements or complete circuit branches.

5. Summary and conclusions

The large number of simulations and design programs being used for rolling mills design have been developed over a period of several years. The mathematical models have been steadily upgraded to include the greatest level of detail possible within the limitations of computer time. Most design organizations have constantly updated the material characteristics to conform to field measurements. The software has generally undergone numerous modifications in order to meet the specific requirements of designers without sacrificing generality. There has also been a persistent effort to make the programs fully automatic as far as possible.

With the availability of interactive graphics facility, the present area of thrust is towards increased use of computer graphics. Wherever possible the calculation programs have been integrated with graphics software as described for the design of roll grooves. Such integration serves to eliminate the tedium of mechanically translating a computer printout into a drawing and allows the rolling mills design engineers to iterate more design concepts and trade-offs in a given time and greatly increase his creativity and productivity.

References

- Bryant G F and Heselton M O 1982 *Met. Technol.* **9** 469
Hitchcock J R 1935 Roll neck bearings, Special Report, ASME
Orowan E 1943 *Proc. Inst. Mech. Eng.* **150** 141
Polukhin V P 1975 *Mathematical simulation and computer analysis of thin strip rolling mills* (Moscow: Mir Publishers)
Siebel E 1925 Berichte des Walzwerksausschusses, Verein deutscher Eisenhuttenleute, No. 37 (also 1924 *Stahl und Eisen* **45** 1563)
Sims R B 1954 *Proc. Inst. Mech. Eng.* **168** 191
von Karman T 1925 *Z. Angew. Math. Mech.* **5** 139

Computer modelling application in life prediction of high temperature components

V M RADHAKRISHNAN

Indian Institute of Technology, Madras 600 036, India

Abstract. Defects introduced in pressure vessel components during fabrication processes act as potential sources for damage accumulation and subsequent catastrophic failure. Cracks nucleate at these stress risers and propagate aided by fatigue type of loading, corrosion and creep. Analysis of crack growth under conditions of 'time-dependent fatigue' is very important for the life prediction of pressure vessel components. In this paper the interaction of creep-hot corrosion and low cycle fatigue is analyzed based on the energy expended for the nucleation of damage at the advancing crack front. The total damage accumulation is divided into that due to (i) fatigue, (ii) corrosion and (iii) creep for modelling purpose. The analysis yields a relation in terms of J -integral which is applicable to both crack propagation and final failure. A corrosion-creep parameter (F_i) has been introduced at the crack propagation stage and raw data from different sources have been analyzed for different types of loading and compared with the theoretical predictions. The total energy in tension which includes the tension going time, appears to be a good parameter for the prediction of time-dependent fatigue life.

Keywords. Life prediction; pressure vessel; high temperature components; fatigue life; computer model; crack growth model.

1. Introduction

Pressure vessels operating in the creep range include steam chests, loop pipes, HP and IP cylinders, turbine parts, valves and numerous items of pipe works. Many of these components will contain crack-like defects specifically at places where joints are made. As large components involve a high capital investment, maximum service life consistent with safety of operation has to be ensured. Failure of many high temperature pressure vessel components due to crack growth has been reported in the literature (Toft *et al* 1976). A typical example is the failure of a welded joint between IP steam chest and a loop pipe (figure 1a) in a 350 MW unit plant in UK. The material of the steam chest was cast 1 Cr-Mo-V steel and that of the loop pipe was 1/2Cr-1/2Mo-1/4 V steel. The steam was at 35 bar pressure and 560°C. The welded joint between steam chest and the loop pipe failed explosively. Investigations revealed a sub-surface crack of 300 mm length in the heat-affected zone of the weld on the steam chest side. The crack was formed during the post-weld stress relief heat treatment and had grown in service. Another example is the failure of a superheater tube (figure 1b) of a 100 MW plant. The material of the tube was 18Cr-12Ni-1Nb (AISI/347) steel and that of the spacers was 25Cr-20Ni. The superheater tubes are kept in alignment and correctly spaced by the use of interlocking spacers which are welded to the tube, but free to move in the vertical plane to accommodate thermal expansion. Tube failures occurred after 12,000 hours of operation and examination revealed cracking at the fillet weld interface.

The significance of crack nucleation and its growth behaviour under dynamic

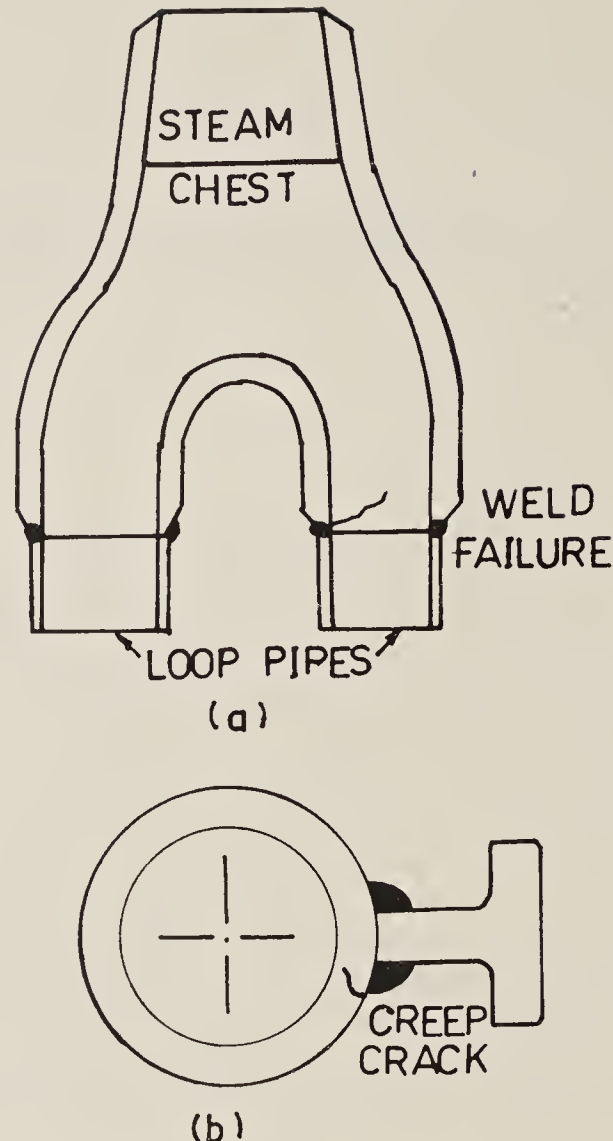


Figure 1. (a) IP steam chest and pipe joint. (b) superheater tube joint.

stresses where creep, corrosion and low cycle fatigue are the main contributing factors to damage processes has started receiving attention only recently. In this paper an analysis is presented to evaluate the time-dependent crack growth and its application in life prediction methods.

2. Crack growth model

In time-dependent fatigue, damage nucleation at the tip of the advancing crack could be in the form of micro-cracks or voids contributed by point and line defects. Both the strain energy at the crack tip δW^* and the thermal energy will contribute to the damage nucleation ahead of the crack tip. The damage nucleated per cycle in a unit volume of the material ahead of the crack can be given as a rate equation in the form (Radhakrishnan 1982)

$$\frac{dD}{dN} = A_1 \exp\left(\frac{-Q + m' \log(\delta W^*/W_0)}{kT}\right), \quad (1)$$

where Q is the activation energy and A_1 , m' and W_0 are constants. A similar da/dN dependence (a = crack length) of the activation energy had been found to be valid in the case of high temperature fatigue of aluminium (Jeglic *et al* 1973). The above relation can be rewritten as

$$\frac{dD}{dN} = A_1 (\delta W^*/W_0)^m \exp(-Q/kT), \quad (2)$$

where $m = m'/kT$.

The damage takes place over a small highly strained volume, represented by its linear dimension R_p . In the case of elastic field this dimension can be identified as the width of the plastic zone given by

$$R_p = (E/\sigma_{ys}^2) J_e, \quad (3)$$

where E is the Young's modulus and σ_{ys} the yield stress. J_e is the J -integral corresponding to the stress field. In the case of high temperature low cycle fatigue, the width of the highly strained volume can be given by a similar type of relation in the form

$$R_p = (E/\sigma_{ys}^2) \delta J. \quad (4)$$

The total damage in the highly strained zone joins the crack and the crack advances through a small distance da at time dN . Hence the crack growth rate can be given as

$$R_p(dD/dN) = A_1(E/\sigma_{ys}^2)(\delta J)(\delta W^*/W_0)^m \exp(-Q/kT). \quad (5)$$

The energy density δW^* at the crack front can be related to the applied energy density δW and the crack length a by (Radhakrishnan 1980a)

$$\delta W^* = (4/r)(\delta W \cdot a), \quad (6)$$

where r is the crack tip radius. It can also be shown that the J -integral range δJ is given by a function of the type (Kaisand and Mowbray 1979)

$$\delta J = \text{constant } (\delta W \cdot a), \quad (7)$$

where δW is the work done during the tensile portion of loading. With (6) and (7) we can write the crack propagation rate as

$$da/dN = A_2(\delta W \cdot a)^{m+1} = A_3(\delta J)^{m+1}, \quad (8)$$

where A_2 and A_3 are constants which include all the other constants.

Under certain conditions of loading, as in vacuum, some of these damages nucleated at the crack front may get healed during compressive loading. Under normal conditions of testing with ambient air, such healing may not be possible. In addition, with hold time or with low frequency, the crack front will be subjected to environmental attack. Hoffmeyer and Speidel (1979) reported that the crack propagation rate is twice higher in air than in vacuum for IN 738LC and IN 939 alloys at 850°C. In addition to the fatigue and corrosion effects, if the tensile-going frequency is sufficiently low, then creep effect will also come into the picture which will generate some more defects at the crack front thereby increasing the crack growth rate. The basic model of the contributions to the crack growth due to the three factors, namely, fatigue, corrosion and creep is schematically shown in figure 2. In these components, $(\delta a)_f$ may be considered to be due to PP type of loading (only due to fatigue). The corrosion component $(\delta a)_{cor}$ is added when the frequency is low or when there is a hold period. Oxide layers will form and if the scale that forms spalls off, then further corrosion may take place. Or else, the corrosion effect will slow down and hold times beyond a certain value will not add much to the damage accumulation. The corrosion effect may be taken as a log function (or any other suitable function) of the time of exposure of the newly formed surface—in this analysis the tensile going time—and can be given by

$$\delta a_{cor} = A_{cor} \log(t/t_0) \text{ func}(\delta J), \quad (9)$$

where A_{cor} and t_0 are constants.

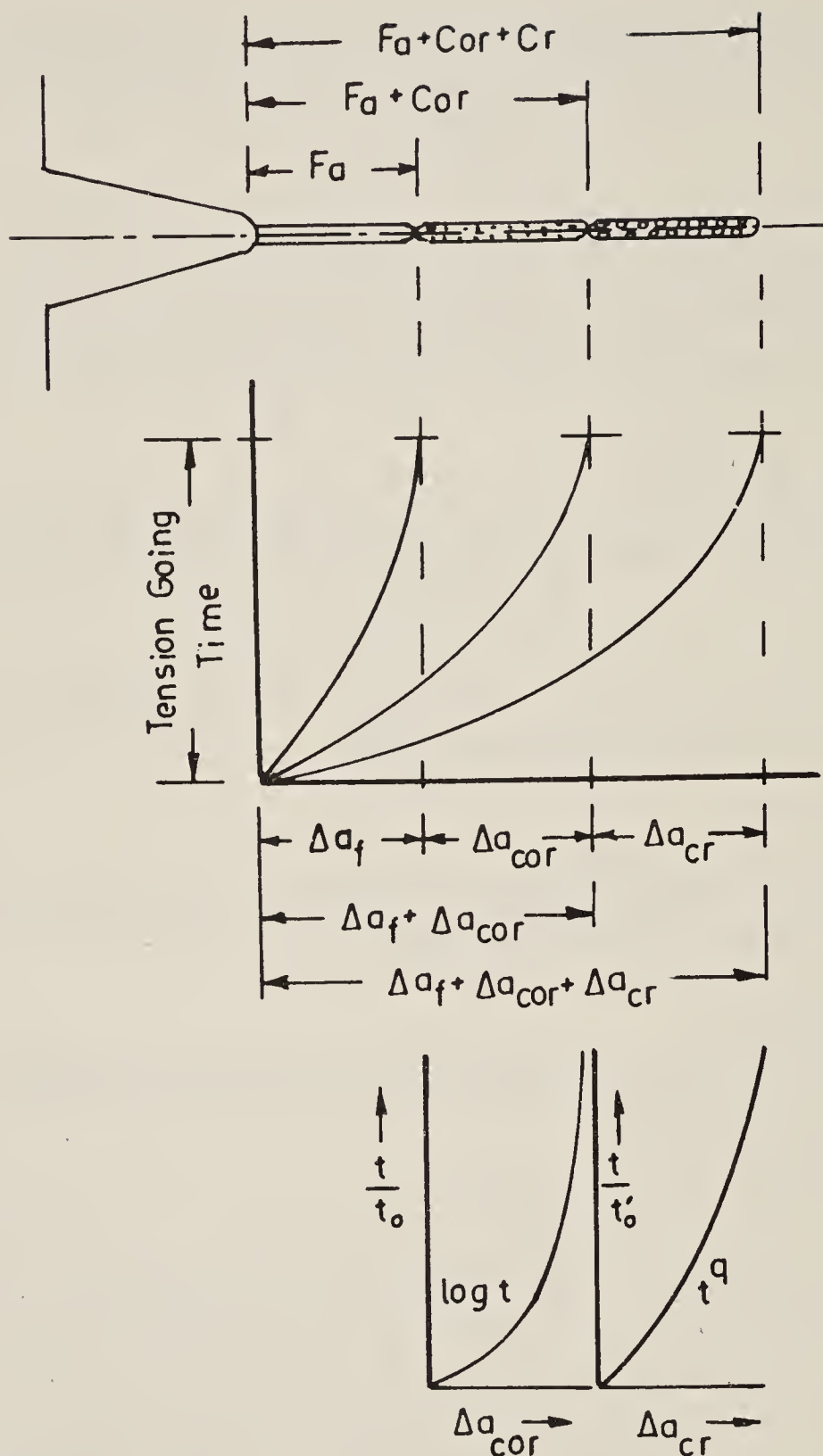


Figure 2. Crack growth model.

When the frequency is very low and the stress generated due to the applied strain range is sufficiently high at the operating temperature to cause creep deformation, then creep damage will also occur at the crack tip during the tensile portion of the cycle. The essential condition is that the creep rate due to that particular stress level must be higher than the imposed strain rate. The creep damage under such a condition can be assumed to be a function of the creep strain. Since during each cycle load is applied afresh, the creep strain will be in the transient stage and so it will follow generally the one third law. So the contribution due to creep for the crack growth, i.e., δa_{creep} can be taken as a power function of the tensile going time and can be written as

$$\delta a_{\text{creep}} = A_{\text{cr}} (t/t'_0)^q \text{ func}(\delta J), \quad (10)$$

where the value of the exponent $q = 0.33$. These growth phenomena are assumed to take place during the tensile going frequency and hence this treatment can be applied to unbalanced hysteresis loops and tensile hold periods.

Now combining the effects of corrosion and creep, the crack growth during each cycle can be given as

$$\delta a = \delta a_f + \delta a_{\text{cor}} + \delta a_{\text{cr}}, \quad (11)$$

which yields the generalized relation in the form (equation (8))

$$\frac{da}{dN} = A_f (1 + \alpha \log(t/t_0) + \beta(t/t'_0)^q) (\delta J)^{m+1}, \quad (12)$$

where $\alpha = A_{\text{cor}}/A_f$ and $\beta = A_{\text{cr}}/A_f$. t_0 and t'_0 are the tensile-going times (the corresponding frequencies being v_0 and v'_0) beyond which corrosion and creep will be active respectively.

The above relation is also applicable when there is a hold period in the stress-strain cycling. When there is a stress hold, the creep effect will come into the picture and the term $\beta(t/t'_0)^q$ will have to be taken in the equation. But when there is a strain hold, then relaxation of stress will take place. Some of the cavities created during the peak stress may collapse. So the effect of stress relaxation will be similar to corrosion and the contribution due to the damage accumulation can be similar to that of corrosion in the form

$$(\delta a)_{\text{relaxation}} = A_r \log(t/t_0) \text{func}(\delta J). \quad (13)$$

3. Data analysis

Expressing the J range (δJ) in terms of LEFM parameter δK in the form $\delta J = \delta K^2/E$, relation (12) can be written as

$$\frac{da}{dN} = A_f (F_i) (\delta K)^{2(m+1)}, \quad (14)$$

where A_f is a constant for a given material and temperature. F_i is the interaction parameter and is equal to $1 + \alpha \log(t/t_0) + \beta(t/t'_0)^q$ or $\alpha' \log(t/t_0)$. Equation (14) is similar to the Paris-Erdogan law given as

$$\frac{da}{dN} = C(\delta K)^n. \quad (15)$$

Crack growth data (James 1972) obtained on a 304 type stainless steel tested at 538°C over a wide frequency range of 6.67 Hz to 0.0014 Hz were analyzed based on (14) and the relation between da/dN and δK is shown in figure 3, with the values of the constant $A_f = 1.7 \times 10^{-8} \text{ mm}/(\text{MPa}\sqrt{\text{m}})^3$, $\alpha = 0.2$ and $\beta = 0.75$. As the frequency decreases there is a decrease in the value of the exponent $(m+1)$. It has been shown (Radhakrishnan 1980b) that in the Paris equation describing the state II crack growth, the constant C and the exponent n are inter-related. As C increases the value of n decreases. In a similar manner, in this case also, as frequency is lowered, the interaction factor (F_i) in (14) will increase with a consequent decrease in the value of the exponent $(m+1)$.

Equation (14) can be rearranged and integrated with crack length a from initiation a_i to critical length a_f and the number of cycles N from nucleation time N_i to final fracture N_f . Assuming the nucleation of the crack to start within a first few cycles and $a_i \ll a_f$, it can be shown

$$(F_i) (\delta W_t)^{m+1} N_{fi} = \text{constant}, \quad (16)$$

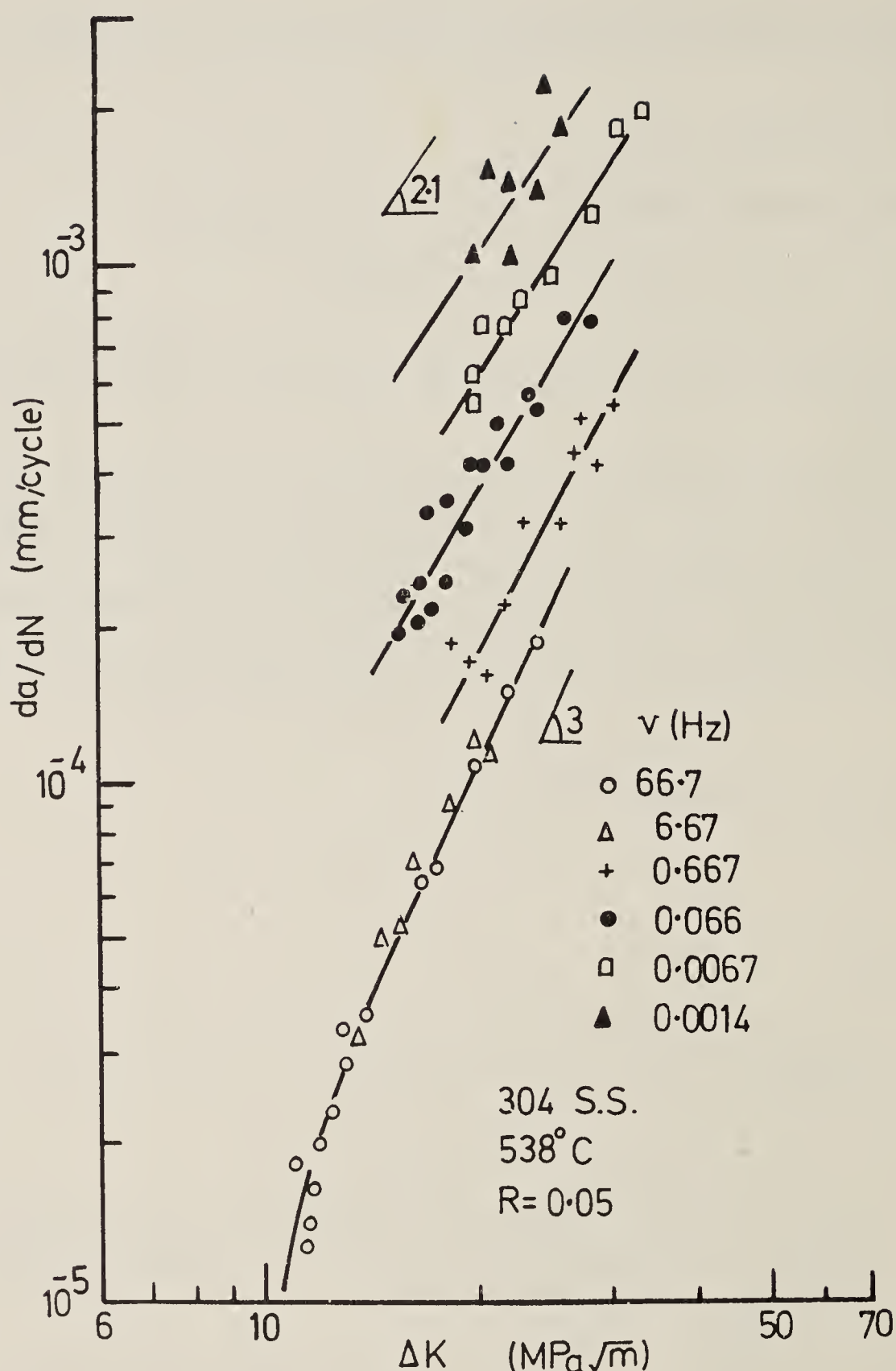


Figure 3. Relation between da/dN and δK .

where δW_t is the tensile energy input per cycle per unit volume. N_{fi} is the number of cycles to failure under interaction conditions. If $(F_i) = 1$, the $N_{fi} = N_f$. If the cyclic stress-strain relation is known, δW_t can be expressed in terms of $\delta\varepsilon$ or $\delta\sigma$. Thus the usual endurance life relation can be established. It can be seen that decreasing the frequency will shift the $\delta\varepsilon - N_{fi}$ relation downwards on the log-log plot. The slope of these lines will be proportional to $1/(m+1)$ and since the value of $(m+1)$ decreases with decreasing frequency or increasing tensile hold period, the slope of the lines $\delta\varepsilon - N_{fi}$ on the log-log plot will increase, thereby showing a rotational effect in addition to a downward shift as the frequency is reduced.

The energy associated with the tensile portion of the cycle depends on the wave shape—typical examples of which are shown in figure 4. In the case of a balanced hysteresis loop with no creep effect, the energy associated with the J integral will be δW_e

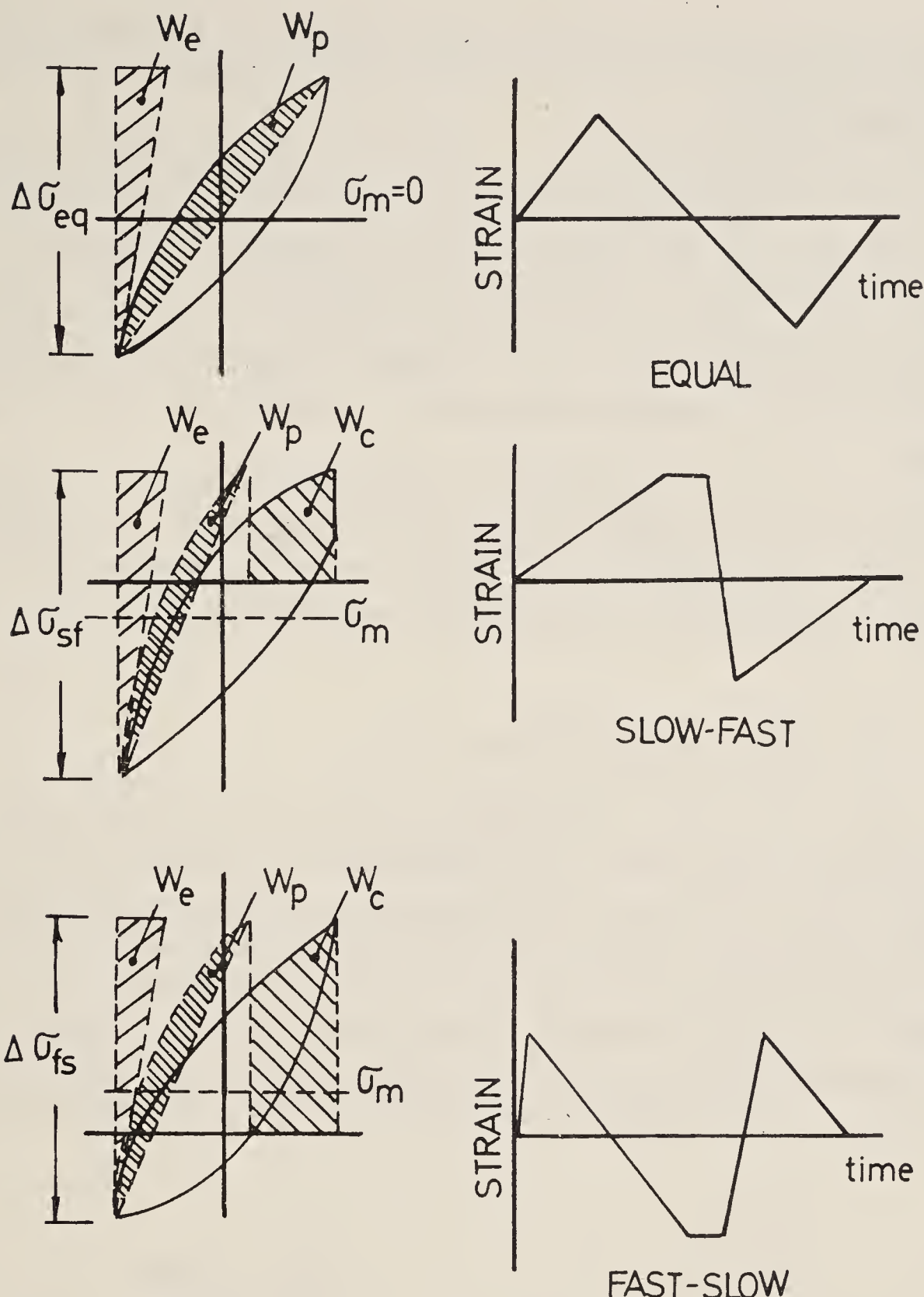


Figure 4. Energy separation method.

and δW_p , the elastic and plastic energy corresponding to δJ_e and δJ_p . This energy term will be

$$\begin{aligned} \delta W_t &= \delta W_e + \delta W_p, \\ &= \frac{\delta\sigma}{2} \delta\varepsilon_{el} + \frac{(1-n')}{(1+n')} \frac{\delta\sigma}{2} \delta\varepsilon_{pl}. \end{aligned} \quad (17)$$

The second term corresponding to the plastic region depends on the cyclic strain hardening exponent n' under the PP type of loading. At high temperatures where the hardening of the material drops, the value of the exponent n' will be small ($= 0.1$ to 0.15) and in such a case relation (16) can be written as

$$(F_i)(\sigma_t \delta\varepsilon_t)^{m+1} N_f = \text{constant}. \quad (18)$$

Raw data from Tarakeshi and McEvily (1981) have been analyzed and typical relations

between the tensile energy δW_t and the cycles to failure N_f for 800 and 800H nickel alloys are shown in figure 5. Here the cycling was rather continuous and the influence of creep could be negligible.

Even when the stress or strain is held constant for a duration either in tension or in compression, if the temperature is not high enough to cause creep damage or stress corrosion cracking in the small interval of time, the interaction parameter (F_i) in (16) will almost be equal to unity and the relation between δW_t and N_f on log-log scale will be a straight line for continuous cycles, tension hold (SF), compression hold (FS) and tension-compression hold (SS). Such a typical correlation at comparatively low temperature where creep damage effect may be negligible, is shown in figure 6 for Cr-Mo steel.

The need to consider the unbalancing in hysteresis loop comes in at temperatures where corrosion and creep effects will be more pronounced. In the model presented here, the entire tensile energy term is divided into three components, W_e , W_p and W_{cr} —the last term being due to tensile stress σ_t and the displacement ε_{creep} . So δW_t is written as

$$\delta W_t = \frac{\delta\sigma}{2} \delta\varepsilon_e + \frac{(1-n')}{(1+n')} \frac{\delta\sigma}{2} \delta\varepsilon_p + \sigma_t \delta\varepsilon_{cr}, \quad (19)$$

where $\delta\varepsilon_{el} + \delta\varepsilon_{pl} + \delta\varepsilon_{cr} = \delta\varepsilon_{total}$. The third term need not necessarily be due to creep under constant stress hold. When the frequency is very low and the stress developed is high enough to cause a creep rate which is higher than the imposed strain rate, the effect of creep will come in. Since the tensile portion of the energy is considered in the analysis, the type of tests PP(FF) and PC(FS) can be considered to be similar and that of CC(SS) and CP(SF) will be similar excepting for the mean stress effect. Figure 7 shows the relation between the tensile energy and the number of cycles to failure under interaction conditions for a turbine disc alloy tested at 750°C. It can be seen that PP and PC types

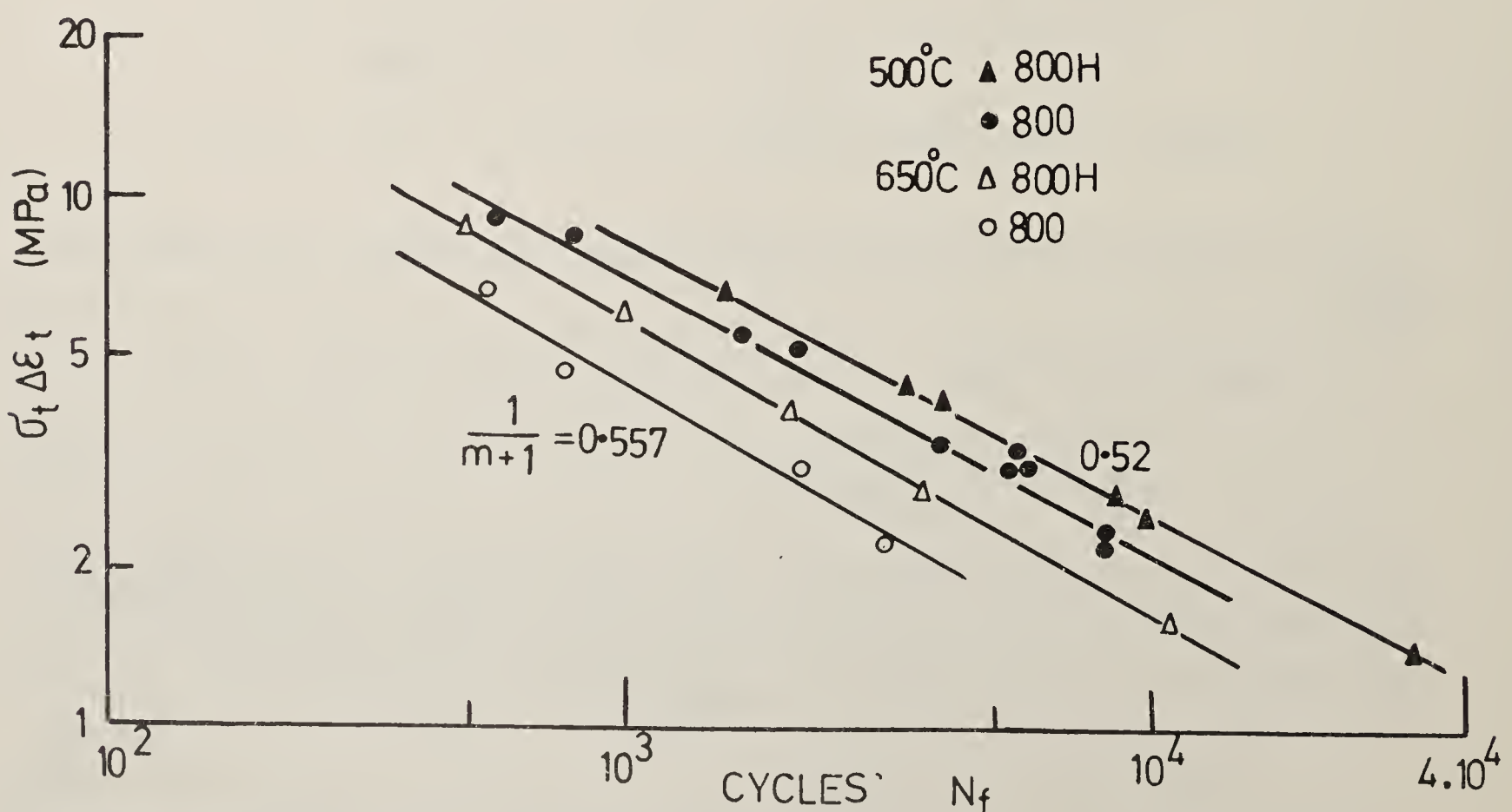
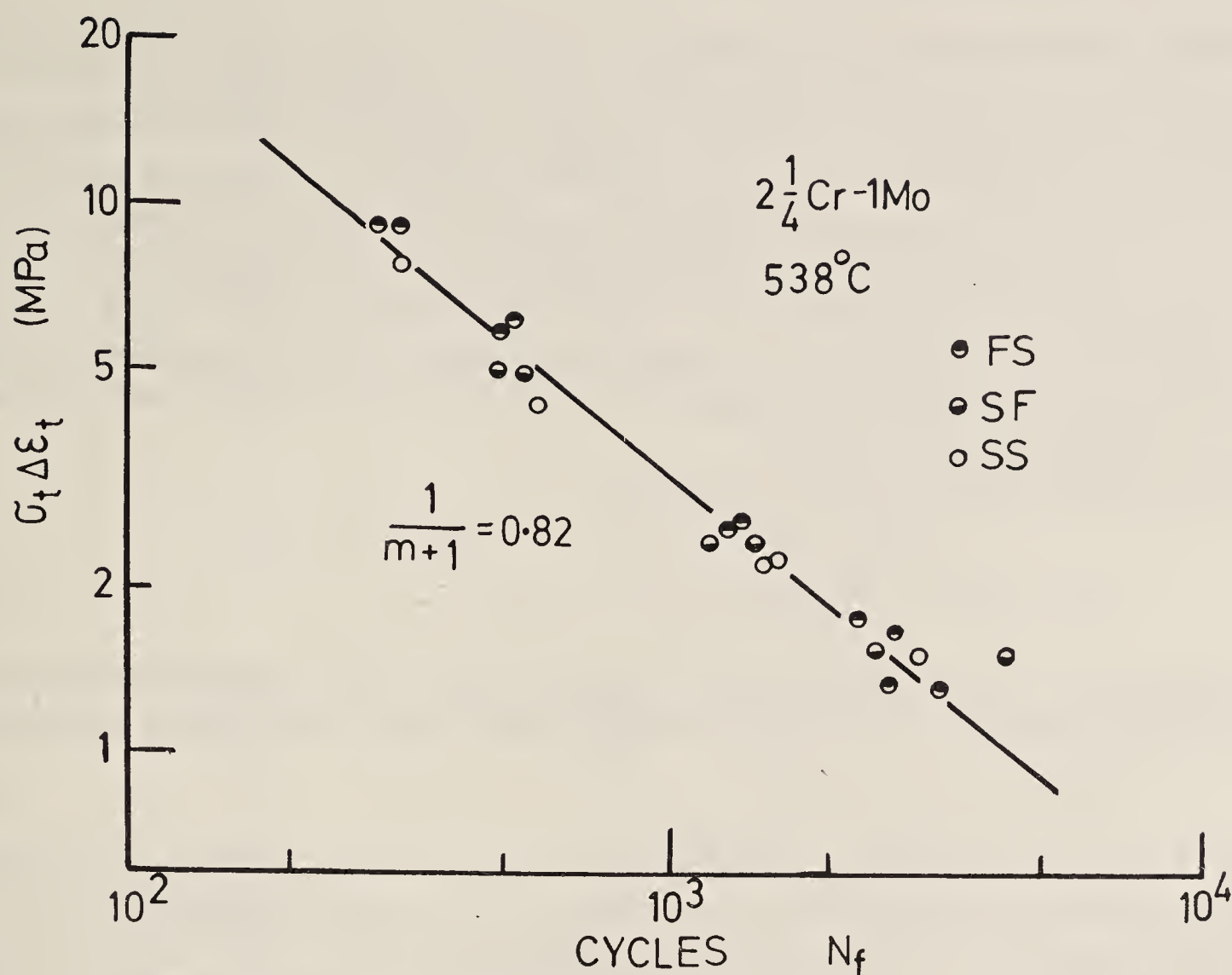
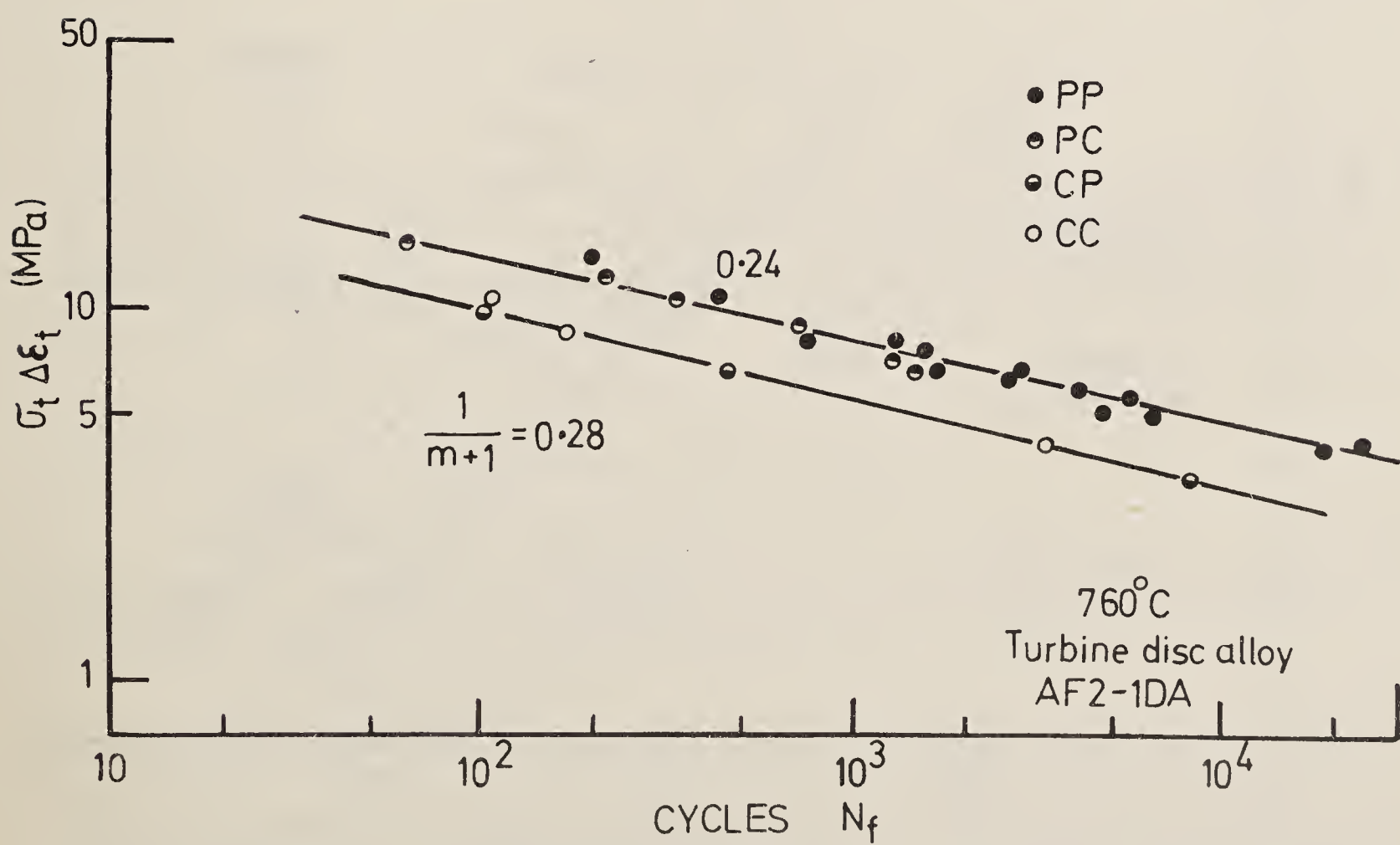


Figure 5. Relation between tensile energy density and cycles to failure.

Figure 6. Relation between δW_t and N_f .Figure 7. Relation between δW_t and N_f .

of loading data fall on one line and that of CP and CC on the other. The interaction factor (F_i) was not taken into consideration. This has resulted in two separate lines for these two types of loading schemes. Figure 8 shows the relation between tensile energy and the number of cycles to failure under different loading frequencies and tensile hold times for type 304 stainless steel. Tensile strain hold times up to 600 minutes were employed. It can be seen from the results that when there is no hold time and the test is of PP type, (curve corresponding to 4 E-03) the slope of the line is 0.5 ($= 1/(1+m)$). As the hold time is introduced or as the frequency is reduced the slope increases to 0.525 and 0.625 as indicated in the figure and the interaction factor (F_i) also increases, because of the corrosion and creep effects.

In (18) which can be written in the form

$$N_{fi} = \text{const.} \frac{(\delta W_t)^{-(m+1)}}{(F_i)}, \quad (20)$$

the exponent ($m + 1$) is dependent on the interaction factor (F_i), as was discussed earlier, and it decreases as the value of (F_i) increases. This relation can be given in the form

$$(m + 1) = A - \gamma \log(F_i), \quad (21)$$

where $A = m + 1$ when there is no interaction i.e., $(F_i) = 1$. γ is a constant. As discussed in figure 8, the value of the constant γ is taken as 1.2 for 304 stainless steel at 593°C.

In many situations it is advantageous to represent the failure cycles N_{fi} as a function of tensile cycle time or tensile hold time. Figure 9 shows the relation between N_{fi} and the cycle time for cast 316 stainless steel and 304 stainless steel. It can be seen that for lower values of the strain range ($\delta\epsilon_t = 0.5\%$) the reduction in interaction cycle for larger

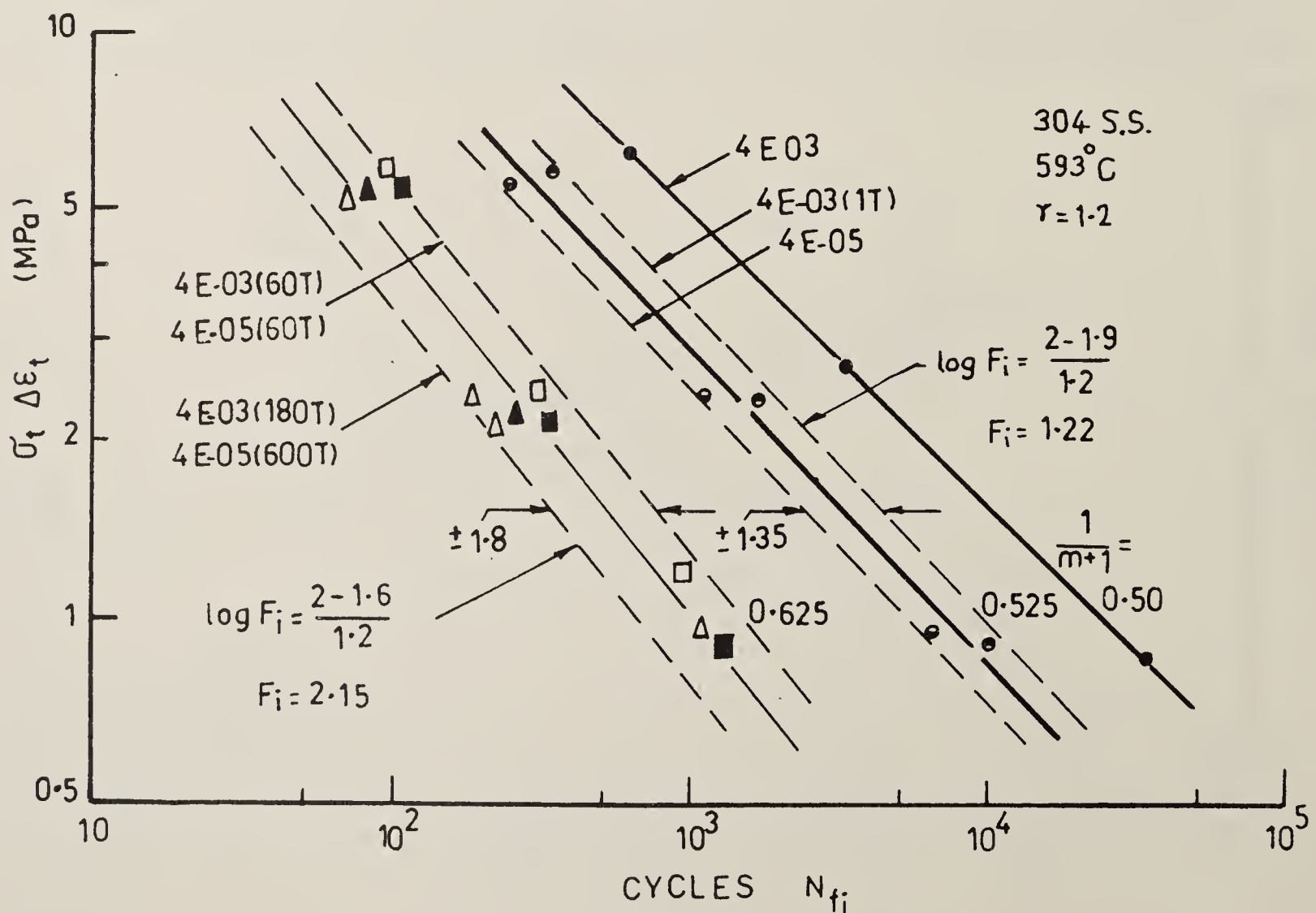


Figure 8. Relation between δW_t and N_f .

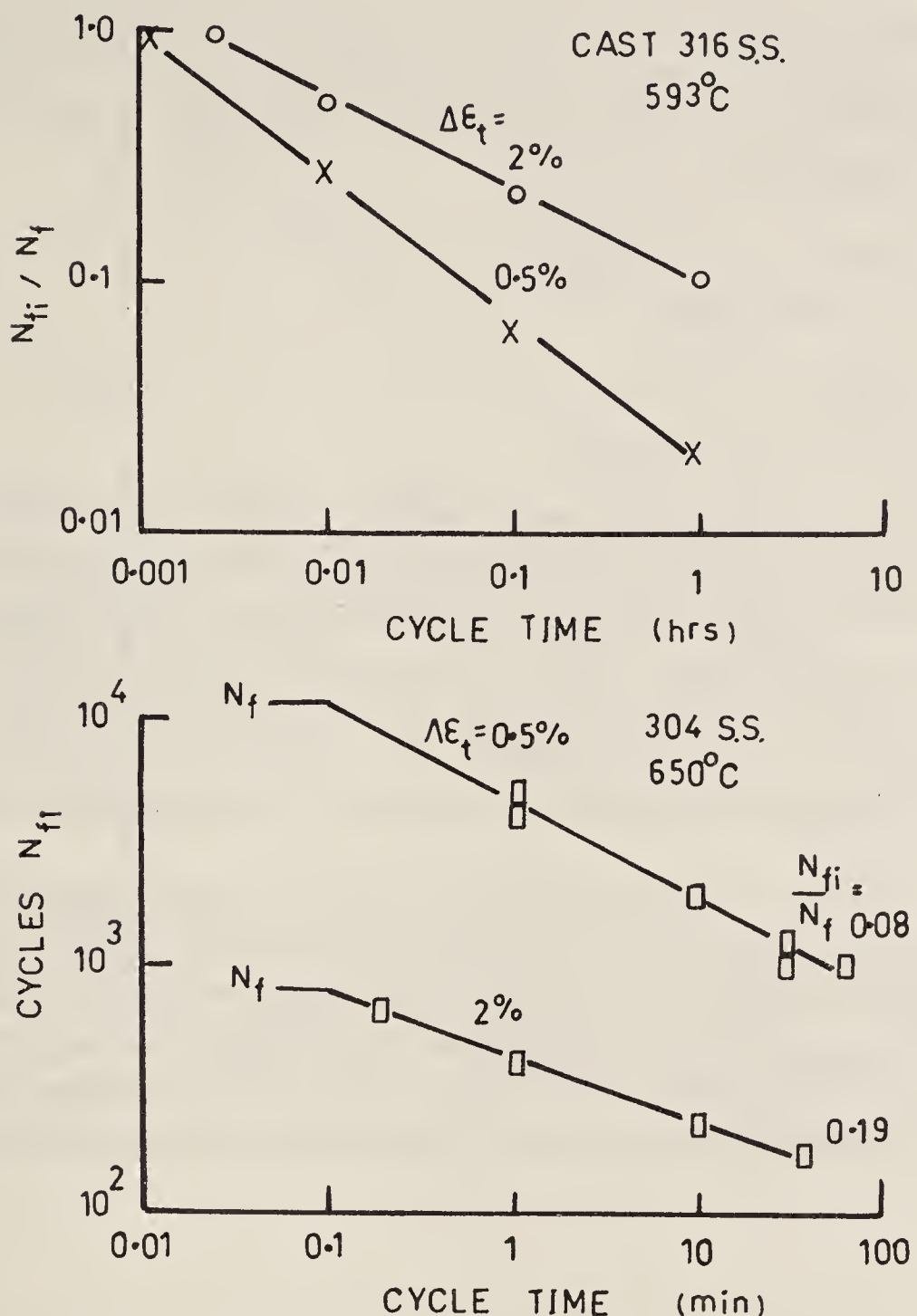


Figure 9. Relation between N_{fi} and cycle time.

cycle time is much higher than for higher strain ranges ($\delta\epsilon_t = 2\%$). Equation (20) is able to explain such a behaviour that has been observed in many other cases also. Assuming a simple relation between stress and strain in the form $\delta\sigma = \sigma_0(\delta\epsilon)^n$ so that $\delta W_t \propto (\delta\epsilon)^{n'+1}$ we get the relation (20) as

$$(\delta\epsilon)^{(n'+1)(m+1)} N_f = \text{constant},$$

for PP type of loading and

$$(F_i)(\delta\epsilon)^{(n'+1)(A-\gamma \log F_i)} N_{fi} = \text{constant}, \quad (22)$$

for interaction conditions. The fatigue life under interaction condition N_{fi} can thus be written as a function of the normal fatigue life N_f as

$$\frac{N_{fi}}{N_f} = \frac{(\delta\epsilon)^{(n'+1)\gamma \log F_i}}{(F_i)}. \quad (23)$$

The above relation shows that N_{fi}/N_f is dependent on the applied strain range—the higher the strain range, the larger is the life ratio. This is what has been observed in the data presented in figure 9 (Wareing 1981).

Equation (23) forms the basis for the construction of the interaction diagram i.e., the relation between the fatigue life under interaction conditions and the tensile going time which can include the stress or strain hold periods. In the case of strain-hold, the interaction factor (F_i) becomes

$$\begin{aligned} F_i &= 1 + \alpha \log(t/t_0) + \alpha' \log(t/t_0) \\ &= 1 + (\alpha + \alpha') \log(t/t_0). \end{aligned} \quad (24)$$

In the case of stress hold, it is given as

$$F_i = 1 + \alpha \log(t/t_0) + \beta(t/t_0)^q. \quad (25)$$

Figure 10 shows the interaction diagram for 304 type stainless steel. The full line is obtained with the interaction factor F_i as given by (24) as this is a case of strain hold and stress relaxation can be expected to occur during the hold period. When the hold is very small, it is the same as normal fatigue without any interaction effect. As the hold time is increased, corrosion comes into the picture. Still further increase in hold time gives rise to corrosion and relaxation to occur. The value of $(\alpha + \alpha')$ is taken as 0.2. Here again it can be seen that the reduction in fatigue life is much more pronounced when the strain range is small.

Figures 11 and 12 show the relation between N_{fi} and the tensile hold period under both stress and strain hold conditions for 304 type stainless steel at 650°C and IN597 alloy at 850°C. It can be seen that with stress-hold the relation between N_{fi} and time on the log-log plot becomes more or less a straight line with a negative slope approximately equal to one at higher hold periods. This means that the life becomes more time-dependent than cycle dependent as the stress hold period is increased. At high tensile

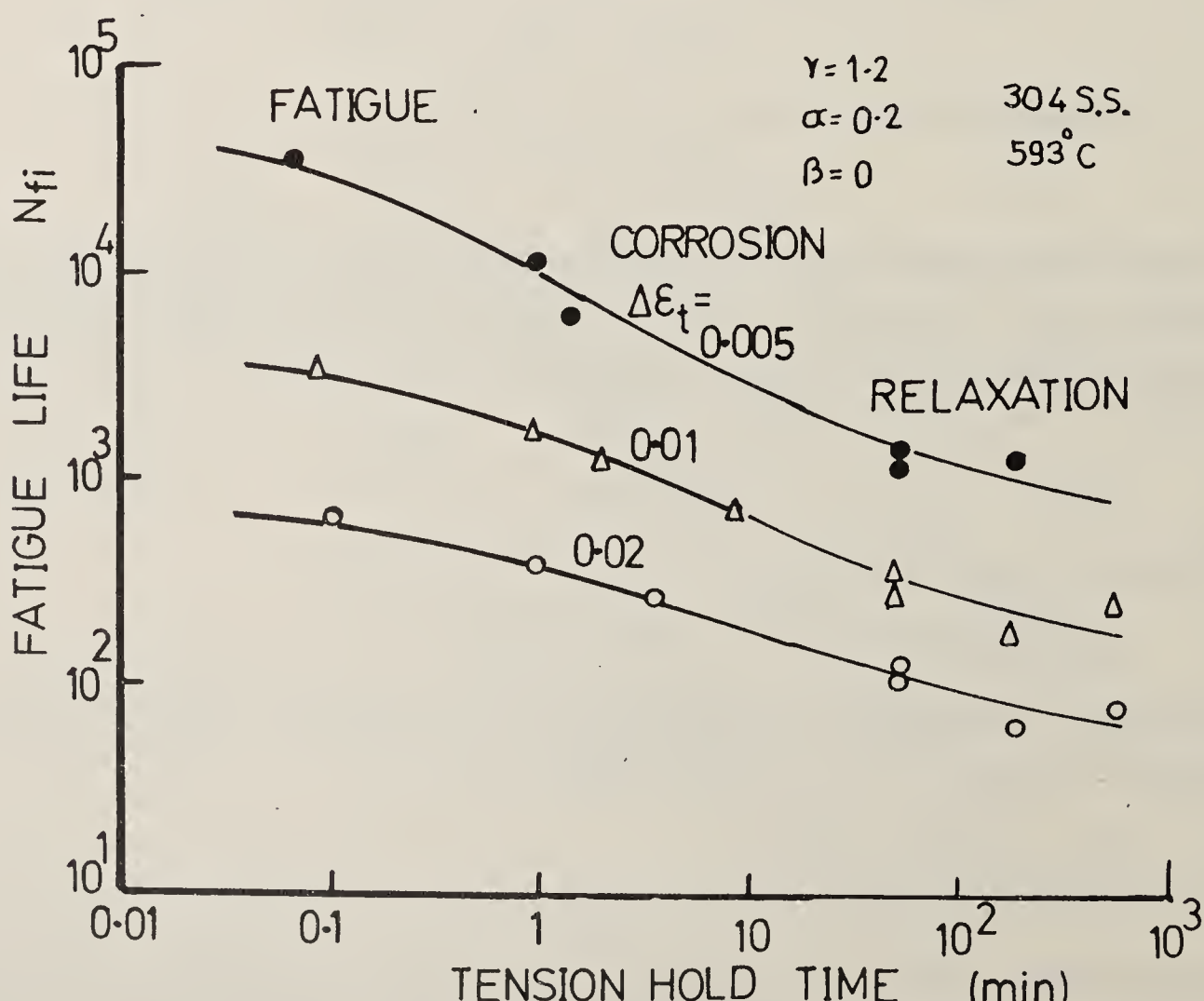


Figure 10. Interaction diagram for 304 stainless steel at 593°C.

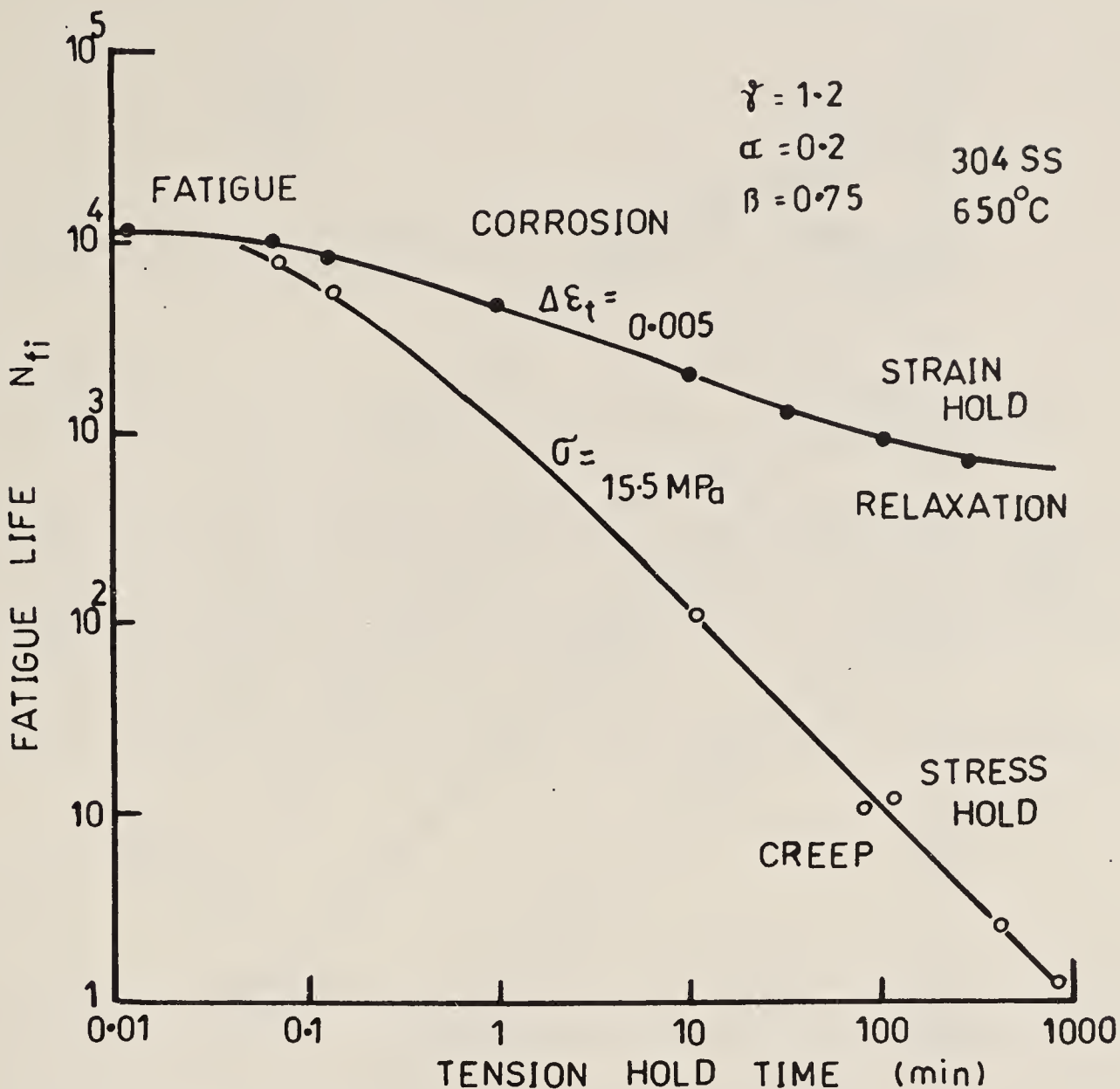


Figure 11. Interaction diagram for 304 stainless steel at 650°C.

hold periods creep plays a dominant role under stress hold conditions. But under strain-hold conditions, a saturation level is reached and the fatigue life appears to be independent of the hold period beyond a certain stage, as relaxation governs the crack tip conditions. The same trend has been observed in all the cases (Radhakrishnan 1983).

The variables involved in the analysis of life prediction of components at high temperature are quite large. Various phenomena like hot corrosion, low cycle fatigue, creep, relaxation and thermal fatigue take place either individually or two or more combinations of them. In addition to these mechanical type of considerations, metallurgical factors such as chemical attack on grain boundaries and general structural degradation are also to be considered. In the model proposed, only the mechanical aspects are considered. This can be improved and extended to metallurgical variables also as more data are analysed.

4. Concluding remarks

In trying to model the damage accumulation and thereby predict the life of the component it is very important to know all the parameters that affect the damage process and their relative weightage. The logic and the governing equations are to be properly evaluated to build the sequence block diagram.

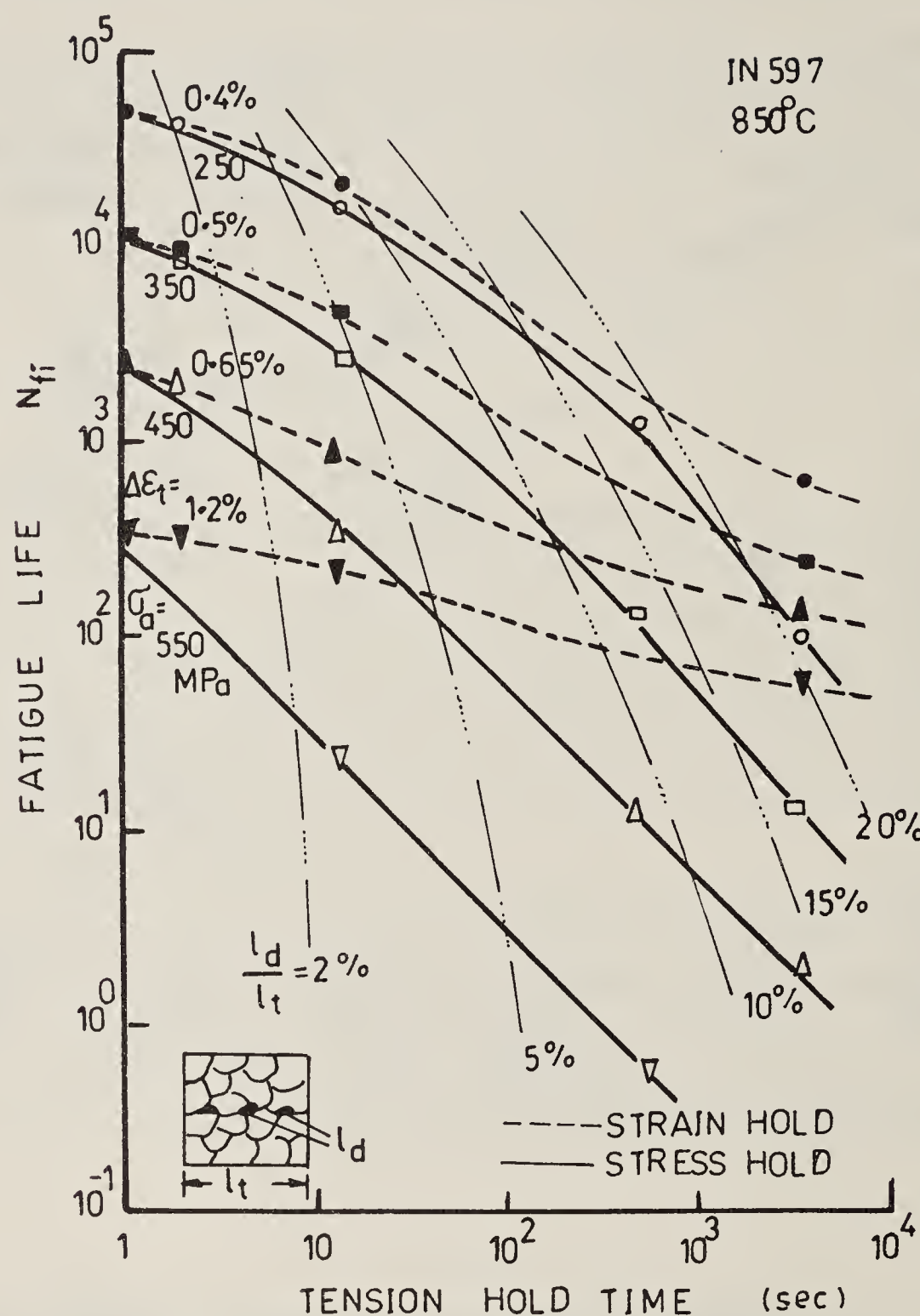


Figure 12. Interaction diagram for IN 597 alloy at 850°C.

References

- Hoffmeyer W and Speidel M O 1979 *Proc. Int. Conf. on High Temperature Alloys in Aggressive Environments*, Petten, The Netherlands, 993
- James L A 1972 American Society for Testing Materials Special Technical Report 513 218
- Jeglic F, Niesen P and Burns D J 1973 ASTM STP 520 139
- Kaisand L R and Mowbray D F 1979 *J. Test. Eval.* 7 270
- Radhakrishnan V M 1980a *Fatigue Engg. Mater. Struct.* 3 75
- Radhakrishnan V M 1980b *Engg. Fract. Mech.* 13 129
- Radhakrishnan V M 1982 *Damage accumulation and fracture life in low cycle high temperature fatigue*, ASTM STP 770 135
- Radhakrishnan V M 1983 Interaction diagram for time-dependent fatigue 1983 *Trans. A.S.M.E. JEMT* 105 273
- Taraneshi H and McEvily A J 1981 *Proc. ICF-5 Cannes*, 1981
- Toft L H, Yeldham D E and Plastow B A 1976 *Proc. Conf. Failure of Components operating in Creep Range I*. Mech. E., London (1976) p. 107
- Wareing 1981 *J. Fatigue Engg. Mater. Struct.* 4 131

Computer applications in the field of furnace design

V S PAKALA

Department of Metallurgy, Regional Engineering College, Rourkela 769 008, India

Abstract. The development of mathematical models of furnaces is briefly reviewed. The basic processes taking place in furnaces and the problems associated with their mathematical formulation and the necessary assumptions are discussed. The difficulty of determining the process parameters, and the methods of their estimation are included. Applications of mathematical models for the study of cooling of ingots, heating of steel, cowper stoves and for the study of erosion of refractories are also discussed.

Keywords. Heating furnaces; mathematical models; process parameters; furnace design

1. Introduction

At the beginning of the present century, a Russian scientist, Groume-Grjimailo, placed the transparent model of a furnace upside down and passed water through it so as to study the flow of combustion products through the furnace. He could thus formulate the principles of design of some furnaces. This probably was the first scientific approach to the design of furnaces, and also the beginning of model studies of furnaces.

With the developments in the field of model studies it soon became evident that a clear understanding of the interaction of various parameters, influencing the process under study, is necessary for setting up an appropriate model. These interactions are best expressed in the form of mathematical relationships i.e. mathematical models.

The development of a mathematical model depends on a knowledge of the laws of behaviour of the system being studied, the capacity of expressing these in the form of mathematical equations, and the ability to solve them.

The basic processes, taking place in furnaces, are known for a long time, but the difficulties associated with the solution of the partial differential equations, with the complex boundary conditions involved, restricted the use of mathematical modelling of furnaces. Thring (1952) made some simplifying assumptions to calculate the heat transfer in open hearth furnaces and this probably is the beginning of mathematical modelling of furnaces.

With the developments in the field of digital computers, the interest in mathematical modelling of furnaces has increased significantly.

In this article, models of only heating furnaces i.e. furnaces where the charge does not undergo any chemical changes, are considered.

2. Types of models

Mathematical models based on the fundamental laws of behaviour of the system are called process models. These are concerned with the activity between start and finish of

the process and describe, among other things, the cause of the variability of the process time. The activities, in general, are continuous and the model consists of equations relating rates of change of variables, describing the system, to their current values i.e. the model consists of differential equations.

In some cases, e.g. logistics of assembly processes, models generating the time history of process are known as simulations. In these models the matters of interest are the start and finish of the process. The model determines the complete history of events from these events and the logistic laws.

Process models serve many purposes, including our understanding of the process and indicate areas where information is limited and further research desirable. In engineering they facilitate experiments which are otherwise not feasible since practical experiments on full scale iron and steel making units are difficult and expensive. Engineering modifications are also costly and almost impossible to examine experimentally on full scale plants. However, once a mathematical model is formulated and verified by plant measurements, it is in principle comparatively easier to carry out the necessary computer experimentation. Even if full scale experimentation is needed it can be restricted to a minimum number of crucial cases.

It must be recognized that every model is imperfect in one aspect or the other, either due to simplifications of the process mechanism that are necessary to evolve a practical model, or due to inadequate understanding of the mechanisms.

3. Formulation of furnace models

For heating furnaces where heating of the charge to a given temperature is the main objective, the model must be able to predict the internal temperature distribution of the charge at any given time. The temperature distribution in a solid charge is given by the conduction equation

$$\frac{1}{\rho c} \cdot \frac{\partial t}{\partial \tau} = K \nabla^2 t, \quad (1)$$

where K is the thermal conductivity of the material, ρ the density, c the specific heat, t the temperature and τ the time. This equation has to be solved with the appropriate boundary and initial conditions to obtain the temperature distribution.

The boundary conditions usually give the heat flux to the surface.

$$q = -K \frac{\partial t}{\partial x}, \text{ at the boundary.} \quad (2)$$

For some simple boundary conditions, (1) can be solved by analytical methods if K , ρ and c are independent of temperature. But in actual practice the boundary conditions are not simple and the values of K and c are dependent on temperature. In such cases only numerical solutions of the equation are possible, the method of finite differences being the most common. These methods have been described by Dusinberre (1961). Thomas *et al* (1984) analyzed the different methods and concluded that for simple geometry of the body, finite difference method is the most suitable. Tocher (1970) briefly analyzed the errors involved in these methods.

The value of q in (2) depends on the rate of heat transfer to the surface of the body from the furnace. This consists of radiation from flame, radiation and convection from the combustion products and radiation from the refractory walls. For precise calculation of the internal temperature of the body, precise formulation of these external heat flows is necessary.

The problems associated with mathematical description of flames were analyzed by Beer (1972). Furnaces usually have turbulent diffusion flames, and it is reasonable to assume that the development of the flame depends only on the mixing of fuel and air. The description of a turbulent flow system, with an exothermic chemical reaction, in terms of spatial distribution of velocity, concentration and temperature requires the simultaneous solution of partial differential equations for mass, momentum and energy transfer. Patankar and Spalding (1970) and Gosman (1969) discussed the solution of these equations. Apart from the complexity of the solution, difficulty arises with the values of the turbulent transport properties, which are not constants for the medium. Added to this is the difficulty to evaluate the development of luminosity in flames.

Most models developed for fuel-fired furnaces use simplifying assumptions for calculation of the external heat flow. Usually the furnace gases are assumed to be non-luminous having uniform temperature within the furnace chamber. In long furnaces, like pusher re-heating type, the furnace may be considered as consisting of a number of isothermal zones. If the temperatures of gas, refractory surfaces and charge surface can be represented by their respective mean temperatures, the heat transfer to the charge can be calculated by standard methods (McAdams 1954; Averin *et al* 1969; Davies *et al* 1970). Salter and Costick (1972) applied experimentally determined flame parameters for modelling a re-heating furnace. Fitzgerald and Sheridan (1970) used measured surface temperature of the charge to calculate the internal temperature distribution.

4. Process parameters

The necessity of considering the variation of physical properties of steel with temperature was mentioned earlier. A fairly comprehensive source of data is a compilation by BISRA (1953). These are experimentally determined values. For temperatures above 1000°C, an error of 8–15% can be expected.

While heating steel, in most of the cases a layer of scale forms on the surface. Reliable data on the properties of scale are not available.

The difficulties involved in calculating the heat flow to the charge were mentioned earlier. In practice either simplifying assumptions have to be made or heat transfer parameters have to be determined from measurements on actual furnace.

The heat flux to the charge can be represented as either

$$q = \sigma F(T_f^4 - T_m^4) + h(T_f - T_m), \quad (3)$$

$$\text{or} \quad q = H(T_f - T_m), \quad (4)$$

where T_f and T_m are the temperatures of furnace and the surface of the metal respectively, σ the Stefan-Boltzman constant, F is a radiation factor, h the heat transfer coefficient by convection and H is the combined heat transfer coefficient. The value of T_f is usually taken as the temperature indicated by the thermocouple located in the furnace chamber. From the measured temperatures of the metal the values of F and h or H are computed by solving the inverse heat transfer problem.

Lambert and Economopoulos (1970) described a method of using probes for determining the heat transfer coefficients. The heat transfer coefficients by convection can be determined with the help of isothermal physical models by making use of an analogy between heat transfer and mass transfer. From the measured mass transfer coefficients the heat transfer coefficients are computed. Davis *et al* (1970) used evaporation of naphthalene and Choudhury and Mukherjee (1979) used transfer of CO₂ from the gases to filter papers soaked in NaOH solution to measure mass transfer coefficients.

5. Application of mathematical models for furnace design

A few of the applications of mathematical models for design of furnaces are discussed below.

5.1 Solidification of ingots

Although solidification of ingots is not a process taking place inside a furnace, the knowledge of internal temperature distribution of hot ingots is necessary for subsequent heating. By optimizing the stripping time and subsequent transit time before charging the ingots into soaking pits, considerable energy can be saved in the soaking pits. This problem was studied by Jackson *et al* (1944) using analogues and by Sargent and Slack (1954) using numerical methods and others.

The peculiarity of the solidification process is the liquid-solid transformation, which is accompanied by the liberation of latent heat. The governing differential equation becomes

$$\rho C \cdot \frac{\partial t}{\partial \tau} = K \nabla^2 t + \rho L \frac{\partial f_s}{\partial \tau} \quad (5)$$

where L is the latent heat and f_s the fraction of solid. This equation can be solved by applying the equivalent specific heat method where the specific heat is increased by an amount equivalent to latent heat in the solidification zone. This method is most widely used. Other assumptions made in formulating the model are: (a) the mould is filled instantaneously; (b) initially there is good thermal contact between the metal and the mould, for 2–3 min, when the heat transfer from metal to mould is by conduction; (c) very soon a solid skin is formed on the ingot, which shrinks away from the mould, leaving an air gap. Further heat transfer is by radiation only; (d) heat losses from the outer wall of the mould are uniform.

Sevrin (1970) calculated the solidification time of ingots and showed that mould thickness and mould temperatures, within limits, have no significant effect on the solidification time. Cherapanov and Kalashnikova (1971) claimed significant saving in the mould weight, based on these calculations.

Making use of the above assumptions the solidification of a 21-tonne ingot was earlier carried out by mathematical modelling (Pakala 1975). The calculated surface temperature was compared with values measured on an ingot, after stripping by optical pyrometer. The results showed good agreement, with a difference of about 10°C just

after stripping. But with further cooling the measured temperatures were lower than the calculated values. This was assumed to be due to scale formation on the ingot which was not considered in the model.

5.2 Heating of steel

Models for heating of ingots and billets were developed by Fitzgerald and Sheridan (1970), Collins (1970), Massey and Sheridan (1971), Massey *et al* (1973) etc. In all these models the furnace gas temperature was assumed to be uniform and the external heat transfer parameters were estimated from measurements on furnaces.

One of the factors to be considered in heating of massive steel ingots and billets is the heating rate. Too fast a heating rate results in a large temperature differential in the part with accompanying thermal stresses. In order to develop a satisfactory heating schedule for cold ingots a model was developed by the present author (Pakala 1975). Here the furnace gases were assumed to be at uniform temperature. The furnace walls were assumed to be perfect reflectors of radiation. This assumption was based on the fact that the wall temperature does not vary much with time and the heat conducted away through the walls is of the same order as the heat received by the walls by conduction.

The heat transfer parameters were calculated using equations reported in literature (Averin *et al* 1969). Variation of thermal conductivity and specific heat was accounted for. The mean gas temperature was calculated for every time step by iteration, assuming that

$$\text{Heat input through fuel and preheated air} = \text{Heat transferred to metal} + \text{wall losses} + \text{waste gas losses.}$$

The fuel gases were assumed to leave the furnace at the mean gas temperature. Restrictions were incorporated in the programme, to ensure that the fuel rate does not exceed a given maximum value, and that the temperature difference between the surface and centre of the ingot does not exceed a given limit while the temperature of the ingot is below 500°C at the centre.

The minimum time of heating of 10 tonne ingots was calculated taking into account a two-dimensional heat flow. The heating schedule was adopted for an industrial unit and the ingots were found satisfactory for subsequent rolling. By this a 10% saving in heating time was achieved.

Chopdar *et al* (1980) calculated the heating time for annealing of open coils of steel strip under controlled atmosphere, and Padhy (1982) calculated the same for tight coils using mathematical models. Both these results were used for design calculations of hood annealing furnaces.

Fitzgerald and Sheridan (1970) described design modifications carried out on a reheating furnace based on the results of mathematical models.

5.3 Cowper stoves

A detailed model of Cowper stove was described by Hoffman and Kappelmayer (1970). Rakesh Kumar and Sugavanam formulated a simplified model of Cowper stoves, for evaluating the effect of fuel rate, duration of on-blast and on-gas periods etc on the performance of stoves.

5.4 Refractory erosion in blast furnace

Erosion of refractories in the hearth of a blast furnace, giving rise to formation of salamander is of primary importance from the point of view of campaign life. Paschkiss and Mirsipassi (1954) considered this purely from the heat transfer point of view and solved the two-dimensional steady state conduction problem on electrical analogue. They considered that only liquid iron can erode the refractories and that the salamander can penetrate to the level of 1150°C isotherm. Das (1981) calculated the isotherm for blast furnace at Rourkela. Singh *et al* (1982) reported monitoring of B.F. hearths by temperature measurements at TISCO.

Yoshikawa and Szekely (1981) considered the problem taking into account convection currents in the hearth. Bandak (1973) described a model for estimating the erosion of lining in the bosh and stak regions of blast furnace.

6. Conclusions

At the present state of knowledge, the mathematical models of furnaces, particularly those involving combustion of fuel, are far from perfect because of the difficulties involved in modelling the external heat transfer. Hence any model set up requires verification on industrial units. Despite these difficulties, considerable information can be obtained from these models for design and operation of industrial furnaces, and can be considered as a necessary tool for improvement of design and performance of furnaces.

References

- Averin S I, Goldfarb A M, Kravtsov A F, Radchenko I I, Rosengart U I, Svinolov N P, Semikin I D and Tait N U 1969 *Calculations of heating furnaces* (in Russian) 2 e Kiev, Technica Chapter 6
- Bandak T A 1973 *Mathematical process models in Iron and Steel making*, Metals Society 26
- Beer J M 1972 *Jl. Inst. of Fuel* 370
- BISRA 1953 *Physical Constants of some commercial steels at elevated temperatures* (London: Butterworth)
- Cherapanov K A and Kalashnikova U K 1971 *Steel in USSR* p. 442
- Chopdar A K, Behera R C and Pakala V S 1980 *Trans I.I.M.* 32 384
- Collins R 1970 Mathematical models in metallurgical process development, The Iron & Steel Institute Sp. report, p. 230
- Das B K 1981 *Salamander penetration and its impact on blast furnace relining*, M.Sc (Engg) Thesis, RE College, Rourkela
- Davies R M, Lucas D M, Master J and Toth H E 1970 Mathematical models in metallurgical process development, The Iron & Steel Institute Sp. report, p. 29
- Dusinberre G M 1961 *Heat transfer calculations by finite differences* (Scranton: Int. Text Book Co.)
- Fitzgerald F and Sheridan A T 1970 Mathematical models in metallurgical process development, The Iron & Steel Institute Sp. report, p. 18
- Gosman A D 1969 *Heat and mass transfer in recirculating flows* (London: Academic press)
- Hoffman E E and Kappelmayer A 1970 Mathematical models in metallurgical process development, The Iron & Steel Institute Sp. report, p. 115
- Jackson R 1944 *Jl. of the Iron & Steel Institute* 150 211
- Lambert N and Economopoulos M 1970 Mathematical models in metallurgical process development, The Iron & Steel Institute Sp. report, p. 133
- Massey I D and Sheridan A T 1971 *Jl. of the Iron & Steel Institute* 391
- Massey I D, Robertson A D, Sanders L M and Sheridan A T 1973 *Jl. Inst. of Fuel* 379
- McAdams 1954 *Heat Transmission* (New York: McGraw Hill)

- Padhy A K 1982 *Design of Hood annealing furnace*, M. Tech thesis, RE College, Rourkela
- Pakala V S 1975 *Combined application of physical and mathematical models to heating furnaces*, Ph.D. thesis, Zdhanov Metallurgical Institute, USSR
- Paschkiss V and Mirsipassi T 1954 *Iron Steel Eng.* **31** 54
- Patanakar S V and Spalding D 1970 *Heat and mass transfer in boundary layers* (London: Int. Text Book Co.)
- Rakesh Kumar and Sugavanam R 1981 *Mathematical model of Cowper Stove*, B.Sc (Engg) Project report, RE College, Rourkela
- Salter F M and Costick J A 1974 *Jl. Inst. of Fuel* **47** 3
- Sevrin R 1970 Mathematical models in metallurgical process development, The Iron & Steel Institute Sp. report, p. 147
- Singh B N, Chatterjee L M and Chatterjee A 1982 *Trans. I.I.M.* **35** 475
- Surgent R J and Slack M R 1954 *Jl. of the Iron & Steel Institute* **177** 428
- Thomas B G, Samarasekera I V and Brimacombe J K 1984 *Met. Trans.* **B15**(2) 307
- Thrig M W 1952 *Jl. of the Iron & Steel Institute* **171** 381
- Tocher K D 1970 Mathematical models in metallurgical process development, The Iron & Steel Institute Sp. report, p. 2
- Yoshikawa F and Szekely J 1981 *Ironmaking Steelmaking* **4** 159

Computer simulation of defects and radiation damage

K KRISHAN, B PURNIAH and S SRINIVASAN

Materials Science Laboratory, Indira Gandhi Centre for Atomic Research, Kalpakkam 603 102, India

Abstract. In this paper, we describe the computer simulation technique and its application to the study of radiation damage. Details of two important methods: the static and the dynamic methods have been discussed. Applications to the study of point defect formation and stability, their clusters, diffusion, dislocations and dislocation-point defect interaction are discussed drawing from our own work wherever possible. A short mention is made of the importance of the interatomic potential. Examples for the case of magnesium and other hcp metals, bcc iron and fcc Ni are cited and numbers for various quantities like formation energy, dipole tensor, interaction energy etc are quoted.

Keywords. Computer simulation; interatomic potential; static method; dynamic method; point defects; dislocations; displacement damage.

1. Introduction

The study of matter in radiation environments has developed into an important area of research due to the technological demand of finding reliable and stable materials for the structural components of nuclear reactor systems. The energetic particles of the radiation displace the atoms in a metal (or alloy) bringing about irreversible changes in the composition and microstructure. These changes at an elementary level involve three processes: the formation of defects, their diffusion and subsequently annihilation. Each of these damage events leaves behind a permanent mark whose cumulative effect results in the changes in alloy properties often referred to as radiation damage. Some examples of these are embrittlement, irradiation creep and swelling. Invariably, these involve the redistribution of radiation-produced defects due to diffusion and are studied with the help of rate equations whose parameters are related to basic 'damage events'. It is in the study of this more basic aspect of radiation damage that computer 'experiments' play a very important role.

The basic damage process occurs over several orders of magnitude in time. In the first 10^{-17} sec an energetic projectile transfers its energy to the nucleus of the metal lattice atom producing a primary knock-on-atom (PKA). In the next 10^{-13} sec the PKA slows down creating a cascade of secondary displacements. The cascade volume dissipates its energy in 10^{-11} sec forming unstable defects which spontaneously rearrange themselves into stable defects. Then begins a long period of several hundreds of seconds when these defects diffuse and eventually annihilate at sinks. This annihilation, or defect annealing, depends on the interaction between the defects and leads to the formation of clusters or complexes depending on their relative stability. The very short times involved and the statistical nature of the events (due to the large number of degrees of freedom) makes it difficult to use analytic methods of investigation or device experiments where each event can be followed. However, the advent of high speed

computers has made it possible to simulate these processes in a way as if they are actually occurring in a solid. It is for this reason that such studies have been termed computer experiments.

Computer experiments deal either with the dynamic aspects of damage like the formation of cascades or with static aspects which concern the formation of stable defect configurations. In §2, we give an account of the computer simulation procedure for both static and dynamic experiments. Section 3 deals with the range of problems which have been studied with typical examples and results drawn from our own work wherever possible. Finally in §4 we give a brief conclusion.

2. Computer simulation technique

In general, in all computer simulation methods, a model crystallite of the required material is constructed in which the atoms are allowed to interact via a suitable interatomic potential. The defect is then placed at the centre of this crystallite. The presence of the defect will cause forces to act on the atoms surrounding it. This configuration is allowed to relax using either the static or dynamic method. The number of atoms in this crystallite usually ranges from a few hundred to a few thousand depending on the complexity of the defect under study and the range of interatomic potential. The computation of the various quantities of interest requires that a neighbour set be generated for each atom in the crystallite. While the generation of the crystallite itself is quite simple once the crystal type is known, generation of neighbours calls for greater efforts and will be treated in greater detail below. After a brief discussion on interatomic potentials we discuss the techniques for relaxation. Several techniques used in computer simulation including sample programmes are discussed in a recent book by Beeler (1983a). Towards the end of this section two specific examples viz the simulation of point defects and dislocations is discussed in slightly greater detail.

2.1 Generation of neighbours

In the case of cubic crystals the position vector of any atom can be conveniently described by a set of three integers if distances are measured in half lattice units. The neighbour positions in an fcc crystal can be generated by a technique of partitioning the squares of the radial distances NR^2 (which occur in multiples of 2) and thereafter by taking the various possible permutations of these partitioned numbers. Thus we have $NR^2 = NX^2 + NY^2 + NZ^2$ where the integers NX , NY and NZ represent the components along the x , y and z directions respectively (see table 1). A given value of NR^2 denotes a particular shell and the atoms in the shell can be obtained by the permutations of the three numbers as shown in the table.

The generation of neighbours in an hcp lattice is more complicated. Firstly, the radius vector of all the atoms in the crystallite is calculated from a given origin and arranged in an ascending order. Atoms having the same radius are grouped together into one shell. These atom co-ordinates are then normalized to yield integer numbers and these are stored for later use. It may be noted that a further complication arises because of the c/a ratio. For instance the fourth and sixth neighbour shells of Mg ($c/a = 1.63$) and Zr ($c/a = 1.86$) get interchanged.

Table 1. Shell-wise neighbour generation for an fcc crystal

NR^2	NX	NY	NZ	X	Y	Z
0	0	0	0	0	0	0
2	0	1	1	0 0	1 -1	1 -1
4	0	0	2	0 0	-1 -1	1 -1
6	1	1	2	1 1	0 0	1 -1
8	0	2	2	-1 -1	0 0	1 -1
10	0	1	3	1 1	1 -1	0 0
12	2	2	2	-1 -1	1 -1	0 0
:	:	:	:	:	:	:

While the above discussion holds for the simulation of point defects, in the case of dislocation simulation, it is convenient to choose the co-ordinate axes along the dislocation line and Burgers vector thereby necessitating a transformation in neighbour co-ordinates.

2.2 Interatomic potential

A crucial aspect of computer simulation is the choice of an appropriate interatomic potential. A large number of diverse interatomic potentials have been proposed in the literature. These can be broadly classified as empirical and pseudopotentials. Examples of the former are the Morse, Lennard-Jones and several polynomial potentials (Johnson 1973). Pseudopotentials are known to represent the interaction better but these have not made much headway in defect calculations. The most widely used polynomial potentials for defect calculations have been the cubic and the quintic splines where the polynomial coefficients are obtained by least squares spline fitting the potential to the elastic constants of the material. Such potentials for cubic metals have been described by Baskes and Melius (1979) while those for hcp metals have been described by Purniah *et al* (1980).

2.3 Relaxation techniques

As already stated, the configuration of the crystallite containing the defect is allowed to relax to a minimum energy configuration. The crystallite is usually divided into two regions to save on computation time. In the inner region I, the atoms are allowed to relax under the influence of the chosen potential. The atoms in the outer region II are constrained to their perfect lattice positions as shown in figure 1. The relaxation of atoms in region I can be done either by the static method or the dynamic method. In the static method, the relaxation is performed by an iterative technique using the Newton-

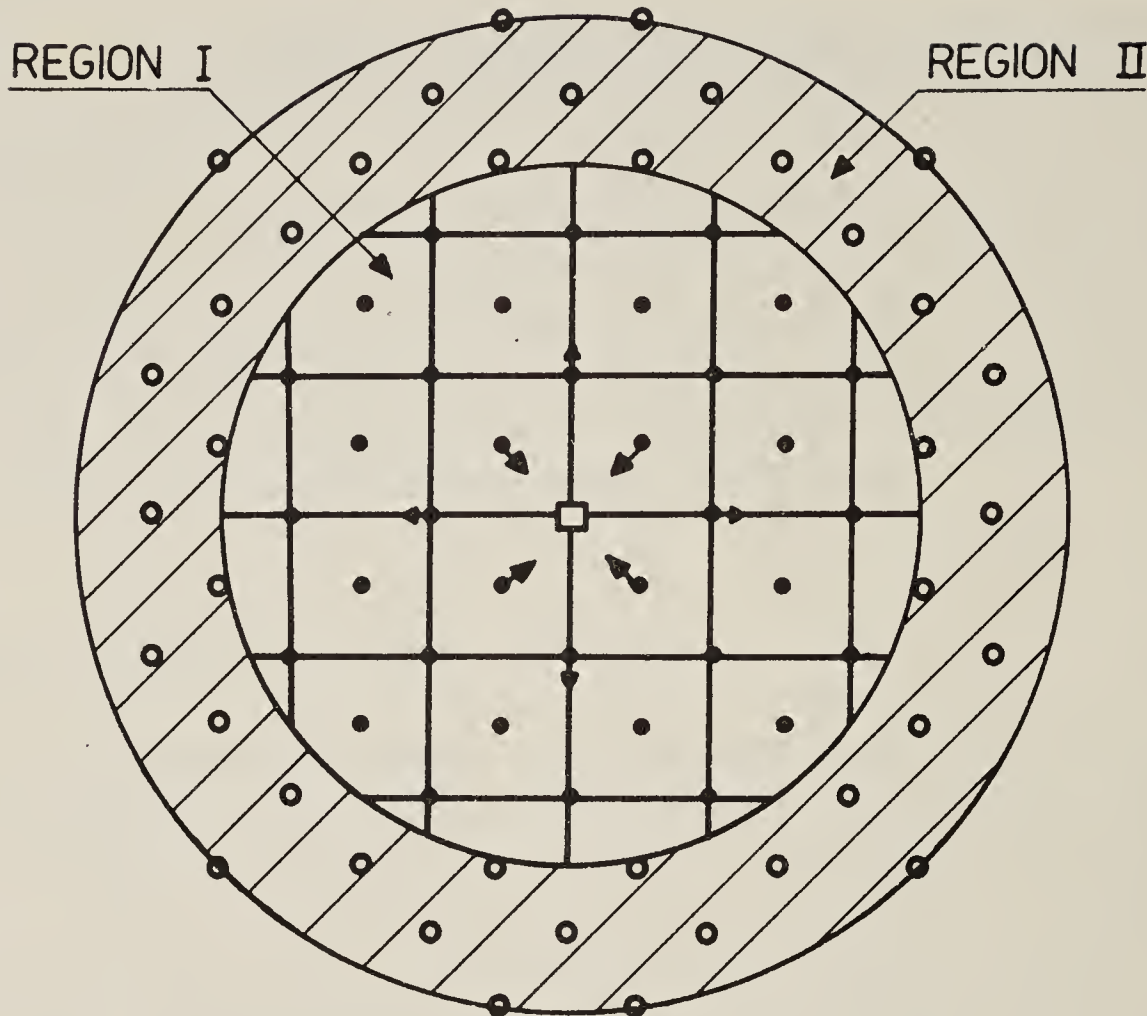


Figure 1. Schematic representation of the two regions in a crystallite used in computer simulation studies. Open circles represent atoms which are fixed while filled circles indicate the atoms which are allowed to move. Also shown by arrows is the displacement of atoms around a vacancy (\square) placed at the centre.

Raphson method. Thus the relaxed position of the n th atom after $k + 1$ iterations is given by

$$X_{k+1}(n) = X_k(n) - \alpha \frac{\partial U}{\partial X(n)} \left/ \frac{\partial^2 U}{\partial X^2(n)} \right|_{X(n) = X_k(n)},$$

where $X_k(n)$ is the co-ordinate of the n th atom after the k th iteration and U is the configuration energy. The convergence factor α ($0 < \alpha \leq 1$) has been introduced to damp out the oscillations which are usually present in the co-ordinates X_k while applying the Newton-Raphson technique directly. The total number of iterations for reasonable convergence may run into several hundred depending on the problem being considered. From the above discussion it is clear that the simulation work requires a large and fast computer. Typically all the programs operate in double precision, occupying 512 kilobytes of core memory and take upto one hour of CPU time.

In the dynamical method also referred to as "molecular dynamics" method, the movement of individual atoms in an assembly is followed using Newton's equations. Given the initial position and the velocity for each atom in the crystallite, the dynamical history is followed by numerically integrating the $3N$ simultaneous equations of motion for the co-ordinate components of the N atoms in the crystallite. In the process, the $3N$ velocity components for the N atoms are also determined.

The dynamical method is very useful in describing temperature effects on Frenkel pair production, annihilation and point defect complexes.

The net force $F(t)$ experienced by an atom at time t is determined by the relative positions of all the other atoms at time t and $a(t) = F(t)/m$. Given $a(t)$, the advanced

time quantities are given by using one of the many schemes available (Gibson *et al* 1960)

$$\begin{aligned} v(t + \Delta t/2) &= v(t - \Delta t/2) + a(t) \Delta t, \\ x(t + \Delta t) &= x(t) + v(t + \Delta t/2) \Delta t. \end{aligned}$$

In these simulations, the value of Δt is in the region of 10^{-14} sec which gives an idea of the time scales which can be probed.

2.4 Simulation of point defects and dislocations

In the case of point defect simulation, the inner region I is chosen to be a sphere. Periodic boundary conditions are employed to essentially generate the large size of the assembly needed to remove any surface effects. This is further checked out by varying the size of region I to see the effect of the boundary region. The defect formation energy is calculated by subtracting the energy of the perfect lattice from the energy of the relaxed lattice with either an extra atom (vacancy case) or an atom-less (interstitial case) at the crystal surface. The relaxation energy is obtained by subtracting the energy of the crystallite with the defect in the relaxed condition from that in the unrelaxed condition.

The inner region for the case of dislocation simulation is chosen to be cylindrical to take advantage of the symmetry in the problem. The direction of the dislocation coincides with the cylinder axis and periodicity along the dislocation line is assumed. The 'introduction' of the dislocation is done by imparting elastic displacements to the atoms by considering a dislocation at the centre of the block (Cotterill and Doyama 1967). The core configuration and other parameters can be obtained by the relaxation technique described. There have been several modifications to the methods described above for dislocations. One of these is the 'flexible' boundary condition method (Hoagland *et al* 1976) where the atoms in region II are moved in response to the changes which occur in the inner region. This enables a smaller crystallite size to be chosen thereby reducing the computation time. It may however be noted that in the study of the dislocation point defect interaction the flexible boundary methods cannot be used since the introduction of the point defect destroys the symmetry in the problem.

3. Application of computer simulation to radiation damage problems

In this section we briefly discuss some of the areas where computer simulation has been successfully used to investigate the behaviour and properties of defects produced by radiation. The selection has been made to cover a range of problems and to emphasize the nature of information obtained by the technique rather than the detailed results.

3.1 Vacancies, interstitials and their clusters and complexes

The study of point defects and their clusters has been one of the important areas where computer simulation experiments have been particularly successful. Here due to the many degrees of freedom available one has to examine from amongst several possibilities, the configurations which would be most stable. For example figure 2 shows three configurations each of di-vacancies and tri-vacancies and the three possible sites for a self-interstitial—namely split, tetrahedral and octahedral for an hcp lattice.

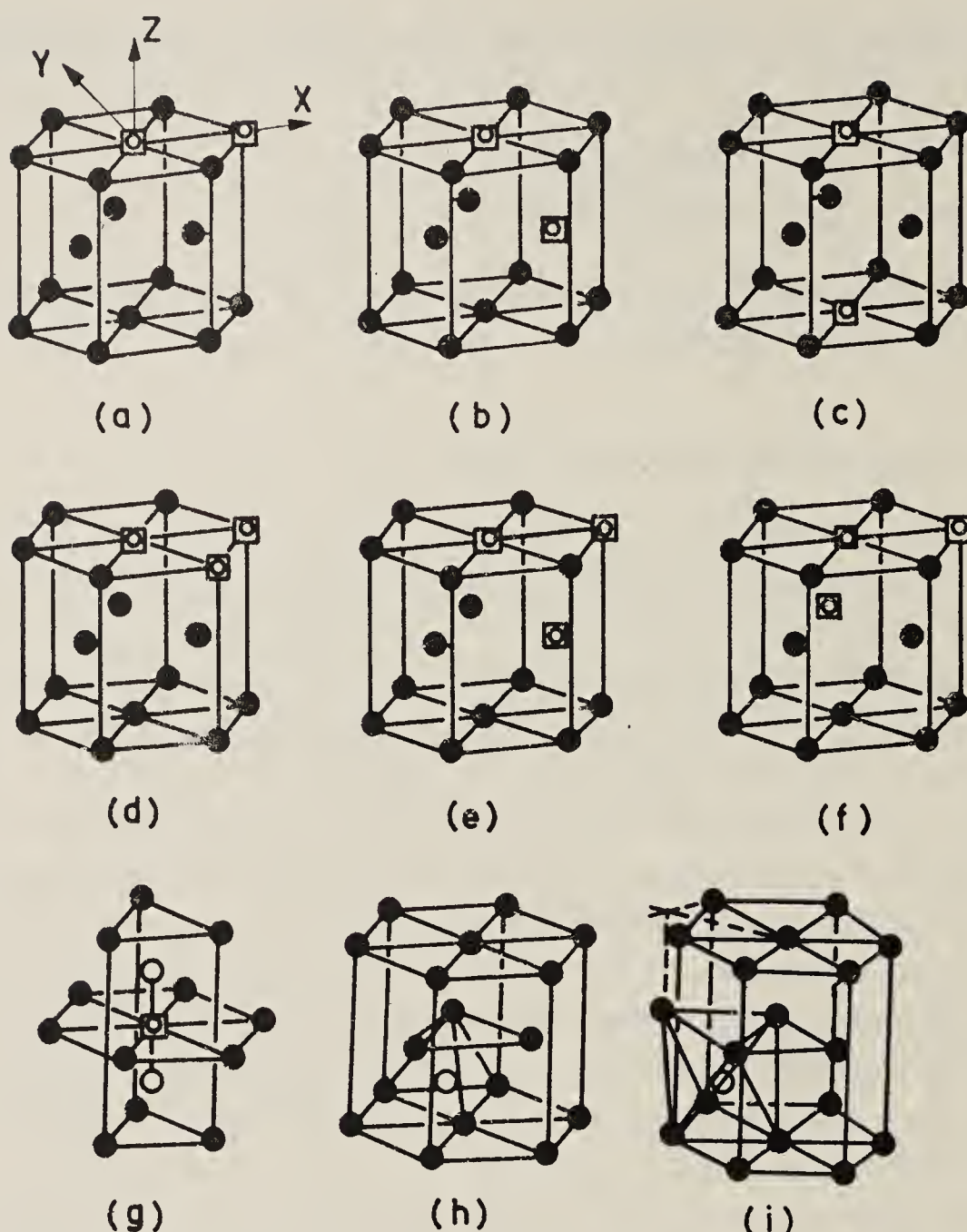


Figure 2. The three possible configurations each of the divacancy (**a, b, c**) and trivacancy (**d, e, f**) in hcp magnesium. The three configurations at the bottom are those for the split, tetrahedral and octahedral interstitial.

These are amongst the more favourable ones and further possibilities cannot be ruled out. Computer simulation has shown that for self-interstitials the split configurations along $\langle 110 \rangle$ for bcc, $\langle 100 \rangle$ for fcc and $\langle 0001 \rangle$ for hcp are most favourable on the basis of minimum energy consideration. A comparison of the strain field of a vacancy and a self-interstitial is shown in figure 3 for hcp Mg as a typical example (Sahu *et al* 1980). Table 2 shows the relaxation field around a monovacancy for several hcp metals (Purniah *et al* 1980). Characteristic of this strain field are the positive and negative displacements of the different neighbouring shells; the maximum displacement at the third neighbour for a vacancy in Mg; nearly an order of magnitude higher strain field for self-interstitials as compared to vacancies. Similar features have been seen in bcc iron and fcc nickel which are some of the metals extensively studied. Very similar to these are investigations on over-sized and under-sized substitutional impurities whose strain fields show similar behaviour. For a 10% over-sized impurity in bcc iron, the energy of each of the first-neighbour atoms increases (+ 0.036 eV) (i.e. high energy atom site) and that of the second neighbours decreases (- 0.026 eV) (low energy atom site). A systematic study of this feature leads to a rule for predicting the geometry of an impurity-vacancy complex (Beeler 1983b). If a high-energy atom site in the substitutional impurity atom displacement field is replaced by a vacancy, the resulting

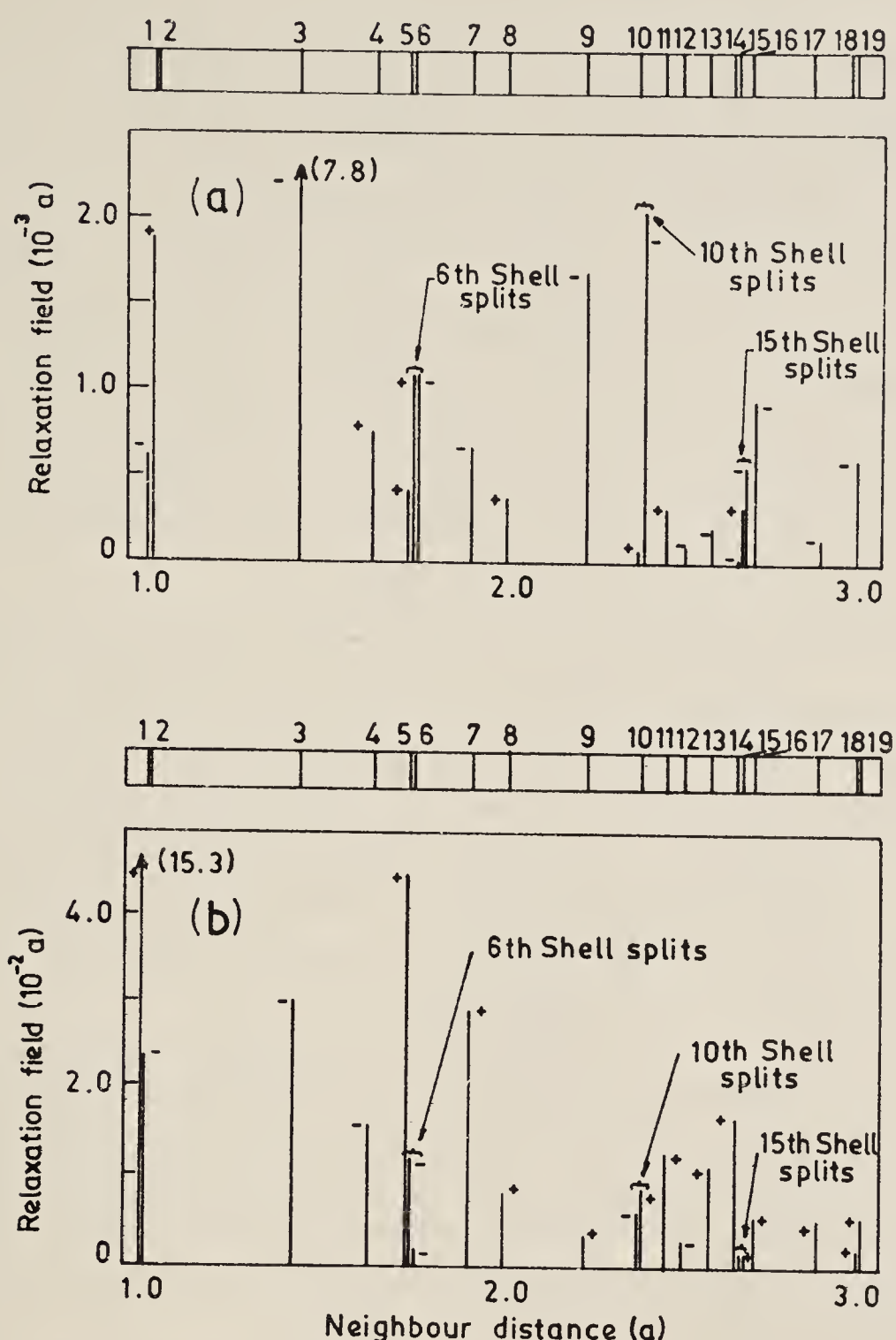


Figure 3. The relaxation field of all shells upto nineteen neighbours around a single vacancy (a) and a split interstitial (b). The bars on top represent the neighbour positions shown separately for clarity. (+ and - signs indicate outward and inward relaxation).

Table 2. Relaxation field around a monovacancy. The numbers 1st, 2nd, 3rd and 4th refer to neighbours. (The + and - signs indicate outward and inward relaxation).

Metal	Relaxation field ($10^{-2} a$)				Relaxation volume $\Delta V/V_{at}$	Dipole tensor (eV)	
	1st	2nd	3rd	4th		$P_{11} = P_{22}$	P_{33}
Hf	-1.32	-0.65	+0.48	+0.41	-0.18	-4.09	-7.94
Mg	-0.40	-0.34	-0.69	+0.01	-0.09	-0.93	-0.95
Re	-0.80	-0.70	+0.12	+0.19	-0.14	-8.16	-11.24
Y	-2.09	+0.70	+1.36	+0.48	-0.21	-1.57	-6.32
α -Zr	-1.62	-1.80	+0.28	+0.35	-0.31	-6.92	-8.36
Be	+6.15	+2.04	+5.65	+3.72	+0.56	+7.74	+1.73

complex will have a positive binding energy while for a low-energy atom it will result in a negative binding energy. Such features are also found in the stability of some defect complexes. For example in bcc iron a second neighbour arrangement of vacancies has been found to be more stable than first neighbours arrangement. In hcp Mg, of the three configurations (a), (b) and (c) shown in figure 2 for di-vacancies the formation (and binding) energies are 1.377 (0.086), 1.379 (0.084), 1.386 (0.077) eV respectively showing that configurations (a) and (b) are likely to be more stable at lower temperatures (Sahu *et al* 1980). Similarly for the tri-vacancy configurations (d), (e) and (f) have energies 1.939 (0.256), 1.942 (0.252) and 1.972 (0.222) eV which favours the planar configuration (d). Extensions of such simulation experiments have been carried out to very large vacancy clusters (~ 40) to examine how such clusters could develop into vacancy dislocation loops or voids (Beeler and Johnson 1967).

Apart from substitutional impurities, light atoms like C, N and O often occupy interstitial locations. The simulation technique in this case is very similar to that for self-interstitials, the important difference arises from the use of an impurity-host potential. Apart from the defect formation energy E_f and migration energy E_m , other important parameters are the defect formation volume and the dipole tensor. Results for some of the calculations are shown in table 3 (Purniah *et al* 1982). The agreement between the estimated E_m and that obtained from experiments is seen to be very good. Further the dipole tensor values compare very favourably in sign and magnitude from those obtained by anelastic data and x-ray measurements.

Studying the behaviour of He in metals has been a problem of great technological interest where computer experiments have been very valuable. Helium can diffuse interstitially and readily forms complexes with vacancies. Computer simulation studies have revealed that as many as six to seven helium atoms can be accommodated in a single vacancy! These studies give detailed information about helium and vacancy binding to a complex of n helium atoms and m vacancies (Wilson *et al* 1976). The structure of some typical complexes is given in figure 4.

The study of diffusion of vacancies, interstitials, clusters and complexes of defects is an area where computer simulation is particularly useful. A defect moving from one equilibrium position to another has to pass through an intermediate unstable saddle point which determines the height for the migration barrier. Computer simulation provides detailed information about these intermediate configurations. As an example figure 5 shows the results of computer simulation of vacancy migration in bcc iron. The nature of the interaction and the positions of the surrounding atoms gives rise to two saddle points SP1 and SP2 as the atom A moves from its site to the vacancy (Beeler 1983c).

Table 3. Simulation results for various quantities for interstitials in α -Fe, Zr and Hf

Interstitials	E_f (eV)	V_f (Ω_0)	E_m (eV)	E_m (expt) (eV)	Dipole tensor (eV)	
					$P_{11} = P_{22}$	P_{33}
C in α -Fe	1.35	0.055	0.86	0.835	-0.053	4.223
C in Zr	1.38	0.048	1.48	1.48	1.472	1.395
O in Zr	2.98	-0.002	1.94	2.04	-0.049	-0.046
O in Hf	3.30	0.0	2.16	2.26	0.001	0.001

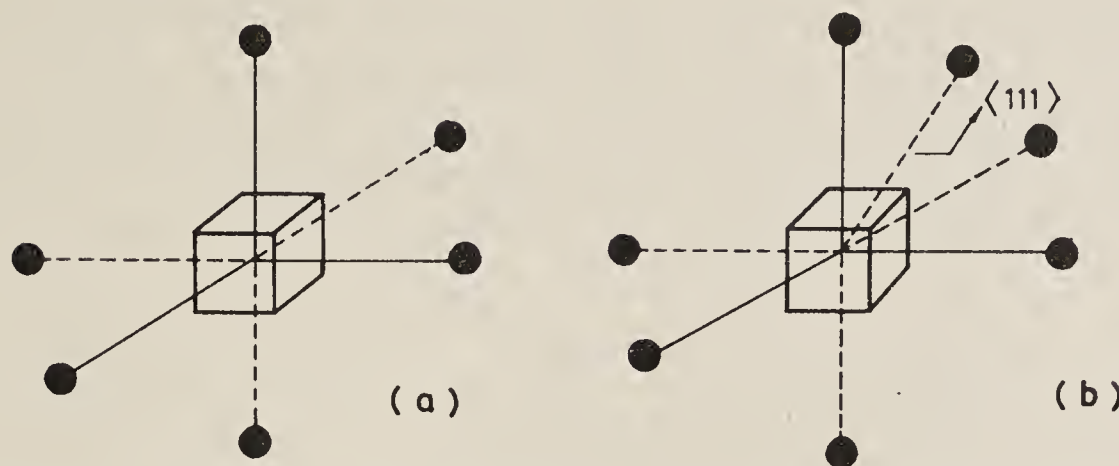


Figure 4. Minimum energy configurations of six and seven helium atoms in a single vacancy in Cu. Helium atoms are described by filled circles and the vacancy by the empty cube.

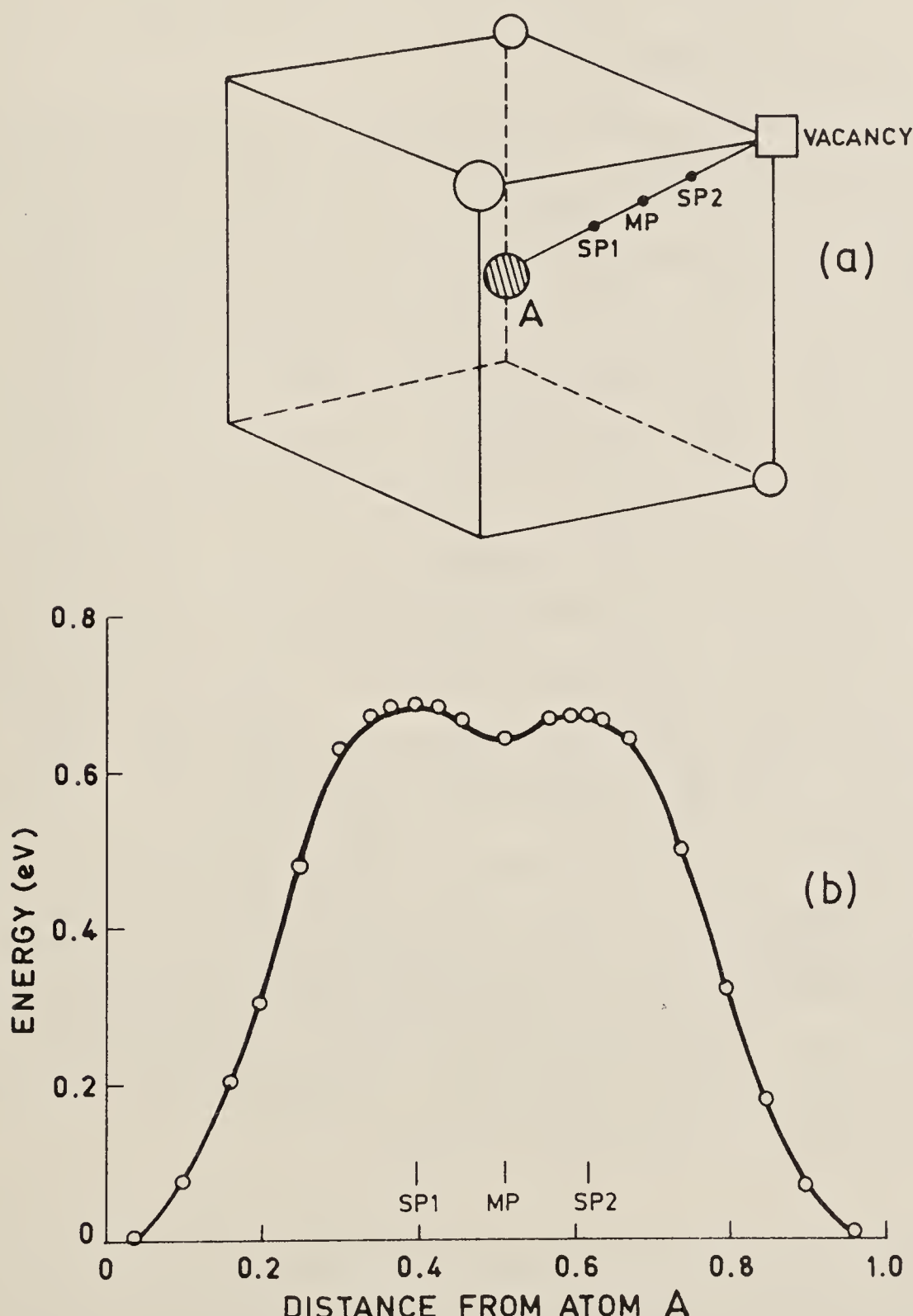


Figure 5. (a) Vacancy migration in bcc iron. The vacancy (\square) migrates to the site A (the body centre position) via the two saddle points SP1 and SP2. MP is the mid-point of the path. (b) Crystal configuration energy change for the vacancy migration path shown above.

Computer simulation has also been employed in the study of dislocations and their interaction with point defects. For example the splitting into partials of an edge dislocation in an fcc lattice has been seen by simulation. Quantities like the stacking fault width and the core structure have been evaluated (Perrin *et al* 1972). A most recent review covering the literature of dislocation modelling in various systems can be found in Puls (1980).

The study of dislocation-point defect interaction is very important to understand many metallurgical processes like strain aging etc. Computer simulation has been effectively utilized to obtain information regarding the configuration and energetics of this interaction. The interaction of a carbon atom with an edge dislocation in fcc nickel has been studied by Purniah *et al* (1985). The salient features of these results are the correct prediction that the small-sized interstitial prefers to sit above the slip plane. Further, the dipole tensor which was originally spherical in the absence of the dislocation becomes monoclinic.

3.2 *Displacement damage simulation*

Most of our knowledge about atomic displacements and cascade damage has come from dynamic computer simulation. A projectile with a given energy and appropriate direction with reference to the crystallographic orientations is allowed to move at time $t = 0$. The subsequent interactions with the lattice atoms are then observed according to the predetermined force laws. Different structures emerge depending on the kinetic energy of the projectile. At energies less than the displacement energy E_d (typically 10–50 eV in most metals), the energy loss is mainly by elastic collisions. This energy loss is channelled normally along crystallographic directions called focussions (Silsbee 1957). At energies around E_d and above, a Frenkel pair is formed. One of the important features of this process is the replacement collision sequence where atoms in a chain exchange positions. The length of such sequences is generally 3 to 10 atomic distances but rather long replacement collision chains (greater than 50 atomic distances) can also exist in certain close packed directions (Lucasson 1975). The minimum displacement energy E_d depends on the relative direction of the projectile with respect to the crystallographic planes and is often obtained as the displacement energy surface as shown in figure 6a. At higher projectile energies the probability of forming more than one Frenkel defect increases (figure 6b). At still higher energies new features emerge. The initial PKA is able to impart enough kinetic energy to atoms to produce secondary collision cascades which normally branch off at right angles to the primary cascades thus resulting in multiple Frenkel pairs. These subcascades can sometimes overlap reducing somewhat the chances of survival of Frenkel pairs. In all these simulation runs the relaxation of atoms, spontaneous reorganization or recombination of unstable configurations is built into the simulation event. A graphical picture of the process at 5 keV obtained by Beeler (1966) is given in figure 7.

4. Conclusions

In this paper we have discussed the computer simulation technique and its application to the study of defects in materials. In particular, we have considered the case of point defects, impurities, dislocations and dislocation-point defect interactions. Several other

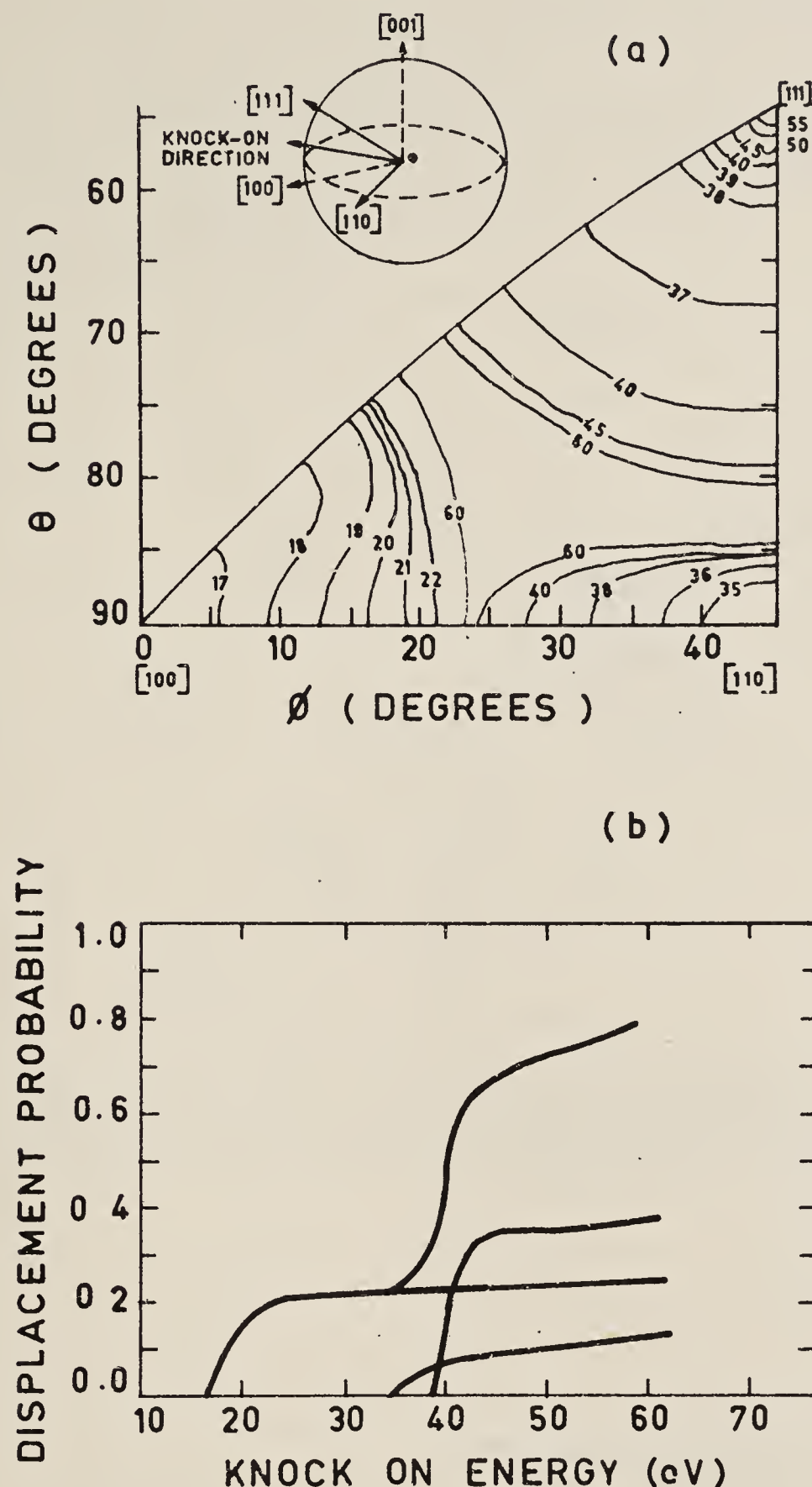


Figure 6. (a) Contours of constant displacement energy threshold (in eV) in bcc Fe. The polar and azimuthal angles define the PKA emission direction (Erginsoy *et al* 1964). (b) Integrated displacement probability $P_d(t)$ for a PKA of energy E and random direction in bcc iron. Contributions to the three low-index directions are shown separately.

areas of study have been omitted due to the limitations of space. Notable among these are studies regarding the behaviour of grain boundaries, slip and other deformation related processes. While the results depend very much on the exact interatomic potential chosen, the wide applicability of this technique makes it a very useful tool of research.

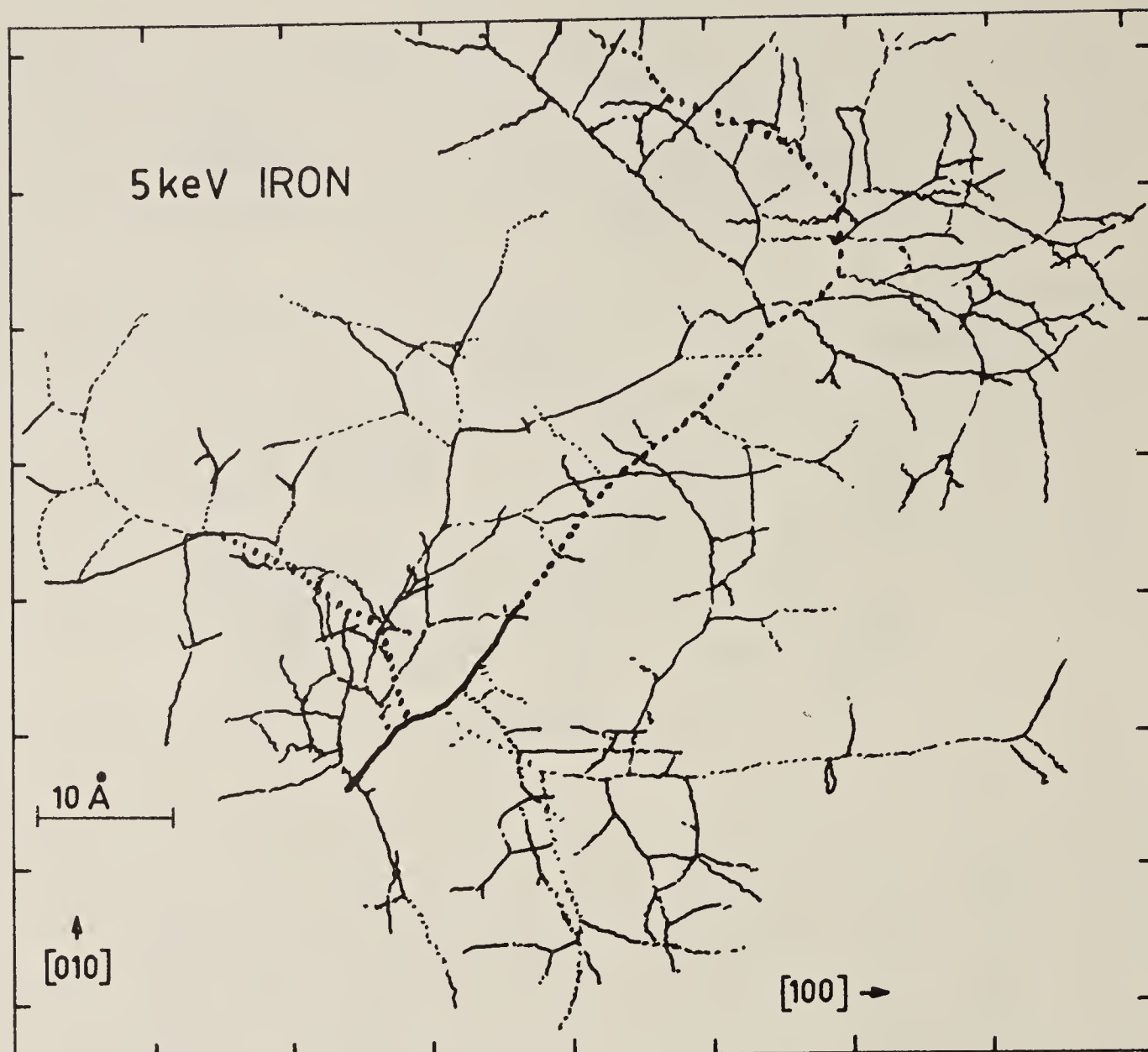


Figure 7. Trajectory map for a 5 keV collision crack in bcc iron. The short thick line represents the PKA trajectory. The 3 main secondary knock on trajectories are represented by heavy dotted lines. For higher order KA the trajectory lines are alternately solid and dashed lines.

References

- Baskes M I and Melius C F 1979 *Phys. Rev. B* **20** 3197
 Beeler J R Jr 1966 *Phys. Rev.* **150** 470
 Beeler J R Jr 1983a *Radiation effects computer experiments* (Amsterdam: North-Holland)
 Beeler J R Jr 1983b *Radiation effects computer experiments* (Amsterdam: North-Holland) p. 318
 Beeler J R Jr 1983c *Radiation effects computer experiments* (Amsterdam: North-Holland) p. 428
 Beeler J R Jr and Johnson R A 1967 *Phys. Rev.* **156** 677
 Cotterill R M J and Doyama M 1967 in *Lattice defects and their interactions* (ed.) R R Hasiguti (New York: Gordon and Breach) p. 20
 Erginsoy C, Vineyard G H and Englert A 1964 *Phys. Rev. A* **133** 595
 Gibson J B, Goland A N, Milgrom M and Vineyard G H 1960 *Phys. Rev.* **120** 1229
 Hoagland R G, Hirth J P and Gehlen P C 1976 *Philos. Mag.* **34** 413
 Johnson R A 1973 *J. Phys. F* **3** 295
 Lucasson P 1975 in *Fundamental aspects of radiation in metals* (eds) M T Robinson and F W Young (US Department of Commerce, National Technical Information Service, Springfield, USA, Report Conf. 751006) Vol. 1, p. 42
 Perrin R C, Englert A and Bullough R 1972 in *Interatomic potentials and simulation of lattice defects*. (eds.) P C Gehlen, J R Beeler Jr. and R I Jaffee (New York: Plenum Press) p. 509
 Puls M P 1980 in *Proc. Int. Conf. on Dislocation Modelling of Physical Systems*, (ed) C S Hartley (UK: Pergamon Press) Special *Acta Met./Scripta Met. Publication*

- Purniah B, Srinivasan S and Krishan K 1980 in *Proc. Nucl. Phys. and Sol. State Phys. Symposium*, Delhi (Department of Atomic Energy) Vol. C23, p. 742
- Purniah B, Srinivasan S and Krishan K 1982 in *Point defects and defect interactions in metals* Proc. Int. Conf., (eds) J Takamura, M Doyama and M Kiritani (Tokyo: Univ. of Tokyo Press) p. 322
- Purniah B and Srinivasan S 1986 *Bull. Mater. Sci.* **8** 247
- Sahu H K, Srinivasan S and Krishnan K 1980 *Pramana (J. Phys.)* **15** 189
- Silsbee R H 1957 *J. Appl. Phys.* **28** 1246
- Wilson W D, Baskes M I and Bisson C L 1976 *Phys. Rev. B* **13** 2470

Some fundamental considerations to precede image analysis

DIETER VOLLATH

Kernforschungszentrum Karlsruhe GmbH, Institut für Material- und Festkörperforschung III, Postfach 3640, D-7500 Karlsruhe, FRG

Abstract. This paper explains the different types of specimens which are of a deterministic or stochastic nature. Especially for stochastic specimens it is pointed out that, before any measurement is done, the problem has to be analyzed as to why we measure. As a size per se does not exist it is shown that particles must be analyzed by size and shape. For this, two methods are indicated, while it is stressed that in materials science the Delfiner approach for description of particle sizes is the most practicable.

Based on Delfiner's concept of size the classification of particles according to their size, shape and orientation is explained. For measuring use of the image transformations *erosion*, *ouverture* is proposed. In addition, a new transformation called "*Template matching*" is explained. This new transformation avoids the disadvantages of erosion and ouverture in case of concave particles. Besides, template matching, in contrast to erosion or ouverture, is able to give true values of area and circumference. The concept of classification is explained by simple examples.

Keywords. Image analysis; erosion; ouverture; template matching.

1. Introduction

Many instruments for image analysis are presently on the market. Each of these instruments has many characteristic features. With the steady increase of computer performance the image analysers offer a growing number of possibilities. The user of these instruments is confused. It is the aim of this paper to give some hints on how to begin measurements with an image analyser. These considerations are made from the standpoint of a materials scientist. Possibly in life sciences the questions are different and likewise the solutions; but, maybe, the basic ideas are similar.

2. Categories of problems

Before a measurement starts the underlying problem must first be defined. This may seem a trivial condition, and it is without any significance as long as there are only limited possibilities of measurement. It becomes relevant only as a result of the fact that the theoretical and technical advances in measurement have made it possible to find answers to a broader range of questions.

When selecting the measuring technique, first of all the character of the sample material must be studied. In this respect, two categories of problems must be distinguished:

- Deterministic problems. They refer to sample material, each detail of which must be analyzed and classified. A typical problem in this category is, e.g., automatic reading of texts in which each and every letter must be identified and classified. Another

- example is the automatic quality control of workpieces for perfection. Also in this case, each individual workpiece must be analyzed and faulty workpieces sorted out.
- Stochastic problems arise if parts of a sample are measured which satisfy a distribution function and the sample satisfies conditions of stationarity. In this sample material it is not important to measure each individual element of the particles of interest. It is sufficient to measure a statistically significant fraction of the sample. However, care must be taken to avoid a bias to be introduced into the statistics by the choice of the fraction of the sample measured. Typical applications of this technique are measurements of segregations in alloys or counts of pore size distributions. The automatic examination for cracks in workpieces does not fall under this category of problems, because in this case even a single crack in a workpiece may mean that the respective item must be scrapped. This is a typical deterministic problem, because every potential crack must be found.

Also the measuring techniques to be applied depend on the problem at hand. In the case of deterministic problems, the individual objects must be singularized before measurement; in general, methods of pattern recognition are applied subsequently. In the case of stochastic samples we are not interested in readings obtained from individual particles. In this case we measure field quantities (Nawrath and Serra 1979), it may even be necessary to carry out transformation before measuring within the image. These techniques are based on Minkowski's operations of sets (Hadwiger 1950) or on correlation functions (Vollath 1981). In this connection, especially the field of mathematical morphology has advanced quite far (Matheron 1967; Haas *et al* 1967a,b; Serra 1969). These are the fundamental papers, which have produced an immense amount of literature.

Occasionally, however, also sample material of a stochastic nature may cause problems which cannot be solved by the familiar techniques applied to analysis of such sample materials. In this case, a roundabout way will have to be found, which involves individual analysis of the particles of the sample and further processing by the rules of statistics of the results of such deterministic analysis.

Table 1 is a summary of these problems and the corresponding methods of evaluation. This paper will be limited to the problems of processing samples of a

Table 1. Problems and methods of evaluation used in image analysis

	Character of sample	
	Deterministic	Stochastic
Structure of sample	Group of significant shapes	Randomly distributed particles
Application	Pattern recognition, sorting out faulty workpieces	Materials analysis, characterization of powders
Methods	All techniques of pattern recognition	Minkowski operations of sets (mathematical morphology), correlation function
Results	Significance of a symbol, yes-no information about the quality of workpieces	Distribution function with respect to one or more parameters

stochastic nature, although a considerable part of the treatment also applies to samples of a deterministic analysis.

3. What to measure?

Once the type of sample has been defined, a technique of measurement can be found. Any measurement must be based on a clear-cut technical or physical problem. In order to allow the measured result to be interpreted in the sense of such a problem, it is necessary to derive from the problem a behavioural model and develop a measuring technique compatible with it.

If we have understood what we wish to measure the next intuitive question will be: What is the size of the particles? If we look at the particles drawn in figure 1 we will realize that a size per se is not existing. If we wish to make a statement about the size of these particles, we have to give additional information about these shapes. We must realize that any information about size of a particle in principle supposes a dimension adequate to the shape of the particle to be evaluated. Consequently, the new demand for taking into account the shape in classifying particles has much more far reaching consequences. It incorporates the need to break up into subsets a group of particles, the descriptors of these subsets being different shapes simple to describe in terms of geometry. The desired result is not a size distribution function, but several distribution functions, which can be assigned to different shapes describable in geometric terms. Each of these distribution functions describes only that fraction of the particles which can be described by the corresponding shape.

When performing an actual analysis we are usually not solely interested in obtaining just data. So we will never ask, e.g., a question such as "how large are the pores in a sintered body with respect to a certain shape". Instead, the question must be, "how large are the pores with respect to a certain property (e.g., thermal conductivity)." Asking for size per se is not meaningful, because any definition of size will also incorporate the shape, and the shapes by which the pores should be analyzed are a function of the model underlying the description of a property. If, e.g., in our example the property is the thermal conductivity of the sintered material the shapes suited for analyzing this property are more frequently ellipses.

Some examples of such correspondence between a physical problem and its description in a model or by image analysis will be given below. For instance, if the technique of image analysis is to be applied to simulate the measuring process in mercury porosimetry when characterizing sintered specimens, this is best done by using an approximately circular structuring element used for the "ouverture" image transformation (Müller 1973; Vollath 1979b). If area measurements are conducted after

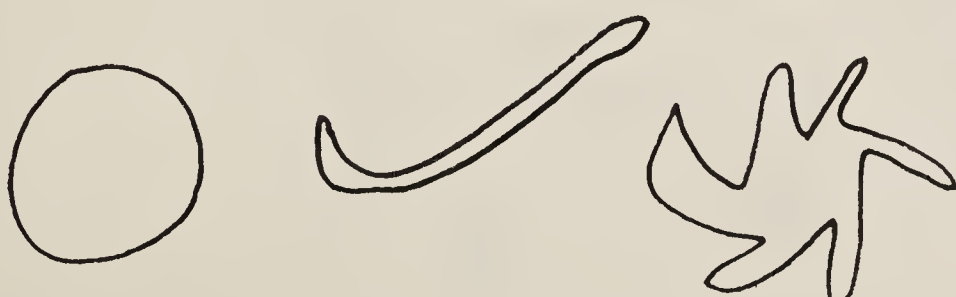


Figure 1. How can we describe these shapes?

these image transformations, comparison with the results of mercury porosimetry will furnish very interesting insights into pore structures (Vollath 1979).

Figure 2 shows a comparison of the principles of mercury porosimetry and image analysis. The fundamental difference that in case of mercury porosimetry pores are filled from outside and in image analysis the pores are filled in a cut plane leads to significant differences of the results giving interesting information of the pore network.

The question about the "size" of particles rich in plutonium in $\text{UO}_2\text{-PuO}_2$ nuclear fuels can be answered if it is known that the size of these particles is limited because of potential overheating in cases of rapidly rising reactor power. Hence, in a first approximation, the maximum heat conduction pathway is the dimension characteristic of size in this case. The maximum heat conduction pathway is indicated in a first approximation by the radius of the largest spheres inscribable in the particles (Vollath 1979a). Refinement of this model leads to the description of particles by ellipsoids (Vollath 1982).

Depending on the method of fabrication adopted sintered bodies sometimes have pores approximately tetrahedral in shape besides those approximately spherical.

Figure 3 depicts the situation observed in a ceramographically prepared specimen.



Figure 2. Comparison of measurement: Hg-intrusion porosimetry vs image analysis.

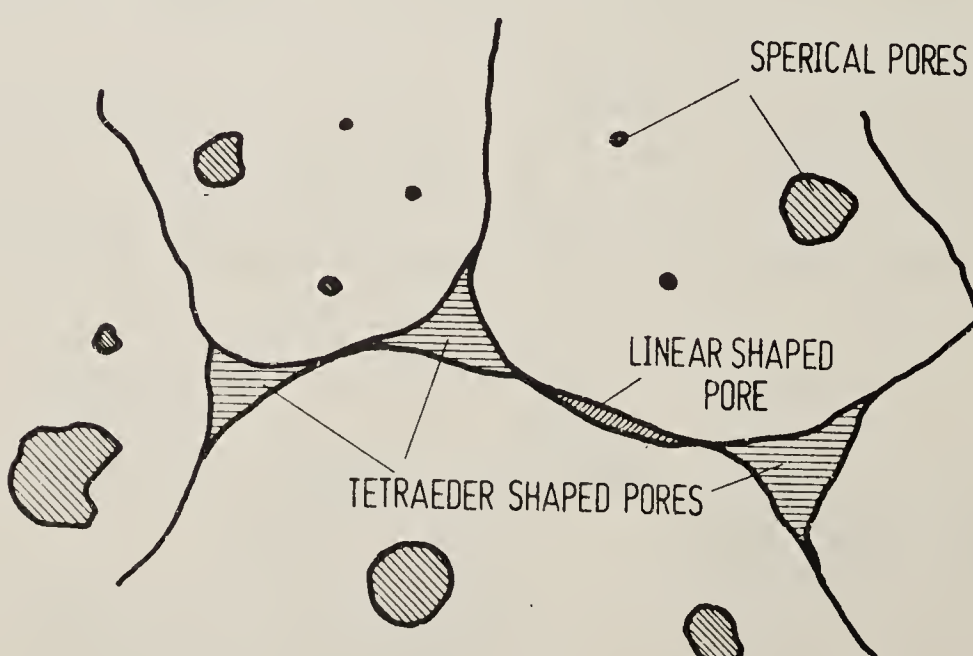


Figure 3. Typical microstructure of a sintered material made of granulated powder.

Some of the physical properties, such as thermal conductivity, strongly depend on the different fractions of these two pore shapes. If the sections of rather spherical pores are approximated by squares and those of more tetrahedral ones by triangles, the fractions of these two types of pores can be estimated (Vollath 1982).

4. How to measure?

We have stated now the type of results we would like to obtain and we have shown a few problems and results of measurements. But we have not considered any method of measurement.

For determining shapes of particles we have in general two philosophies which could be applied. The first is to singularize the particles of an image and to determine shape factors for each of these particles. Having done this we collect all the measures for size and shape factors and calculate a new distribution function.

Information about shape factors does not always give the true relationships. For example, if we consider the shape factor given by the ratio of area to circumference of a particle it is maximum for a circular figure. As the circle is deformed to form an ellipse the shape factor decreases as the axis ratio of the ellipse increases. It is thus possible with this shape factor to obtain information about the shape of the particles. This information is not, however, unequivocal. If a circular particle has a wavy or even a frayed border, it is certainly possible to take measures in this particular case to obtain usable results but it must be remembered that in some special cases these measures will induce inaccuracies.

Even if there are many disadvantages resulting from the use of shape factors, in the case of complicated patterns such as concave particles there is even now no choice of the method.

If we wish to analyze more or less convex particles and if we are satisfied with describing these particles by simple patterns the concept of size proposed by Delfiner (1972) is unequalled today. Delfiner defines the size of a particle P by the largest template T ("structuring element") which can be inscribed.

The data obtained by this method can be evaluated by mathematical morphology pioneered by Serra (1969) and Matheron (1967). If we analyze our specimens with templets of different shapes we can obtain a classification of particles by size and shape.

5. Definition of a particle size

In particles of simple shapes, such as circles, particle size can be defined unequivocally, e.g., through the diameter of the circle. In a similar way it is also possible to describe in simple terms the size of linear particles. However, in most cases much more complicated particle shapes are encountered. In those cases, description by way of maximum chord lengths or maximum dimensions (Feret diameters) are inadequate.

In the light of this problem Delfiner (1972) proposed a generalized concept of particle size. Delfiner assumes a basic pattern of any given shape and establishes a monotonic sequence of elements which are homothetic of the basic pattern selected. The size of a particle is then given by the largest element of this sequence which can be inscribed in this particle.

Let us consider sets (particles) G which are to be compared with other sets T_i (templates). The sets T_i are subsets of the ordered set T . All subsets of T are supposed to be homothetic.

$$T_i \subset T_{i+j} \quad j > 0 \quad i, j \in \mathbf{N}.$$

The size of G with respect to the elements of τ is given by

$$G =: G_{T_i} \Leftrightarrow T_i \subset^* . \wedge . T_{i+j} \not\subset^* G \quad i, j \in \mathbf{N} \quad (1)$$

(Vollath 1982) with

$$T_i \subset^* G: \exists \underset{x}{(X(x) \oplus T_i)} \subset G.$$

The set $X(x)$ shifts T_i by x as a result of a connection. \oplus stands for Minkowski addition (Hadwiger 1950; Matheron 1967; Serra 1982).

If the criterion (1) is met, the particle G has the size i relative to the sequence of structuring elements given by T . Classification in accordance with (1) can be clearly conceived as involving the use of templates of different sizes of the shape T . Out of the inventory of such templates one selects the largest template particle G will fit. As a coefficient of size measurement, the particle is assigned the number i of the largest fitting template.

If the possible sets T are restricted to the class of convex sets, the size can be determined by means of a Minkowski set operation. The elements of the sequence T can be determined from a convex unit element T_1 as partial sums of a Minkowski series (Meschkowski and Ahrens 1974),

$$T_i = T_0 \oplus \bigoplus_{k=1}^i T_1 \quad i, k \in \mathbf{N}, \quad (2)$$

where the set T_0 generally only consists of the origin. T_i can also be represented by means of the recursion formula (Vollath 1982)

$$T_i = T_{i-1} \oplus T_1 \quad i \in \mathbf{N}.$$

The classification of sets G in accordance with elements of T now can be arranged by means of Minkowski subtractions in analogy with (1). G can be assigned to the class i of a sequence T (Vollath 1982) if

$$G = G_{T_i} \Leftrightarrow G \ominus T_i \neq \phi \wedge G \ominus T_{i+j} = \phi \quad i, j \in \mathbf{N} \quad (3)$$

The particle G to be classified is the subset of an image B . In processing an image one proceeds by eroding the image by Minkowski subtractions. A sequence of deformed images is obtained,

$$B_{T_i} = B \ominus T_i.$$

According to Matheron (1967), the two Minkowski set connections can be linked so as to form another operation suitable for classification, the ouverture. A sequence of images is obtained, which were deformed by the ouverture transformation

$$B'_{T_i} = (B \ominus T_i) \oplus T_i. \quad (4)$$

\oplus stands for the Minkowski addition (Hadwiger 1950; Matheron 1967; Serra 1982).

\ominus stands for the Minkowski subtraction (Hadwiger 1950; Matheron 1967; Serra 1982).

In the transformed images B'_{T_i} it is now possible to determine areas, perimeters and particle numbers as coefficients of measure.

The quantities measurable in the images transformed by erosion or ouverture will not always generate the required information. Thus, e.g., dumb-bell shaped particles may disintegrate into two separate particles after erosion or ouverture. This may have a disturbing effect on particle counting. There are also measuring problems when particles are to be classified in accordance with given patterns, but also the coefficients of measure are to be determined in the unchanged particles. In such cases, classification must be carried out by means of a template matching procedure. For the case of a sequence T of convex templates the following method can be used for image transformation in which, first of all, the particles in the image are classified by erosion,

$$B_{T_i} = B \ominus T_i$$

and the original shape of the particles is then reconstructed by the recursion formula

$$B_{T_i}^*(k+1) = \bigcup_{j=1}^8 (B_{T_i}^*(k) \oplus S_j) \cap B. \quad (5)$$

The first element B_{T_i} of the sequence of sets produced is

$$B_{T_i}^*(1) = B_{T_i}.$$

The set S_j always consists of the origin and one of its eight neighbourhood points. The process of iteration must be continued until the condition

$$B_{T_i}^*(k+1) = B_{T_i}^*(k)$$

is met.

In the following sections, which will deal with classification by shape and size, it will be assumed that classification has already been carried out by one of the three methods of classification discussed (erosion, ouverture, or template matching).

6. Classification of particles in accordance with several sequences of patterns

Let us now consider the case of particles of a sample being classified in accordance with M different sequences of convex template T^l . Each set T^l consists of N^l elements of the size j , $T_j^l \in T^l$. The subset T_j^l is used to determine in the images such measures as particle numbers or areas. For the sake of simplicity we assume that these measures were determined by means of the template matching technique of classification. When measuring with the templates T_j^l the cumulative frequencies, H_j^l are determined. These cumulative frequencies, result from the class frequencies h_k^l through the sum of

$$H_j^l = \sum_{k=j}^{N^l} h_k^l \quad l \in \{1, \dots, M\}. \quad (6)$$

From the matrix of measured values (H_j^l) a matrix (h_j^{*l}) is now to be determined of the class frequencies at which also separation by shapes will be performed. Such separation may be carried out on the basis of two different principles.

6.1 Separation by inclusions

For all elements of the sequences of patterns T^m it holds that

$$T_i^m \subset^* T_{i+j}^m \quad i, j \in \mathbf{N}. \quad (7)$$

If we compare two sequences of patterns, we always find pairs of elements obeying the following relationship:

$$T_i^m \subset^* T_{l(i, m, n)+j} \quad i, j, l, m, n \in \mathbb{N}. \quad (8)$$

The element $T_{l(m)}^n(i, m, n) + 1$ is the smallest element of the sequence T^n containing the element T_i^m as a subset. Obviously, in determining the class frequencies h_j^{*m} , corrected by shapes, the numbers and areas, respectively, of all patterns must be subtracted in which T_i^m is fully contained.

$$h_j^{*m} = H_j^m - \sum_{k=1}^M \sum_{i=l(j, m, k)+1}^N h_i^{*k} \quad (9)$$

Consequently, calculating the class frequencies, h_j^{*m} presupposes knowledge of the class frequencies h_i^{*k} of the elements T_i^k in which T_j^m is contained. Evaluation of the formula (9) is started with the element T_i for which no further element in the series of measurements contains T_i^k .

As a simple example, figure 4 shows two ordered sequences of patterns. The sequences T^1 consists of squares, the sequence T^2 consists of right angled isosceles triangles. Below the images those elements are indicated which contain elements T_i^k .

6.2 Separating shapes by given measures

Instead of the inclusions (7) and (8), also a measure, $\mu(T_i^m)$, to be assigned to the pattern T_i^m , can be used to distinguish by different shapes. The only measure to be used for this purpose are areas. We then obtain the following relationships as the basis on which to

T_1^1	T_2^1	T_3^1	T_4^1	...
T_1^2	T_2^2	T_3^2	T_4^2	...
$T_1^1 \subset T_i^1$ $T_1^1 \subset T_i^2$	$i > 1$	$T_2^2 \subset T_i^1$ $T_2^2 \subset T_i^2$	$i > 0$ $i > 1$	
$T_2^1 \subset T_i^1$ $T_2^1 \subset T_i^2$	$i > 2$	$T_2^2 \subset T_i^1$ $T_2^2 \subset T_i^2$	$i > 1$ $i > 2$	
$T_3^1 \subset T_i^1$ $T_3^1 \subset T_i^2$	$i > 3$	$T_3^2 \subset T_i^1$ $T_3^2 \subset T_i^2$	$i > 2$ $i > 3$	
$i(j, 1, 1) = j$ $i(j, 2, 2) = j$		$i(j, 2, 1) = j - 1$ $i(j, 1, 2) = 2j - 1$		

Figure 4. Separating particle shapes by inclusions.

assign particles to the different patterns:

$$\mu(T_i^m) < \mu(T_{i+j}^m) \quad i, j \in \mathbb{N}. \quad (10)$$

Since we take into account only positive and monotonic measures this condition is identical with (7). For assignment to different sequences of patterns one uses

$$\mu(T_i^m) < \mu(T_{l(i, m, n)+j}^n) \quad i, j, l \in \mathbb{N}.$$

The element $T_{l(i, m, n)+1}^n$ is the smallest element in the sequences T^n whose measure is larger than that of T_i^m .

The class frequencies corrected by shapes are determined in accordance with (9) also in this case.

For the example shown in figure 4 it is outlined in figure 5 which elements have larger areas than an element T_i^k . The example of classification by squares and triangles also indicates another major characteristic of classification by shapes. While for a square of the given size there is only one orientation, the triangle used in principle can be at any of four orientation. Consequently, if it is not known in advance that the triangles in the sample can have only one orientation, all four possible congruent triangles must be used as templates. In the given example this would imply the need to analyze not for two, but for five sequences of patterns. However, if one is not interested in the additional discrimination of triangles of different orientations, the measured results obtained from the four orientations can be combined in the evaluation (Vollath 1982).

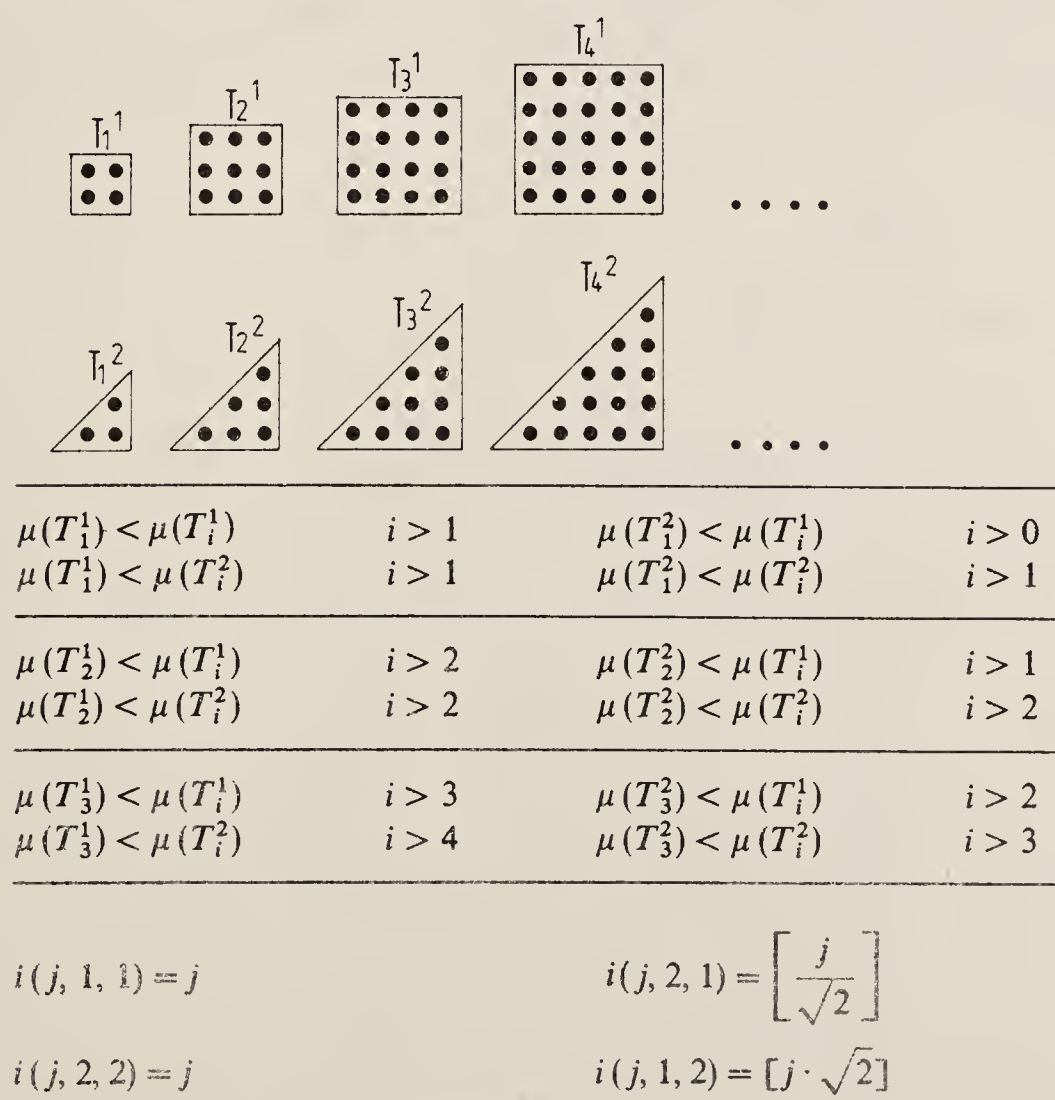


Figure 5. Separating particle shapes by given measures.

7. Classification of particles by multi-parameter sequences of patterns

So far we have looked at sequences of patterns T whose elements depended on only one parameter describing the size. Let us now consider sequences T whose elements obey the law of formation

$$T_{i,j} = T_{0,0} + T_{i,0} \oplus T_{0,j}. \quad (11)$$

With

$$T_{i,0} = T_{0,0} \oplus \bigoplus_{m=1}^i T_{1,0} \quad i, j, m, n \in N_0$$

$$T_{0,j} = T_{0,0} \oplus \bigoplus_{m=1}^j T_{0,1}.$$

As in (2) also in this case the set $T_{0,0}$ consists of only one point, normally the origin. The sets $T_{0,1}$ and $T_{1,0}$ are the two basic patterns from which the two-parameter sequence of sets considered is built up. Naturally, also multi-parameter sequences of sets can be built up in accordance with scheme (11) or, as in §6, several multi-parameter sequences of sets can be combined with each other. However, it should be avoided that, as a result of the introduction of too many classes, insufficient, i.e., insignificant, coverage in the individual classes is produced.

Figure 6 shows a simple two-parameter sequence of patterns built up of the unit vectors, e_1 as $T_{1,0}$ and e_2 as $T_{0,1}$. In this example one clearly sees the typical structure of such a two-parameter family of structuring elements. Adding the two diagonal vectors $[1]$ and $[-1]$, one obtains a system of templates which in a first approximation, come close to the size, the axial relationships and the orientations of ellipses approximated by octagons. In a similar way, in a hexagonal grid, one obtains by continued Minkowski additions of the three basic vectors, a system of hexagons to approximate ellipses.

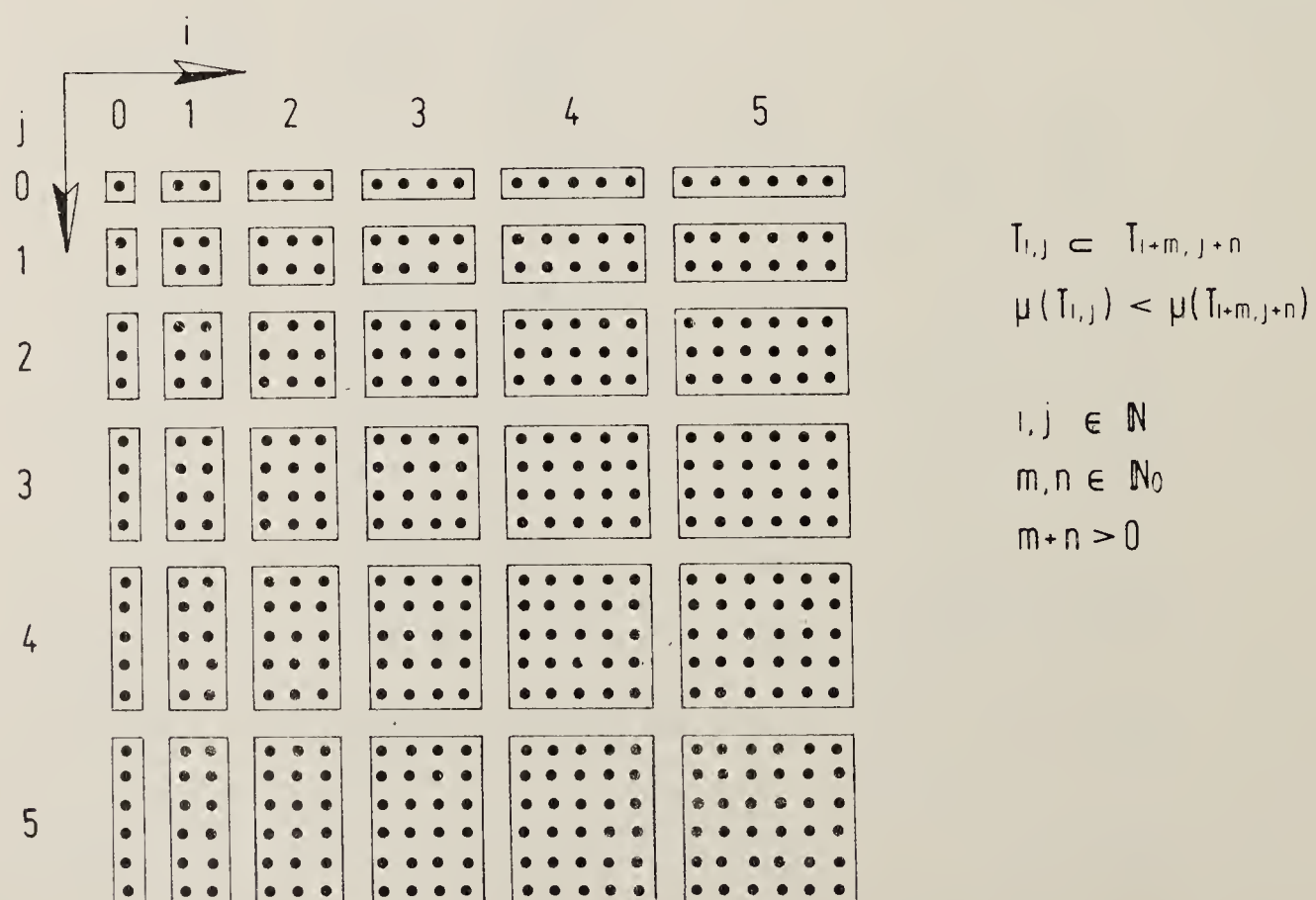


Figure 6. Example of a two-parameter sequence of structural elements.

On the basis of the law of formation of patterns $T_{i,j}$ it is seen that

$$T_{i,j} \subset^* T_{i+m, j+n} \Leftrightarrow \mu(T_{i,j}) < \mu(T_{i+m, j+n})$$

$$i, j \in N, m, n \in N$$

$$m + n > 0.$$

Hence, unlike in the case of classification by several single parameter sequences of patterns, one should not distinguish between two criteria of classification. Since in this case the measurement proceeds analogously to that described above, one obtains, by using the same argument for the corrected class frequencies,

$$h_{i,j} = H_{i,j} - \sum_{m=i+\delta_1} \sum_{n=j+\delta_2} h_{m,n}^* \quad i, j, m, n \in N$$

$$\delta_i \in \{0, 1\} \quad \delta_1 + \delta_2 > 0.$$

Also in this case, calculation of $h_{i,j}^*$ must be started with the largest element. To explain this evaluation in more detail, a simple image (figure 7) has been constructed as an example so that the "particles" it contains can be described by the elements shown in figure 6. Table 2 shows the measured frequencies $H_{i,j}$, from which the class frequencies $h_{i,j}^*$, corrected for shapes and directions were calculated. The $h_{i,j}^*$ values are summarized in table 3.

Another example is depicted in figures 8 and 9 (Vollath 1982). In this example the analysis of pores into more tetrahedral and more spherical shapes is shown. In figure 8 we see the results obtained for the selected templates (squares and triangles) and figure 9 depicts these results after separation by inclusion according to (9) (see also figures 3, 4 and 5).

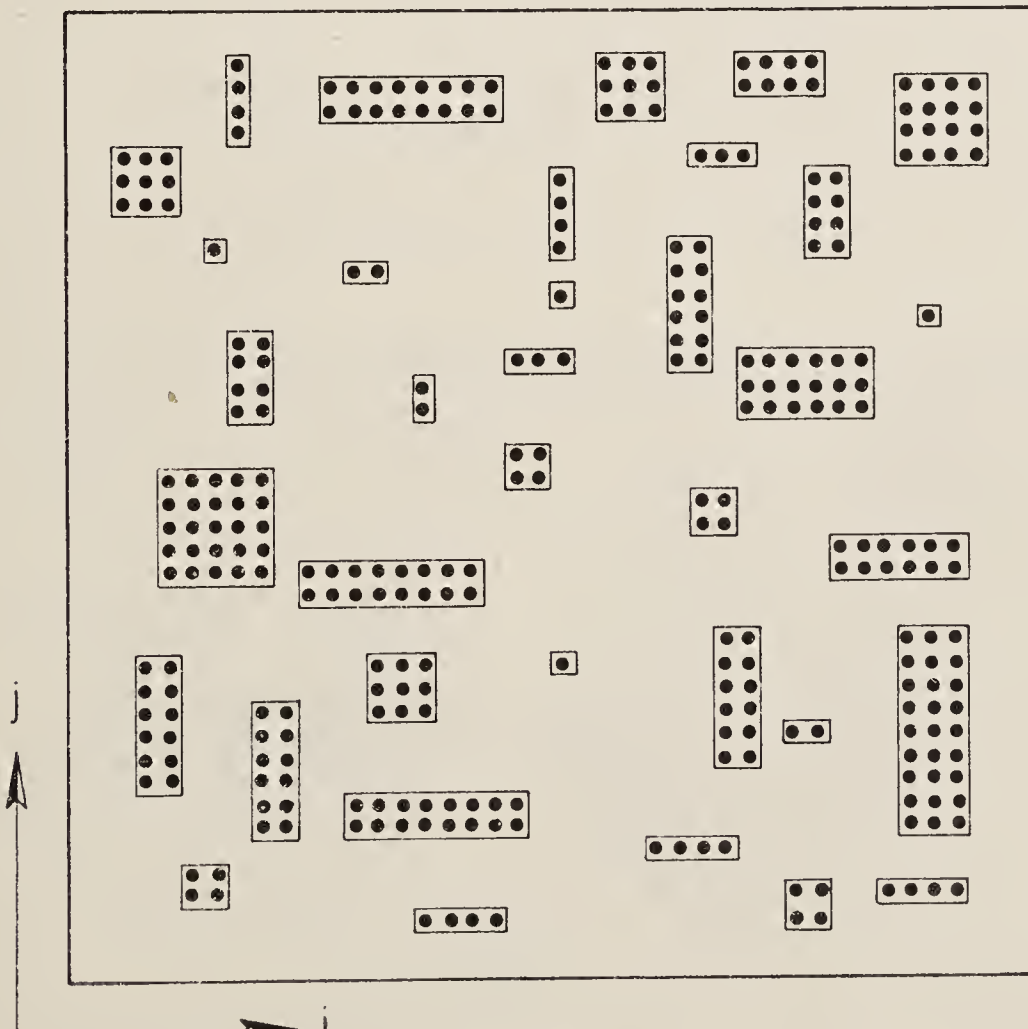


Figure 7. Example of a sample for classifying particles by shape, size and orientation.

Table 2. Particle numbers obtained in figure 7 after application of the structural elements in a measurement (e.g., erosion) as represented in figure 6. The subscripts i and j have the same meaning as in figure 6.

j	i	1	2	3	4	5	6	7	8
1	36	29	17	11	6	5	3	3	
2	25	22	11	8	6	5	3	3	
3	15	13	7	3	2	1			
4	11	9	3	2	1				
5	6	6	2	1	1				
6	5	5	1						
7	1	1	1						
8	1	1	1						
9	1	1	1						

Table 3. Particle numbers of figure 7 corrected for size, shape and orientation. The subscripts i and j have the same meaning as in figure 6.

j	i	1	2	3	4	5	6	7	8
1	4	2	2	3					
2	1	4		1		1		3	
3			3			1			
4	2	2		2					
5					1				
6		4							
7									
8									
9			1						

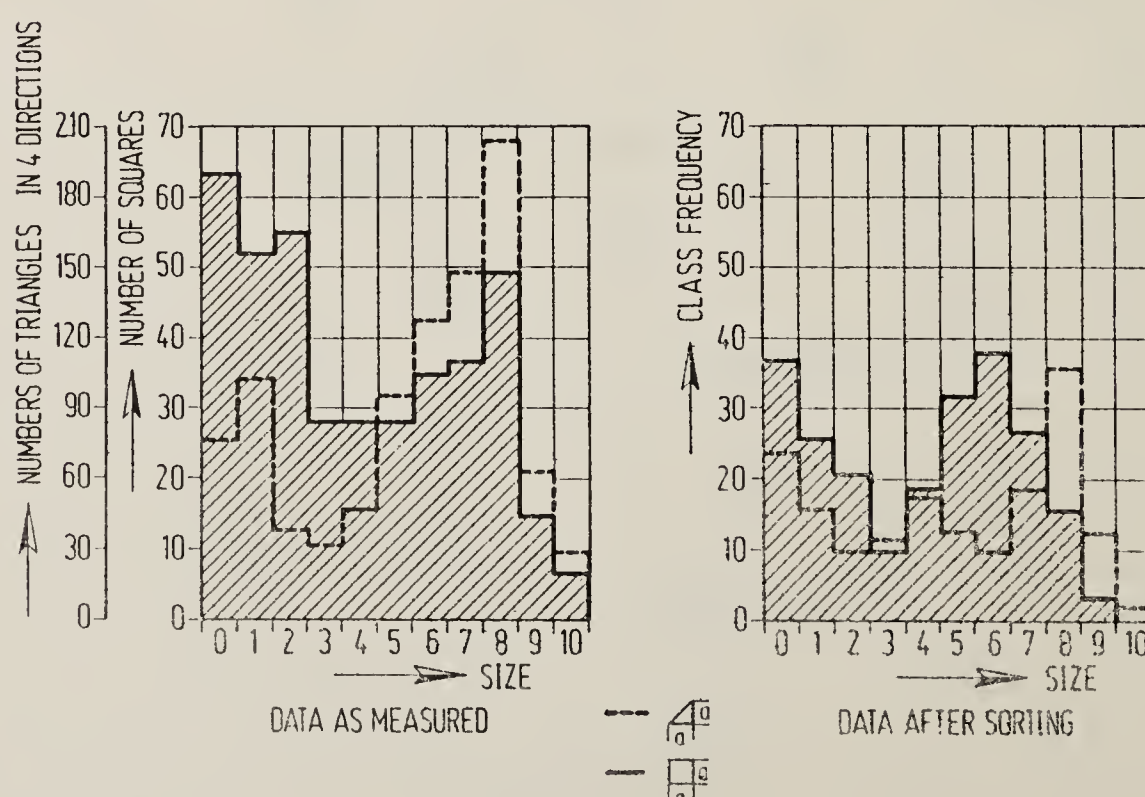


Figure 8. Separation of pores in a sintered material due to their shapes (separation by inclusion).

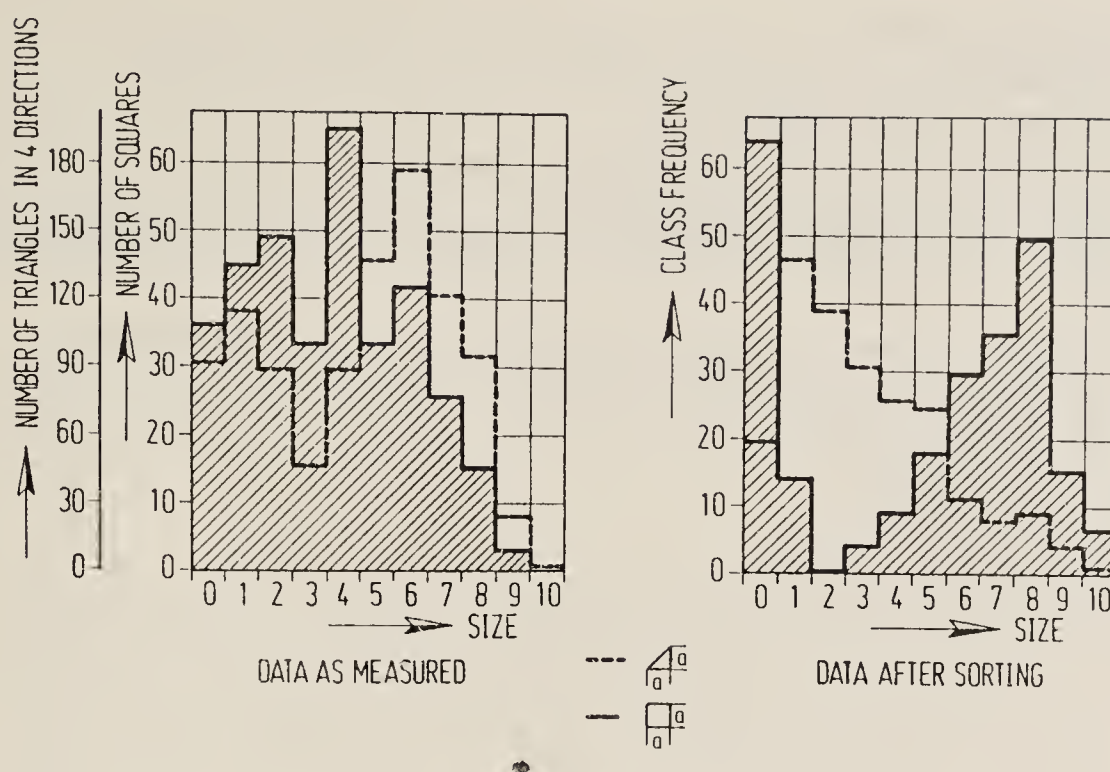


Figure 9. Separation of pores in a sintered material due to their shapes (separation by areas).

8. Conclusions

In this paper a few basic considerations have been explained which are necessary for beginning in image analysis. The major point stressed was that before starting any measurement the physical problem imposing an analysis, e.g., particle sizes, must be examined. From this examination we have to derive a behavioural model and develop a measuring technique compatible with it.

It has been shown in this study how to extract measured values from an image, which characterize the individual elements of the image in terms of size, shape and orientation. The basis used throughout was a description of the image and of its elements by means of the methods of the theory of sets. Based on Delfiner's concept of shapes a method of particle classification was developed using erosion, ouverture or template matching as image transformation for classification. A new transformation, "template matching", for particles is explained.

This transformation avoids the disadvantages of erosion or ouverture in case of concave particles. Nevertheless, template matching is also restricted to application of convex templates.

Acknowledgements

Thanks are due to Dr Pecht and Mr Stiller of IMF III/PBE for their critical review of the draft of this paper.

References

- Delfiner P 1972 *J. Microsc.* **95** 203
- Haas A, Matheron G and Serra J 1967a *Ann. Mines XI* 736
- Haas A, Matheron G and Serra J 1967b *Ann. Mines XII* 767

- Hadwiger H 1950 *Math. Z.* **53** 210
- Matheron G 1967 *Elements pour une Theorie des Milieux Poureux* (Paris: Masson)
- Müller W 1973 *Leitz Mittl. Suppl.* **1** 101
- Meschkowski H and Ahrens I 1974 *Theorie der Punktmengen*, Bi-Wissenschaftsverlag, Mannheim
- Nawrath R and Serra J 1979 *Microsc. Acta* **82** 101
- Serra J 1969 *Introduction a la Morphologie Mathematique Cahier du Centre de Morphologie, Mathematique ENSMP No. 3*
- Serra J 1982 *Image analysis and mathematical morphology* (New York: Academic Press)
- Vollath D 1979a *Leitz-Mitt. Wiss. Tech.* **7** 129
- Vollath D 1979b *J. Nucl. Mater.* **81** 115
- Vollath D 1981 *J. Microsc.* **122** 35
- Vollath D 1982 *J. Nucl. Mat.* **10** 71
- Vollath D 1982 *Prakt. Metallogr.* **19** 7, 94

Computer-aided roll pass design for continuous billet mill

ASHOK KUMAR, SUDHAKER JHA and V RAMASWAMY

Research & Development Centre for Iron and Steel, Steel Authority of India Limited, Ranchi, India

Abstract. A mathematical model has been developed for computing the geometrical dimensions of square-diamond square pass sequence for a continuous billet mill. The model is based on derivation of shape and size factor from the geometry of the pass taking into account pass filling, pass rounding etc. Using these factors and a basic equation of spread for flat rolling, a governing equation incorporating angle of diamond and reduction in consecutive passes has been formulated. Newton's substitution method has been used to solve the equation. With known reduction between consecutive passes, geometrical dimension of square and diamond passes are computed. A model has been used to calculate pass design of a finishing train of a continuous billet mill producing 60 mm square billet from 120 mm square bloom. The elongation values have been optimized by varying the apex angle of diamond. A close agreement between computed and actual values shows the validity of the model.

Keywords. Geometrical dimensions; square-diamond pass; computer-aided model; pass sequence; apex angle; rolling force; torque

1. Introduction

Diamond-square pass sequence is used in the finishing group of stands of a continuous billet mill to produce round-cornered squares. Conventionally the sequence is designed (Burtsev 1973) by obtaining elongation coefficient on the principle of having width of any given pass equal to the height of the preceding pass. Form changes in diamond passes have also been studied experimentally (Zaitsev and Anufriev 1969) and nomograms have been prepared for obtaining pass dimensions. However, these methods generally require trial and error to establish roll pass design and at the same time do not effectively utilise available biting ability, mill power etc of different mill stands. To overcome these shortcomings, a software package was developed at this centre for computer-aided pass design for continuous billet mill. This paper outlines the approach adopted and compares the results obtained from the computer model developed with the actual mill performance.

2. Approach

Diamond-square pass sequence can be fully developed if the elongation coefficient (λ) between two consecutive passes is known. In the present work the coefficient is obtained by converting the diamond square passes into equivalent rectangles having width equal to their effective width and the Ekelund spread formula (Jha 1980) has been modified and made use of. This offers the advantage of calculating reduction sequence starting from the last finishing pass and is superior in accuracy to other spread formulae

A list of symbols appears at the end of the paper.

(Jha 1980). With the calculated value of λ , for an assumed angle of diamond, the dimension of pass in the next mill stand is obtained. Limitations of permissible angle of bite, mill speed, power force parameters etc have been observed. If needed a change in apex angle of diamond pass is effected and this in turn changes the value of λ and pass dimensions. Computation is repeated for all the mill stands and the dimensions of ingoing bloom entering the finishing mill are figured. If there is a limitation on bloom size as well, λ is readjusted again by changing the apex angle of diamond in passes of different mill stands.

2.1 Elongation coefficient

Figure 1 shows a diamond bar going into square pass along with their equivalent rectangles. If

$$\delta = b_1/h_1; n = h_2/b_2 \quad \text{and} \quad \gamma = h_2/h_1.$$

Elongation coefficients (λ) for the pair of pass will be

$$\lambda = A_1/A_2 = b_1 h_1 / b_2 h_2 = n \cdot \delta / \gamma^2. \quad (1)$$

The modified Ekelund spread equation is given as

$$\beta = 1 + \frac{2(1 - \gamma)}{1 + \gamma} \cdot \frac{M}{M + 1},$$

where $M = \frac{0.8}{(b_1/ld)^2} \left[2 - \frac{3(h_1 - h_2)}{ld} \right]$.

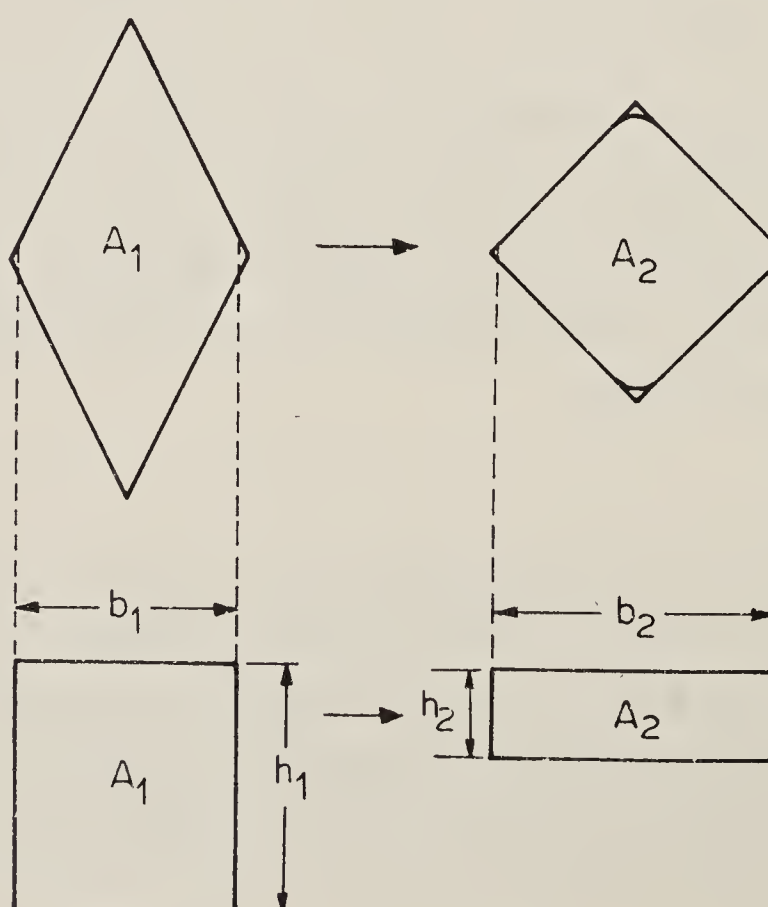


Figure 1. Diamond and square passes with their equivalent rectangles.

The final equation can be written as

$$n = \frac{(\gamma/\delta)}{1 + \frac{2(1-\gamma)}{1+\gamma} \left[\frac{0.4\gamma(1-\gamma) \left\{ 2 - 3 \left[\left(\frac{2(1-\gamma)}{\gamma} \right) \left(\frac{h_2}{D} \right) \right]^{1/2} \right\}}{\delta^2 \frac{h_2}{D} + 0.4\gamma(1-\gamma) \left\{ 2 - 3 \left[\left(\frac{2(1-\gamma)}{\gamma} \right) \left(\frac{h_2}{D} \right) \right]^{1/2} \right\}} \right]} \quad (2)$$

Equations (1) and (2) can be used for determining elongation coefficients (λ) if δ , n and h_2/D are known.

2.2 Shape factors

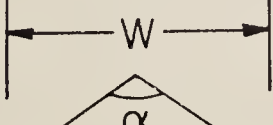
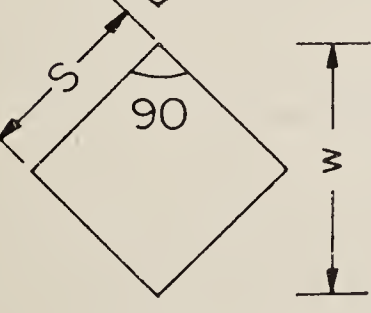
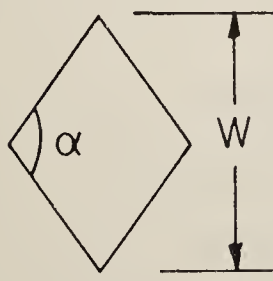
δ and n largely depend on the geometrical shape of passes and are therefore termed shape factors. For any pass, $\delta \cdot n = 1$. Considering pass filling and apex rounding of diamond and square passes, the shape and size factor (h_2/D) can be written as shown in figure 2.

2.3 Rolling force and torque

Roll separating force and rolling torque were computed using the following equations, which are derived from the basic theory of deformation for rolling of square and diamond sections (Jha *et al* 1983).

2.4 Roll force

$$F = \sigma \cdot ld \cdot n_\sigma \left[\frac{2W}{3} - \frac{H_1 \cdot W}{10R} \right].$$

Shape	δ (in going)	n (out going)	h_2/D (out going)
	$2 \cdot f_h^2 \tan(\alpha/2)$	$\frac{\cot(\alpha/2)}{2 \cdot f_h^2}$	$\frac{\cot(\alpha/2) W}{2 \cdot f_h \cdot D}$
	1.73	0.578	$\frac{W}{1.7 \cdot D}$
	$2 \cdot f_v^2 \cdot \cot(\alpha/2)$	$\frac{\tan(\alpha/2)}{2 \cdot f_v^2}$	$\frac{W}{2 \cdot f_v \cdot D}$

f_h & f_v Denotes the degree of pass filling

Figure 2. Shape and size factors for diamond and square passes.

Here

$$n_\sigma = \frac{\frac{ld}{W} \left[\frac{1 - H_1/4R}{(H_0 + H_1)/W} + \frac{W}{8R} \frac{(H_0 + H_1)}{(H_0 - H_1)} \right]}{2/3 - H_1/10R}$$

$$\sigma = \frac{K \cdot \varepsilon^{0.6235} \dot{\varepsilon}^{0.087}}{e^{0.0037t}}$$

2.5 Rolling torque

$$T = 2 \cdot \sigma \cdot \psi \cdot ld^2 \cdot W \left[M_1 \left(0.5 - \frac{H_1}{8R} \right) + \frac{0.25}{M_1} \right]$$

$$M_1 = ld/H_m$$

$$ld = [R(H_0 - H_1)]^{1/2}$$

The terms used in the above mathematical expressions are explained in the list of symbols given at the end of the paper.

3. Mathematical model

A mathematical model has been developed for diamond square sequence using the shape and size factor of the pass along with elongation and spread equations. The flow charts of the computer program developed for the above model are shown in figures 3a, b. Figure 3a shows the flow chart of the program taking the limitation of initial square size and optimizing the apex angle. Figure 3b shows how elongation coefficient was optimized at all mill stands by considering the limitation of power force parameter and biting ability etc and compute the geometrical dimensions of the passes. The program (figure 3a) computes the shape and size factor from the initial assumed value of the diamond angle. Using the shape and size factor, the reduction (γ) was computed from the spread equation given by (2). The spread equation has been solved by employing Newton's substitution iterative method. For this we start with an arbitrary value of γ in the first iteration and a new value of γ is obtained. The process is repeated until convergence (accuracy: 10^{-3}) is achieved, normally after 6 iterations. After getting the value of γ and taking the finish square size as the starting dimensions, the elongation, bite angle etc were computed using the corresponding subroutine. The process was repeated till the required pass. If the square size so obtained after the last pass is less than the required initial size, the apex angle of last diamond pass is increased by 2° and the initial square size is again computed. If again the computed square size is less than the required size of square, the apex angle of pre-last and subsequent diamond passes are increased by 2° and the square size is computed.

The process is repeated until the calculated square size is greater than the required square size. If the apex angle is given for all the diamond passes then starting with the finish size the program will compute the required initial square size for that finish square size. It is essential to have the following initial data for operation of the computer model: (a) mode of pass sequence; (b) no. of passes; (c) roll diameter at each stand; (d) roll gap at each stand; (e) final rolling speed; (f) final product size; (g) initial

size and (h) apex angle of all the diamond passes. Once this is computed it can be compared with the actual mill parameter.

4. Results and discussion

To ascertain the accuracy of the model developed, a case study was made. In this, geometrical dimensions of square-diamond-square pass sequence for a known 4-pass

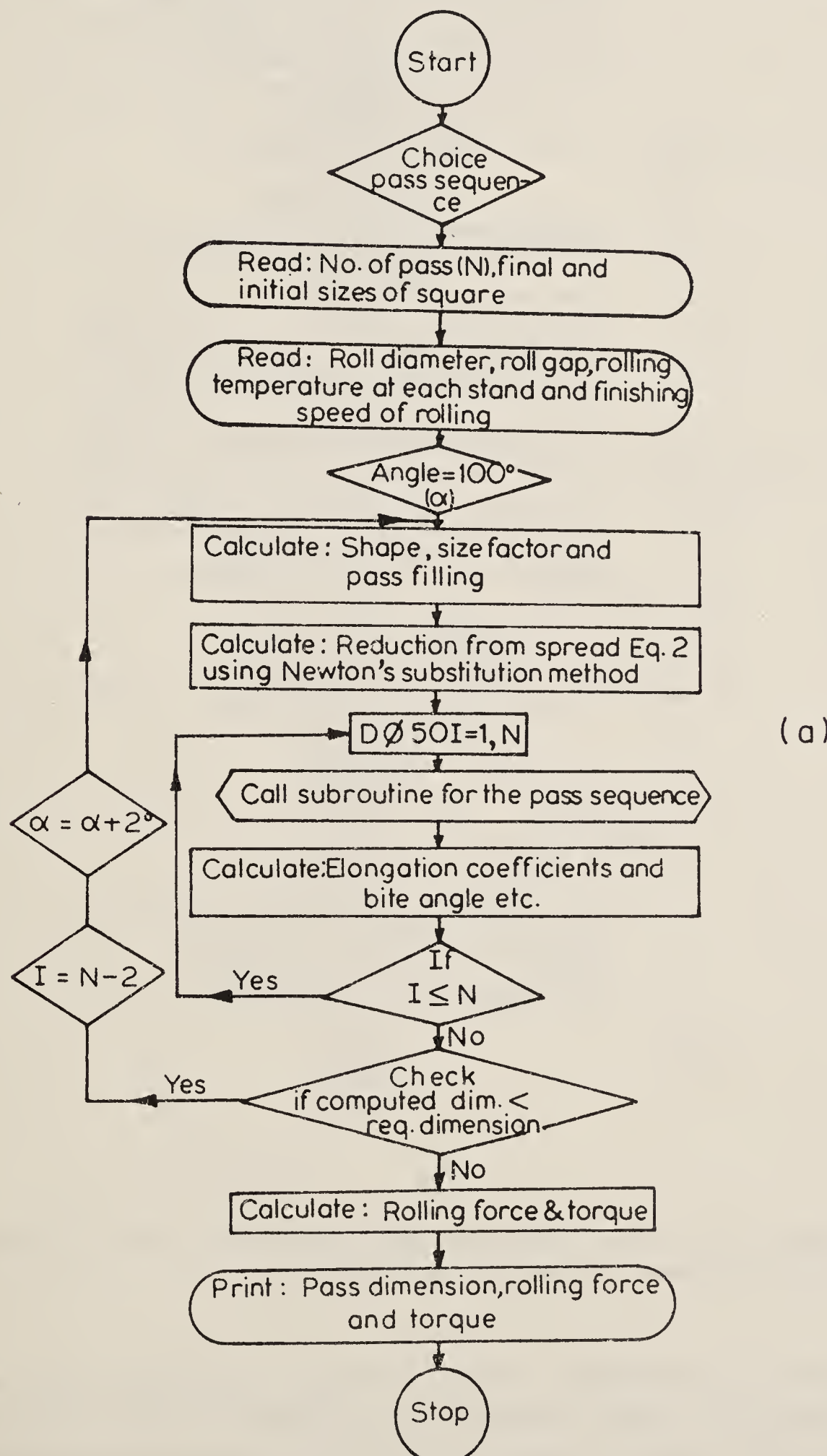
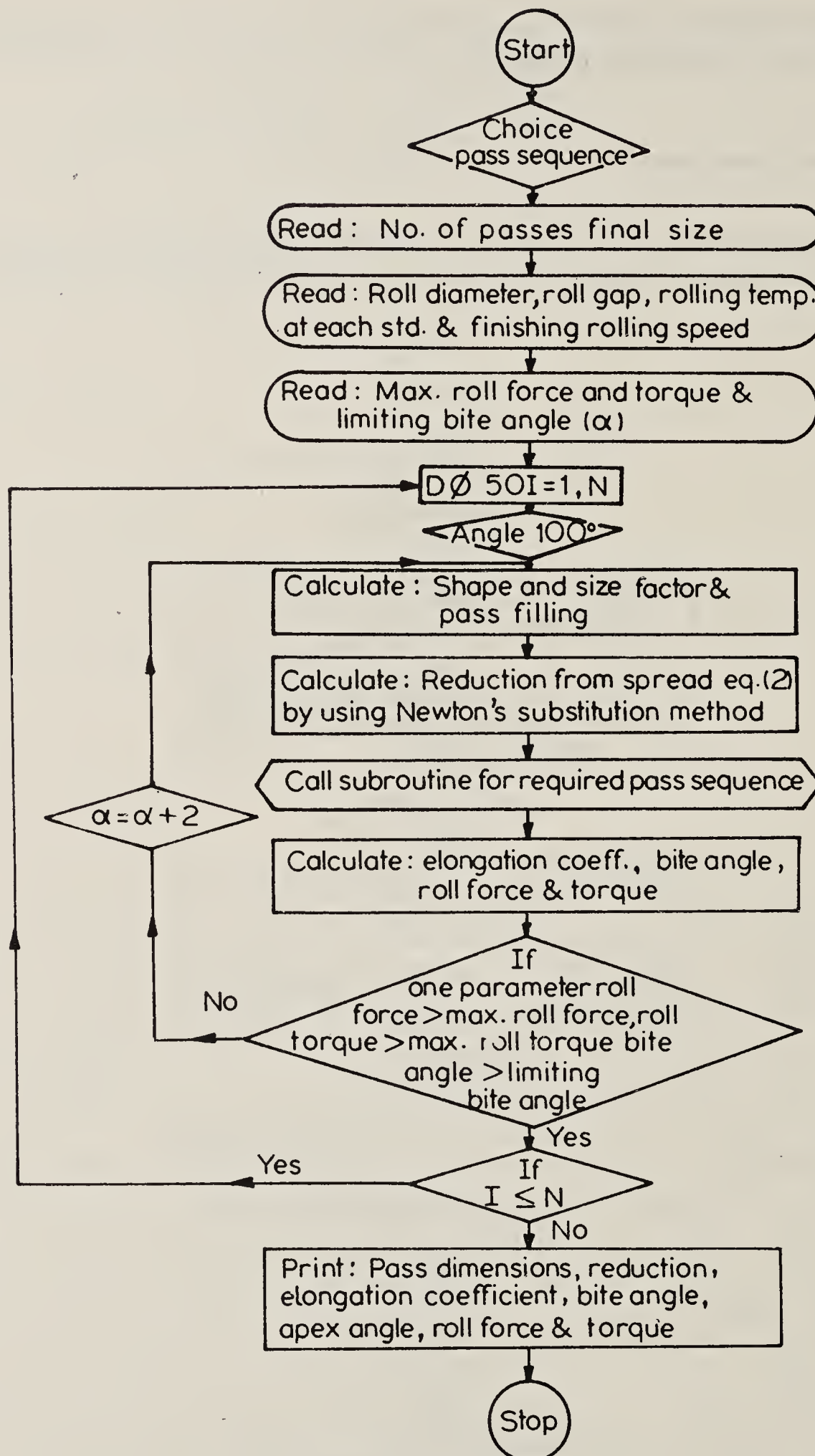


Figure 3a. for caption, see p. 188.



(b)

Figure 3. Flow chart of computer program for calculating roll passes with limitations of
a. initial square size. b. Power force and biting angle.

sequence (Bakhtinov and Shternov 1953) are computed using the above model by taking the final square size of 99.7 mm as the starting dimensions. The roll diameter, roll gap and apex angle of diamond used for calculating the geometrical dimensions are given in the table 1 along with the elongation value and reduction in each pass. The

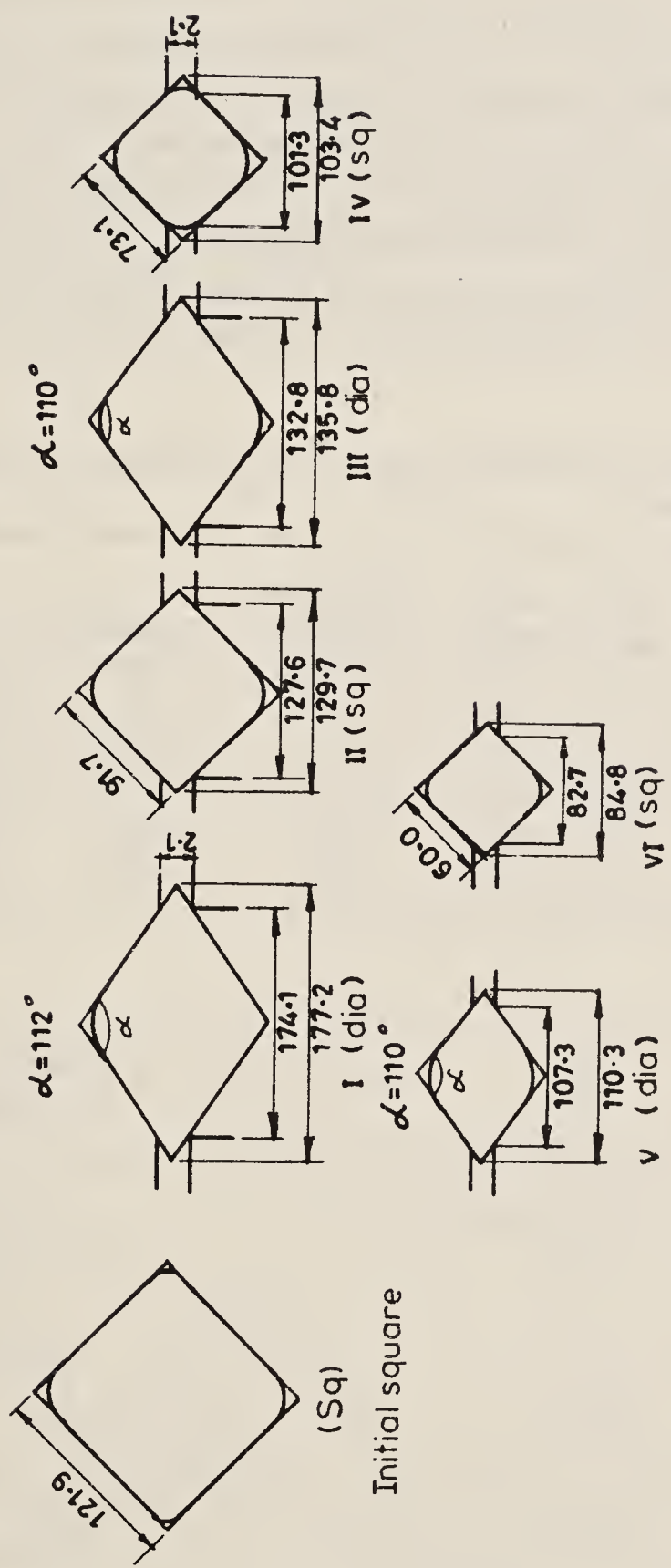


Figure 4. Roll pass design obtained by model for rolling 60 mm billet from 121.9 billet.

calculated square and diamond sizes are compared with the actual data obtained from the mill. This is also shown in table 1. A comparison between these two values shows a close agreement. Discrepancy in the width of the diamond pass may be due to the extent of pass filling and pass rounding which was considered in the above model.

4.1 Roll pass design

A model has been used to design roll passes for the finishing train of a continuous 530 mm billet mill producing 60 mm square billet from input square of 120 mm in six passes. The results are shown in figure 4 with geometrical dimensions of passes. The apex angle of diamond passes has been manipulated in the model to achieve the desired input square. As can be seen in figure 5, with increasing apex angle of diamond, the elongation coefficient increases. With diamond angle of 110° in all the passes, the initial square size permitted according to model is 119.25 mm. This necessitates increasing the apex diamond angle to 112° in the first pass. It can also be observed from figure 5 that

Table 1. Comparison between computed and in practice roll pass design (starting size of square(s) 99.7 mm)

Pass No.	Shape	Roll dia	Roll gap	Apex angle	Elongation coefficient	Reduction (R)	Geometrical pass dimension	
		(d) (mm)	(mm)	(α)	(λ)		Computed	In practice
1	Diamond	800	10	108	1.19	0.78	$W = 177.0$	$W = 169.0$
2	Square	800	10	108	1.23	0.77	$S = 118.1$	$S = 119.5$
3	Diamond	780	10	111.2	1.232	0.75	$W = 223.9$	$W = 229.0$
4	Square	780	10	111.2	1.32	0.72	$S = 150.4$	$S = 150.0$

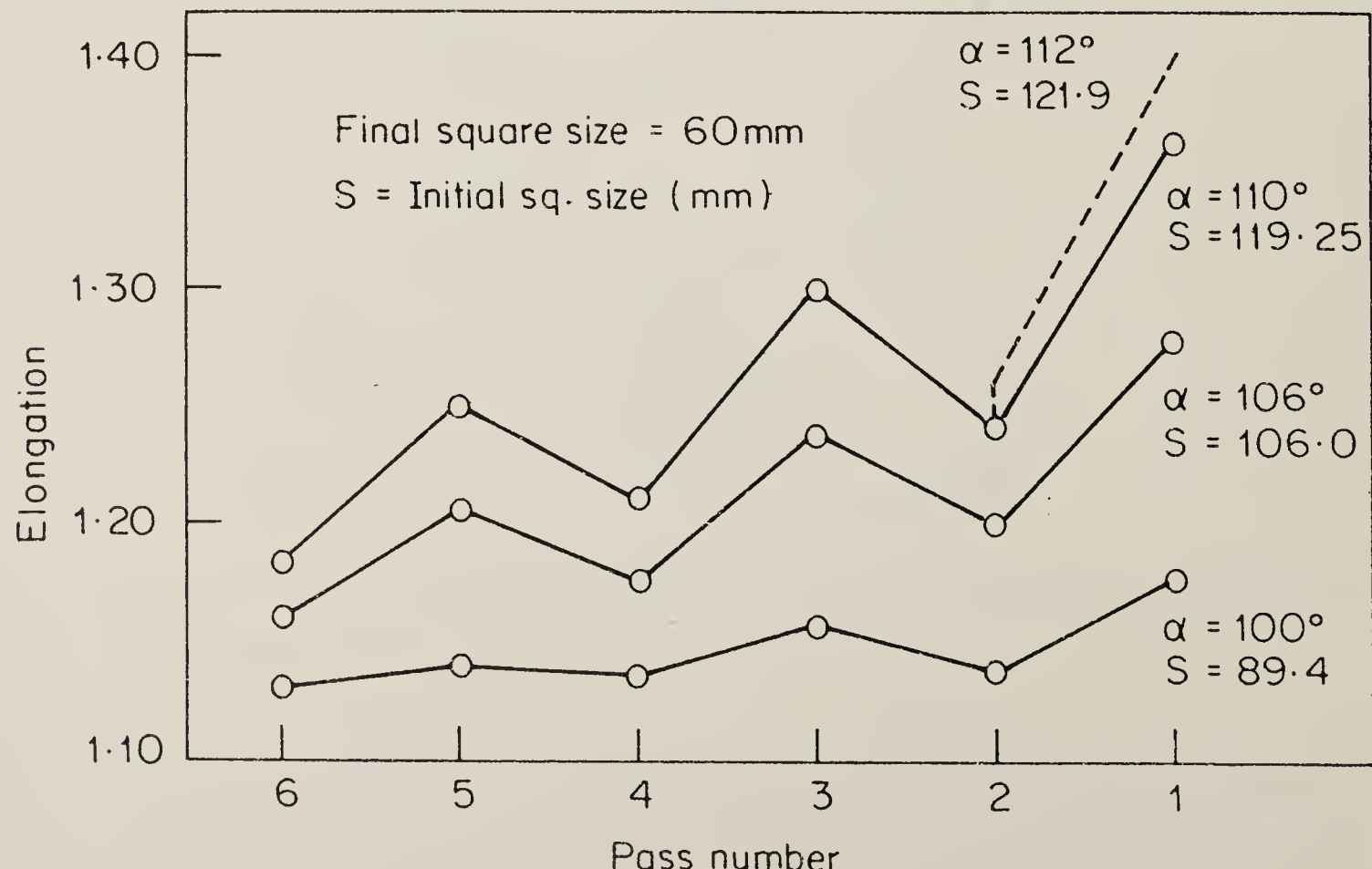


Figure 5. Effect of apex angle on elongation for different passes.

elongation in square passes is higher compared to those of diamond passes. Non-uniformity of elongation in diamond and square pass increases with increase in apex angle of diamond.

Pass design developed above is being implemented in one of our continuous billet mills.

5. Conclusions

A computer-aided roll pass design has been developed for producing billet. The software package accurately calculates the geometrical dimensions of diamond and square passes either under the limitation of rolling force, rolling torque, biting angle etc or the input bloom size for different mill stands thus avoiding trial and error method normally practised by pass designers. The model has been verified with actual plant data and it is shown that the calculated and observed size of the passes is in close agreement.

References

- Bakhtinov and Shternov 1953 *Roll pass design* (Moscow: Metallurgia) p. 232
 Burtsev K 1973 *Rolling practice* (Moscow: Mir Publishers) p. 146
 Jha S 1980 *Steel India* 3 1
 Jha S, Acharya N K and Sengupta D 1983 *Investigation into rolling technology of continuous billet mill*, Internal Report, Research and Development Centre for Iron and Steel, Ranchi, 16.02.480.85
 Zaitsev M L and Anufriev G V 1969 *Stal* in English, 8x Vol. 8, p. 727

List of symbols

D	working diameter of outgoing pass	R	collar diameter of rolls
F	rolling force	S	square size (outside)
H_0, H_1	initial and final height of pass	t	rolling temperature
H_m	average height	T	rolling torque
h_2/D	size factor of pass	W	width of diamond pass
K	constant	γ	reduction at pass
ld	arc of contact	δ, n	shape factor of passes
M	$\frac{0.8}{(b_1/ld)^2} \left[2 - \frac{3(h_1 - h_2)}{ld} \right]$	$\varepsilon, \dot{\varepsilon}$	strain and strain rate
n_σ	stress coefficient	λ	elongation coefficient
		σ	yield stress
		ψ	lever arm ratio

Computer-aided composition-treatment-structure-property correlation studies in steels

K VIJAYARAJU and E S DWARAKADASA

Department of Metallurgy, Indian Institute of Science, Bangalore 560 012, India

Abstract. Internal structure of materials uniquely decides their properties. The structure is a complicated function of composition and thermal and/or mechanical treatment. Inter-relation is so complex that a highly generalized correlation is very difficult. Steel is a very good example to illustrate this complexity. Advent of mini- and microcomputers have now paved way for handling such multiparametric problems in a more rational way, with greater ease and increased confidence. This paper is an attempt to develop a computer software which will assist the user in three different ways: (a) to determine the treatments that will generate a desired structure, when compositions are known; (b) to determine composition limits within which desired structure will result having defined the treatments, and (c) to predict structures that can be generated when composition and treatments are limited. This program has immense utility of (i) best use of available inventory, (ii) reduction of standards, varieties and inventory and (iii) most importantly to decide the best purchase based on treatment limitations in the shop. A large data bank is being built to support the program.

Keywords. Steel; property; structure; correlation; software; computer handling.

1. Introduction

Microstructure plays a very important role in deciding the properties of a material. Microstructures can be altered by changing material composition and by imparting suitable thermal and/or mechanical and thermomechanical treatments. The problem of alloy chemistry is complex and treatment variables are many. The case of ferrous materials, steels in short, is a typical example in hand. Investigations over the past several centuries have generated innumerable steel compositions and treatments. The result, as we see today, is the huge inventory and list of standards the materials engineer has to cope up with. There is an urgent need to rationalize the picture and many attempts are being made. Structure property correlation studies have been looked into in great detail to derive constitutive but empirical relationships that may be used to predict the properties. However, these studies are of limited application as they are governed by severe restrictions. The advent of mini- and microcomputers has now changed our approach to the problem and further offers tremendous possibilities. It only needs a serious investigation to utilize the data available to fit in meaningful relationships into an objectively built program. To take the specific example of steels, problems may be defined in terms of a few typical goal oriented questions.

- (i) Property limits for a particular application are defined, what would constitute a set of ideal conditions of composition, structure and treatment that will satisfy this situation?
- (ii) A given set of steel varieties are available in the yard. What would be the minimum and maximum properties that can be achieved making use of all applicable treatments? What would be the microstructure in each case?

- (iii) A certain microstructure is to be generated. What are the steel compositions and treatments that will result in this microstructure?

Even with these three goals, the dimension of the problem becomes huge and underlines the need for computer handling of the problem. A long term plan to build a software facility to handle this problem has been initiated (Vijayaraju 1984). This paper describes the first phase of the development of an interactive program in which the composition, microstructure and treatment are interrelated to yield the mechanical properties. The program has been mainly developed based on a number of empirical relationships that relate composition and/or structure with the resulting properties, and hence is applicable only within certain limiting conditions that have been imposed such as medium carbon steels, single continuous cooling, straight forward microstructures, etc. The long term plan is to develop a set of programs in all dimensions to make it applicable to all steels universally.

2. Software description

The methodology of the development of the software is shown in figure 1. As a first step, the composition data are fed into the program. Based on this data the program calculates the various transformation temperatures M_s , AC_1 , AC_3 , MS using equations (1)-(3) (Cias 1977).

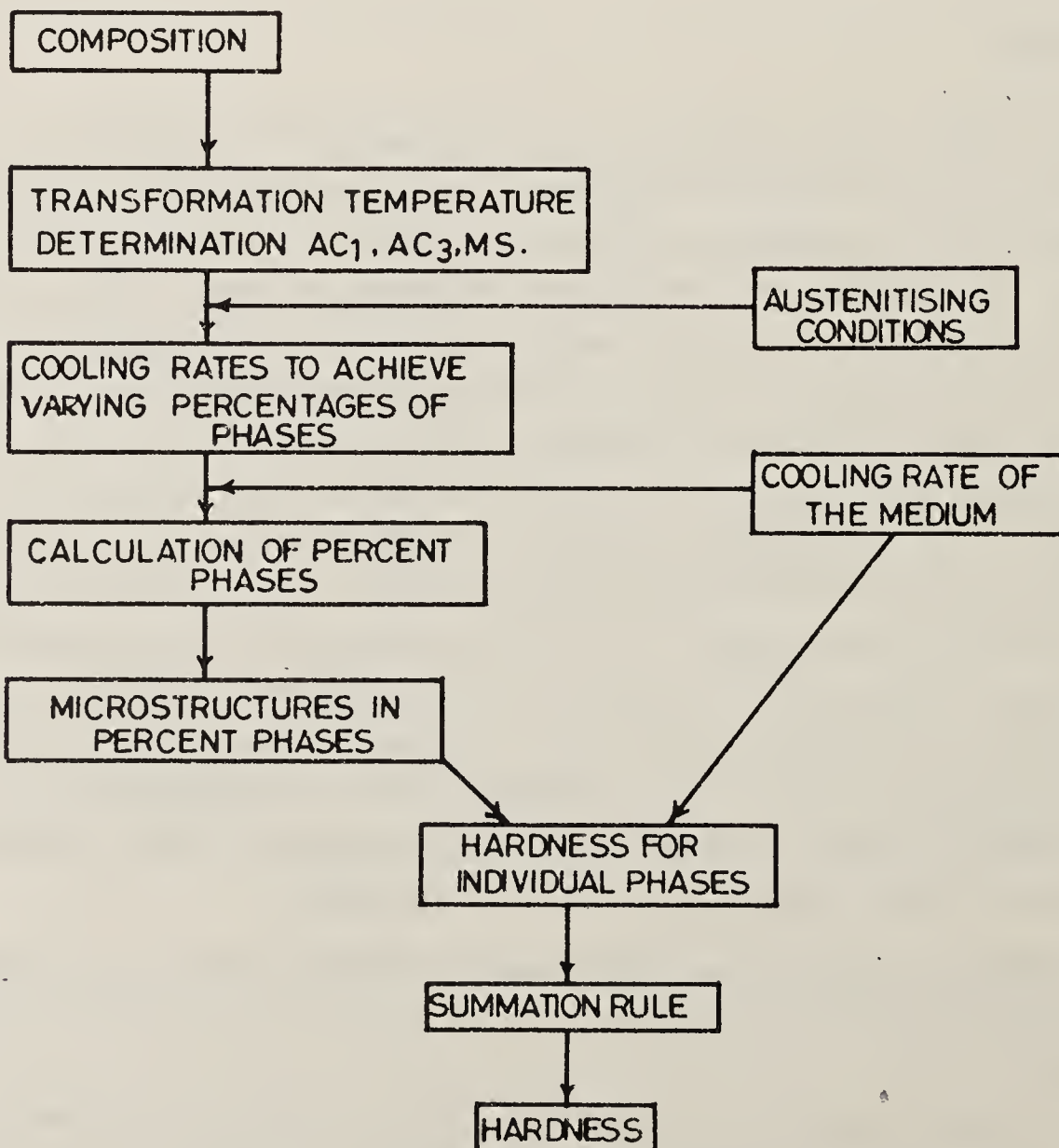


Figure 1. Methodology of the software development.

$$AC_1 = 712 + 20.4 \text{ Si} - 17.8 \text{ Mn} - 9.8 \text{ Mo} + 11.9 \text{ Cr} - 19.1 \text{ Ni} \quad (1)$$

$$AC_3 = 871 - 254.4 \text{ C} + 51.7 \text{ Si} - 14.2 \text{ Ni}, \quad (2)$$

$$M_s = 531 - 39.2 \text{ C} - 43.3 \text{ Mn} - 16.2 \text{ Cr} - 21.8 \text{ Ni}. \quad (3)$$

Then from these results the user can prefer the austenitization temperature and the time of austenitization from the section size and geometry. Now to take care of the grain growth during the austenitization, a parameter called 'austenitization parameter', P_A , is defined and can be calculated from the equation given below (Maynier *et al* 1978):

$$P_A = \left[1/T - \frac{nR}{H} \log(t/t_0) \right]^{-1}, \quad (4)$$

where T is the austenitization temperature ($^{\circ}\text{K}$), R is the gas constant, H , the activation energy for the grain growth and t, t_0 is the time of austenitization and unit time. Using the data on composition and transformation in the following set of equations the cooling rates to obtain a particular combination of percentage phases are calculated (Maynier *et al* 1978)

$$\log V_1 = 9.81 - (4.62 \text{ C} + 1.05 \text{ Mn} + 0.54 \text{ Ni} + 0.50 \text{ Cr} + 0.66 \text{ Mo} + 0.00183 P_A), \quad (5)$$

$$\log V_2 = 10.17 - (3.80 \text{ C} + 1.07 \text{ Mn} + 0.70 \text{ Ni} + 0.57 \text{ Cr} + 1.58 \text{ Mo} + 0.0032 P_A), \quad (6)$$

$$\log V_3 = 6.36 - (0.43 \text{ C} + 0.49 \text{ Mn} + 0.78 \text{ Ni} + 0.27 \text{ Cr} + 0.38 \text{ Mo} + 2\sqrt{\text{Mo}} + 0.0019 P_A) \quad (7)$$

$$\log V_{190} = 8.76 - (4.04 \text{ C} + 0.96 \text{ Mn} + 0.49 \text{ Ni} + 0.58 \text{ Cr} + 0.97 \text{ Mo} + 0.0010 P_A) \quad (8)$$

$$\log V_{290} = 10.55 - (3.65 \text{ C} + 1.08 \text{ Mn} + 6.77 \text{ Ni} + 0.61 \text{ Cr} + 1.60 \text{ Mo} + 0.0032 P_A) \quad (9)$$

$$\log V_{390} = 7.59 - (9.38 \text{ C} + 0.35 \text{ Mn} + 0.93 \text{ Ni} + 0.11 \text{ Cr} + 2.31 \text{ Mo} + 0.0033 P_A) \quad (10)$$

$$\log V_{250} = 8.50 - (4.12 \text{ C} + 0.86 \text{ Mn} + 0.57 \text{ Ni} + 0.41 \text{ Cr} + 0.94 \text{ Mo} + 0.0012 P_A) \quad (11)$$

$$\log V_{250} = 8.74 - (2.23 \text{ C} + 0.86 \text{ Mn} + 0.56 \text{ Ni} + 0.59 \text{ Cr} + 1.60 \text{ Mo} + 0.0032 P_A), \quad (12)$$

where V_1 = minimum quench velocity to attain a complete martensitic structure, V_2 = critical cooling velocity resulting in entirely bainitic structure with small amounts of martensite, V_3 = critical cooling velocity to achieve a completely annealed structure, i.e., ferrite and pearlite, V_{190} = critical cooling velocity giving 10% bainite and 90% martensite, V_{290} = critical cooling velocity giving 10% ferrite-pearlite and 90% bainite, V_{390} = critical cooling velocity giving 90% ferrite-pearlite and 10% bainite, V_{150} = critical cooling velocity giving 50% martensite and 50% bainite, V_{250} = critical cooling velocity giving 50% bainite and 50% ferrite-pearlite.

From the various critical cooling rates to attain different discrete combinations of martensite, bainite and ferrite-pearlite, two second order polynomial equations have been fitted. Using this, the intermediate combinations of different phases are calculated

for any cooling rate. This results in the final microstructures in terms of percentage of martensite, bainite and pearlite. Equations (13)–(15) are taken from the literature (Maynier *et al* 1978) for the determination of hardness values of the individual phases, i.e., 100% martensite or 100% bainite or 100% ferrite-pearlite. The hardness of the final microstructure is calculated using the summation rule:

$$HVM = 127 + 949 C + 27 Si + 11 Mn + 8 Ni + 16 Cr + 21 \log (Cv), \quad (13)$$

$$\begin{aligned} HVB = & 323 + 185 C - 330 Si + 153 Mn + 65 Ni + 144 Cr + 194 Mo \\ & - \log Cv (89 + 53 C - 55 Si - 22 Mn - 10 Ni - 20 Cr - 30 Mo) \end{aligned} \quad (14)$$

$$\begin{aligned} HV(F+P) = & 42 + 23 C + 53 Si + 30 Mn + 12.6 Ni + 7 Cr + 19 Mo \\ & - \log Cv (10 - 19 Si + 4 Ni + 8 Cr + 130 V), \end{aligned} \quad (15)$$

Cv = cooling velocity, HVM = hardness of 100% martensitic structure, HVB = hardness of entirely bainitic structure, $HV(F+P)$ = hardness of completely annealed structure, i.e., fully ferrite-pearlitic structure.

A graphical representation of the variation of the percentage of each phase with the cooling rates is shown in figure 2. Similarly the variation of the hardness values (VHN) with the cooling rate is shown in figure 3.

3. Limitations

The validity of this study is limited to the following ranges of composition and conditions of austenitization and tempering.

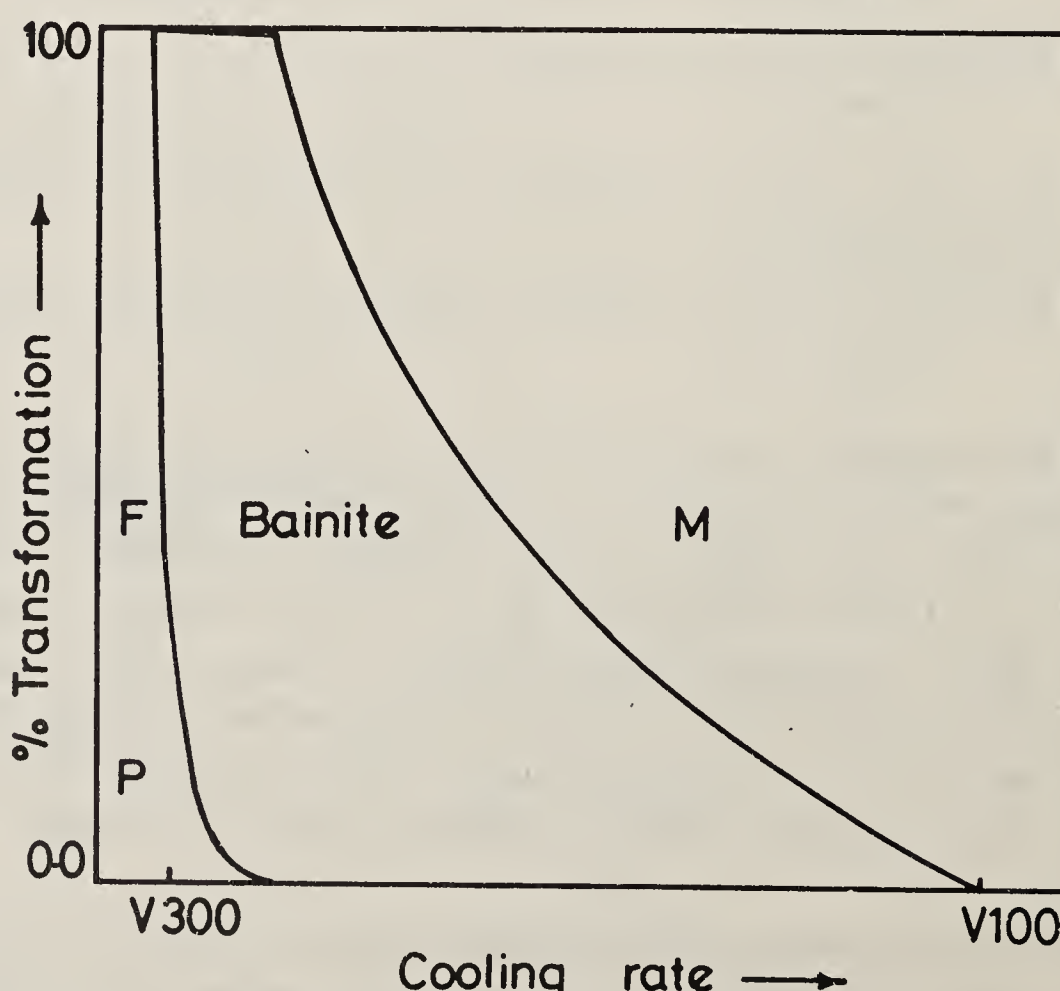


Figure 2. Identification of product as a function of cooling rate.

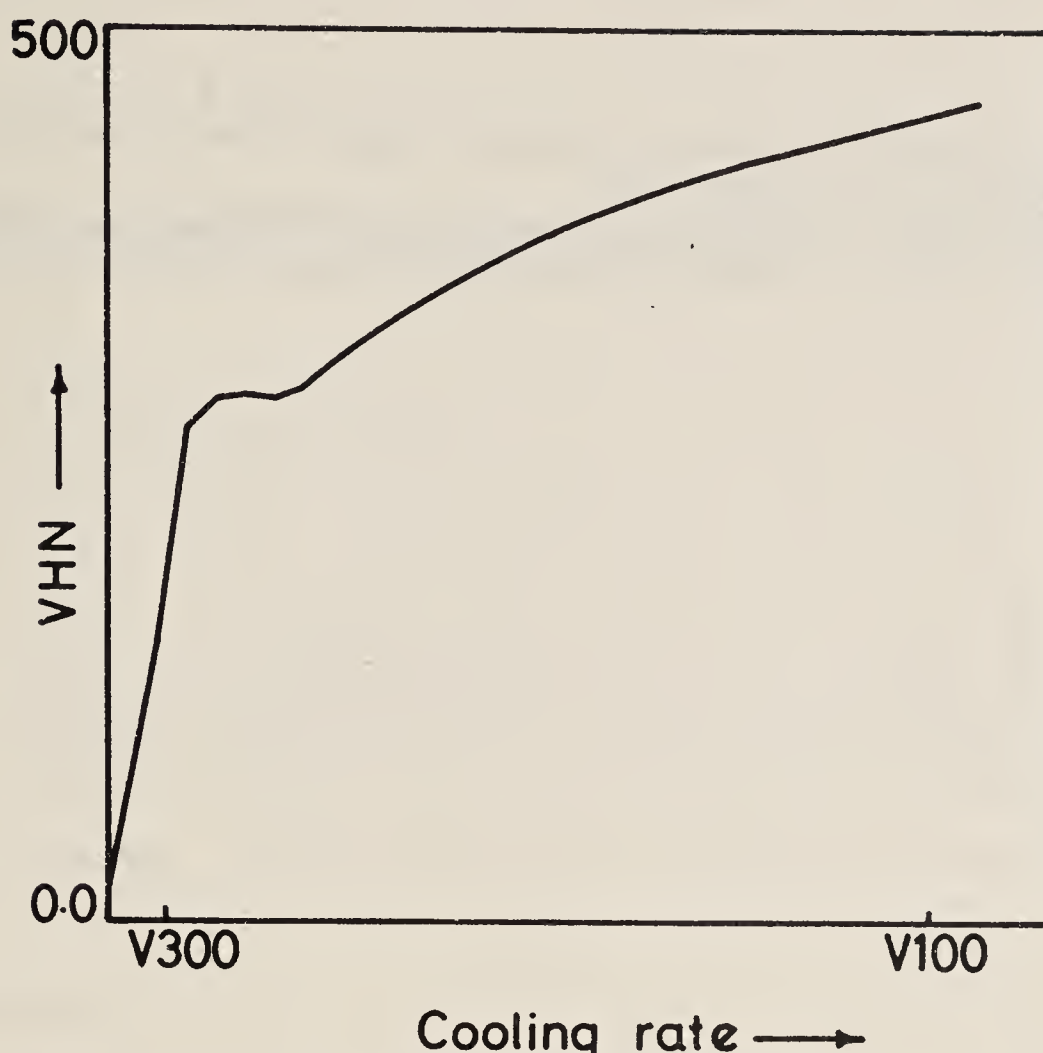


Figure 3. Variation of hardness of steel as a function of cooling rate.

3.1 Composition range: (weight %)

$0.1 < C < 0.5$; $Mn < 2$; $Ni < 4$; $Cr < 3$; $Si < 1$; $Mo < 1$;
 $V < 0.2$; $Cu < 0.5$; $Mn + Ni + Cr + Mo < 5$; $0.01 < Al < 0.05$.

3.2 Austenitizing conditions

It should be between 800°C for 1 hr and 1100°C for 1 hr. Tempering conditions should be between $500^{\circ}\text{C} - 1$ hr and $700^{\circ}\text{C} - 200$ hr. Intercritical treatment is not included. Alloying additions like Nb, Ti, B and Zr are not included in this study.

4. Conclusion

The present study opens up many physical and mechanical metallurgical aspects of steels for theoretical predictions. The predicted results are comparable with the experimental points within an allowable variation. Although the flow chart shown in figure 1 gives the methodology of the present study, it is possible to trace back the path that will result in the optimization of composition and treatment for a required set of mechanical properties. Presently this work is being projected to cope up with the variety of steels and extending the operating range of composition and treatment conditions, although limited by certain factors. The value of the prediction will be greatly enhanced if the microstructure is simulated on the Visual Display Unit (VDU) for the given set of compositions and treatments.

References

- Cias W W 1977 Phase transformation kinetics of selected wrought structural steels, Report, Climax Molybdenum Co., Greenwich, Connecticut, USA
- Maynier Ph, Dollet J and Bastien P 1978 *Proc. Symp. Met. Soc. AIME*, (Philadelphia: AIME) p. 163
- Vijayaraju K 1984 B E Project Report, Department of Metallurgy, Indian Institute of Science, Bangalore

Computer simulation of pressure sintering

N RAMAKRISHNAN, T BALAKRISHNA BHAT and
V S ARUNACHALAM*

Defence Metallurgical Research Laboratory, Hyderabad 500 258, India

*Scientific Adviser to Defence Minister, New Delhi 110011, India

Abstract. The densification process during pressure sintering has been analyzed using finite element analysis. This analysis uses an iterative solution algorithm. With this the densification process in complex geometries with complex boundary conditions can be analyzed and this technique is particularly suited for tackling material nonlinearity. Evolution of dense structures with gradual closure of pores is described for two typical geometries.

Keywords. Computer simulation; pressure sintering; finite element analysis; creep modulus

1. Introduction

Pressure sintering is a technique in which a powder aggregate is subjected to high pressures at high temperatures to achieve simultaneous compaction and sintering. Theoretical analysis of pressure sintering is greatly restricted due to the complexities involved in the geometries and the nonlinear material properties. Usually, powder aggregates are idealized to simple geometries (McKenzie 1948; Coble 1970; Kovalachenko and Samsonov 1961; Wilkinson and Ashby 1975; Notis and Krishnamachary 1975) disregarding the spatial and size distribution of pores or the interaction of pores. These problems can be reduced substantially by the use of numerical techniques and we have chosen finite element method (FEM) for analyzing pressure sintering with all its complexities, as it provides a simple and direct approach to handle complex geometries, boundary conditions and material behaviour (Ramakrishnan *et al* 1984).

2. Simulation of powder aggregates

Two types of two-dimensional configurations have been identified for simulating the powder aggregates: (i) randomly packed spheres of log normal size distribution (figure 3a) (ii) randomly distributed spherical pores of log normal size distribution in a homogenous matrix (figure 4a). To construct the first geometry, a hypothetical arrangement of circular discs of log normal size distribution placed in a rectangular box has been considered. The packing is done starting from the bottom row ensuring the mechanical stability of the arrangement. This geometry represents the initial stage of compaction of powder aggregates.

The second geometry is formed by randomly placing circular pores of log normal size distribution in a rectangular material matrix. This geometry depicts the final stage of sintering where pores become spherical due to surface tension and the material matrix

becomes nearly continuous. These geometries are subdivided into a number of small rectangular and triangular elements for finite element analysis. As the stress varies rapidly near the pores, a finer discretization is performed there.

3. Analysis of densification of powder aggregates

Densification in pressure sintering takes place mainly through creep processes such as diffusion creep, dislocation creep and grain boundary sliding. These processes are driven by the local stresses. Therefore for the analysis of densification it is necessary to compute the stresses at various locations in the material matrix for the applied external pressure and the boundary conditions. These stresses are in turn used to compute the strains and the displacements for a given interval of time at the corresponding locations to obtain the new geometry. Again the new geometry is subjected to similar analysis and this process is continued in an iterative fashion until the porosity reaches the desired low value. The increments in time are decided in such a way that the change in geometry in any particular iteration is small.

4. Finite element analysis (FEA) of creep deformation

In FEA of creep deformation, the behaviour of each element is described in terms of force-displacement rate relationship. The governing system of equations for the whole geometry is established by the assembly of elemental behaviour, subject to compatibility and dynamic equilibrium conditions at each node. These equations are solved to yield stresses and displacement rates at various nodes.

4.1 Basic equations

The force-displacement rate relation is given by

$$\{F\}^e = [K]^e \{\dot{q}\}^e, \quad (1)$$

where $[K]^e$ represents the stiffness matrix, $\{\dot{q}\}$ the displacement rate vector and $\{F\}^e$ the nodal force vector. On assembly, these equations assume the following global form:

$$\{F\}^g = [K]^g \{\dot{q}\}^g. \quad (2)$$

The stresses and strain rates in terms of displacement rates are given by the following equations:

$$\{\dot{\varepsilon}\} = [B] \{\dot{q}\}, \quad (3)$$

$$\{\sigma\} = E_c^e [C] \{\dot{\varepsilon}\}, \quad (4)$$

where $[B]$ is the coefficient matrix, purely dependent on the geometry of the element and $[C]$ is given by (Donea 1978)

$$[C] = \frac{1}{(1-2\gamma)(1+\gamma)} \begin{bmatrix} 1-\gamma & \gamma & 0 \\ \gamma & 1-\gamma & 0 \\ 0 & 0 & 2(1+\gamma) \end{bmatrix}$$

for plain strain condition where γ is the Poisson's ratio. E_c^e is the elemental creep modulus and for the constant strain elements we define it as

$$E_c^e = \sigma_*^e / \dot{\varepsilon}_*^e, \quad (5)$$

where σ_* and $\dot{\varepsilon}_*$ are effective stress and strain rates respectively. The stress-strain rate relationship is nonlinear and is generally represented in the form of power law

$$\dot{\varepsilon}_* = A_c \sigma_*^n, \quad (6)$$

where A_c and n are creep constants which depend on the material and the temperature.

4.2 Procedure for determining the stiffness matrix

The minimum potential energy condition is used to establish the stiffness matrix. The potential energy can be represented as

$$\pi = [\iiint \{\sigma\}^T \{\dot{\varepsilon}\} dV - \iint \{P\} \{\dot{q}\} dS] \Delta t, \quad (7)$$

where $[P]$ represents forces per unit area and Δt a small interval of time. Using (3) and (4), (7) can be modified to

$$\pi = [\iiint E_c^e \{\dot{q}\}^T [B]^T [C] [B] \{\dot{q}\} dv - \iint \{P\} \{\dot{q}\} dS] \Delta t. \quad (8)$$

For dynamic equilibrium $\delta\pi/\delta\dot{q} = 0$. Assuming the displacement rates to be constant in a sufficiently small interval of time, the above criterion can be shown to give,

$$F = 2E_c^e [B]^T [C] [B] \{\dot{q}\} h S_e, \quad (9)$$

where h and S_e are the thickness and the area of the element respectively, within which strain is assumed constant. Hence stiffness matrix for creep is given by

$$[K]^e = 2h S_e [B]^T [C] [B] E_c^e. \quad (10)$$

4.3 Procedure for analyzing densification

To start with, the elemental creep modulus of all the elements are assumed to be identical and an arbitrary E_c^e is assigned to all the elements. The displacement rates $\{\dot{q}\}$ and nodal forces $[F]$ are obtained by solving (9) for the given boundary conditions. $\{\sigma\}$ and $\{\dot{\varepsilon}\}$ are then computed using (3) and (4). These stresses do not correspond to actual stresses and the actual stresses can be calculated only by an iterative procedure that gives a convergent, compatible solution. Effective stresses σ_* and effective strain rates $\dot{\varepsilon}_*$ are calculated using the equations

$$\sigma_*^2 = (\sigma_1 - \sigma_2)^2 + (\sigma_2 - \sigma_3)^2 + (\sigma_3 - \sigma_1)^2, \quad (11)$$

where $\sigma_1, \sigma_2, \sigma_3$ are the principal stresses

and $\dot{\varepsilon}_* = A \sigma_*^n$.

The creep moduli for the subsequent iteration is computed by the equation

$$E_c^e = (1/A)^{1/n} (\dot{\varepsilon}_*)^{1/n-1}. \quad (12)$$

Using these creep moduli, new displacement rates are obtained. These calculations are continued until the stresses converge in each element. After the convergence, the nodal

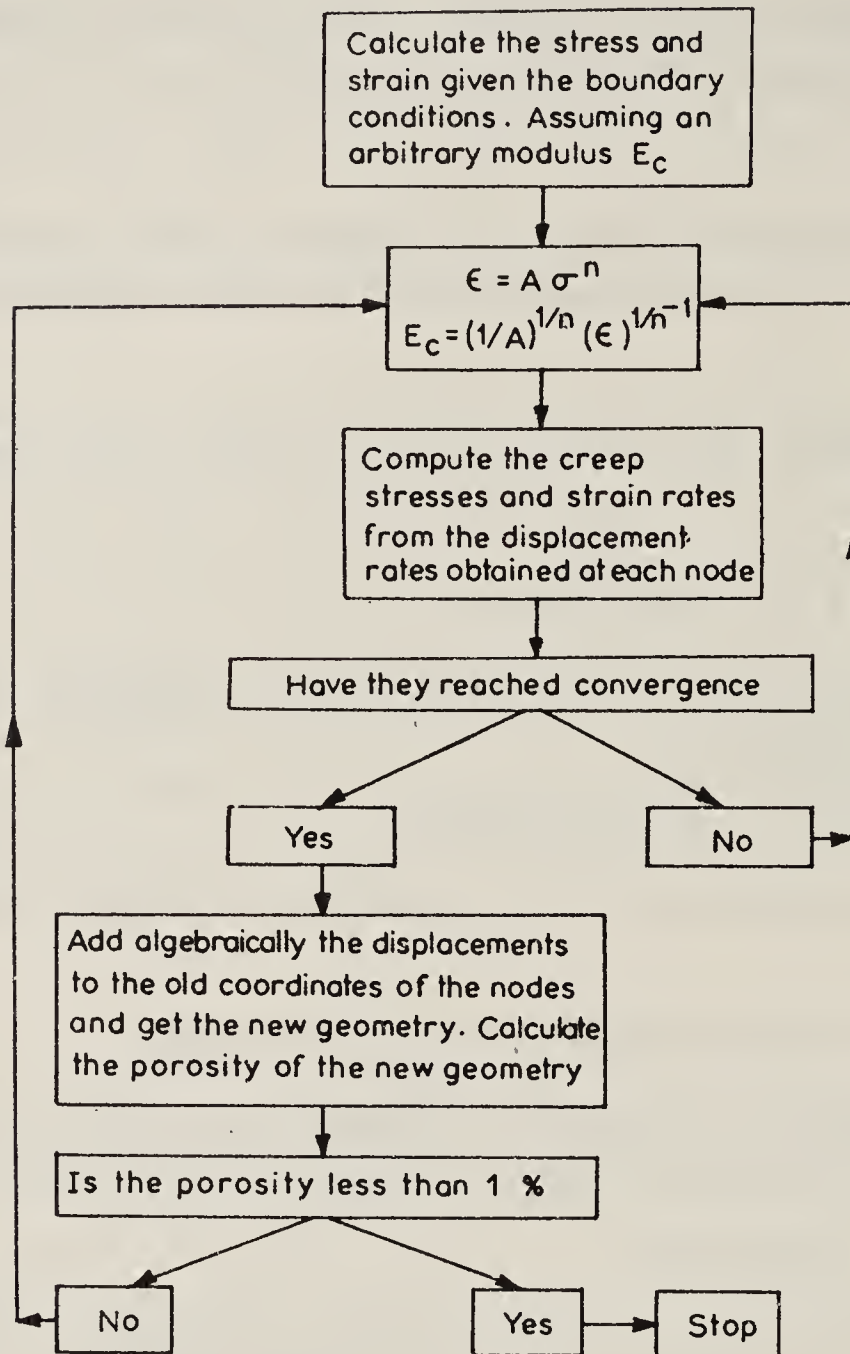


Figure 1. Flow chart for computer simulation of pressure sintering.

co-ordinates are updated using the displacements at each node and the procedure is repeated for the new porosity. In figure 1, the whole procedure is given in the form of a flow chart.

4.4 Boundary conditions

Either force boundary conditions or displacement rate boundary conditions can be thought of for this analysis; the first one appears apparently simple and more relevant as what we know in practice is only the external pressure. But if we impose force boundary conditions, the displacement rates computed for all the boundary nodes may not be perfectly same as we are not dealing with a perfectly random system. The distortions in the geometry introduced by this becomes increasingly pronounced in subsequent iterations. To overcome this problem the following procedure is adopted.

Unit displacement rate is imposed on the boundary nodes ensuring that there are no contradictions, in representing the actual situation. For example in isostatic pressing as in figure 2a, the boundary conditions given are,

for $x = l, \{\dot{q}_x\} = -1$; for $y = l, \{\dot{q}_y\} = -1$;

for $x = 0, y = 0, \{\dot{q}_x\} = \{\dot{q}_y\} = 0$.

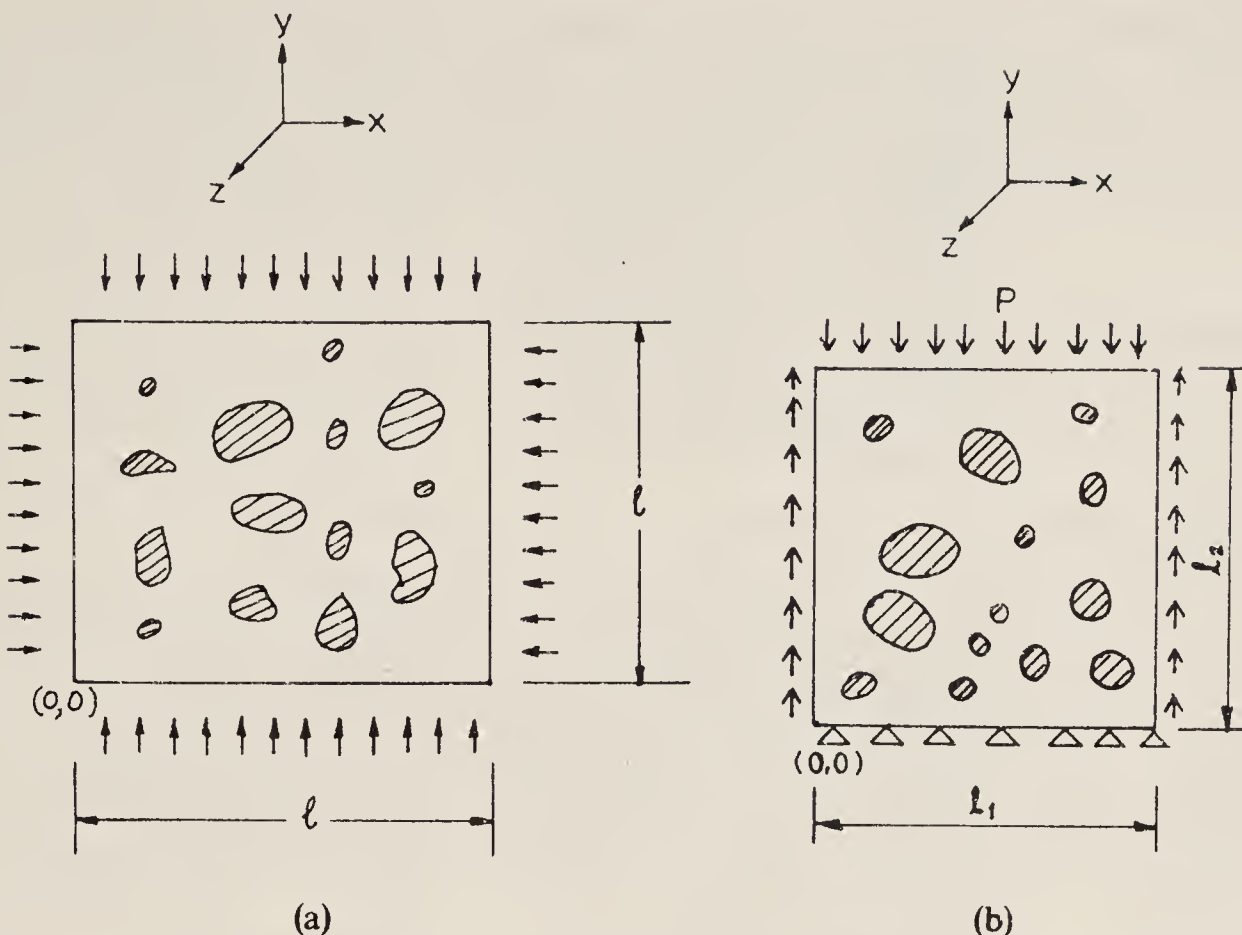


Figure 2. Boundary conditions for (a) isostatic pressing (b) uniaxial pressing with boundary wall friction.

Using (2) we can obtain the forces at various nodes needed to produce these displacement rates. These forces can be used to calculate the dummy pressure P' and if P is the actual pressure, we normalize all the calculated values using the scaling factor

$$\lambda = P'/P. \quad (13)$$

The relationship between dummy and actual displacement rates is given by

$$\{\dot{q}'\} = \lambda \{\dot{q}\}. \quad (14)$$

The actual boundary conditions used in this analysis for (i) isostatic pressing (ii) uniaxial pressing are shown in figures 2a, b respectively.

4.5 Updating the geometry

Once the convergence of stresses is established for any particular porosity, the displacements are calculated at each node for a given time increment and these are algebraically added to the original coordinates of the nodes to get the new geometry. To have a control over the change in the geometry with densification, the incremental boundary displacements are fixed instead of fixing the incremental time intervals and for each step, time increment is actually calculated.

It is often necessary to refine and regenerate the mesh at regular intervals. Otherwise the elements may start overlapping when a particular pore is completely closed. If two nodes come very close, then one of the nodal data is removed from the nodal information directory and correspondingly element directory is modified. If the segments joining the nodes surrounding the pores intersect, a new node is created at the

point of intersection and the nodal and elemental directories are appropriately altered. The resulting node number sequence may increase the bandwidth of the stiffness matrix. Therefore the region of interest is scanned and the nodal and the elemental directories are modified in the whole region to bring down the bandwidth.

5. Results of the computer simulation

5.1 Evolution of pore geometries

During pressure sintering, the geometry of the powder compact undergoes a variation with time. Figure 3 is a typical sequence depicting this variation in a powder aggregate. It may be seen that the smaller particles and the boundary regions of coarser particles only get deformed significantly and not the interior of a large particle. Figure 4 represents isostatic pressing and figure 5 represents uniaxial pressing with die wall friction taken into account. Figure 5 particularly brings out the density variation at various locations similar to earlier experimental curves obtained for uniaxial pressing (Jones 1960).

5.2 Pore size variation

The decrease in pore sizes with densification is depicted in figure 6. It is very clearly seen from the figure that the distribution of pore sizes narrows down with densification. Also

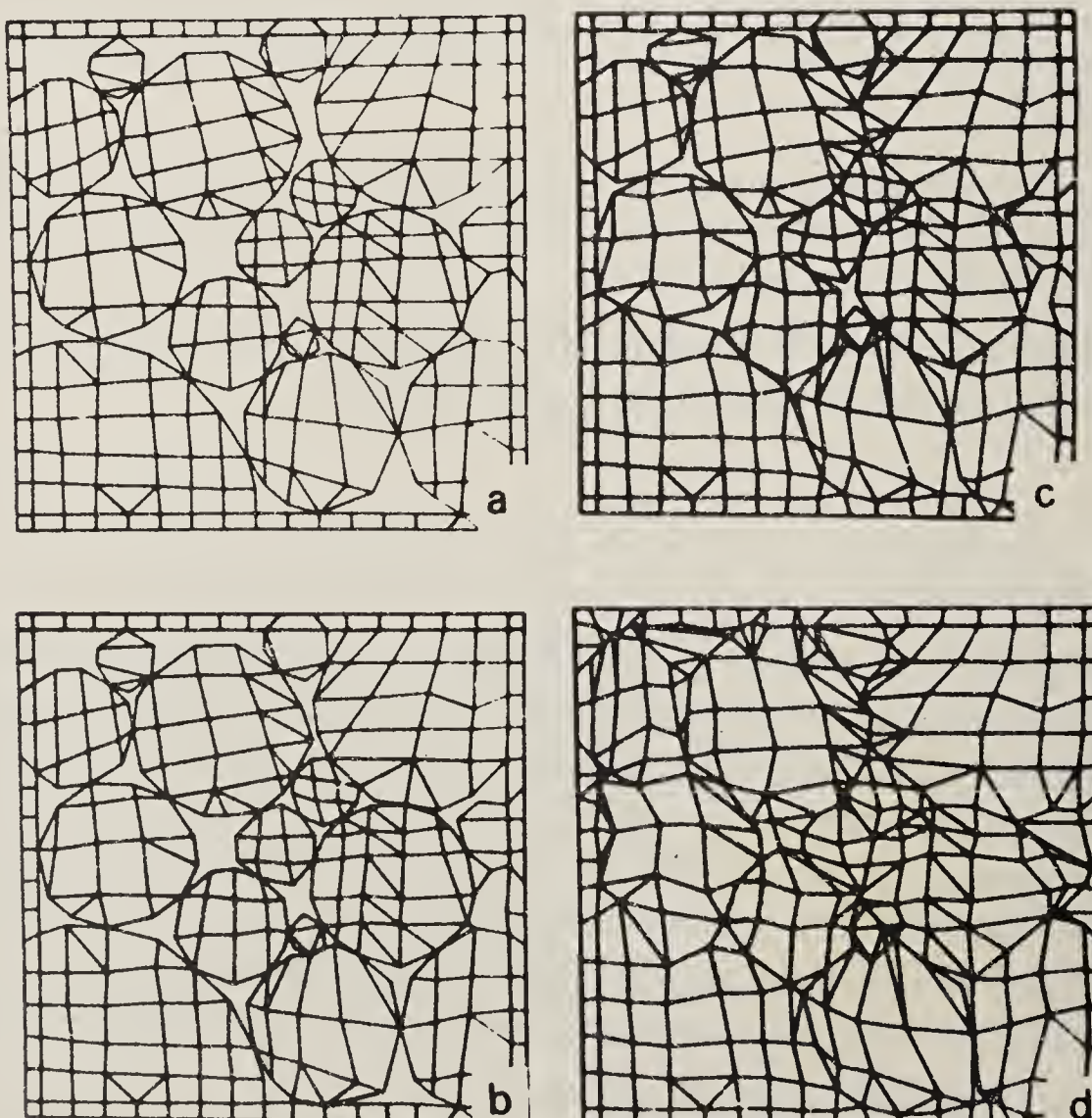


Figure 3. Sequence of closure in a powder compact during isostatic pressing.

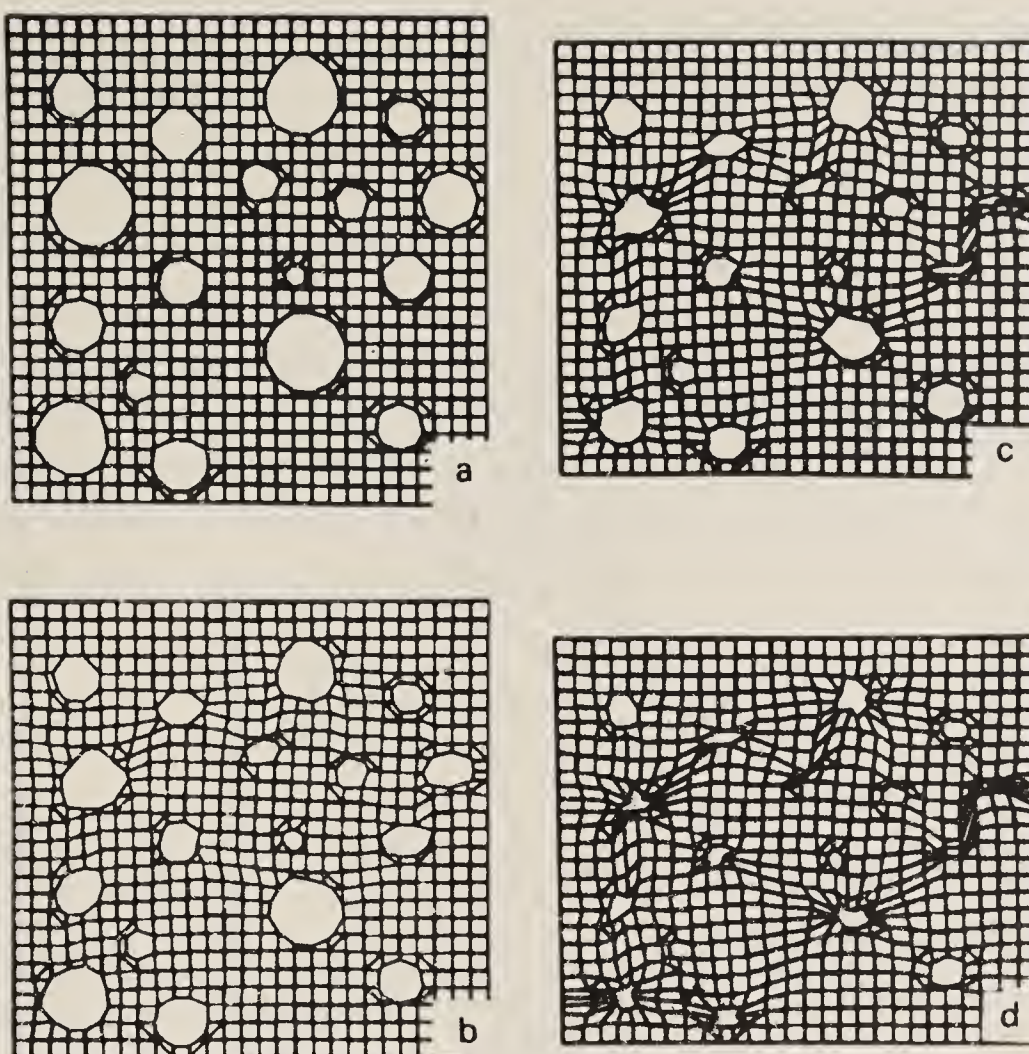


Figure 4. Sequence of pore closure in a compact with initially rounded pores during isostatic pressing.

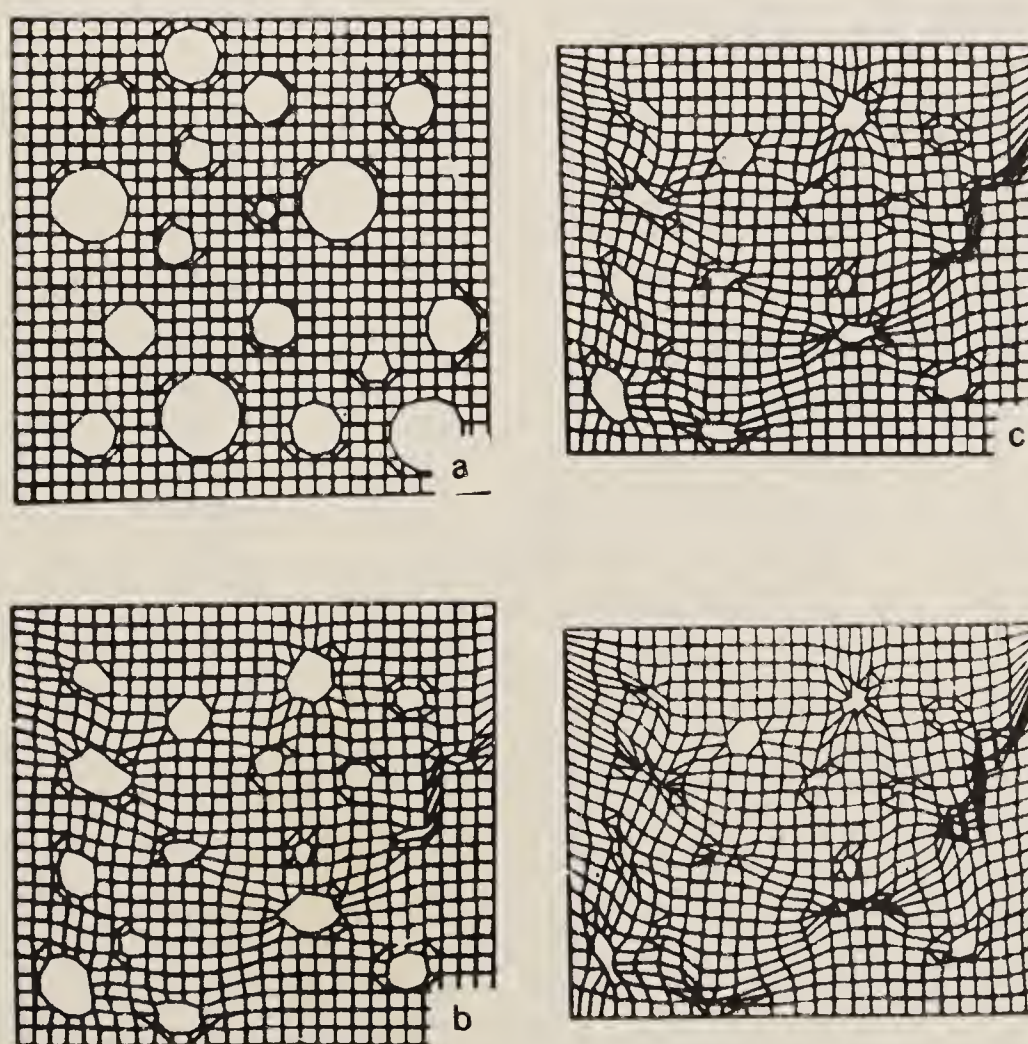


Figure 5. Sequence of pore closure in a compact with initially rounded pores during uniaxial pressing with boundary wall friction.

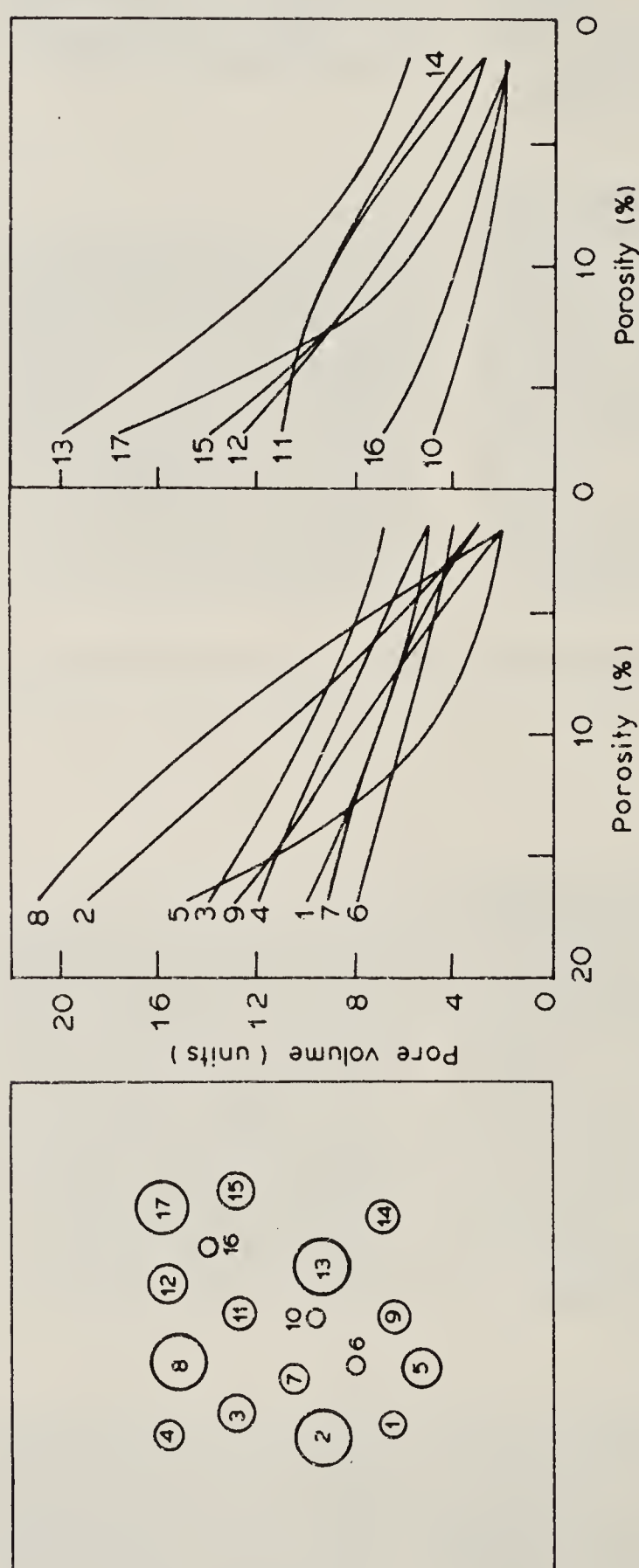


Figure 6. Variation of individual pore size with progressive densification. The curve number corresponds to pore identity.

curves crossing each other suggests that the closure rate not only depends on its size but also on its neighbours.

6. Conclusion

Finite element analysis can be used to analyze complex geometries of porous aggregates sintering under pressure. Even nonlinear material flow behaviour can be taken into account using a concept of creep modulus to provide a globally convergent solution. The technique applied to a compact containing a set of pores indicates that the closure of any given pore is governed not only by its own size but also its neighbourhood.

References

- Coble R L 1970 *J. Appl. Phys.* **41** 4798
Donea J 1978 *Creep in engineering materials and structures* (eds) G Barnasconi and G Piat (London: Applied Science Publishers) p. 34
Jones W D 1960 *Fundamental principles of powder metallurgy* (Leeds; Arnold) p. 299
Kovalachenko M/S and Samsonov G V 1961 *Poroshkov Metall.* **1** 3
McKenzie J K 1948 *Proc. R. Soc. (London)* **B62** 833
Notis M R and Krishnamachary V 1975 *Sintering and catalysis* (eds) G C Kuczinsky (New York; Plenum Press) p. 493
Ramakrishnan N, Balakrishna Bhat T and Arunachalam V S 1984 *Acta Metall.* **32** 357
Wilkinson D S and Ashby M F 1975 *Acta Metall.* **23** 1277

Computer simulation of serrated yielding

K NEELAKANTAN

Indira Gandhi Centre for Atomic Research, Kalpakkam 603 102, India

Abstract. A model for serrated yielding based on the negative resistance characteristics of materials is discussed. An analog computer based on this model is described. The simulated curves show oscillations which are regular and uniform in amplitude. To simulate more realistic tensile test curves, a refined model which includes the effects of fluctuations in dislocation density and velocity is described. Some simulated curves using this refined model are presented. These results are close to observed tensile test curves.

Keywords. Serrated yielding; machine equations; electronic analog; noise.

1. Introduction

The phenomenon of serrated yielding during tensile test experiments has been widely observed (Keh *et al* 1968; Brindley and Worthington 1970; Hall 1970) and is discussed in the literature under various names such as the Portevin-Le Chatelier effect, jerky flow etc. Experiments have shown that serrated yielding is affected by temperature, strain rate and composition. On the theoretical side the basic idea has been that of dynamic strain ageing going back, in a sense, to Cottrell and Bilby (1949).

While the strain ageing concept no doubt gives an insight into the physical origin of serrated yielding, it does not by itself provide a description of the temporal behaviour observed during experiments. It is interesting to examine the stress oscillations in terms of the interplay between the machine kinematics and the defect kinetics. The crucial point is that the dislocation drag mechanism has a negative resistance characteristic (Cottrell 1953).

In this paper, the temporal behaviour of the stress oscillations is examined in terms of the Cottrell model (which incorporates a negative resistance feature). A simple electronic analog computer (Neelakantan and Venkataraman 1983) to simulate the behaviour of the material during a constant strain rate test is described. It will be seen that the serrations are regular and uniform in amplitude unlike the ones in real life tensile test curves. However the circuit describes the observed behaviour in other respects. A refined model (Neelakantan and Venkataraman 1986) which takes into account the fluctuations in dislocation density and velocity is then described. Results from numerical simulation using this refined model are presented.

2. The machine equations

The starting point is the machine equation which quantifies the material response during tensile testing. The machine schematic is shown in figure 1a. Figures 1b and c show the mechanical and electrical equivalent (to be discussed in § 3). The cross

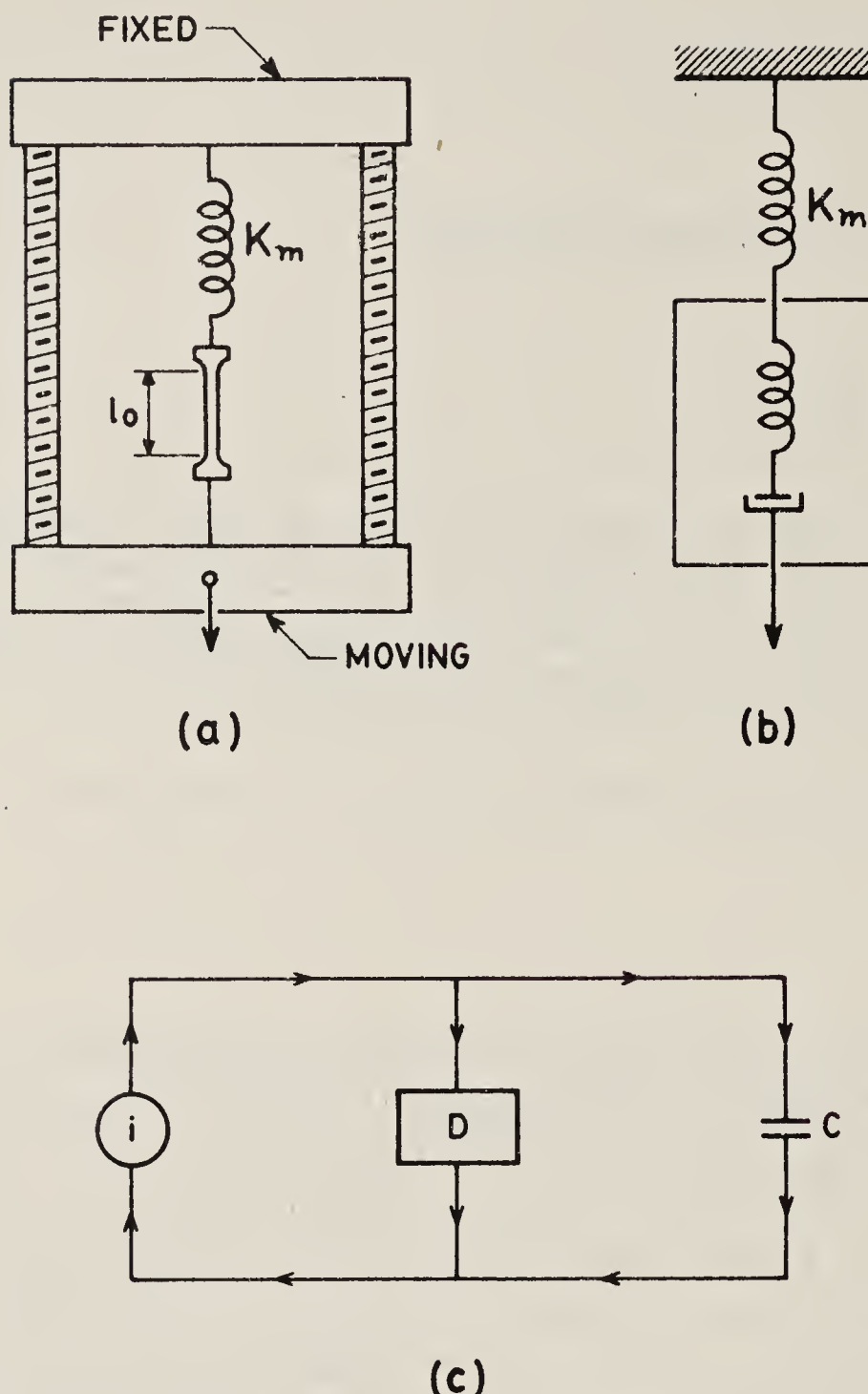


Figure 1. (a) Machine schematic for tensile testing (b) Mechanical equivalent. (c) Electrical equivalent.

head moves with a constant speed S . If the machine stiffness is K_m then at time t

$$St = P/K_m + (Pl_0/AE) + \varepsilon_p l_0, \quad (1)$$

where A is the area of cross-section of the specimen, E its elastic modulus and ε_p the plastic strain. The load P is given by $A\sigma$ where σ is the stress developed. Defining an effective stiffness K_{eff} as

$$1/K_{\text{eff}} = A/l_0 K_m + 1/E, \quad (2)$$

we get

$$\dot{\varepsilon} = \dot{\sigma}/K_{\text{eff}} + \dot{\varepsilon}_p, \quad (3)$$

where $\dot{\varepsilon}$ is the applied strain rate.

Now $\dot{\varepsilon}_p$ is described by Orowan's equation

$$\dot{\varepsilon}_p = gb\rho u, \quad (4)$$

where g is a parameter, b is the Burger's vector, u the velocity and ρ the density of mobile

dislocations. The dislocation density can be modelled as (Bergstrom and Roberts 1973)

$$\rho = \rho_0 \exp(-\Omega \varepsilon_p) + \rho_f (1 - \exp(-\Omega \varepsilon_p)), \quad (5)$$

where ρ_0 and ρ_f are the initial and final dislocation densities and Ω is a parameter related to the remobilization rate. For low values of plastic strain we can write (5) as

$$\rho = \rho_0 + B \varepsilon_p. \quad (6)$$

Now the only thing that remains to be specified is the dislocation velocity. This is a highly nonlinear function of the stress. Choosing the Cottrell model which is schematically shown in figure 2 and taking into account the work hardening effect one can write (Nabarro *et al* 1964)

$$u = f(\sigma - \alpha \varepsilon_p^m), \quad (7)$$

where α is the work hardening coefficient and m is a parameter.

3. The electronic analog

Going back to figure 1c which shows the electrical equivalent of the tensile test, one sees the following correspondences

$$\dot{\varepsilon} \leftrightarrow i \text{ (current)} \text{ and } \sigma \leftrightarrow v \text{ (voltage).}$$

In the circuit shown, the capacitor represents the compliance and the device D simulates the complex nonlinear behaviour of the plastically deforming material. Maintaining a constant strain rate is equivalent to driving the circuit with a constant current source.

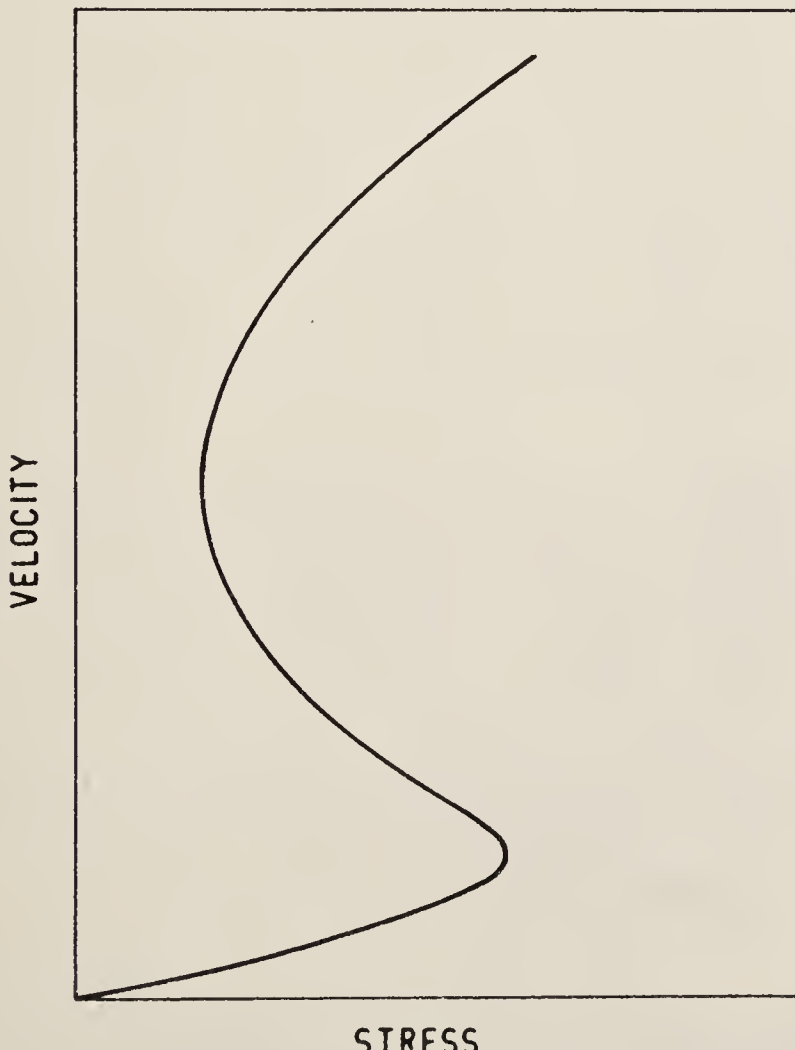


Figure 2. Schematic of dislocation velocity versus stress.

Initially, when the circuit is switched on, both i and the voltage v will be zero. After switching on, the system will evolve towards an operating condition where the load line (applied current) intersects the device characteristics. The device characteristics will however, evolve with the plastic charge (plastic strain) as shown in figure 3 which shows that initially the load line intersects the device characteristics in a region where the device exhibits a positive slope (curve a). Hence the circuit will be stable and no oscillations will be seen. As some 'plastic current' flows through the device D, its characteristics evolve through curves b and c. The load line then intersects curve c in a negative slope region and hence the circuit is unstable and shows oscillations. Later, when the characteristics evolve to curve d, the oscillations will cease.

In order to simulate such behaviour, a tunnel diode was used to mimic the negative slope characteristics of the material. The circuit schematic is shown in figure 4. The capacitor C represents the compliance of the specimen. The voltage across the capacitor is buffered by OPAMP A1 and suitably amplified by A2. The output of A2 is applied to a tunnel diode TD. The current drawn by the tunnel diode is sensed by A3 and the output of A3 represents the dislocation velocity. OPAMP A4 acts as an integrator and its output represents the plastic strain. The output of A6 represents the dislocation density. The outputs of A3 and A6 are multiplied by the multiplier M whose output controls the current ('plastic current') through the transistor T. The work hardening effect is incorporated through A5 whose output subtracts from the voltage across the capacitor.

The curve in figure 5 was obtained using the circuit described above. It can be seen that the features of a tensile test curve namely the initial yield drop, the delayed onset of serrations and the serrations themselves are all manifested in the curve. Several different biasing conditions were tried and the results showed that the simulation was faithful

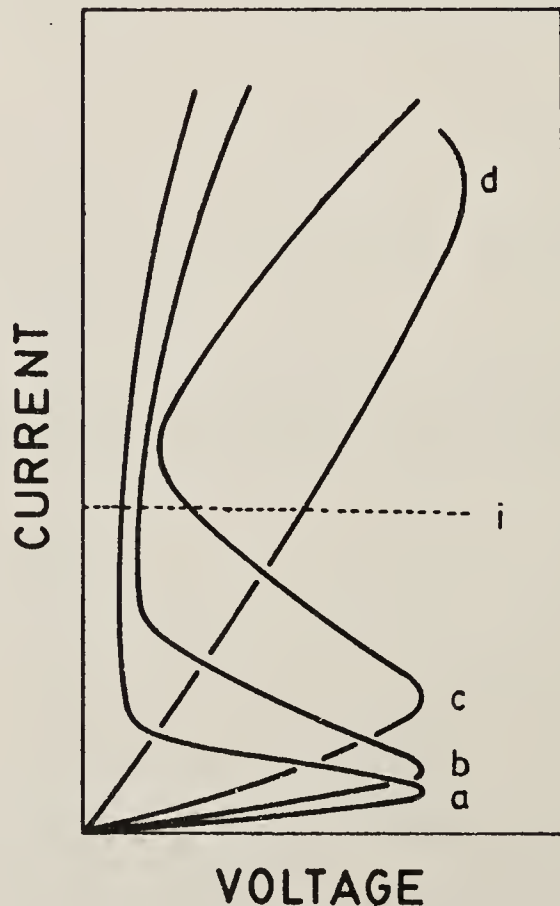


Figure 3. Evolution of the material characteristics with plastic strain. The curves a, b, c and d represent the material characteristics as the specimen is strained. The dotted line is the applied strain rate.

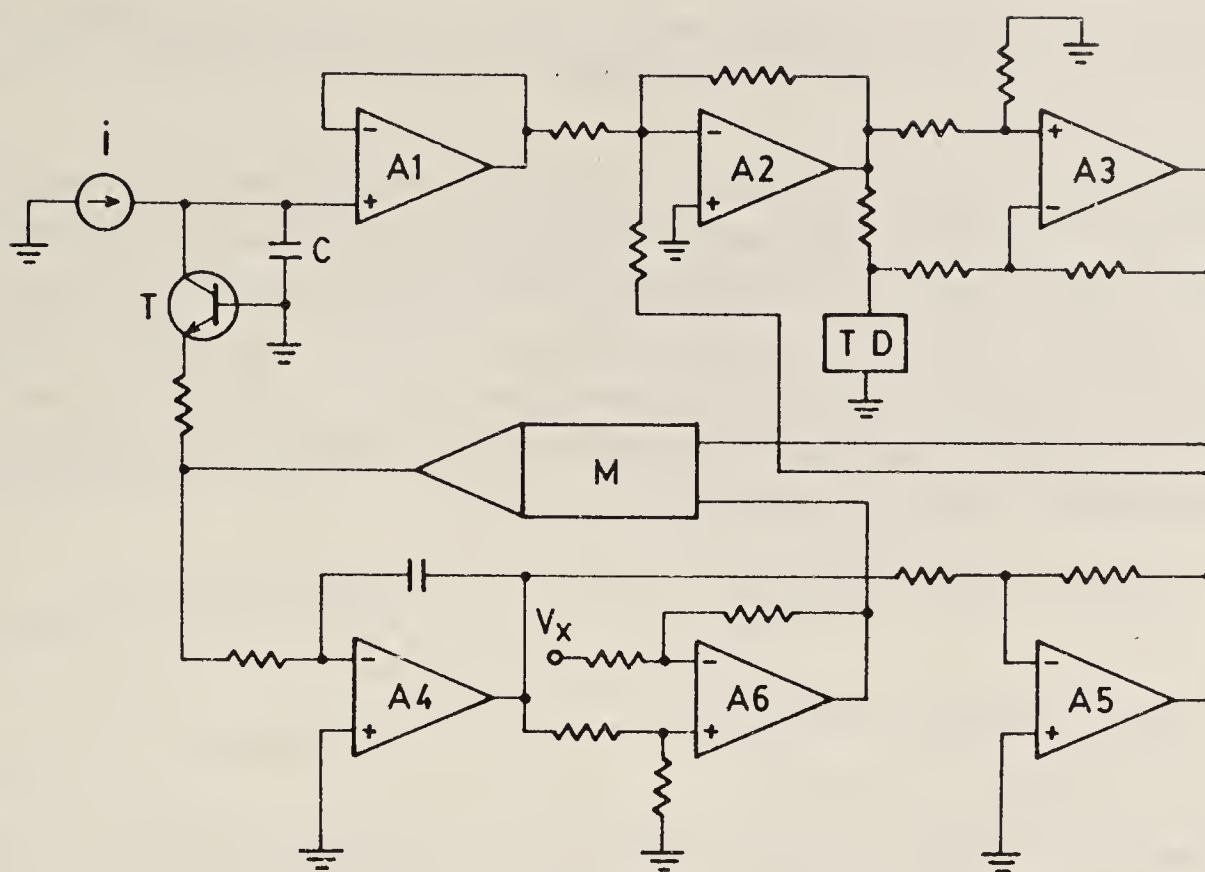


Figure 4. Circuit schematic for the analog computer.

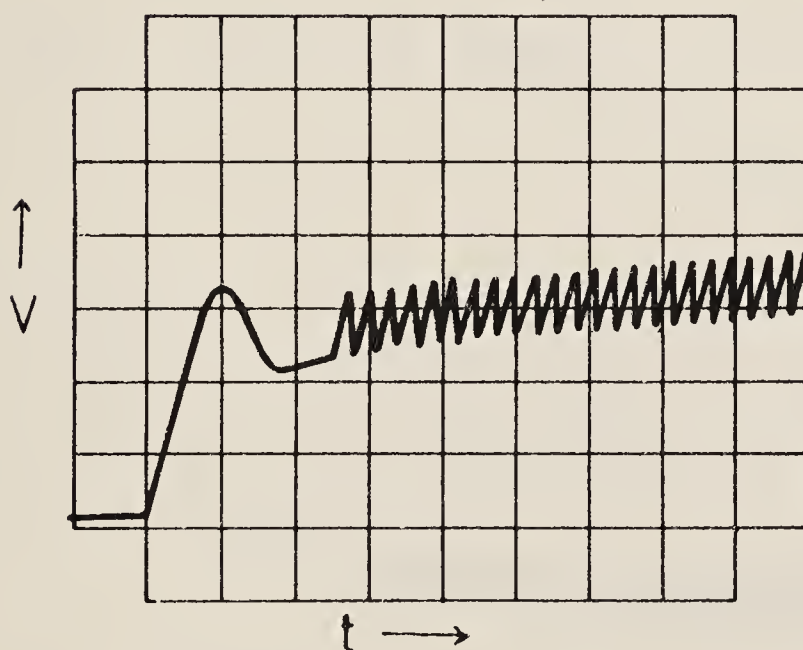


Figure 5. Output of the analog computer when the circuit is biased in the negative resistance region.

except for details of pulse shape, frequency and amplitude. These details cannot be reproduced by a circuit in which some necessary simplifications are made. Two major simplifications are the assumption that the dislocation density follows (6) with a relatively small value of B (compared to reality) and the assumption that m is unity in (7).

One major drawback of the above model is that it ignores the effects of fluctuations in the dislocation density and velocity. This is considered in the next section.

4. Role of noise

The few models available for serrated yielding (Malygin 1973; Kubin *et al* 1982; Neelakantan and Venkataraman 1983) all predict regular serrations whereas the

observed ones are usually irregular and occur in various types (Pink and Grinberg 1981). In this section, a realistic simulation of the various types of serrations is described.

We start with equations (3), (4), (5) and (7). Using a three-piece linear approximation to the S-shaped σ - u curve, the system of equations describing the phenomenon was solved numerically. However, during the straining, dislocations are not only born and annihilated but also temporarily immobilized as well as unlocked. The dislocation velocity is also a random variable as it depends on thermal interactions with the lattice etc. To take into account the fluctuations in these quantities, the dislocation density and velocity are made random according to

$$u(\sigma) = \langle u(\sigma) \rangle + \beta(\sigma) \eta, \quad (8)$$

and

$$\rho(\varepsilon_p) = \langle \rho(\varepsilon_p) \rangle + \gamma(\varepsilon_p) \eta, \quad (9)$$

where η is a fluctuating quantity.

A wide variety of tensile test curves have been simulated and figures 6 and 7 offer a selection of the results. The various types of serrations reported in the literature have

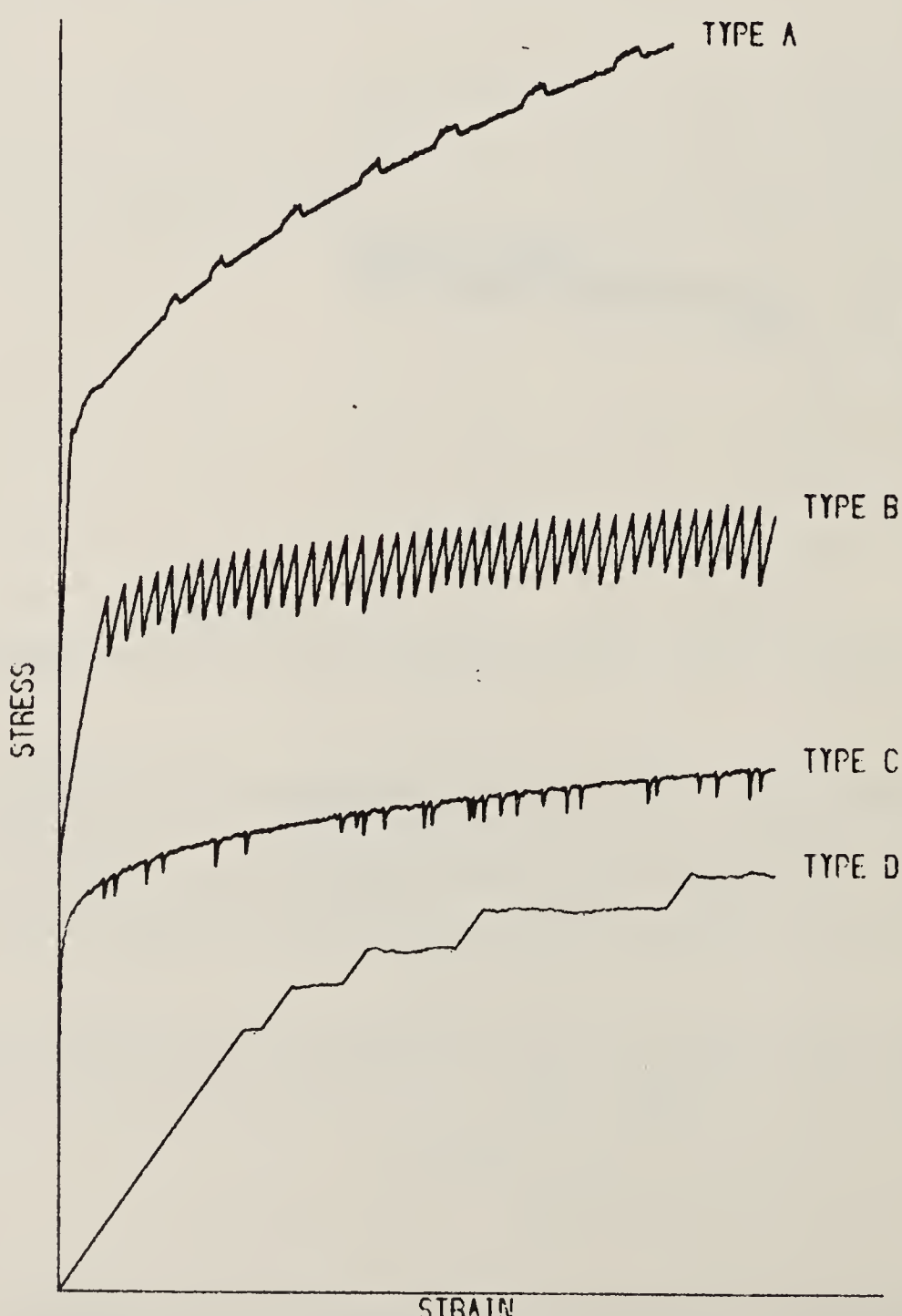


Figure 6. Various types of serrations obtained by numerical simulation.

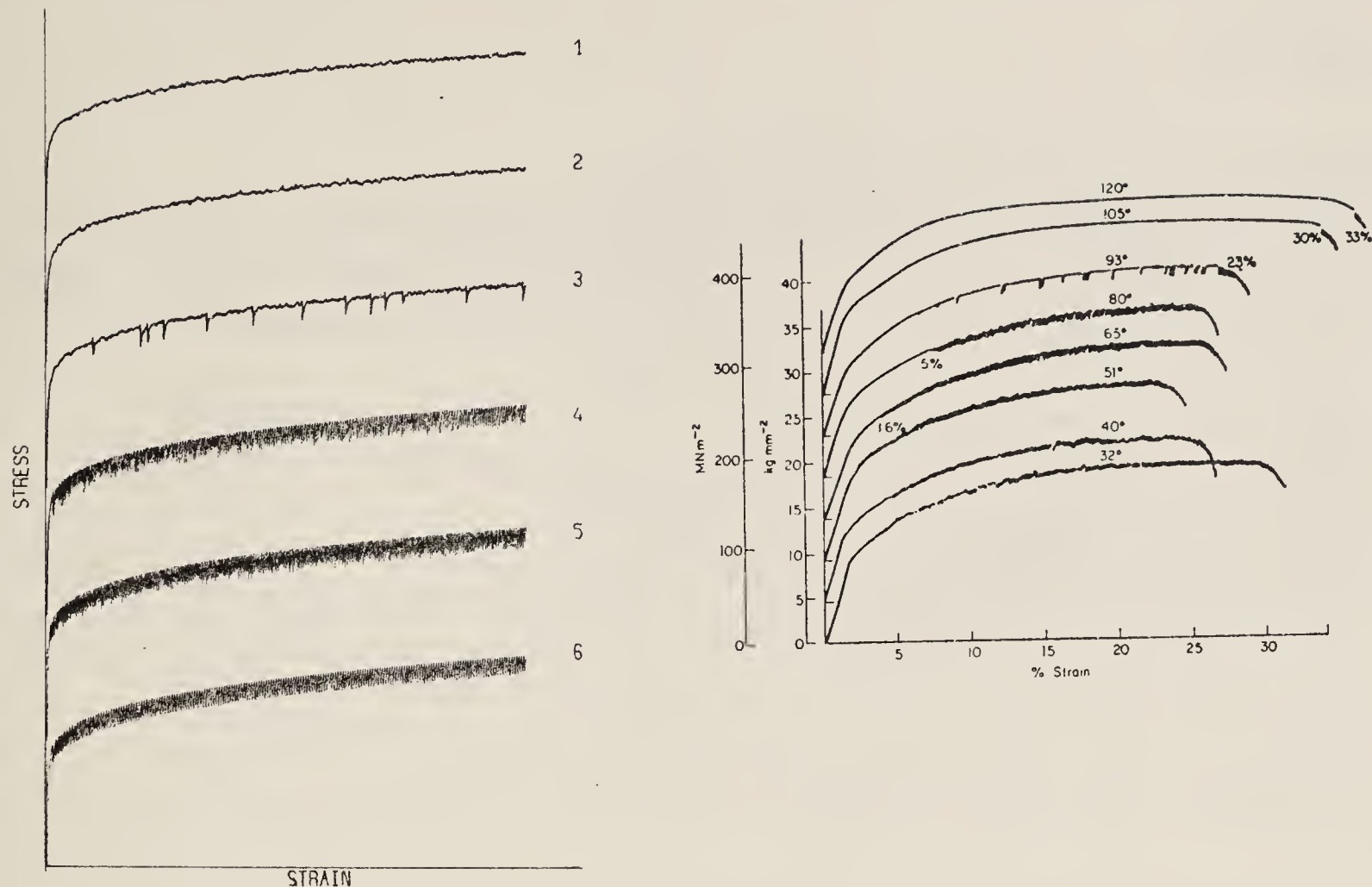


Figure 7. On the left are simulated curves. Curve 6 is for the same conditions as curve 4 but without noise. On the right are the observed curves for an Al-Mg alloy (Hall 1970).

been simulated in figure 6. The shapes depend upon the point of intersection of the load line with the material characteristics (among other factors). If the bias is near the threshold of oscillations, noise triggers random repeated yields (type C in figure 6). Figure 7 shows a family of curves corresponding to a situation where the strain rate is held constant but the temperature is varied. The similarity to observed patterns is striking.

5. Conclusions

A model for serrated yielding behaviour has been presented. Simulations on an analog computer using this model results in serrations which are regular. However, the inclusion of fluctuations in dislocation density and velocity refines the model to the extent that the simulated curves are very close to actual observed tensile test curves.

More than mimicking reality, the message is that the random aspects of serrations need to be studied and understood. Attention must be paid to spatial inhomogeneity also.

Acknowledgement

The author wishes to thank Dr G Venkataraman for suggesting the problem and for innumerable discussion and constant encouragement.

References

- Bergstrom Y and Roberts W 1973 *Acta Metall.* **21** 741
Brindley B and Worthington P J 1970 *Metall. Rev.* **15** 101
Cottrell A H 1953 *Dislocations and plastic flow in crystals* (Oxford: Clarendon Press)
Cottrell A H and Bilby B A 1949 *Proc. Phys. Soc.* **A62** 49
Hall E O 1970 *Yield point phenomena in metals and alloys* (New York: Plenum)
Keh A S, Nakada Y and Leslie W C 1968 in *Dislocation dynamics* (eds) A H Rosenfield, G T Hahn, A L Bement and R I Jafee (New York: McGraw Hill) p. 381
Kubin L P, Ph. Spiesser and Estrin Y 1982 *Acta Metall.* **30** 385
Malygin G A 1973 *Phys. Status Solidi.* **A15** 51
Nabarro F R N, Basinski Z S and Holt D B 1964 *Adv. Phys.* **13** 193
Neelakantan K and Venkataraman G 1983 *Acta. Metall.* **31** 77
Neelakantan K and Venkataraman G 1986 (to be published)
Pink E and Grinberg A 1981 *Mat. Sci. Eng.* **51** 1

An absolute method for the determination of surface tension of liquids using pendent drop profiles

S RAMESH BABU

Department of Metallurgy, Indian Institute of Science, Bangalore 560 012, India

Abstract. Drop formation at conical tips which is of relevance to metallurgists is investigated based on the principle of minimization of free energy using the variational approach. The dimensionless governing equations for drop profiles are computer solved using the fourth order Runge-Kutta method. For different cone angles, the theoretical plots of X_T and Z_T vs their ratio, are statistically analyzed, where X_T and Z_T are the dimensionless x and z coordinates of the drop profile at a plane at the conical tip, perpendicular to the axis of symmetry. Based on the mathematical description of these curves, an absolute method has been proposed for the determination of surface tension of liquids, which is shown to be preferable in comparison with the earlier pendent-drop profile methods.

Keywords. Surface tension; drop profiles; regression analysis; Runge-Kutta method

1. Introduction

The importance of the understanding of interfacial phenomena in many metallurgical processes has been rightly recognized (Richardson 1973, 1974; Szekeley 1979). For any study pertaining to interfacial phenomena, a good knowledge of the interfacial tension/surface tension of liquids is indispensable. Therefore, the methods available for the determination of this important physical property warrant considerable attention. While there are a number of methods available for this purpose (Paday 1969), very few methods are applicable for the determination of surface tension of liquid metals. Among these, White (1962) recommends the pendent drop profile method as most suitable. Again, among the various versions of the pendent drop profile methods (Hartland and Hartley 1976), the method proposed originally by Andreas *et al* (1938) which has subsequently been refined, particularly with the advent of modern fast and reliable computing facilities (Stauffer 1965; Winkel 1965), is recommended for accurate work. While the pendent drops at capillary tips have been investigated since the time of Rayleigh, excepting a simple dimensional analysis by Brown and McCormick (1948) that lead to a comparative method for the surface tension determination, no other significant work on drop formation at conical tips has appeared in literature. It may be mentioned that the drop formation studies at conical tips can also lead to an understanding of drop formation at the tip of melting rods, which will be of relevance to metallurgists as in the area of ESR process. The computer-aided analysis of drop formation at conical tips leading to an absolute method for the determination of surface tension of liquids using pendent drop profiles, is discussed in this paper.

2. Model

The principle of minimization of free energy has been used to develop a model to predict the pendent drop profiles at conical tips (see figure 1) using the 'variational approach' (Ramesh Babu 1985a). The governing equations, in dimensionless form are given by

$$\frac{d\theta}{dS} = \left(\frac{2}{B}\right) - \left(\sin\theta/X\right) - Z, \quad (1)$$

$$\frac{dX}{dS} = \cos\theta, \quad (2)$$

$$\frac{dZ}{dS} = \sin\theta, \quad (3)$$

$$\frac{dV}{dS} = \pi X^2 \sin\theta. \quad (4)$$

With the following boundary conditions

$$\text{at } Z = 0, X = 0; \frac{dX}{dZ} = \infty \text{ and } V = 0, \quad (5)$$

$$\text{at } Z = Z_0, \frac{dX}{dZ} = \tan\beta, \quad (6)$$

where, $X = x C^{1/2}$; $Z = z C^{1/2}$; $S = s C^{1/2}$; $V = v C^{1/2}$; $B = b C^{1/2}$; $C = g(\rho_d - \rho_L)/\gamma$; b = radius of curvature at the drop apex, s = arc length, ρ_d = density of the drop, and ρ_L = density of the surrounding fluid, γ = interfacial tension at the drop-fluid interface and v = drop volume.

The same governing equations have also been shown to be deducible by an alternate approach using the concept of double buoyancy effect (Ramesh Babu 1984). Choosing a particular value of B , equations (1) to (4), together with the boundary conditions, equations (5) to (6), were solved simultaneously by the 'fourth order Runge-Kutta procedure', for which a computer program was developed ensuring an accuracy better than a part per million in the computed values (Ramesh Babu 1985b). The method of 'Regula-Falsi' was also incorporated in the program for calculating the interpolated values of interest. The flow chart highlighting the programme logic is given in figure 2.

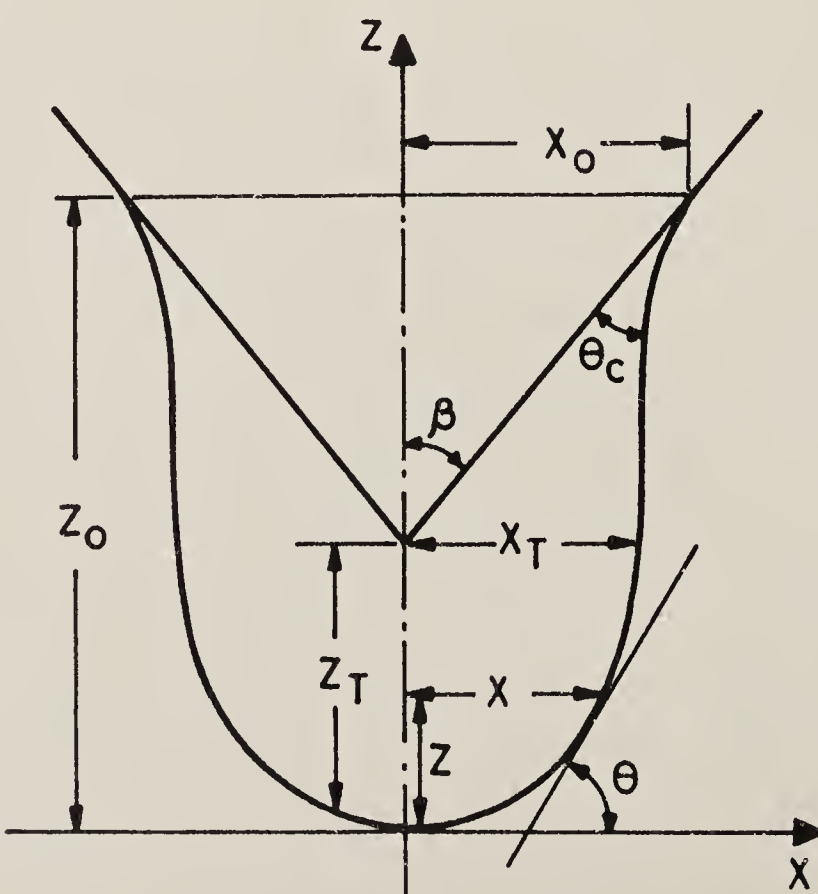


Figure 1. Axisymmetric pendent liquid drop at an infinite conical tip.

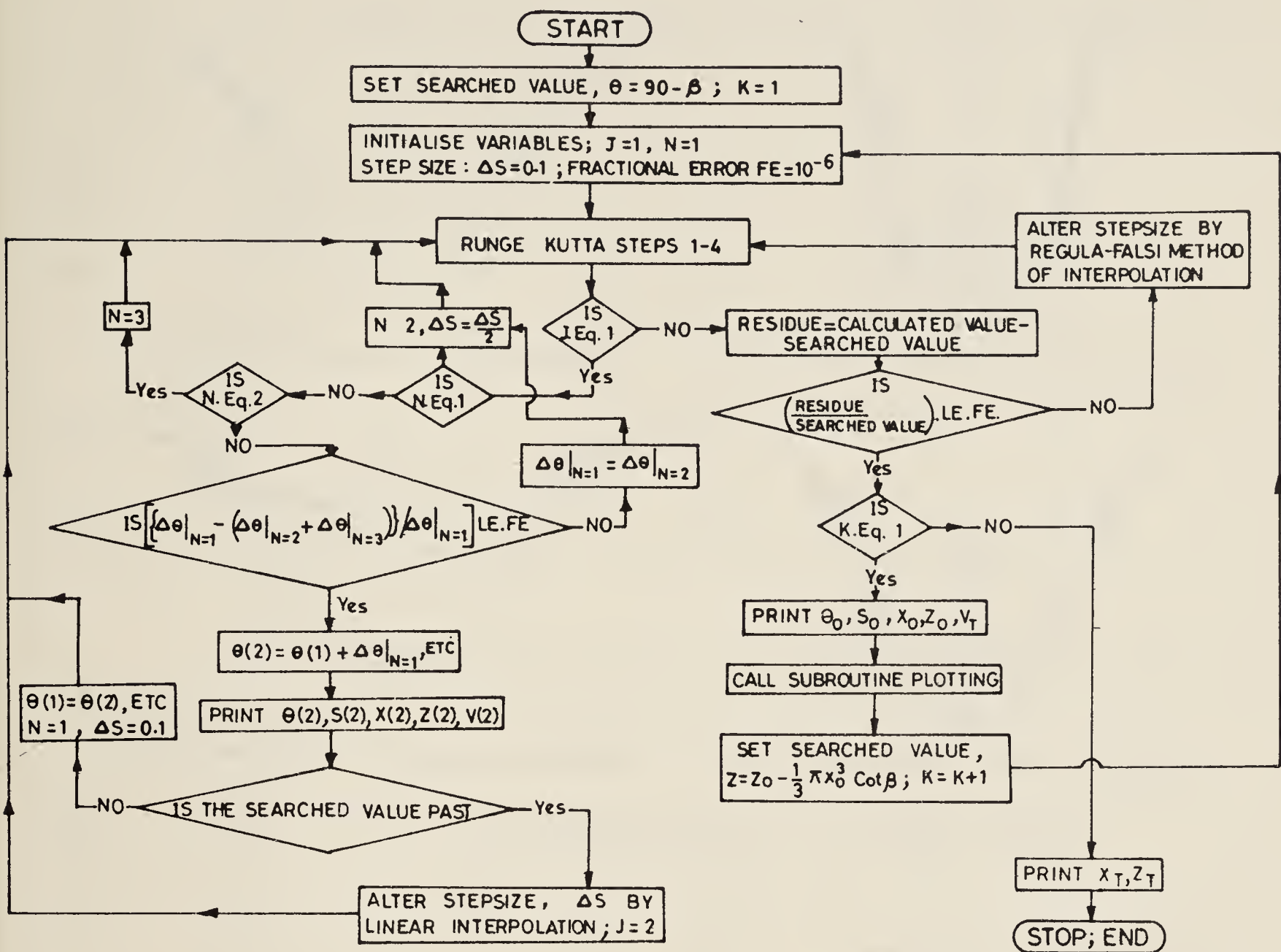


Figure 2. Flow chart highlighting the programme logic for generating pendent drop profiles at conical tips.

The maximum drop volume was obtained numerically. The significance of the numerical results obtained for various cone angles is discussed elsewhere (Ramesh Babu 1985a). The model permits the calculation of drop volume as well as to follow the changing sequence of drop profiles until the onset of instability. The sequence of drop growth at different conical tips is illustrated in figure 3.

3. Determination of surface tension

Considering the equilibrium situation of a pendent liquid drop at a conical tip as shown in figure 1, for a specified cone angle, it is possible to theoretically calculate the values of X_T corresponding to Z_T , and hence their ratio, during the drop formation until it enters the instability stage, where,

$$X_T = x_T \left(\frac{(\rho_d - \rho_L)}{\gamma} g \right)^{1/2}, \quad (7)$$

and

$$Z_T = z_T \left(\frac{(\rho_d - \rho_L)}{\gamma} g \right)^{1/2}. \quad (8)$$

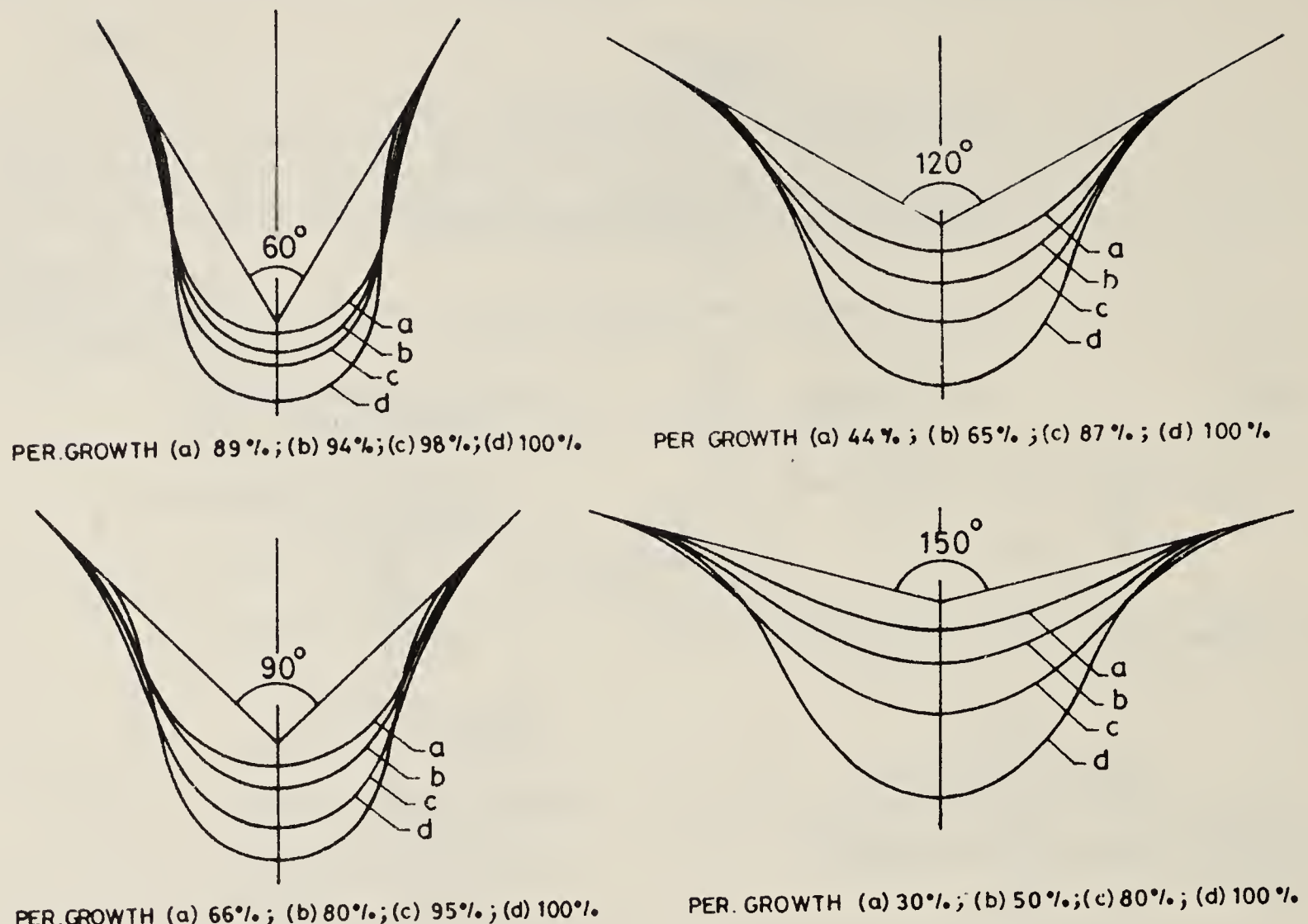


Figure 3. Sequence of drop growth at conical tips.

Dividing (8) by (7), we get

$$Z_T/X_T = z_T/x_T. \quad (9)$$

Therefore, by photographically measuring the values of x_T and z_T , in view of (9) the corresponding X_T and Z_T can be calculated. The interfacial tension can be calculated using (7) or (8).

4. Regression analysis

To facilitate quick computation of γ , it is desirable to have a relation between X_T and Z_T and their ratios. Figures 4–7 illustrate the variation of both X_T and Z_T with X_T/Z_T and Z_T/X_T in the range $0 \leq Z_T \leq Z_T^{\max}$, where, Z_T^{\max} corresponds to the critical profile enclosing the maximum drop volume, for each of the cone angles 60° , 90° , 120° and 150° . Each of these plots was statistically analyzed using a computer algorithm that has been shown to be superior even to Gauss elimination technique upto fifth order polynomial (Ramesh Babu 1985c). The coefficient of variation defined below was used as the criterion for choosing the best fit polynomial.

$$CV = \frac{SD}{\bar{y}} \times 100; \quad SD = \left(\frac{\sum_{i=1}^n (y_{LF} - y_i)^2}{n - (K + 1)} \right)^{1/2}, \quad (10)$$

where, SD is the standard deviation, y_{LF} is the least square fitted value of y_i , \bar{y} is the average of y_i and K is the degree of the polynomial fitted onto n data points.

Table 1. Summary of the regression analysis of the curves X_T vs X_T/Z_T and Z_T vs X_T/Z_T

Curve investigated		X_T vs X_T/Z_T			Z_T vs X_T/Z_T			
Cone angle	Range of X_T/Z_T	n	K	PEM (%)	CV (%)	K	PEM (%)	CV (%)
60°	1.34–6.60	16	2	4.52	1.03	2	87.34	11.992
	1.34–2.88	12	5	0.32	0.239	2	3.59	1.456
90°	0.97–3.48	22	1	2.66	1.387	2	25.31	4.059
	0.97–3.14	21	2	2.48	1.223	2	15.96	3.011
120°	0.90–18.39	27	2	44.91	6.076	2	2402.30	41.84
	1.11–3.61	19	2	2.03	1.046	2	16.79	3.172
150°	0.95–23.16	24	2	30.68	5.575	2	2355.5	49.87
	1.08–5.21	17	2	3.44	2.003	2	41.56	7.52

Table 2. Summary of the regression analysis of the curves X_T vs Z_T/X_T and Z_T vs Z_T/X_T

Curve investigated		X_T vs Z_T/X_T			Z_T vs Z_T/X_T			
Cone angle	Range of Z_T/X_T	n	K	PEM (%)	CV (%)	K	PEM (%)	CV (%)
60°	0.15–0.75	16	2	0.27	0.175	2	26.78	1.782
	0.35–0.75	12	2	0.19	0.114	2	1.17	0.371
90°	0.28–1.03	22	2	2.22	0.823	5	6.88	0.785
	0.32–1.03	21	2	1.84	0.727	5	4.11	0.558
120°	0.05–1.12	27	2	26.16	3.567	1	706.65	5.291
	0.28–0.90	19	2	1.80	0.705	5	3.90	0.518
150°	0.04–1.05	24	2	47.58	6.365	5	599.96	5.399
	0.19–0.93	17	2	4.64	1.887	5	5.31	0.668

Since the analysis showed too large values of CV, the analysis was repeated by reducing the range. The results are summarized in tables 1 and 2. The significant improvement in the CV value upon reducing the range is obvious. It could also be seen that the descriptions of the plots X_T vs Z_T/X_T and Z_T vs Z_T/X_T are far more desirable than the other two. The coefficients of the best fit polynomial to these curves are tabulated in tables 3 and 4. Utilizing these results, tables have been prepared in intervals of 0.001 of Z_T/X_T over a sufficiently wide range of practical utility for each of the 4 cone angles.

5. Results and discussion

A common feature of all the curves (see figures 4–7) is that the slope of the curve increases with cone angle, which suggests that a 60° cone is preferable. While the plots of Z_T vs Z_T/X_T show a uniform gradient throughout, the plots of Z_T vs X_T/Z_T show steep gradients in the range of practical interest. The plots of X_T vs Z_T/X_T indicate that

Table 3. Coefficients of the best fit polynomial to the curve X_T vs Z_T/X_T

Cone angle	Range of Z_T/X_T	CV (%)	$X_T = A_1 + A_2(Z_T/X_T) + A_3(Z_T/X_T)^2$		
			A_1	A_2	A_3
60°	0.35–0.75	0.114	-0.00054	1.91325	-1.11559
90°	0.32–1.03	0.727	0.11320	2.01519	-1.10914
120°	0.28–0.90	0.705	0.17625	2.73173	-1.67780
150°	0.19–0.93	1.887	0.48231	3.59968	-2.49335

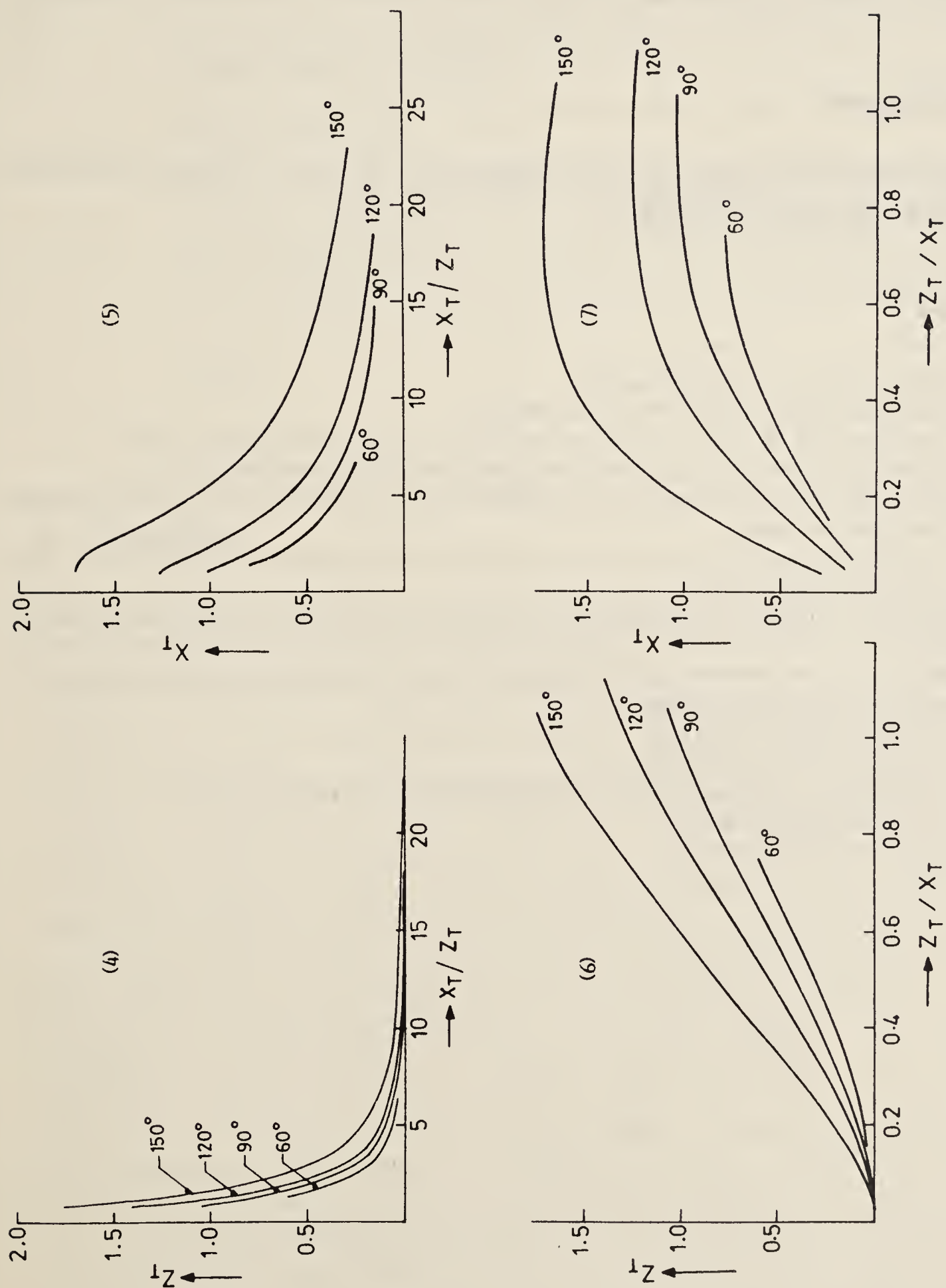
Table 4. Coefficients of the best fit polynomial to the curve Z_T vs Z_T/X_T

Cone angle	Range of Z_T/X_T	CV (%)	$Z_T = A_1 + A_2(Z_T/X_T) + A_3(Z_T/X_T)^2 + A_4(Z_T/X_T)^3 + A_5(Z_T/X_T)^4 + A_6(Z_T/X_T)^5$					
			A_1	A_2	A_3	A_4	A_5	A_6
60°	0.35–0.75	0.371	-0.16413	0.96421	0.08756	—	—	—
90°	0.32–1.03	0.558	-0.22483	1.31150	-0.00061	-0.00056	-0.00003	-0.05832
120°	0.28–0.90	0.518	-0.23624	1.61267	-0.00063	-0.00068	-0.00006	-0.09064
150°	0.19–0.93	0.668	-0.21477	2.09723	0.00012	-0.00129	-0.00045	-0.19713

over a wide range of Z_T/X_T the curves are almost parallel to the x -axis, hence errors in the measured Z_T/X_T will not significantly affect the accuracy of the corresponding X_T value.

The proposed method has several distinct advantages over the other methods employing the pendent drop profiles at capillary tips (Padday 1969):

- (i) The method is free from empiricism, as it is based on a sound theory;
- (ii) The well-defined conical tip inside the drop enables accurate measurements of x_T and z_T ;
- (iii) The measurement of the linear dimensions being independent of each other, the undesirable cascading error in the method of selected planes (Andreas *et al* 1938) is obviated;
- (iv) A single cone is sufficient to form drops of desirable shapes. This is in sharp contrast to the extra care required in selecting a suitable capillary to obtain a desired drop shape, in all the earlier methods.
- (v) Since different drop shapes could be obtained from a single cone, a number of measurements of x_T and z_T could be made, providing as many cross checks for γ as required. In addition, each set of x_T and z_T values permits the calculation of γ by two independent methods vide (7) and (8).
- (vi) Formation of drops at conical tips is much simpler and easier compared to any other method of drop formation reported in literature.



Figures 4-7. 4. Variation of Z_T with X_T/Z_T . 5. Variation of X_T with X_T/Z_T . 6. Variation of Z_T with Z_T/X_T . 7. Variation of X_T with Z_T/X_T .

The design of a simple experimental set-up to form drops at conical tips under desired controlled flow rates has been described elsewhere (Ramesh Babu 1985b). Drops could also be formed at conical tips by immersing a metal cone in the liquid bath and gradually moving it away from the liquid surface or vice versa. This method of drop formation is particularly suited for liquid metals. In view of the several advantages of the proposed method, application to liquid metals deserves considerable attention.

Acknowledgement

The financial assistance received from the Department of Atomic Energy, Government of India is gratefully acknowledged.

References

- Andreas J M et al 1938 *J. Phys. Chem.* **42** 1001
Brown R C and McCormick H 1948 *Philos. Mag.* **39** 420
Hartland S and Hartley R W 1976 *Axi-symmetric fluid-liquid interfaces* (Amsterdam: Elsevier)
Padday J F 1969 *Surf. Colloid Sci.* (ed.) E Matijevic (New York: Wiley Interscience) Vol. 1
Ramesh Babu S 1984 *Proc. 29th Congress of The Indian Society of Theoretical and Applied Mechanics, KREC, Surathkal (to appear)*
Ramesh Babu S 1985a *Proc. Int. Conf. on progress in metallurgy; Fundamental and applied aspects*, Indian Institute of Technology, Kanpur
Ramesh Babu S 1985b *Studies on drop formation at conical tips*, Ph.D. Thesis, Indian Institute of Science, Bangalore
Ramesh Babu S 1985c *An alternative algorithm for least square polynomial fitting* (unpublished research)
Richardson F D 1973 *Trans. ISIJ* **13** 369
Richardson F D 1974 *Trans. ISIJ* **14** 1
Stauffer C E 1965 *J. Phys. Chem.* **69** 1933
Szekely J 1979 *Fluid flow phenomena in metals processing* (New York: Academic Press)
White D W G 1962 *Trans. Q.* **55** 757
Winkel D 1965 *J. Phys. Chem.* **69** 348

Personal computer-based CAMAC system for data acquisition

S K KATARIA, V S RAMAMURTHY, V G GAONKAR and
SURENDRA KUMAR*

Nuclear Physics Division and *Electronics Division, Bhabha Atomic Research Centre,
Bombay 400 085, India

Abstract. A single board auxiliary CAMAC crate controller for a Z80-A based personal computer ZX-spectrum to drive the CAMAC crate housing multiple ADC, TDC, DAC and 16 I/O ports has been developed. The CAMAC crate controller used in this system is of A2 type which supports multiple auxiliary crate controllers. A CAMAC exerciser/training software for the use of CAMAC commands in process control as well as data acquisition has been developed.

Keywords. Personal computer; Z80-A CPU; CAMAC; auxiliary crate controller; CAMAC trainer software.

1. Introduction

Data gathering and analysis in experimental sciences has been undergoing a major revolution in the last quarter of this century due to the appearance of low cost digital computers. It has significantly altered the instrumentation around an accelerator or a nuclear research reactor, which are being increasingly made with built-in microprocessor (μP). These inexpensive μP can very easily and rapidly transform the raw data into elaborate computed results in a user friendly form. We are all aware of the concept of modularity in nuclear electronics equipment. The first internationally accepted standard in nuclear electronics is the well known NIM standard. As digital information began to supplement the analogue instrumentation in nuclear environment a new standard CAMAC (computer automation in measurement, acquisition and control) was designed about a decade ago by ESONE group (EUR 4100e, 1969). It is now being widely used in industrial process control and nuclear instrumentation around a reactor or in an accelerator laboratory. A very large number of CAMAC modules e.g. intelligent crate controllers (cc), analog-to-digital converters (ADC), multichannel digital-to-analog converters (DAC), time-to-digital converters (TDC), scalers, motor controllers, are available off the shelf from a number of competitive vendors. One can easily configure spectrometer, or a multiparameter data acquisition system or an accelerator control panel using these standard CAMAC modules. The use of CAMAC-based systems is being favoured (Satyamurthy and Kataria 1984) since one can easily enhance or reconfigure the system using alternate functional units in the CAMAC crate. Kataria (1984) had earlier developed a pulse height analyzer and data analysis system based on Sinclair ZX-spectrum personal computer. In the present work we report the interfacing of the ZX-spectrum (PC) through a locally designed auxiliary crate controller (ACC). In this way, we can easily use the various standard CAMAC modules without any further hardware interfacing.

2. System configuration

The present CAMAC based data acquisition system consists of a single CAMAC crate with A2 type controller, a 12-channel ADC, an 8-channel TDC and a dataway display module. The A2 type controller supports intelligent modules and auxiliary crate controllers within a single crate for local data processing and control. In the present work, we report an ACC which communicates to the CAMAC dataway on the one hand and to a personal computer Sinclair ZX-spectrum on the other. Figure 1 shows the system configuration.

Personal computer ZX-spectrum is based on Z80-A, 8-bit CPU and has in-built interfaces for use of a standard TV as display unit and for an audio cassette recorder as a program/data storage device. It has its own keyboard and thermal printer. Its basic interpreter is in 16K ROM and 48K RAM is available to the user for his software. For interfacing to user equipment the Z-80 bus (address, data and control lines) is available on a 56 pin connector.

2.1 ACC design fundamentals

The ACC has been designed to fully conform to the standards described in ANSI/IEEE Std. 675-1982. This standard has been defined so that many intelligent ACC can reside in the same crate and process locally the data and control without any conflicts. The ACC functions, in conjunction with A2 type controller residing in CAMAC crate station Nos 24 and 25, on various modules residing in other normal stations, in the crate. Since the

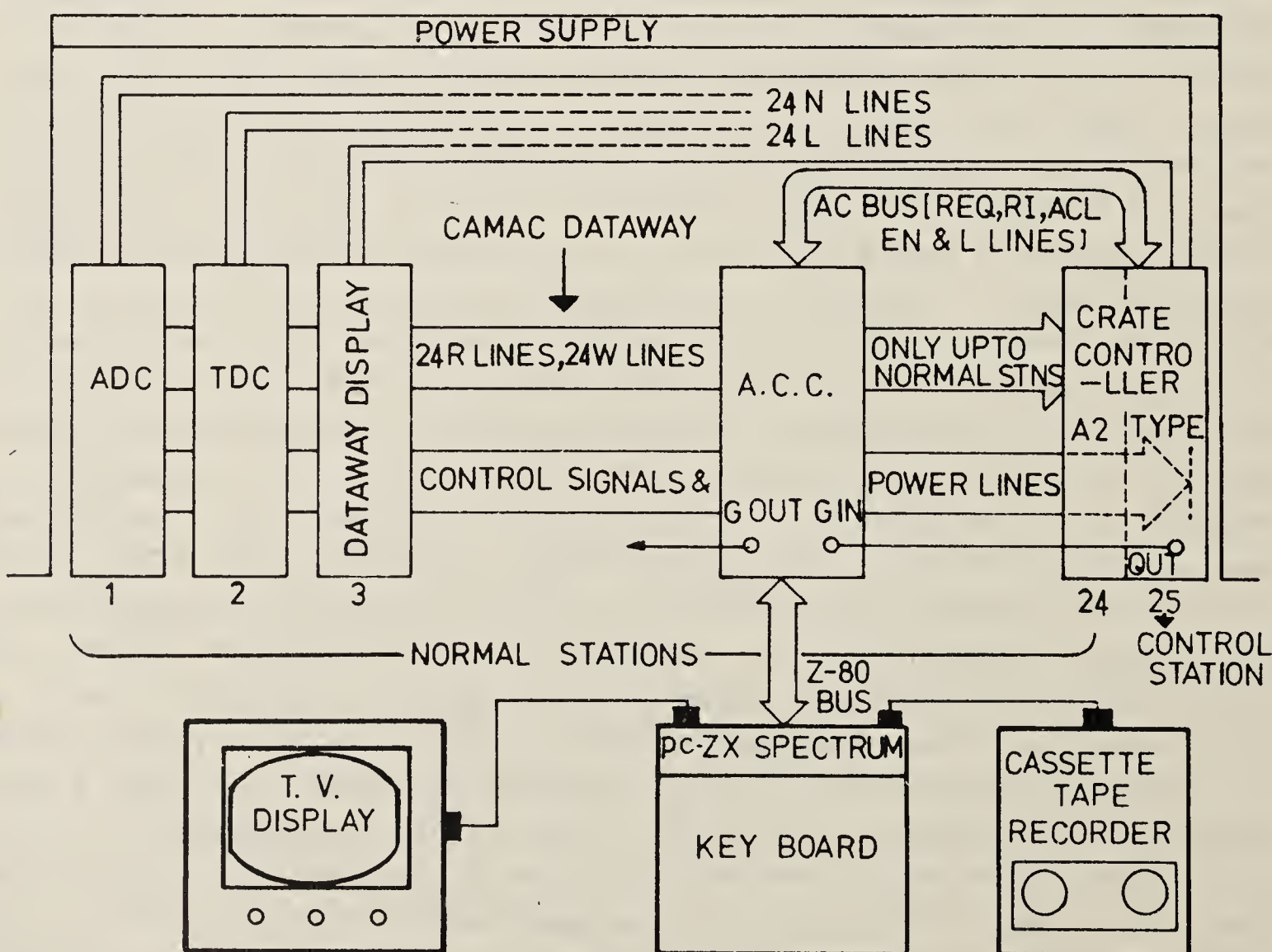


Figure 1. Typical system configuration.

facility to address or to respond to any normal station is given through the crate controller (cc) in order to accommodate ACCS, two features are required: (i) access to the N and L lines at normal stations and (ii) priority arbitration for control of dataway.

Access to the N lines is necessary to allow an ACC to issue a complete addressed command operation. Access to the L-lines is necessary for an ACC to respond to "look at me" (LAM) signals from the modules or controllers or both. Priority arbitration protocol ensures that at any time only one controller is permitted to have control of the crate. It also provides the means for assigning control of the dataway on the basis of preassigned priority. Access to the N and L lines and other signals necessary for priority arbitration protocol is provided through auxiliary controller bus (ACB) as shown in figure 2.

2.2 Hardware developments

Figure 2 shows a general block diagram of the ACC developed in-house. Data transfers over Z-80 bus is 8-bit wide and on CAMAC dataway it is 24-bit wide. As shown in the block diagram, ACC first assembles the CAMAC commands from the information received from personal computer properly in accordance with the CAMAC dataway protocol, then it raises request flag (Req) for taking command of dataway. After getting grant-in, ACC starts its dataway cycles operation. During the dataway operation, the status of X, Q and B signals are latched. During CAMAC read operation, it latches the information from R-lines, so that one can transfer the 24-bit data to personal computer byte by byte later on. Wired OR (VECTOR) interrupt facility is provided for L lines, so that the personal computer can respond to the request from the modules for servicing. In the present system, the data are being acquired in interrupt mode.

In the present design, two modes of priority arbitration protocol have been provided (i) request/grant (R/G) and (ii) auxiliary controller lockout (ACL); the preferred mode is the R/G protocol. In this mode, when a request is raised, it checks for grant-in signal. If grant-in is present, busy and request inhibit signals are generated and the sequence of timing signals for dataway operation is started. If grant-in is not present i.e. dataway is already in command of some other controller, the auxiliary controller requesting dataway, waits for that operation to be completed. In R/G protocol, this type of delay is to be accounted for. In ACL mode, where a controller cannot wait for this delay, the dataway operation of lower priority controller will be aborted and dataway will be given to higher priority controller. The lower priority controller will resume its operation subsequently.

3. Functional description

ACC receives the CAMAC commands operation to be performed on CAMAC modules from personal computer. During addressed command operation, it generates the 5-bit binary code (EN) for the station number associated with the command and then transmits it via the EN lines of the ACB. The cc receives this station number code (EN) decodes it and then addresses the appropriate normal station. AC also establishes other necessary signals on the B, AN, FN, S1 and S2 lines appropriate for the command operation to be performed and to define the timing of the operation. During addressed command operations involving data, the ACC transmits or receives data via W or R lines. The

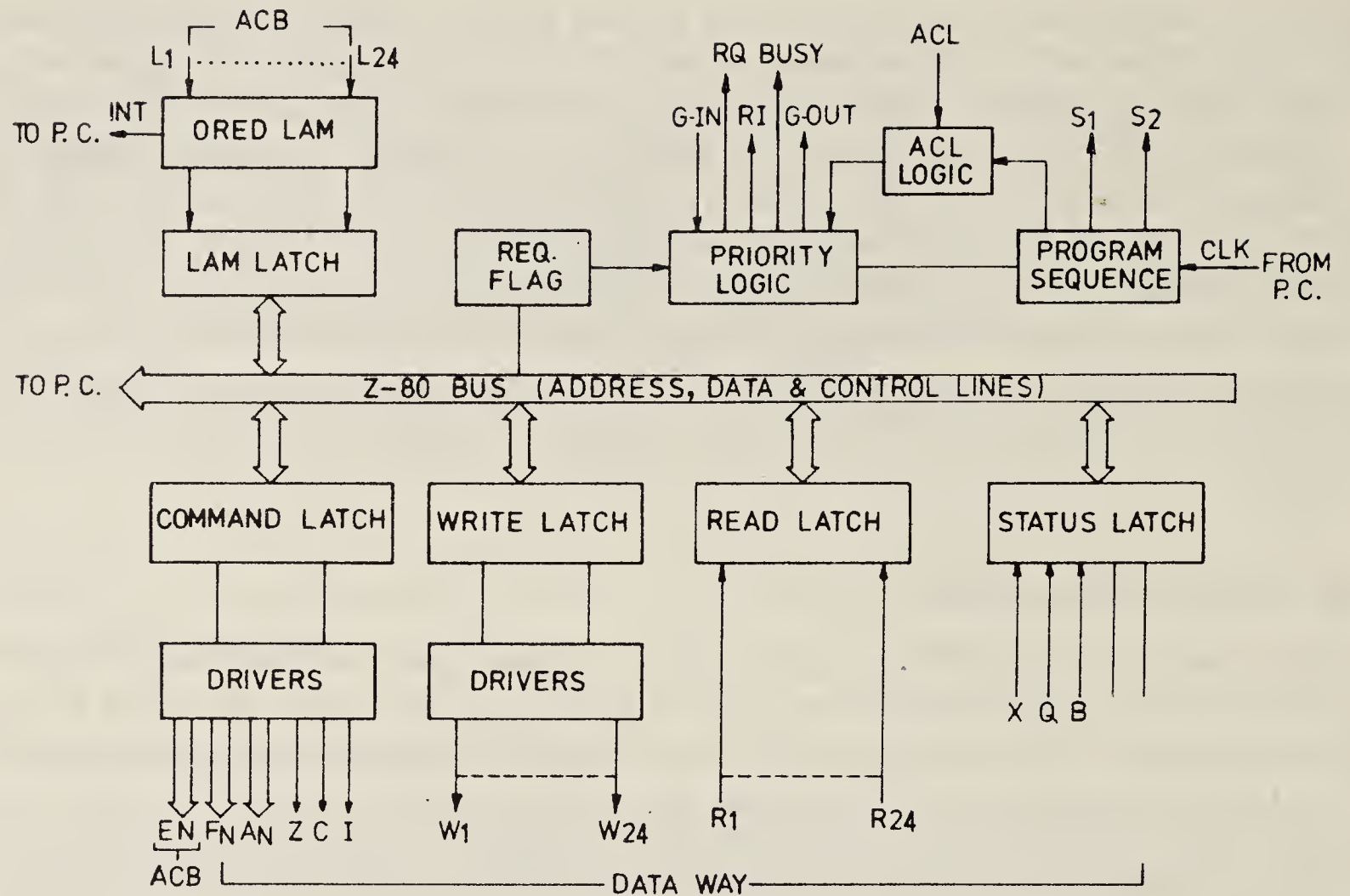


Figure 2. Block diagram of auxiliary crate controller.

unaddressed operations, e.g. dataway initialize Z and dataway clear C, do not require use of EN-signals of the ACB. But ACC still establishes the necessary signals B, S1 and S2 and Z or C lines. Figure 3 shows the sequence of signals for an ACC to gain control of dataway for an addressed command operation.

3.1 Software developments

A general purpose software for training in the use of various CAMAC commands has been developed. In the help mode (H), the software displays at a glance all the CAMAC commands e.g. common control commands Z, C, I and dataway commands. In debug-mode (D), one can execute each CAMAC command one by one, using friendly mnemonic symbols (R for read, W for write) and thus debug the CAMAC modules and the associated software. In one session with the training software, one achieves remarkable familiarity with CAMAC system. In the extended mode (X), one can easily write CAMAC subroutines for data acquisition from multiple units in CAMAC crate and debug them extensively from both the software and hardware aspects. This software is written in BASIC language, and can therefore be easily transported to other personal computers.

A dedicated software package for multiparameter data acquisition using a 12-channel nuclear ADC and a 8 channel TDC and display and test module has also been written. In order to achieve faster rate of data acquisition, parts of the software are in machine code e.g. the interrupt service routines, real time one and two parameter data display routines etc. The main program controlling the data acquisition, and setting up the various initial conditions e.g. (choosing the no. of ADC, TDC) is in BASIC language, and has been planned carefully keeping in view the needs of the experimentalists. After defining the parameters of an experiment, the data acquisition is carried out using

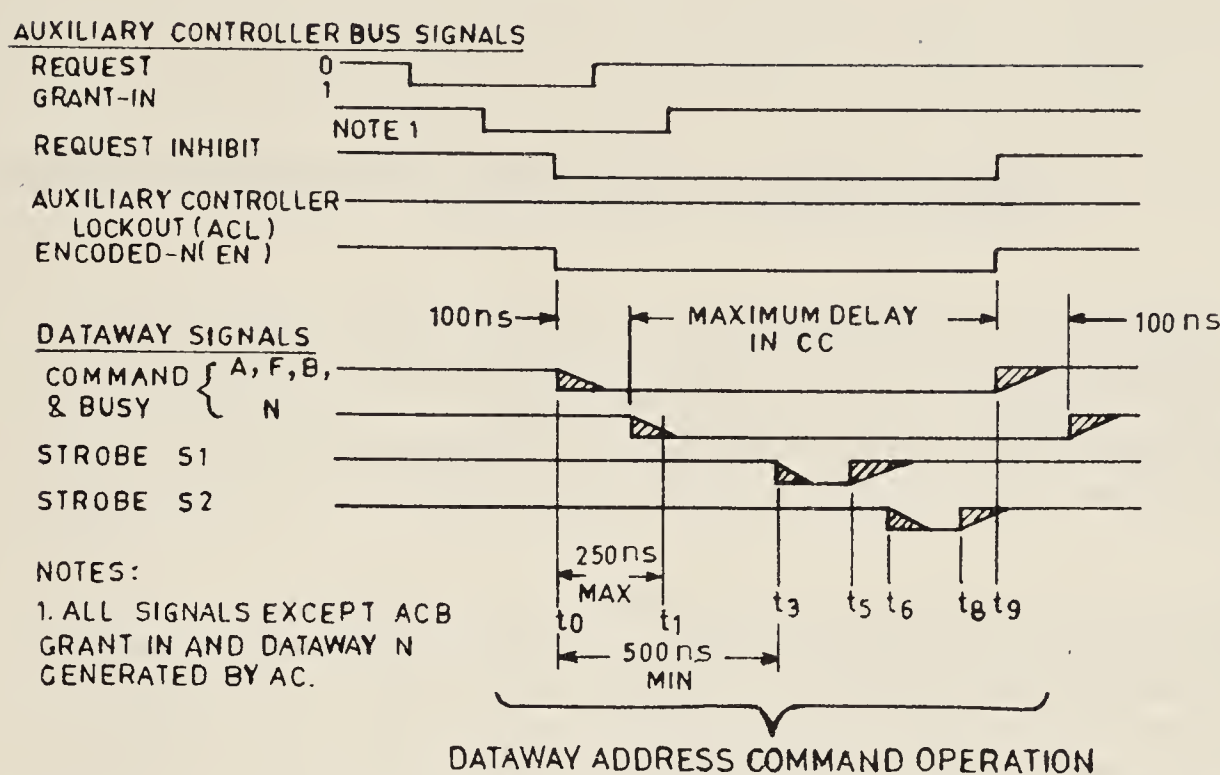


Figure 3. Sequence of signals for an ACC to gain control of dataway for an addressed command operation.

interrupt facilities; and data display and control is carried out in the background. A number of BASIC routines for spectrum analysis are also available and further they are easy to modify to suit the individual requirements of the experimentalists. At present, the acquired data can be stored only on audio cassette tape at a speed of 1100 baud rate.

Acknowledgement

We are thankful to Dr S S Kapoor for encouragement.

References

- CAMAC 1969 A modular instrumentation system for data handling, ESONE report EUR4100
- Satyamurthy N S and Kataria S K 1984 Keynote address in RCA Workshop of IAEA on the "Use of microprocessors in research reactor utilisation", BARC/I-806
- Kataria S K 1984 Personal computers, p. 323, BARC/I-806

Image analysis system for quantitative metallography

V K CHADDA, D G JOSHI, S N MURTHY, S V KULGOD,
C BABURAO*, D K BHATTACHARYA* and BALDEV RAJ*

Reactor Control Division, Bhabha Atomic Research Centre, Trombay, Bombay 400 085, India

* Radio Metallurgy Programme, Indira Gandhi Centre for Atomic Research, Kalpakkam 603 102, India

Abstract. This paper describes a Z-80 microprocessor-based image analyzer developed for global parameter evaluation of images over a 256×256 pixel frame. It consists of a microscope, CCD scanner, 6-bit video ADC, Z-80 computer and an image display monitor. Facilities are provided for feature erosion/dilation and halo correction. The paper also presents the details of another more powerful user microprogrammable HP1000 minicomputer-based image analysis system under development. This system consists of an optical microscope/epidiascope coupled to a chalcogenide scanner. Here the 512×512 pixel image is acquired with 8-bit resolution. It provides for shading correction, auto-delineation, image processing and image analysis functions for evaluation of various basic and derived parameters.

Both the systems are software intensive and are realised according to requirements of quantitative metallography. They can also be used for analysis of images obtained in the fields of biology, medicine, geological survey, photography and space.

Keywords. Pixel; erosion; dilation; bit quad; global parameters; feature extraction; image analysis; metallography.

1. Introduction

Metallographic image analysis is essential for objective correlation of material properties with its microstructure. It is carried out by examining them under suitable electronic/optical instruments and analysing the image obtained.

A Z-80 microprocessor-based image analysis system with 256×256 pixel resolution has been developed indigenously. It provides estimation of different phases in microstructures through grey level detection (64 levels) and computation of their geometrical parameters.

An HP-1000 computer based image analysis system is also being developed with 512×512 pixel resolution incorporating facilities for image enhancement, auto-delineation, shading correction, light pen interaction and feature specific measurements.

2. Z-80-based image analysis system

A block diagram of the system is shown in figure 1 and described below:

2.1 Imaging

The image to be analyzed is obtained from samples observed under an optical microscope/epidiascope. It is projected on to the sensor array of a CCD video camera.

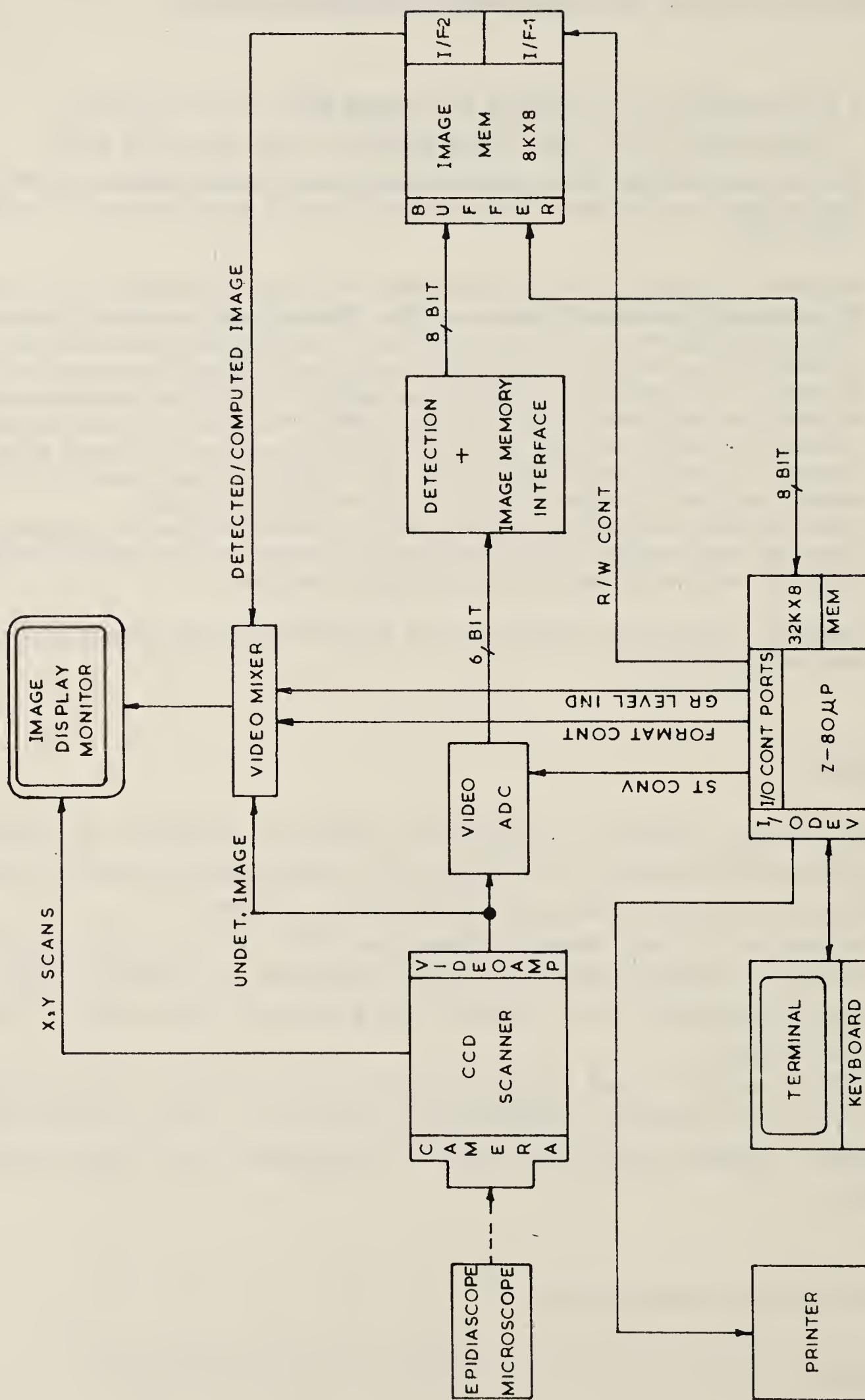


Figure 1. Block diagram of Z-80 microprocessor based Image Analyser.

For image analysis 256 lines, 256 pixel matrix is selected. The remaining part of the frame is used to display a band of 64 grey levels and two cursors indicating the selected grey slice as shown in figure 2.

2.2 Data acquisition

The scanner output is presented to a 6-bit video ADC for digitization. A simple scheme based on threshold detection was employed with upper and lower threshold levels. Detection constitutes obtaining a binary image (logic 0-1 pattern) containing selected features. Logic '1' in the binary image corresponds to pixels lying in the selected grey slice and logic '0' for the background (Jenkinson 1982).

This binary image is compacted into byte format and stored into an $8\text{ K} \times 8$ bit memory for flicker-free image display and transferred to the computer memory for analysis.

2.3 Data analysis

Image analysis is carried out for evaluation of desired basic metallographic parameters on global basis. The system has facilities for erosion, dilation and halo error correction.

2.3a Basic parameter evaluation: Here sets of 2×2 pixel patterns called bit quads are computed as shown in figure 3a. Each pixel A_0 of the binary image is scanned and its associated bit quad (A_0, A_1, A_0^N, A_1^N) is examined. These are represented as C_0, C_1, \dots, C_{15} where $C_1 = 2^3 A_1^N + 2^2 A_0^N + 2^1 A_1 + 2^0 A_0$. At each pixel position one of the 16 combinations is encountered. A table is created in the memory to determine count of each C_i over the entire frame. Based on combination of these C_i values quad counts Q_1, Q_2, Q_3, Q_4 and Q_D are computed as shown in figure 3b. Basic global parameters of an image over the entire frame are expressed in terms of the quad counts as follows (Pratt 1978).

$$\begin{aligned} A_{(\text{area})} &= 1/4 (Q_1 + 2Q_2 + 3Q_3 + 4Q_4 + 2Q_D), \\ P_{(\text{perimeter})} &= Q_2 + 0.707 (Q_1 + Q_3 + 2Q_D), \\ E_{(\text{Euler count})} &= 1/4 (Q_1 - Q_3 - 2Q_D). \end{aligned}$$

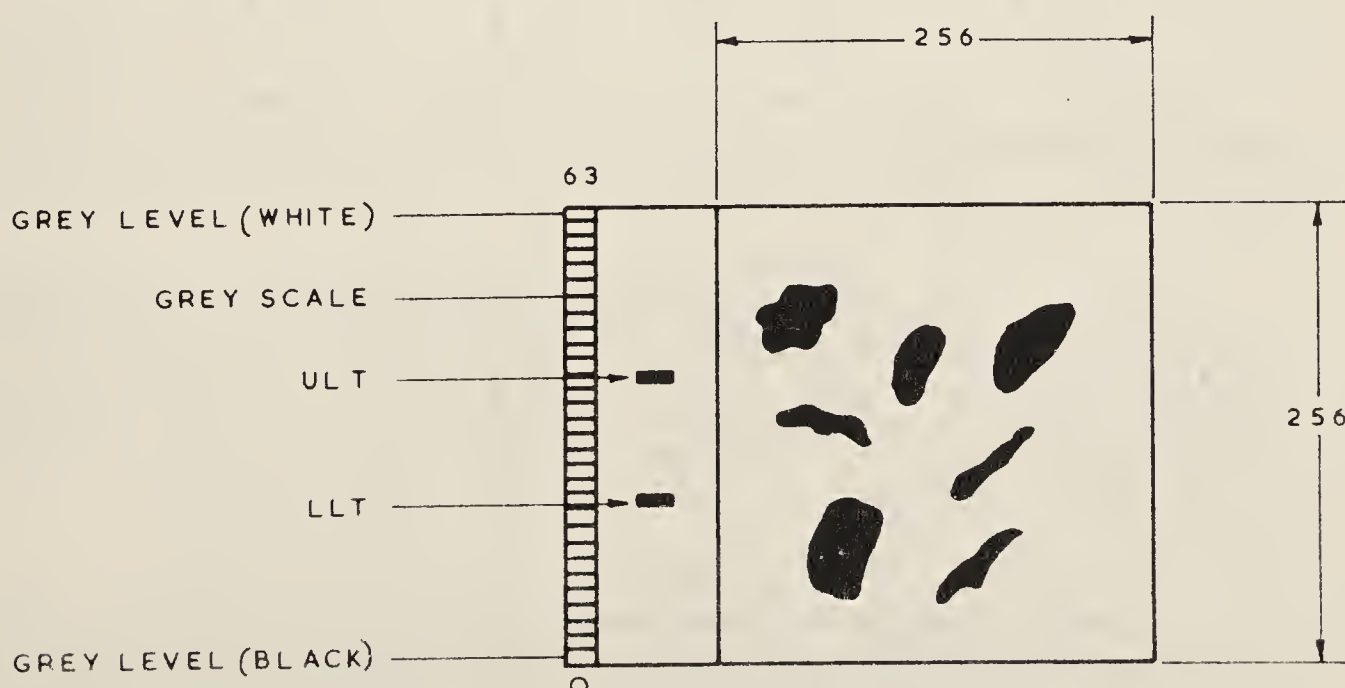


Figure 2. Format of image display on monitor.

Feature count C is related to Euler count by $E = (C - H)$ where H = number of holes. If the number of holes is small in comparison with number of features, Euler number can be taken as a good estimate of feature count.

For horizontal projection H_p , 0–1 transition in the horizontal direction is observed as shown in figure 3c and H_p is given by

$$H_p = C_2 + C_6 + C_{10} + C_{14}.$$

Similarly 0–1 transition in the vertical direction is observed as shown in figure 3d and vertical projection V_p is given by

$$V_p = C_4 + C_6 + C_{12} + C_{14}.$$

Estimation of these parameters requires about 2.5 seconds.

2.3b Erosion and dilation: In the process of erosion, the touching objects are uniformly shrunk along their perimeters until a separation is achieved. Dilation is used to join separated parts of detected images.

For erosion and dilation, a reference pixel is considered in relation to its four nearest structuring elements as shown in figure 3e. During erosion the reference pixel is

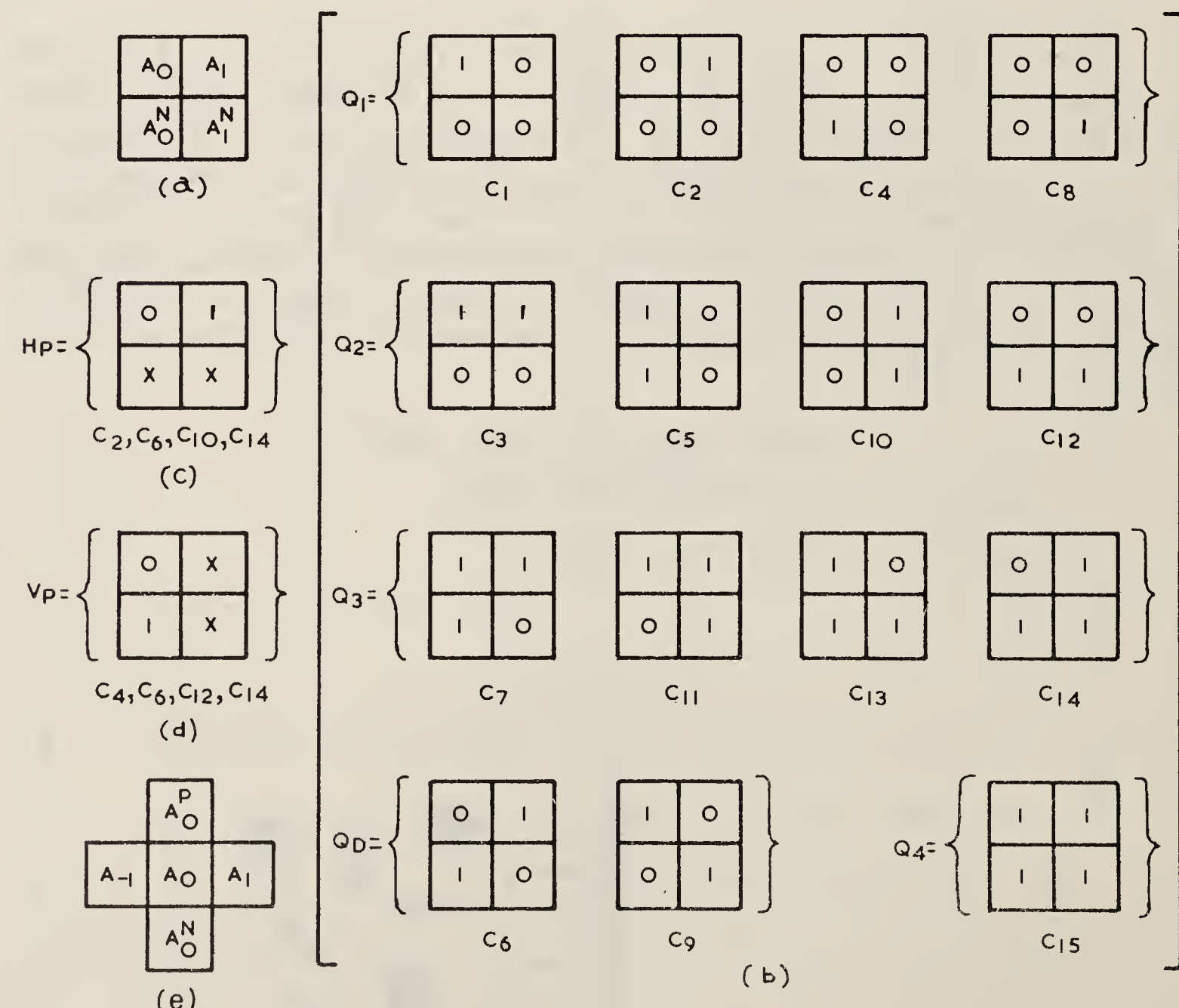


Figure 3. Image computation patterns. (a) Typical 2×2 pixel pattern. (b) Area, perimeter and feature count computation patterns. (c) Horizontal intercept pattern. (d) Vertical intercept pattern. (e) Structuring element for erosion and dilation. Note: 0 = logic '0'; 1 = logic '1'; X = don't care.

replaced by 'ANDING' of all the five pixels whereas dilation is accomplished by 'ORing' of the same over the entire image frame. Time of execution for one step of erosion/dilation operation is about 0.7 sec.

2.3c Halo error correction: In a multiphase sample, when an intermediate phase is detected for computation using threshold level detection errors can occur due to finite system resolution. This has the effect of producing a 'halo' i.e. an apparent grey perimeter around a dark feature which is detected. Special algorithm has been developed based on repeated dilation and logical operations for halo error correction.

2.4 Operator interaction

Operator interaction with the system is accomplished under the control of a system monitor (Terrell 1978). A query procedure guides the user step by step making the dialogue user friendly. Additionally, the monitor provides for execution of I/O operations like setting of undetected, detected and computed image display. Also there is a provision for print out of results in a standard format as shown in table 1.

3. HP1000-based image processing and analysis system

A powerful image processing and analysis system is being developed with 512×512 pixel resolution incorporating facilities such as shading correction, auto-delineation, image enhancement, light pen interaction and feature-specific measurements.

3.1 Schematic details

The system is based on a user microprogrammable HP1000-model 27 computer system. Figure 4 shows the block diagram of this system. Its imaging section consists of an optical microscope/epidiascope coupled to a chalcogenide scanner. The video signal output is stored into a $512 \times 512 \times 8$ pixel frame grabber. Peripheral operations i.e. light pen interaction, autofocus, stage control, console scanning and image display monitor control are carried out by the Apple II computer. The image is transferred to HP1000 computer system via IEEE-488 bus for processing and analysis.

3.2 System software

After shading correction and auto-delineation image processing and analysis functions for various basic and derived parameters are carried out in FORTRAN-77. Repetitive

Table 1. Micromet. (Radiometallurgy Programme, Kalpakkam)

Sl. No.	UT	LT	Count	Area	Peri	Vert	Horz
1	16	09	38	8402	2391	818	635
2	38	26	86	19410	10017	3313	2732
3	51	45	54	11692	3939	1391	945

User: ABC; Specimen: Sensitized nuclear grade SS 316 sample.
Date: 19 January 1985; SP No. 1147.

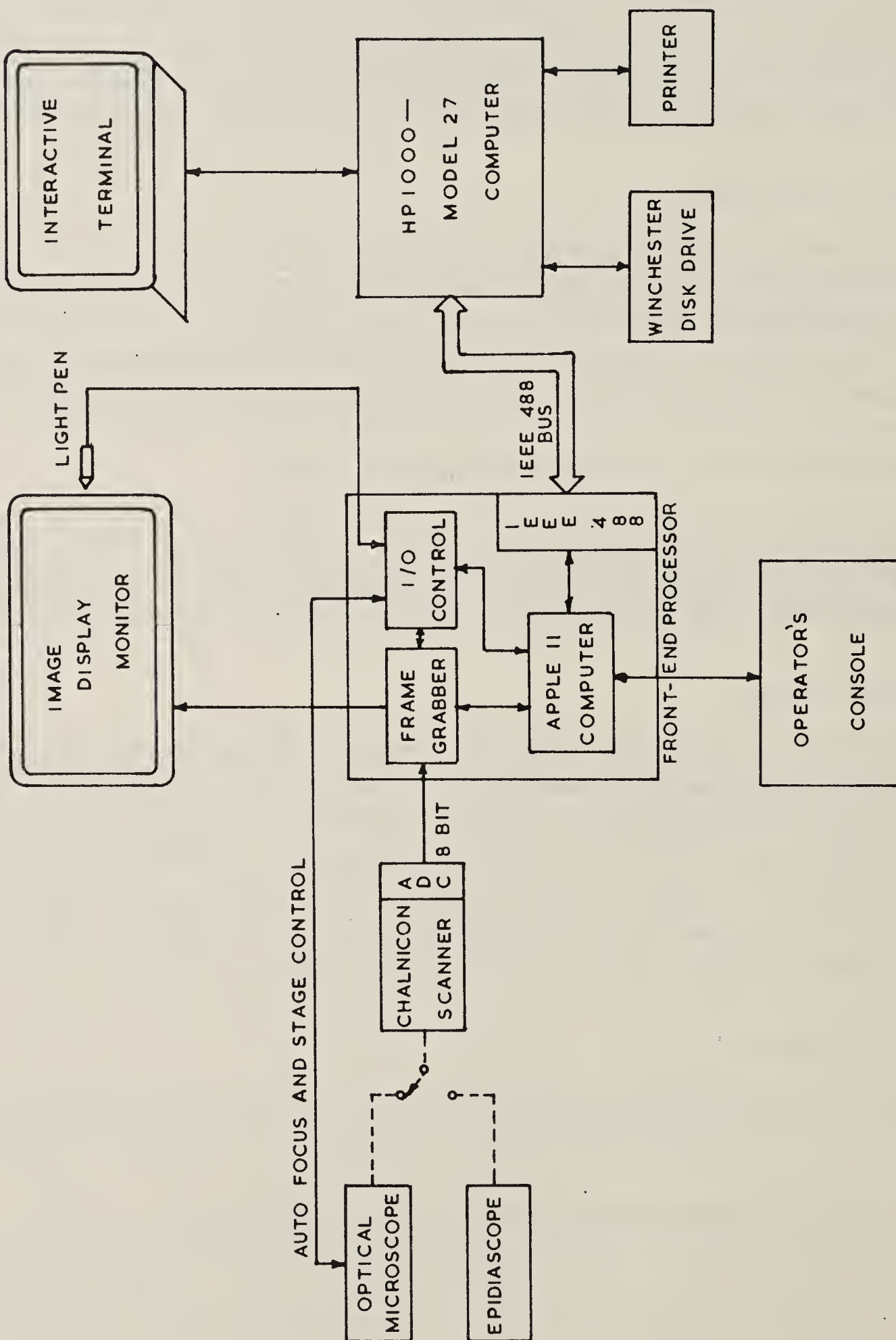


Figure 4. Block diagram of HP1000 computer-based image processing and analysis system.

operations are microprogrammed for fast execution. Two specific schemes adopted for image analysis are continuous scan and features extraction methods.

3.2a Continuous scan method: Here parameters of each individual feature are measured separately. The detected binary image is continuously scanned. Whenever a feature is encountered it is indexed and the basic parameters are accounted for that feature. This technique provides accurate size distribution, spatial distribution and various derived parameters.

3.2b Feature extraction method: During evaluation of length, breadth and perimeter of a particular feature presence of other features interferes with the analysis. This can be avoided by using feature extraction method. In this technique, contour of the feature is traced. The complete feature is copied into another sector of memory and analyzed independently.

4. Conclusion

The Z-80 based image analyser is an inexpensive solution for measuring structural features in the image frame under view with limited resolution. It is a versatile tool for field-specific basic parameter evaluation. Provision exists for erosion/dilation and halo error correction. An HP1000 computer based image processing and analysis system is under development. The features being incorporated in this system are image enhancement, 2-D detection, shading correction, light pen interaction and feature-specific measurements. Both the systems being software intensive provide flexibility in selecting a particular operation and are open ended for further upgradation.

Though the image analysis is automated, the results obtained are still subjective. Human factors involved are in the preparation of samples/micrographs, selecting the desired features and in editing of images. Therefore, expert attention is indispensable for obtaining accurate results.

The systems are being realized taking into consideration the requirements of quantitative metallography. They are equally powerful for analysis of images obtained in the fields of photography, biology, medicine, geology, meteorology and space.

Acknowledgements

The authors are grateful to Dr P R Dastidar, Dr P Rodrigues and Sri S N Seshadri, for constant encouragement and providing facilities to develop the image analysis system.

References

- Jenkinson G W 1982 Technical Exchange and Symposium on Image Analysis, University of Iron and Steel, Beijing
- Pratt W K 1978 *Digital image processing* (New York: John Wiley & Sons)
- Terrell A C 1978 *Microscope* 26 49

Modern computer assisted methods in metallurgy

G W JENKINSON and T KELLY

Cambridge Instruments Limited, Rustat Road, Cambridge, England

Abstract. Image analysis systems have been used in metallurgy for over two decades and play a vital role in quality assessment for the steel industry. One major application is the characterization of steel by counting and measuring the non-metallic inclusion content. Visual steel assessment, relying on the comparison with idealized 'charts' of varying inclusion content, for example as defined by ASTM and SEP, is the most common manual method employed.

However, this has proved to be most difficult to automate due to the degree of subjectivity associated with the manual methods. This has previously restricted the acceptance of image analysis systems for routine quality control. The increased software power of the more modern instruments has enabled the installation of systems which satisfactorily mimic the skilled observer in a reproducible manner. These work with an economically attractive throughput and produce results in the accepted standard format.

A limitation of these systems is that they grade a field on the basis of the majority inclusion type present. This can lead to significant but lesser inclusions being ignored altogether and presenting a false picture of the sample. This paper describes a new method which separately identifies individual inclusions in a field. The grade number of a field can then be determined for each inclusion type. This is known as the mixed field method. This paper describes this method and its implementation on the Cambridge Instruments' QUANTIMET 920 image analysis system.

Keywords. System operation; inclusion type; inclusion grade; mixed fields; worst fields.

1. Introduction

The mechanical properties of steel are greatly influenced by the type and dispersion of non-metallic inclusions, and the inclusions themselves are often characteristic of the steel making practice.

The evaluation and description of the inclusion content of steel is carried out on a routine basis in every quality monitoring laboratory in the steel industry, and for economic and historical reasons, visual chart comparison procedures such as the ASTM E45 method (American Society for Testing and Materials, 1963) and the SEP 1570-1 method (Stahl-Eisen-Prufblatt 1971), are frequently used. Despite their shortcomings (Johansson 1974) these chart-based methods do provide a common ground for intercompany and manufacturer-user dialogue but the precision of the results obtained by the visual methods is often far from satisfactory. Repeat evaluations by a single operator, and evaluations obtained by different operators examining the same sample, show wide variations, and to such a degree that it can be difficult to draw genuine conclusions concerning assessment carried out at different times and places by different operators (Johansson 1974). This is precisely the effect that the visual method is supposed to avoid. Automatic image analyzers such as the Cambridge Quantimet systems set out to minimize this effect by providing a standardized operation procedure for the evaluation of the inclusion fields, so that results are independent of where the evaluation is performed or who operates the system.

It has been shown (Pohl 1979a, b) that the same measurements can be obtained by automatic image analysis as by visual comparison for the assessment of non-metallic inclusions. The first analyzer to do this for ASTM E45 and SEP 1570-71 was the Quantimet 720 Steelscan (Polzin 1977, 1978). Since then, however, more rigorous application of the standards has called for the ability to determine the content of each type of oxide in a field rather than to classify a field on the basis of the most likely single inclusion type. This is a significantly more difficult function and this paper describes the methods used and illustrates the implementation on the Quantimet 920 image analyser.

2. General description of system operation

A conventionally prepared specimen either mounted in plastic or as a free block, in accordance with local practice, is scanned automatically by a motorized XY stage under a microscope equipped with a high-speed autofocus system. There are few limitations on specimen size; samples up to 10 cm × 10 cm can be accommodated though a total inspection area of 250 or 500 mm² is typical. Specimens are examined under the conditions prescribed in the chart method ($\times 100$) so the images are familiar to the operator and this allows direct confirmation of the system interpretation of field ratings.

The optical image is presented to a high resolution (720 line) plumbicon scanner, necessary to allow correct separation of the sulphide and oxide inclusions at the relatively low magnifications involved. The parameters required for the evaluation of inclusion type and rating are measured and the decoding of this quantitative data into the familiar chart terms is carried out by the systems' microprocessor. On completion of an analysis, the traditional evaluation table is printed (table 1 shows an ASTM example) and if required the 'worst fields' of any inclusion type can be recalled, displayed and rejected if necessary.

3. Determination of inclusion type

The primary classification into oxide and sulphide inclusion types is performed by an automatic detector which is sensitive to the grey tone differences of these two major inclusion types. It duplicates therefore the discrimination process of a human operator but includes fine detail enhancement to ensure that all visually recognised inclusions are identified to the system. The detection system also compensates for variations in background illumination generated in all optical microscopes and whose presence could severely limit the useful field of measurement. The separation of the oxide and sulphide inclusion types is therefore a straightforward process and is illustrated in figure 1.

The next requirement, the classification of the oxide inclusion into the three visual types (recognized as B, C, D in the ASTM procedure and OA, OS, OG in the SEP method) is more complex. The essential differences between the three oxide types are of morphology and patternness as can be seen from the schematic representation of the chart fields in figure 2. The silicate type is characterized by having an elongated morphology relative to the alumina and globular types which are morphologically very similar. There is a very different patternness for the alumina and globular types which

Table 1. Typical ASTM E45 chart print-out

Grade	Sulphides		Aluminates		Silicates		Globular	
	Thin	Thick	Thin	Thick	Thin	Thick	Thin	Thick
Based on observed specimen area of 199.091 mm ²								
0.5	121	59	6	0	115	40	108	118
1.0	91	102	0	1	34	12	0	168
1.5	7	22	1	0	2	38	0	18
2.0	0	142	0	2	0	137	0	0
2.5	0	8	0	3	0	3	0	0
3.0	0	2	0	0	0	1	0	0
3.5	0	0	0	0	0	0	0	0
4.0	0	0	0	0	0	0	0	0
4.5	0	0	0	0	0	2	0	0
5.0	0	0	0	0	0	0	0	0
Based on standard specimen area of 250 mm ²								
0.5	152	74	8	0	144	50	136	148
1.0	114	128	0	1	43	15	0	211
1.5	9	28	1	0	3	48	0	23
2.0	0	178	0	3	0	172	0	0
2.5	0	10	0	4	0	4	0	0
3.0	0	3	0	0	0	1	0	0
3.5	0	0	0	0	0	0	0	0
4.0	0	0	0	0	0	0	0	0
4.5	0	0	0	0	0	3	0	0
5.0	0	0	0	0	0	0	0	0

Number of fields rejected: 0

can be characterized by the degree of clustering along and about the direction of elongation as described by the charts.

Figure 3 describes the decision logic which classifies a given field in terms of the measurements made by the Quantimet. This logic requires the individual classification of each inclusion in the field and this is achieved by measurement of the aspect ratio, X and Y position and vertical length of each inclusion. The photographs of figure 4, which show identified inclusions, can be compared with figure 2. The annotation on the photographs is performed by the system while operating in 'review mode' which allows the operator to check the decisions being made by the system. The codes used to annotate the inclusions are as follows:-

SUL - Thick } sul - Thin }	Sulphide	(A or SS)
ALU - Thick } alu - Thin }	Alumina oxide	(B or OA)
SIL - Thick } sil - Thin }	Silicate oxide	(C or OS)
GLO - Thick } glo - Thin }	Globular oxide	(D or OG)

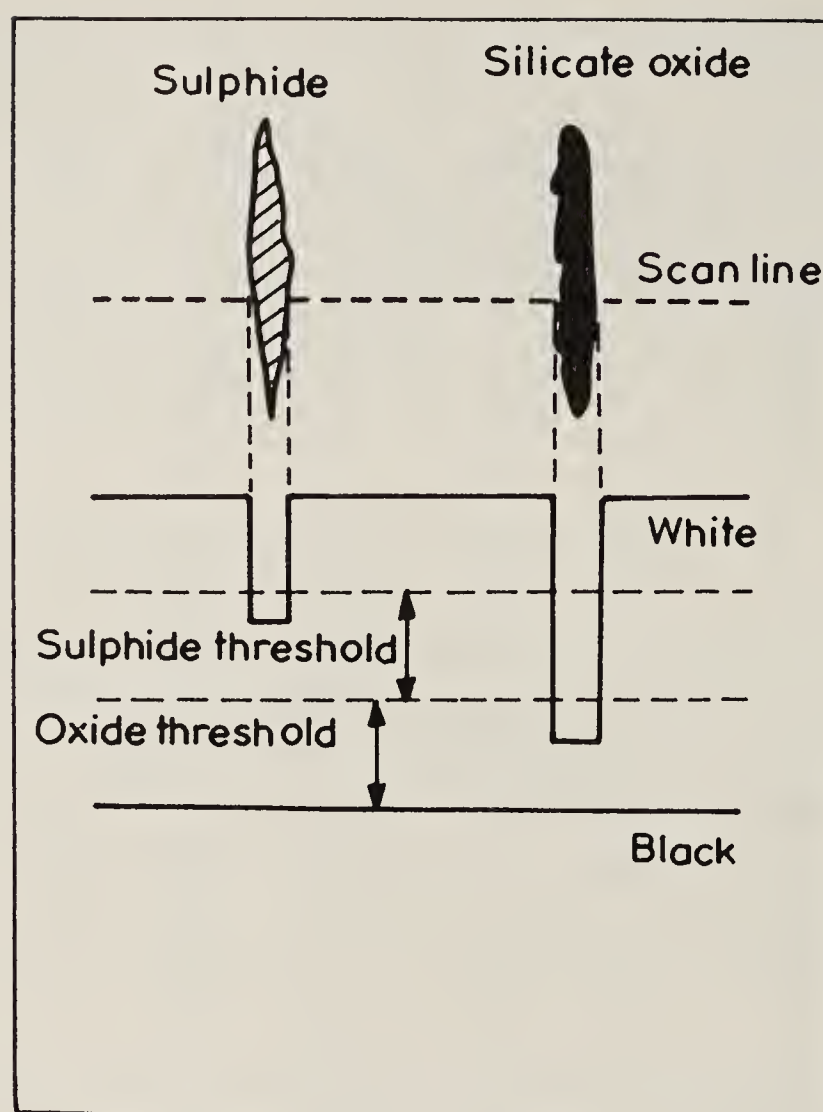


Figure 1. Separation of oxides from sulphides by grey-level

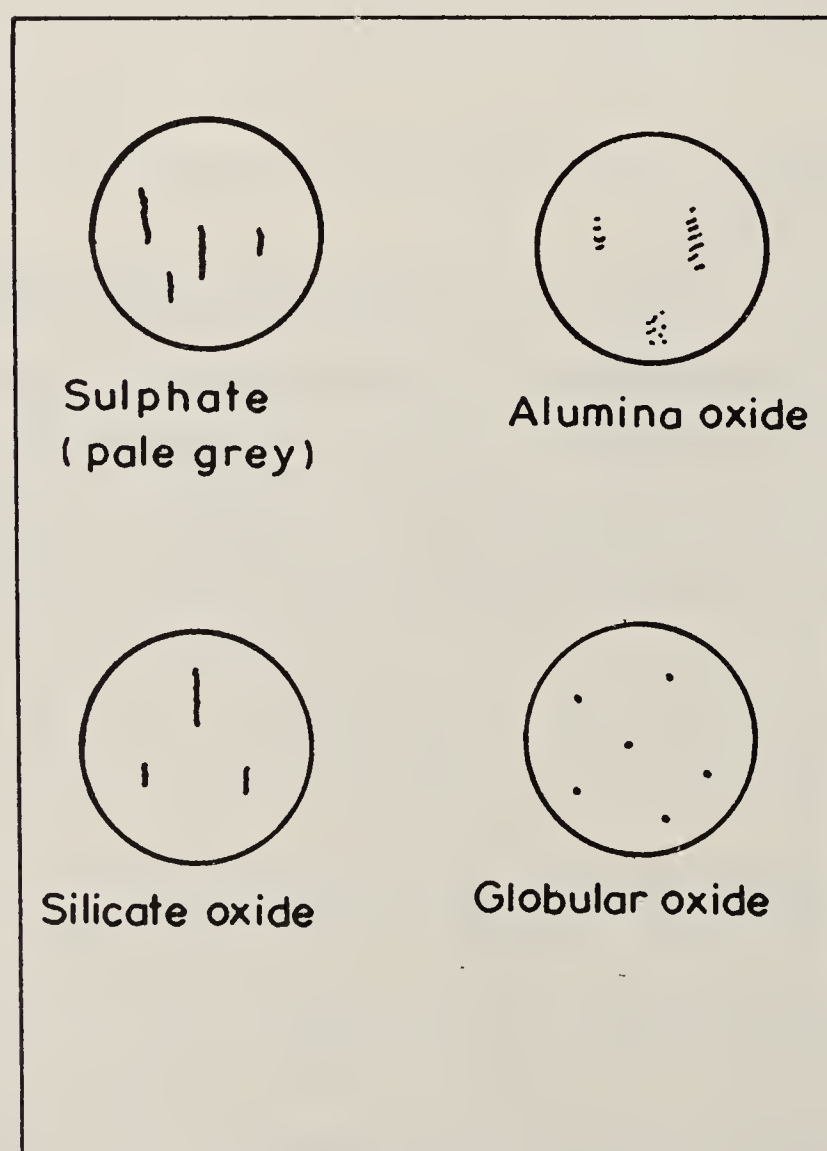


Figure 2. Schematic representation of chart fields

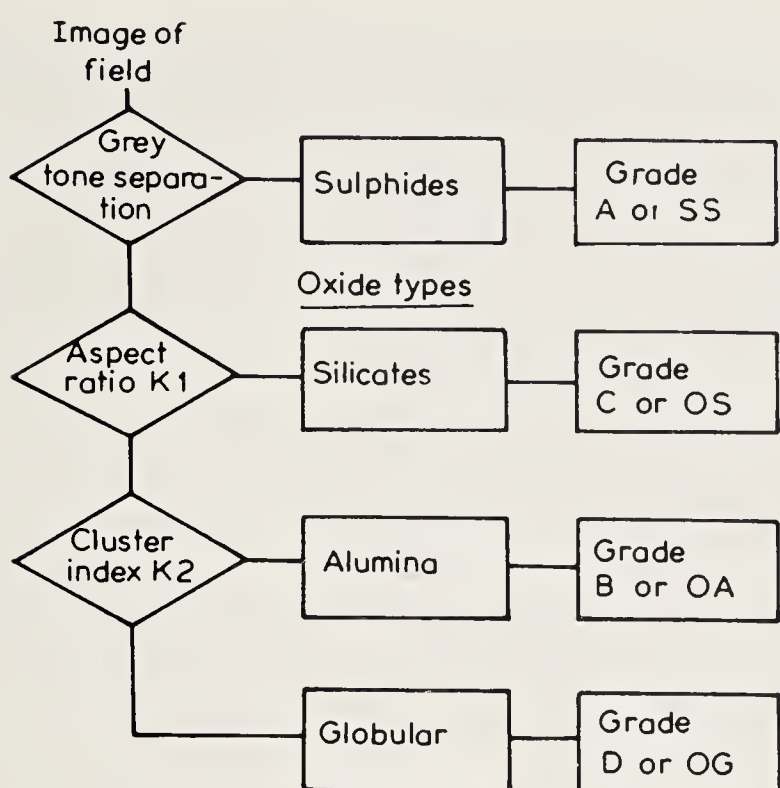


Figure 3. Classification algorithm for automatic rating: K1 is a constant which is specified to separate silicates from other oxides on the basis of aspect ratio; K2 is a constant which is specified to determine the cluster spacing which separates alumina and globular oxides.

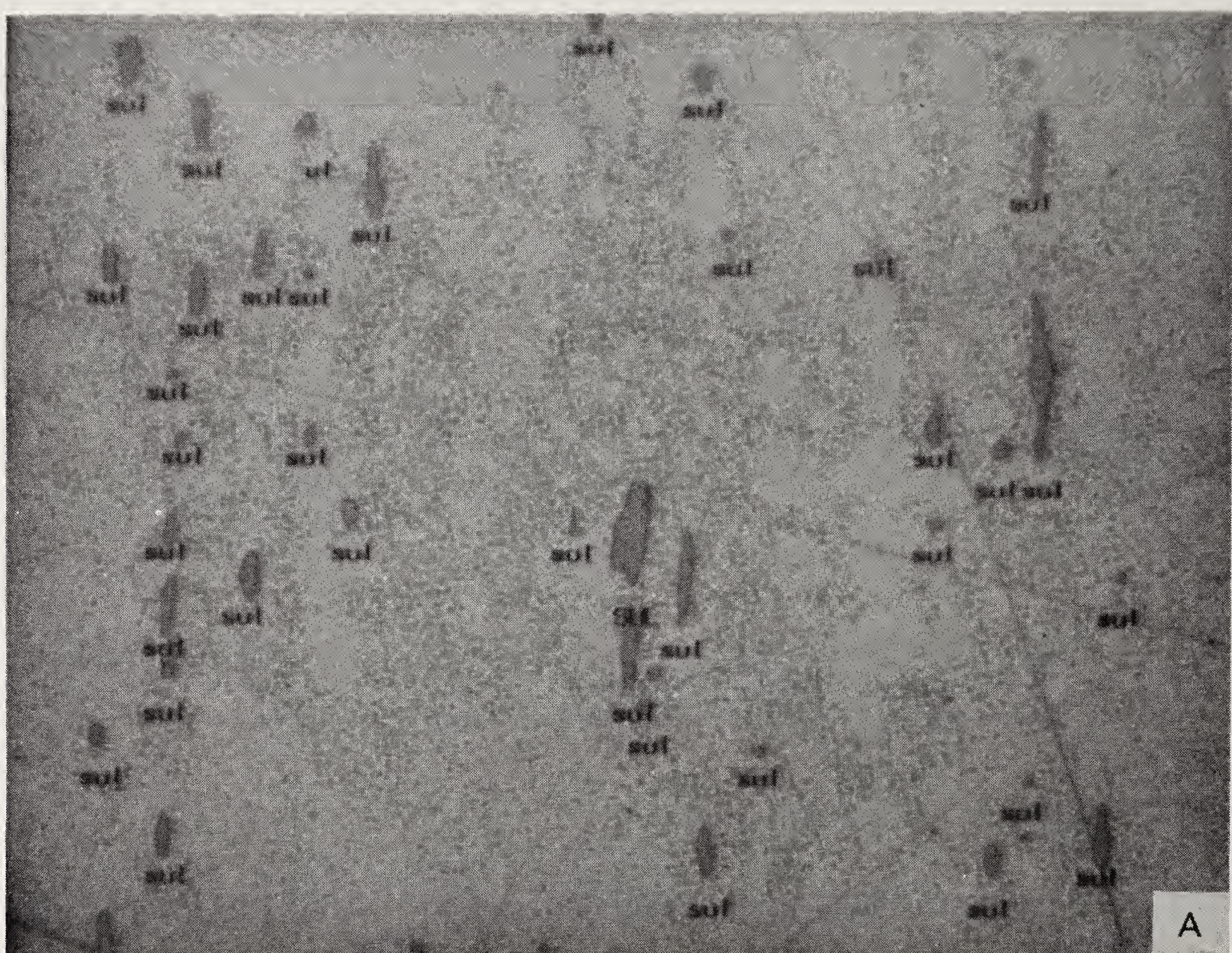
4. Determination of inclusion grade

Having identified the inclusion type as described, it is then a straightforward matter to assign a grade number (0–8) to the type. Each column of the ASTM or SEP chart shows an increase in total inclusion length as we progress through the range 0–8 and since this is a parameter measured by the Quantimet it can be used to assign a grade number to the observed field. If required the grading can be further refined into the ‘thick’ or ‘thin’ categories allowed for in the charts. The values characteristic of each ASTM or SEP grade are defined in the respective standard so these are used in the analysis programme. As can be seen from table 1, two tables are printed. The first table shows the actual number of 0·5 mm² fields which have been measured. The lower table has been normalized to the standard specimen area of 250 mm². It is often preferable to scan a reduced area as this is of sufficient accuracy while improving throughput.

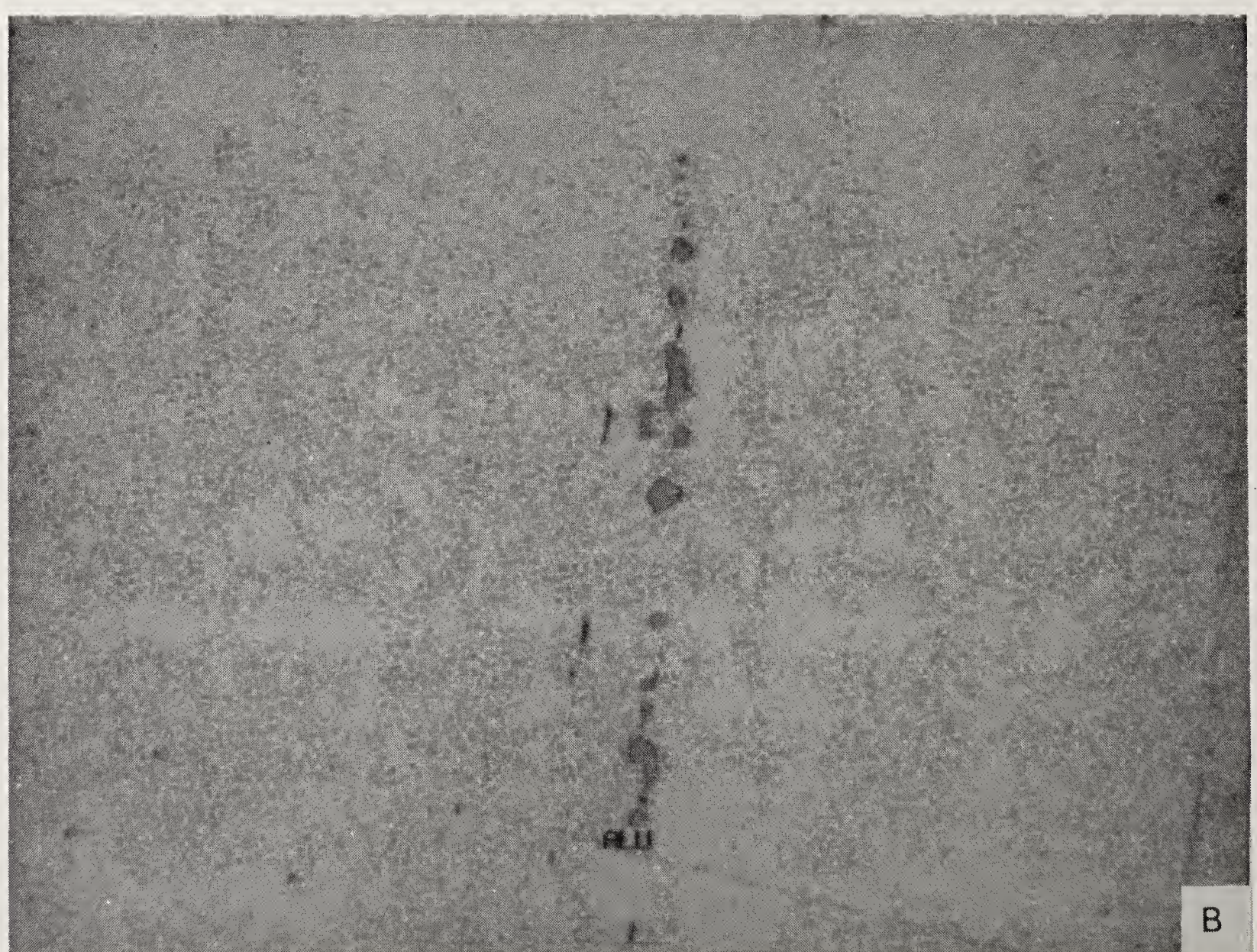
5. Mixed fields

Assigning a grade number to an observed field by comparing it with the chart representation is subjective and influenced by several factors. The occurrence of a ‘severe’ sulphide field will influence the operator’s decision concerning the oxides in that field. Automatic image analysis gives unbiased results. The presence of ‘mixed’ oxide fields (alumina with globular or silicate with globular) also causes confusion.

In previous systems mixed oxide fields were not partitioned into different types and a majority field type was assigned. In the logic implemented by the Quantimet 920, each individual inclusion is identified, and its contribution to the grade number determined even for mixed oxide fields. Clearly this is a much more demanding protocol to implement and reproduction of human classification cannot be perfect. However, the provision of a review facility allows the operator to verify that the system is performing satisfactorily before making fully automatic analysis.



A



B

Figure 4.



Figure 4. (A) Identified sulphide inclusions. (B) Identified alumina inclusions. (C) Identified silicate and globular inclusions.

6. Worst fields

Preparation methods used for automatic analysis need to be of a consistent high quality. However, dust or dirt cannot be entirely avoided. The worst field review facility enables the operator to check on the fields which have unusually high ratings. They can be excluded from the analysis if found to be due to dirt or debris.

The worst field for each inclusion type can also be recalled. The system remembers the X-Y location of the worst fields. The operator selects from the list presented (figure 5) which type of field to examine. The system moves this field of the specimen into the analysis field of view by moving the automatic motorised microscope stage. The operator can decide to accept or reject this field. The next worst field will then be presented and so on until sufficient fields have been reviewed.

7. Conclusions

This paper has described how the image analysis techniques for chart grading of steel cleanliness have been extended to work with mixed fields of oxides.

The implementation on the Quantimet 920 also provides for the review and rejection

***** WORST FIELD REVIEW *****

- 0- TERMINATE
- 1- THIN SULFIDE
- 2- THICK SULFIDE
- 3- THIN SILICATE
- 4- THICK SILICATE
- 5- THIN GLOBULAR
- 6- THICK GLOBULAR
- 7- THIN ALUMINA
- 8- THICK ALUMINA

SELECT FIELD TYPE TO REVIEW**Figure 5.** World field review selection.

if necessary of the worst fields found after this analysis run is complete. A verify facility permits system operation to be checked for each field.

References

- ASTM 1963 American Society for Testing and Materials. "Recommended practice for determining the inclusion content of steel," ASTM E45-63
- Johansson S 1974 Tech. Rept. Sandviken. "The rating of nonmetallic inclusions by image analysis."
- Pohl W and Fischer A 1979a Microscopia Acta, Supplement 3, S. 77-82. "Experience in Steel Cleanliness Assessment by the Automatic Image Analyser QUANTIMET 720/10M"
- Pohl W and Fischer A 1979b Sonderbande der Praktischen Metallographie, Band 10, S631-640. "Erfahrungen bei der Reinheitgradbestimmung mit dem Automatischen Bildanalysator QUANTIMET 720/10M."
- Polzin T 1977 Microscopia Acta, Supplement 1, S 19-31
- Polzin T 1978 Praktische Metallographic, Band 15, S 277-286. "QUANTIMET 360/2 and QUANTIMET 720/10M - two new systems for microscopic evaluation of non-metallic inclusion content in steel."
- Stahl-Eisen-Prufblatt 1971 Verlag Stahleisen, Dusseldorf. "Microscopic examination for non-metallic inclusions with reference inclusion charts."

Computer simulation of dislocation-carbon interaction in nickel

B PURNIAH and S SRINIVASAN

Indira Gandhi Centre for Atomic Research, Kalpakkam 603 102, India

Abstract. An atomistic computer model based on a rigid boundary method has been developed to estimate the interaction energy between a single edge dislocation and an impurity carbon interstitial in nickel. The simulation was carried out using the static relaxation technique on a total of 600 atoms, using an appropriate host-host pair potential. The impurity-host potential has been chosen to be a cubic function in this calculation. In the absence of the dislocation the dipole tensor for the octahedral site is seen to be spherical. Two impurity positions, one above and one below the slip plane were investigated. The carbon-dislocation interaction energies obtained were 1.4 eV and 0.7 eV respectively for the two impurity positions. The dipole tensor for the impurity in the presence of the dislocation was found to be non-diagonal.

Keywords. Computer simulation; impurity defects; dislocation; lattice statics; interaction.

1. Introduction

Many important physical and technological phenomena occur as a direct consequence of the interaction between impurity point defects and dislocations. A well-known example is that of strain aging which involves the migration of interstitial impurities to dislocations. This interaction can be studied very effectively by internal friction experiments (Nowick and Berry 1972). The quantitative interpretation of internal friction experiments needs the estimation of the dipole tensor which is a measure of the elastic distortion caused by the defect in question. In this paper we describe such a calculation for a straight edge dislocation and a carbon impurity interstitial in fcc nickel. The simulation is carried out in two steps. Section 2 describes the choice of an interatomic potential. Section 3 describes the simulation of an edge dislocation and §4 describes the simulation of the dislocation-point defect interaction.

The simulation of an edge dislocation described here is based on a rigid boundary method (Bullough and Tewary 1979). To obtain the atomic configurations associated with the straight edge dislocation, a rectangular parallelopiped of freely interacting atoms was set up. The defect configuration is introduced at the centre of this crystallite which has two regions. In the inner region (region I), the atoms are allowed to freely relax to the equilibrium positions via a given nonlinear potential. In the outer region (region II), the atoms are constrained to remain in positions given by the linear elasticity theory. Region I was chosen to be sufficiently large compared to region II such that the influence of the surface or boundary effects are minimized. Some improved methods involving flexible boundaries (Hoagland *et al* 1976) have been developed and used in dislocation simulation. However, these flexible boundary methods cannot be used for a combined point defect-dislocation model.

There are two main techniques followed in literature to relax the atoms in Region I. These are the static and the dynamic relaxation techniques. The static method which is

basically a gradient method is used here to minimize the total energy of this region (Sahu *et al* 1980). To determine the interaction energy, we need to evaluate the difference in the energy of formation of the point defect in a perfect and a lattice with a dislocation. This is accomplished by a separate evaluation of the energy of the dislocation and the point defect-dislocation combination.

2. Interatomic potentials

The interatomic potential is of crucial importance in atomistic models. They can be classified into two broad categories, namely the empirical potentials and the pseudopotentials. The pseudopotential method, which has been successful in predicting various physical properties of the perfect lattice has been shown to be inadequate for defects such as vacancies, dislocations, surfaces etc., which produce large inhomogeneities in the electron distribution. Empirical potentials are, however, more suited for defect studies (Johnson 1973). The simulation of dislocations in fcc metals require pair potentials which incorporate stacking-fault energies. We have used such a potential developed by Baskes and Melius (1979) for the host lattice where the cut-off distance for the potential is taken to be between the third and fourth neighbour. The functional form of the potential is a cubic spline between a number of fixed nodal points. The impurity-host potential was chosen to be a cubic function (Johnson *et al* 1964). The general shape was similar to the host-host potential i.e. a strong repulsion at close distances, a minimum at some intermediate distance and going to zero with zero slope at a cut-off distance. The potential parameters were determined with the help of experimental quantities like the carbon atom migration energy, activation volume and carbon-vacancy binding energy.

3. Simulation of edge dislocation

The edge dislocation studied in this case lies along $[1\bar{1}2]$ direction. Its Burger's vector was of the type $a/2\langle 110 \rangle$ (see figure 1). The faces of the crystallite were appropriate $\{110\}$, $\{112\}$, and $\{111\}$ crystallographic planes and the dislocation was arranged to lie through the centre of the assembly and orthogonal to the two $\{112\}$ faces. In the direction of the dislocation line, specifically the $[1\bar{1}2]$ direction (y -axis), the assembly was only six lattice planes thick and periodic boundary conditions were imposed across the two end $(11\bar{2})$ faces (Cotterill and Doyama 1967). In the other two orthogonal directions ($[1\bar{1}0]$ - the x direction and $[111]$ - the z direction) the assembly was made up of 49 $\{110\}$ lattice planes and 19 $\{111\}$ planes. The parallelopiped was deliberately extended in the x -direction to accommodate the dissociation into Shockley partials of the glissile edge dislocation. The initial defect configuration was achieved by first imposing the appropriate anisotropic elastic displacements on all the atoms in the crystallite. This configuration is designated as the elasto-atomic model.

Next, the atoms in region I, numbering approximately 600, were allowed to relax towards equilibrium under the influence of the host pair potential already described. During the simulation of the undissociated dislocation (also called complete dislocation) the atoms were *not* permitted to relax in a direction parallel to the dislocation line. The strain energy of a dislocation inside a certain radius is given by

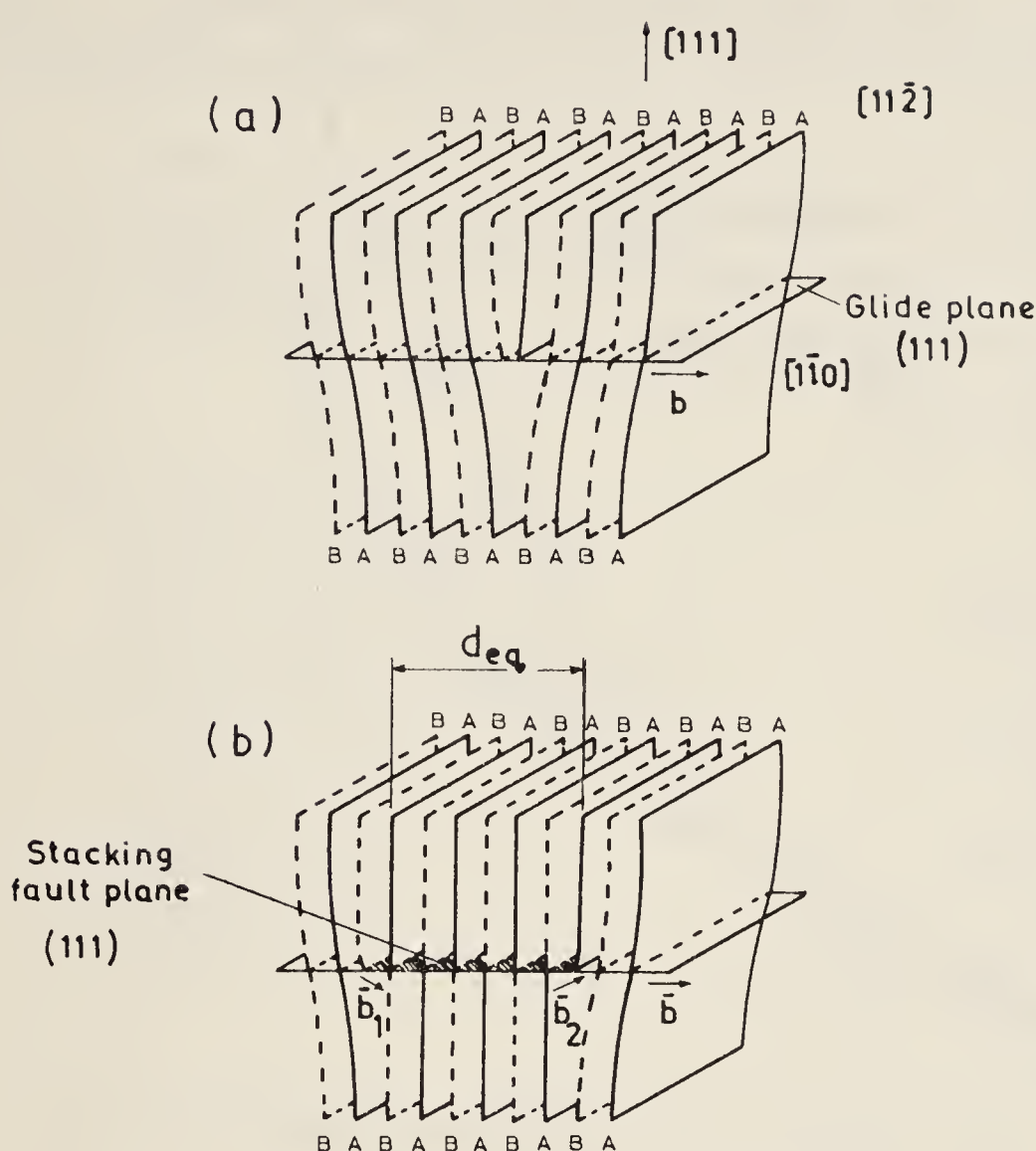


Figure 1. Spatial representation of an edge dislocation with a Burger's vector $a/2 [1\bar{1}0]$ in the fcc structure. (a) Complete edge dislocation. (b) Dissociated edge dislocation. (\bar{b} , \bar{b}_1 and \bar{b}_2' indicate the Burger's vector of the complete and the two partial dislocations).

$E_d = 1/2 \sum_i^n (E_i - E_0)$, where n is the number of atoms inside that radius, E_i is the energy of the i th atom *after* relaxation and E_0 in the perfect lattice. The factor $1/2$ is required because each interatomic bond is counted twice in the calculation. Figure 2 shows the energies of the elasto-atomic model and the complete edge dislocation plotted as a function of distance.

It is known in fcc metals that the edge dislocation dissociates into a pair of partial dislocations separated by an intrinsic stacking-fault on the (111) plane (Heidenreich and Shockley 1948). To study this dissociation, the atoms in region I were also allowed to relax parallel to the dislocation line. The parallelopiped was extended to 49 planes in the x -direction (as already stated) to accommodate the splitting of the dislocation into partials leading to a stacking-fault along this direction. The final positions attained by the atoms in complete dislocation were used as the initial positions for the case of the dissociated dislocation. It was found that the complete dislocation splits into partials separated by a distance of $8b$. The energy of the dissociated dislocation is also plotted in figure 2. It can be seen that the energy of the dissociated dislocation is indeed less than that of the complete dislocation.

4. Dislocation-carbon interaction

To obtain the interaction energy between the dislocation and carbon impurity, it was necessary to extend the parallelopiped in the y -direction and drop the periodic

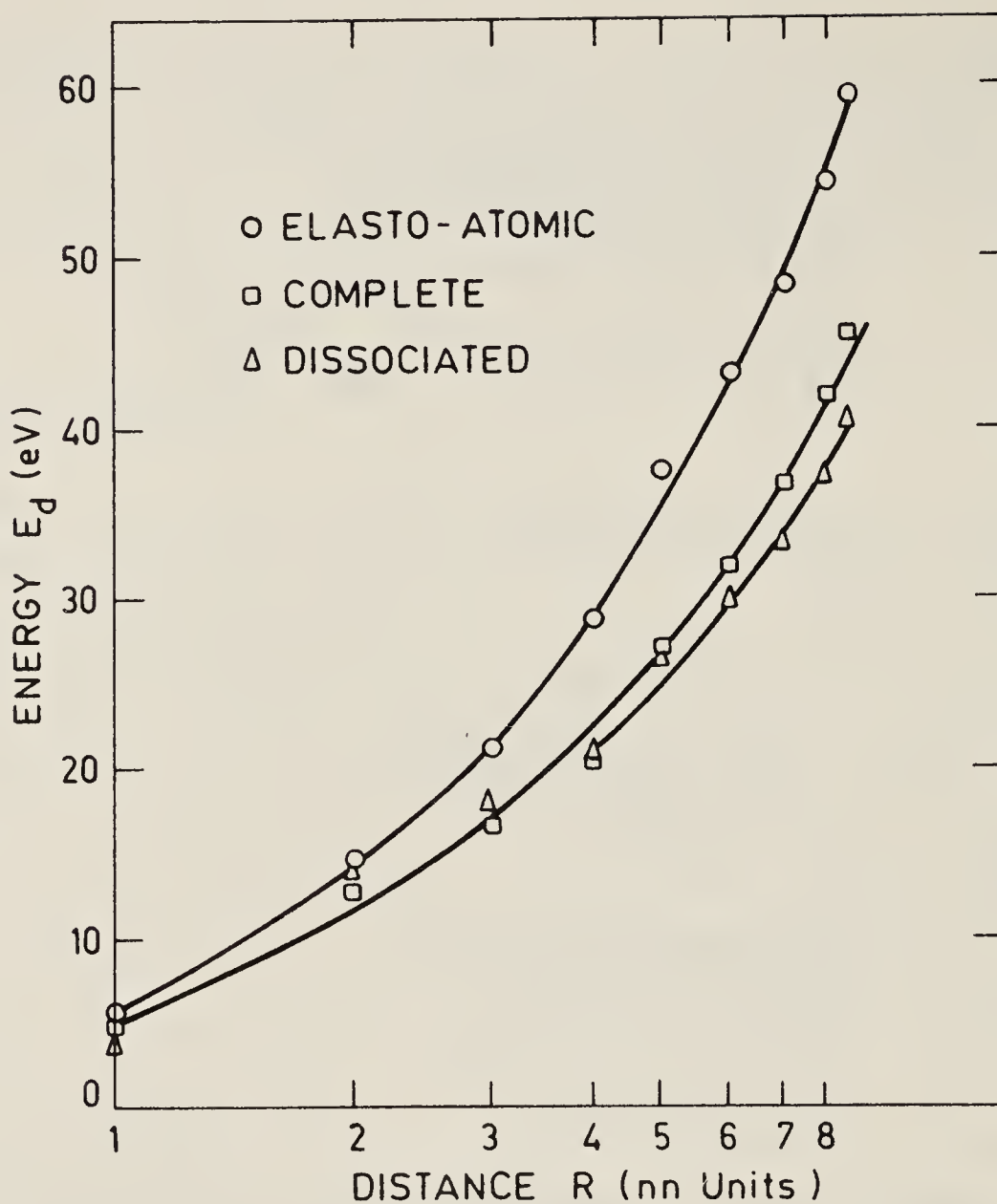


Figure 2. The energy as a function of the radius from the centre of a edge dislocation shown for the three cases, elasto-atomic, complete and dissociated dislocation.

boundary conditions on these faces. The crystallite was made 30 planes thick as against the six originally taken. Of this assembly, the central region containing 627 atoms was allowed to relax. The boundary atoms were held in their previous relaxed dissociated dislocation positions and the position of the point defect (in this case the carbon impurity in octahedral site) relative to the dislocation was varied. Two impurity positions were chosen. One position at $(3, -3, 1.5)$ was above the slip plane and the other at $(3, -3, -1.5)$ was below the slip plane. The co-ordinates are with reference to the dislocation centre located at $(0, 0, 0)$. The carbon interstitial formation energy in the perfect lattice was obtained using a point defect simulation program (Sahu *et al* 1980).

5. Results and discussion

The results of the simulation are summarized in table 1. The edge dislocation lying along $[11\bar{2}]$ direction was found to dissociate into partials when the atoms in region I were allowed to relax freely in all three directions. The equilibrium distance of separation between the partials was found to be $8b$. For the two impurity configurations, one above and one below the slip plane, the formation energy, interaction energy and dipole tensor were obtained. A few points can be seen from the table. The (undersized) carbon atom prefers to sit above the slip plane as is known from the

Table 1. Values of carbon impurity formation energy, interaction energy, dipole tensor and stacking-fault distance obtained from computer simulation of an edge dislocation in Ni.

Property	Value
1. (a) Carbon impurity formation energy in perfect lattice	1.624 eV
(b) Dipole tensor of carbon interstitial (eV)	$\begin{pmatrix} 2.56 & 0.0 & 0.0 \\ 0.0 & 2.56 & 0.0 \\ 0.0 & 0.0 & 2.56 \end{pmatrix}$
2. Edge dislocation	
(a) <i>Interstitial above the slip plane</i>	
Formation energy (3, -3, 1.5) (with dislocation)	0.25 eV
Carbon-dislocation interaction energy	1.374 eV
(b) <i>Interstitial below the slip plane</i>	
Formation energy (3, -3, -1.5) (with dislocation)	0.91 eV
Carbon-dislocation interaction energy	0.714 eV
3. Stacking-fault distance	8.0 b
4. Dipole tensor, P_{ij} (eV)	
(a) Interstitial above the slip plane	$\begin{pmatrix} 6.78 & -0.81 & -0.44 \\ -0.81 & 2.32 & -0.01 \\ -0.44 & -0.01 & 4.25 \end{pmatrix}$
(b) Interstitial below the slip plane	$\begin{pmatrix} 4.09 & -3.05 & -1.59 \\ -3.05 & 9.16 & -2.98 \\ -1.59 & -2.98 & 3.00 \end{pmatrix}$

Cottrell formula using linear elasticity theory. Further, the dipole tensor which is spherical in the absence of the dislocation has a monoclinic symmetry in the vicinity of the dislocation. This is true both above and below the dislocation.

References

- Abrahamson A 1969 *Phys. Rev.* **178** 76
 Baskes M I and Melius C F 1979 *Phys. Rev.* **20** 3197
 Bullough R and Tewary V K 1979 in *Dislocations in solids* (ed.) F R N Nabarro (New York: North-Holland) Vol. 2, p. 1
 Cotterill R M J and Doyama M 1967 in *Lattice defects and their interactions* (ed.) R R Hasiguti (New York: Gordon and Breach), p. 20
 Heidenreich R O and Shockley W 1948 Report on Conference in Strength of Solids, p. 57
 Hoagland R G, Hirth J P and Gehlen P C 1976 *Philos. Mag.* **34** 413
 Johnson R A 1973 *J. Phys.* **F3** 295
 Johnson R A, Dienes G J and Damask A C 1964 *Acta Metall.* **12** 1215
 Nowick A S and Berry B S 1972 *Anelastic relaxation in crystalline solids* (New York: Academic Press)
 Sahu H K, Srinivasan S and Krishan K 1980 *Pramana (J. Phys.)* **15** 189

Water reactor fuel performance code PROFESS and its application for predicting the behaviour of the fuel elements of D-Com blind problem

D N SAH, D VENKATESH and E RAMADASAN

Radiometallurgy Division, Bhabha Atomic Research Centre, Trombay, Bombay 400 085, India

Abstract. This paper gives a brief description of the sub-models of important phenomena treated in computer code PROFESS and presents some results of PROFESS calculations for the fuel elements of D-Com blind problem.

Keywords. Computer modelling; computer code; nuclear fuel element; water reactor; code verification; fuel performance; irradiation effects; irradiation behaviour.

1. Introduction

The first version of computer code PROFESS (performance analysis of rod-type oxide fuel elements under steady state) was completed in the beginning of 1983. To check the predictive capability of the code and its sub-models, it was necessary to simulate a few documented irradiation experiments and to compare the predictions with the experimental results. At that time, a code exercise was being organized as part of an IAEA co-ordinated research programme on development of computer models (D-Com) to investigate the predictive capability of the existing codes. A detailed data package on an irradiation experiment was made available to the participants of the exercise and it was known as D-Com blind problem. The predictions of the different codes participating in this exercise were to be compared with the actual experimental findings, which had been held secret till calculations of all codes had been submitted. This provided a good opportunity to check the predictive capability of PROFESS by participating in this exercise. This paper briefly describes the models of some important phenomena treated in the code and gives some of the results obtained on the fuel elements of D-Com blind problem.

2. Computer code PROFESS

Computer code PROFESS is applicable to rod-type fuel elements used in water-cooled nuclear reactors. A typical water reactor fuel rod consists of a number of sintered UO_2 or $\text{UO}_2\text{-PuO}_2$ fuel pellets stacked inside a zircaloy cladding tube which is sealed at both ends.

The general features of PROFESS have been described elsewhere (Sah *et al* 1983; Sah and Venkatesh 1984). The flow chart of calculation followed in PROFESS is given in figures 1 and 2. The models incorporated in this code are listed in table 1. The general

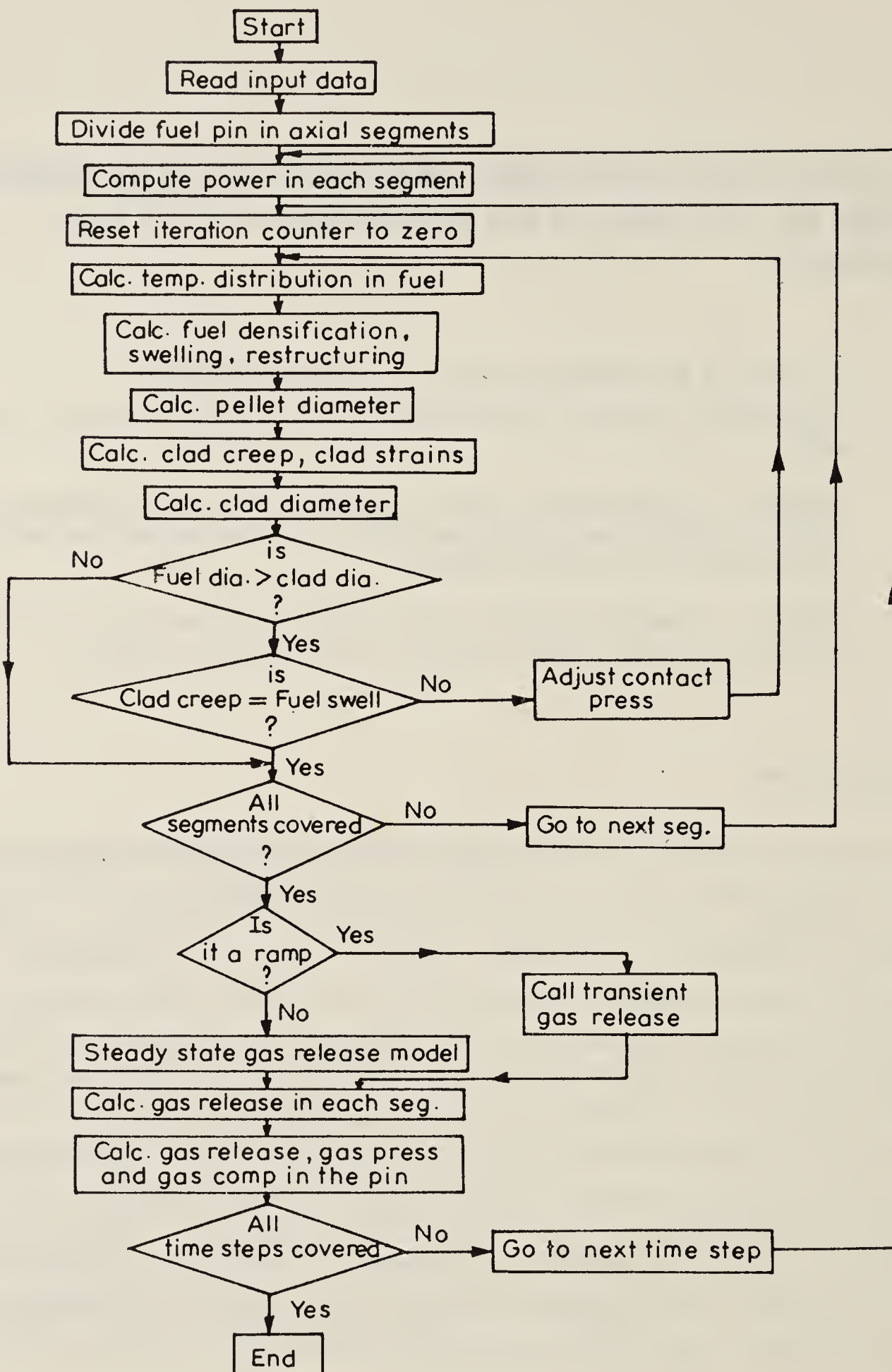


Figure 1. Flow chart of the calculations followed in PROFESS.

method of thermal and mechanical analysis of fuel element is described elsewhere (Roy and Sah 1985). Models of important phenomena treated in PROFESS are briefly described below.

2.1 Gap conductance model

The heat flow through the fuel clad gap/interface is considered to take place by thermal conduction and radiation. The gap conductance is evaluated by the Ross-Stout model

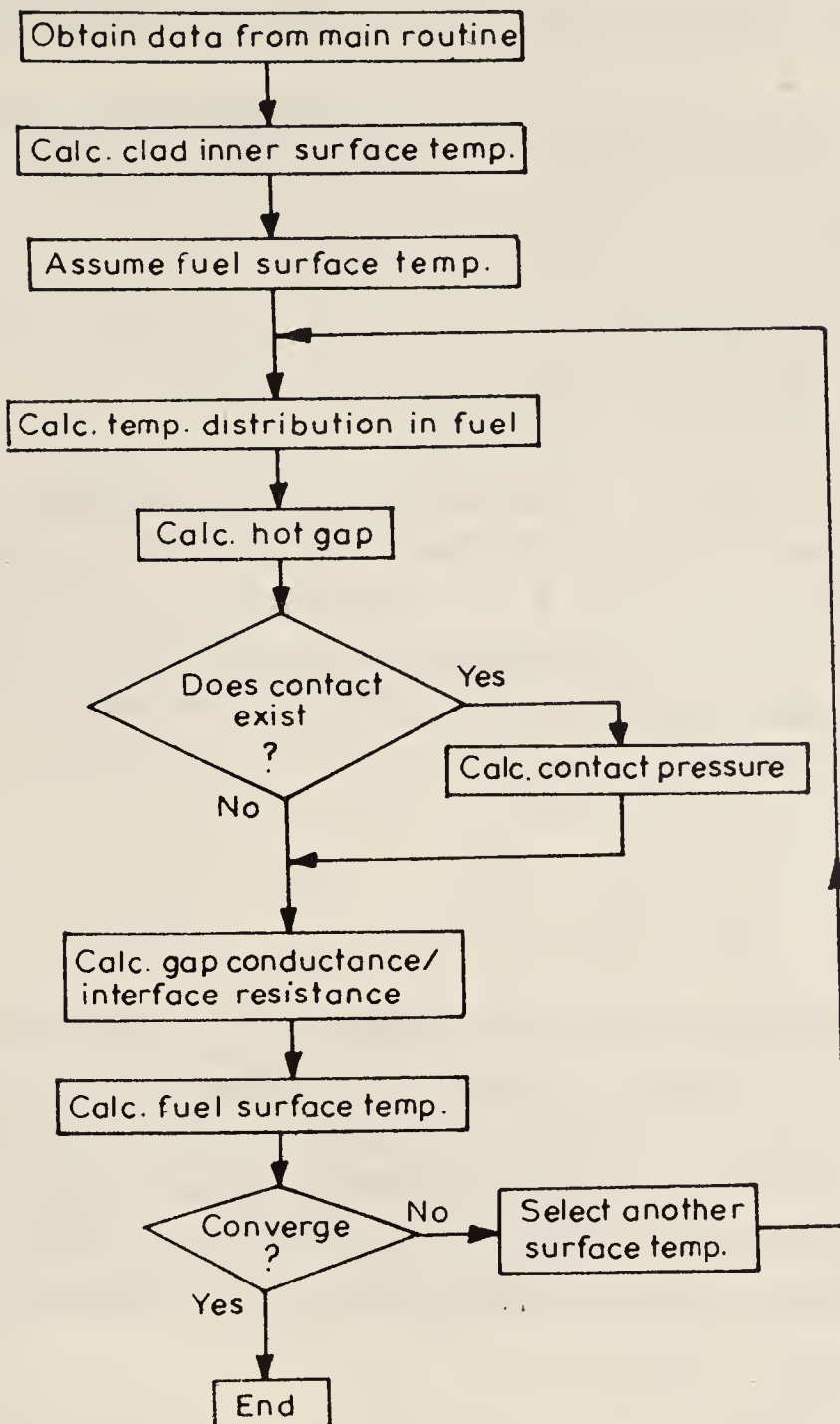


Figure 2. Flow chart of the calculation of radial temperature distribution in the fuel pin cross-section.

Table 1. Models in computer code PROFESS

<i>Analytical models</i>	<i>Material properties models</i>	<i>Phenomenological models</i>
Cladding surface temperature	Thermal expansion of UO ₂	Fuel clad gap conductance
Temperature drop across cladding	Thermal expansion of zircaloy	Solid and gaseous fission product swelling
Temperature drop across fuel clad-gap	Thermal conductivity of UO ₂	In pile fuel densification
Radial temperature distribution in fuel	Thermal conductivity of zircaloy	Fission gas release (steady state)
Elastic deformation of cladding	Thermal conductivity of gases, He, Xe	Fission gas release (transient)
Void volume	Thermal conductivity of gas mixture	Equiaxed grain growth
Internal gas pressure	Jump distance of gases	Columnar grain growth
Fission gas generation	Yield strength of zircaloy	Fuel relocation
Gap gas dilution	Poisson's ratio of zircaloy	Zircaloy in-pile creep
Plenum temperature	Meyer's hardness of zircaloy	
Neutron flux depression	Elastic modulus of zircaloy	

(Ross and Stout 1962) modified to account for the effect of fission gas, gas pressure and pellet eccentricity.

When the fuel-clad gap is open, the heat transfer coefficient in the gap is given by

$$h_{\text{gap}} = h_{\text{cond}} + h_{\text{rad}},$$

where $h_{\text{cond}} = K_{\text{gas}}/(X_{\text{gap}} + \delta + g_f + g_c)$,

$$h_{\text{rad}} = (4\sigma T^3)/\{(1/E_f) + (1/E_c)\} - 1,$$

K_{gas} = thermal conductivity of the gas, δ = sum of the surface roughness of fuel and cladding, $g_f g_c$ = jump distances of the gas in the fuel and in the cladding, X_{gap} = fuel-clad gap, σ = Stefan-Boltzmann constant, $E_f E_c$ = emissivity of the fuel and the cladding and T = temperature in the fuel clad gap. When the fuel-clad gap is closed i.e. the fuel and cladding are in contact with each other, the heat transfer co-efficient through the interface (h_{cont}) is given by

$$h_{\text{cont}} = \frac{K_{\text{gas}}}{\delta + g_c + g_f} + C \frac{2K_f K_c}{(K_f + K_c)} \cdot \frac{P_c}{\delta^{1/2} H},$$

where K_f, K_c are thermal conductivities of fuel and cladding, P_c is the contact pressure between fuel and cladding, H is the Meyer's hardness of cladding and C is a constant.

In the gap conductance model used in PROFESS it is assumed that when the pellet is placed eccentrically, its effect can be evaluated by assuming that even in the open gap condition a certain fraction of fuel surface is in pressureless contact with the cladding. This contact area fraction depends upon the existing gap and is defined as follows:

$$CA = 1 - \left(\frac{\text{hot gap}}{\text{cold gap-Ao}} \right)^{1.5\epsilon^2},$$

where ϵ denotes the extent of eccentricity and has a value between 0 and 1, for a fully concentric pellet, ϵ is zero resulting in a contact area fraction of zero and A_0 is a constant. The method of solution in the gap conductance model used in PROFESS is similar to the method used in COMETHE code (Hoppe *et al* 1982).

2.2 In-pile fuel densification

The irradiation-induced densification of uranium dioxide fuel is considered to be a function of the initial fuel density, the amount of unstable porosity in the fuel and the fuel burn-up. The model in PROFESS considers that the initial unstable pores disappear exponentially with the progress of fuel irradiation. The volume change in the fuel due to in-pile densification is given by the following correlation (Pedersen 1978),

$$(\Delta V/V)_{\text{dens}} = (P_0 - P_s) \left[\exp\left(\frac{-\text{BU}}{500}\right) - 1 \right],$$

where $(\Delta V/V)_{\text{dens}}$ is the volumetric change in the fuel, P_0 is the initial porosity fraction, P_s is the fraction of stable porosity in the fuel and BU is fuel burn-up. The densification is considered isotropic.

2.3 Solid and gaseous fission product swelling

The fission product swelling model incorporated in PROFESS considers free swelling of fuel when the fuel clad gap is open and a restrained swelling occurs when the fuel and cladding are in pressure contact with each other. The swelling correlations have been derived from the experimental data reported in literature (Zimmermann 1979; Hilbert *et al* 1971). Below 900°C free swelling is a linear function of fuel burn-up and above this temperature the swelling is considered as a function of fuel burn-up and fuel temperature both. The restrained swelling is linearly related to fuel burn-up and it is taken as 1% ($\Delta V/V$) per at. % burn-up.

2.4 Fission gas release

There are five optional fission gas release models (Sah *et al* 1984) in PROFESS for calculating the steady state fission gas release from fuel. The transient fission gas release is estimated by a model given below (Pati and Ritterbusch 1980).

$$F = 1 - \exp(-mt^n),$$

where F = fraction of pre-transient gas released during the transient, t = time at transient (seconds), m = temperature dependent variable (given by $2.22 \times 10^{-7} \times (T - 1000)^2$), T = fuel temperature °C and $n = 0.25$. In the above model the gas release occurs only if the fuel temperature exceeds 1000°C. The generation of fission gas during transient is ignored and the release occurs from the retained gas available in the fuel. At fuel burn-up higher than 20,000 MWD/MTU a correction factor is used to account for burn-up enhancement of the steady state release.

2.5 Fuel restructuring

Two important microstructural changes in fuel e.g. equiaxed grain growth and columnar grain growth have been modelled in PROFESS. The correlations used are given below.

Equiaxed grain growth is represented by the following correlation

$$D^2 = D_0^2 + 2.92 \times 10^{-8} \left[\exp \left(-\frac{2.67 \times 10^5}{8.314 T} \right) \right] \cdot t,$$

where D_0 is the initial grain size and D the final grain size. The grains are allowed to grow to a limiting size which is given by

$$D_{\max} = 2.23 \times 10^{-3} \exp(-7620/T).$$

The columnar grain growth is represented by a time temperature relationship given by $t = t_0 \exp(A/T + 273)$, where t is the time required to form columnar grains at a temperature T (°C), A and t_0 are constants.

2.6 Cladding creep

The creep rate of zircaloy cladding is considered a function of cladding stress, fast neutron flux (> 1 MeV) and the cladding temperature. The correlation used in PROFESS is given below (Wood and Watkins 1971).

$$\dot{\varepsilon} = A \exp\left(-\frac{14000}{RT}\right) \phi^{0.85} \sin(\sin h(0.165\sigma))$$

where A is a constant, ϕ is the fast neutron flux, σ is cladding stress kg/mm², T is cladding temperature (°C) and R is the gas constant.

3. Results of PROFESS calculation of D-Com blind problem

3.1 D-Com blind problem

The D-Com blind problem refers to an irradiation experiment in which three (AG11-8, AG11-9 and AG11-10) pre-pressurised mini-fuel elements were irradiated together to a fuel burn-up of about 32000 MWD/MTU at fairly low heat ratings. Two of these fuel elements were subjected to a power ramp (referred as bump test) at the end of life. The third fuel element (AG11-8) had been taken out of reactor prior to the bump test. The design of the fuel elements, the axial power profile in the fuel assembly and the power history of irradiation is shown in figure 3. Misfeldt (1982) compiled the details of this irradiation experiment and the data package used for the code calculations.

3.2 PROFESS calculations

PROFESS was used to calculate the following parameters as a function of irradiation time (i) fuel centre temperature (ii) gap conductance (iii) fission gas release in the fuel element (iv) fuel restructuring and (v) fuel element diameter. The detailed results of the calculation have been reported elsewhere (Sah *et al* 1984). Some important results related to the gap conductance, fission gas release and fuel restructuring are presented below.

3.2a Fuel-clad gap conductance: The variation of gap conductance as a function of irradiation time in the three fuel elements at their mid-stack location is shown in figure 4. A gradual increase in the gap conductance is observed in all the three fuel elements in the beginning, followed by an abrupt increase to a comparatively high value at about 10,000 hrs. The sudden increase in the gap conductance indicates the occurrence of fuel-cladding contact in the fuel elements. However it is seen that the value of gap conductance in the three elements is different from each other, even though the fuel clad gap has closed in all the three. This difference is because of the different amount of fission gas released in the three fuel elements (see §3.2b). Since fission gases, Xe and Kr, have very low thermal conductivity a higher gas release in a fuel element results in a lower value of gap conductance. The results presented in this figure, when compared with the experimentally measured fission gas release in the three fuel elements, indicates that PROFESS is able to simulate the gap conductance behaviour very well.

3.2b Fission gas release: The amount of gas release calculated by PROFESS in the three fuel elements is given in table 2 along with the experimentally measured values. There is satisfactory agreement between the predicted and measured gas release in the fuel element AG 11-8. However an underprediction of about 30% is noted in the bump tested elements AG11-9 and AG11-10. Comparison of the PROFESS predictions with the

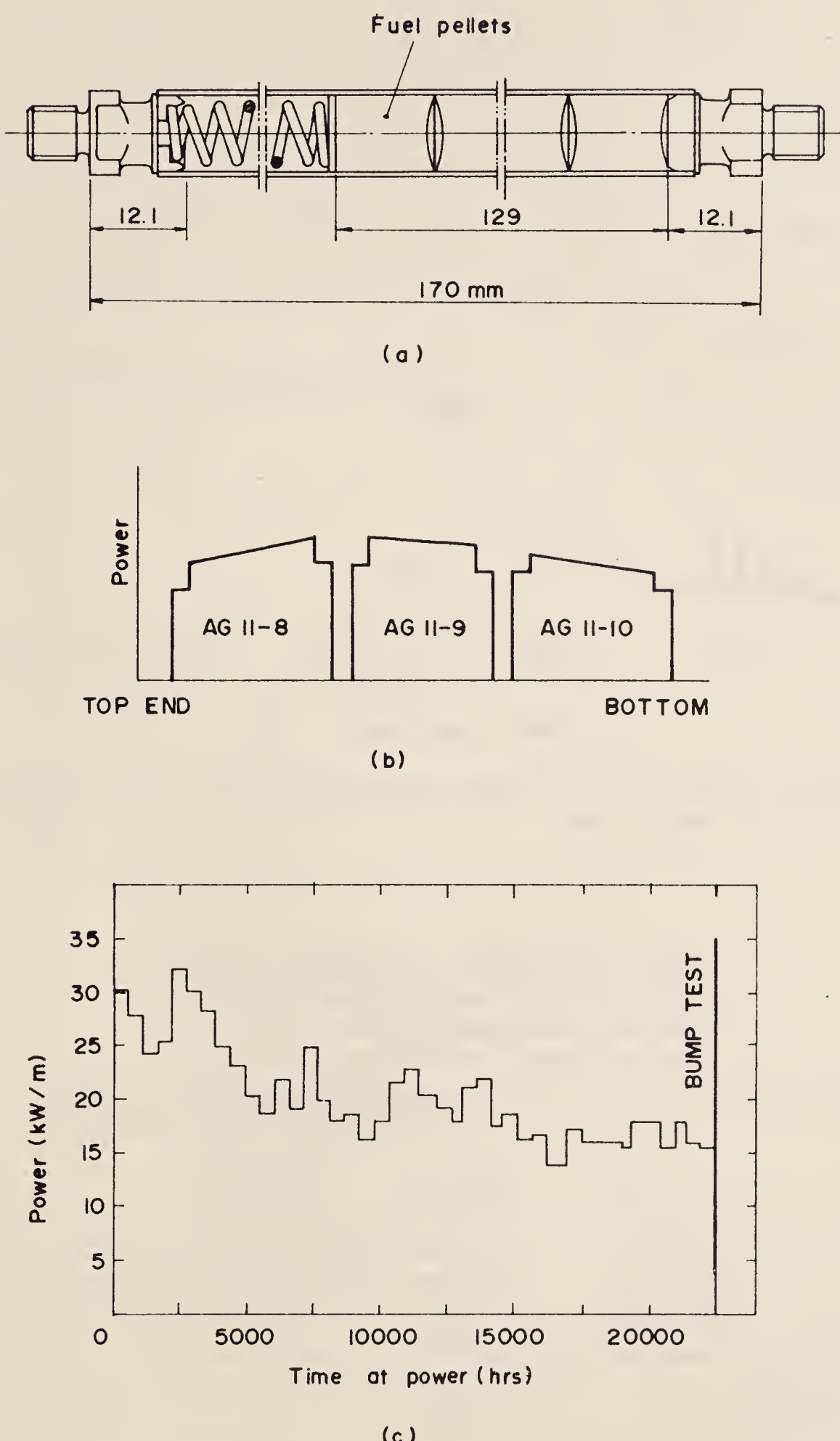


Figure 3. The design and the irradiation history of the fuel elements of D-Com blind problem; (a) fuel pin schematic design (b) power profile in the fuel pin assembly and (c) irradiation power history.

prediction of some other codes (figure 5) revealed that most of the codes tended to underpredict the gas release in these fuel elements. This indicates that the model of transient gas release adopted by the codes are presently inadequate for accurate prediction.

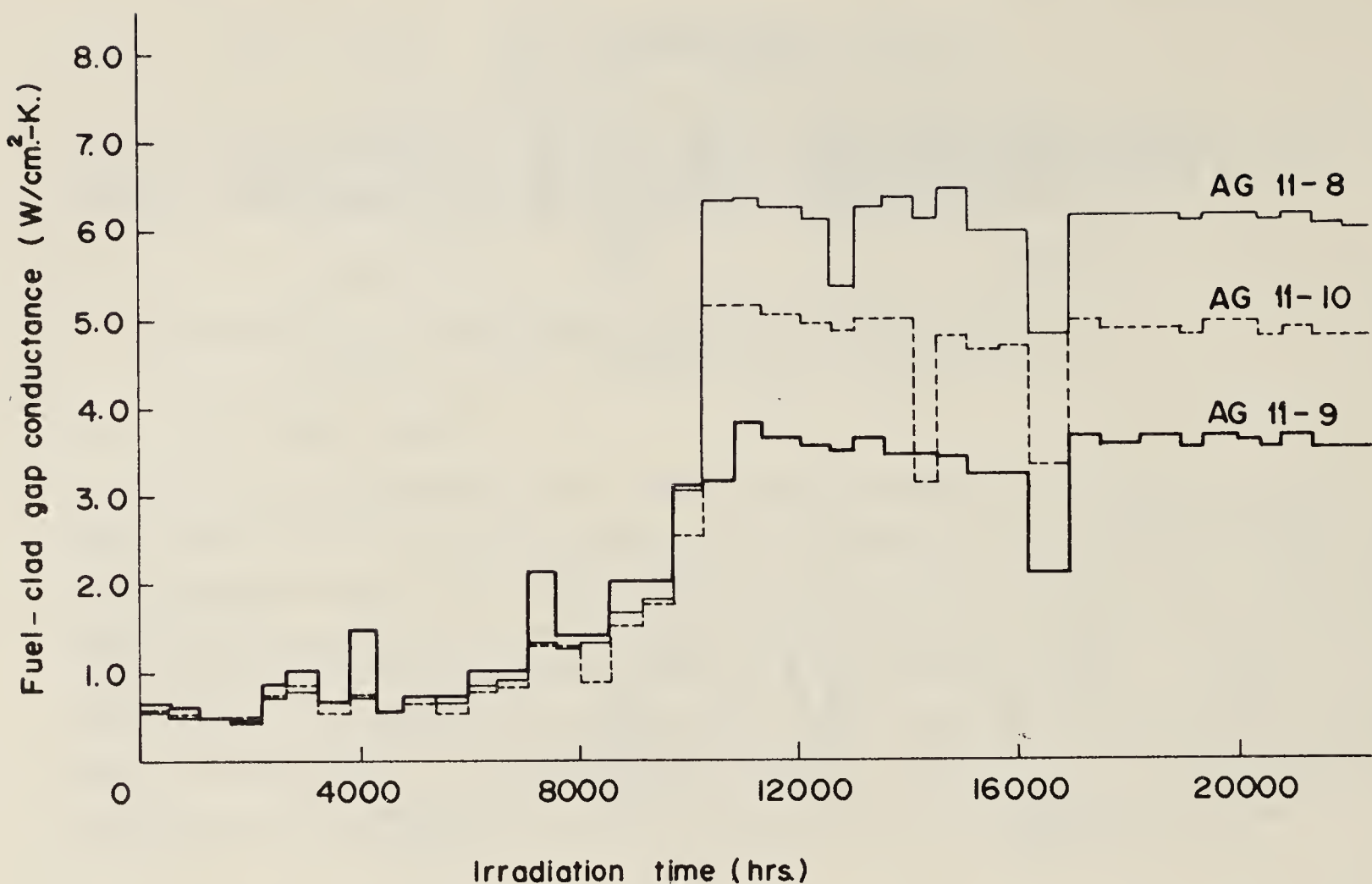


Figure 4. Fuel-clad gap conductance at the mid-stack location in the three fuel elements, as a function of irradiation time.

Table 2. Comparison of the predicted and the measured values of fission gas release in the three fuel elements of D-Com blind problem

Fuel element	Fission gas release (cc STP)	
	PROFESS prediction	Experimentally measured
AG 11-8	1.25	1.5
AG 11-9	9.0	12.5
AG 11-10	2.81	4.5

The gas release behaviour (as a function of irradiation time) calculated by PROFESS in AG 11-9 and AG 11-10 is shown in figure 6. It is interesting to note that in AG 11-9, the major amount (about two third of the total) of gas release occurred during the bump testing. This trend was in agreement with the conclusion arrived from the experiment (Misfeldt 1983).

3.2c Fuel restructuring: The calculations indicated that no grain growth occurred in the fuel element AG 11-8. This prediction is in agreement with the experimental finding. PROFESS prediction of the extent of grain growth at fuel centre and the size of the equiaxed grain growth region in the fuel element AG 11-9 was found to be in very good

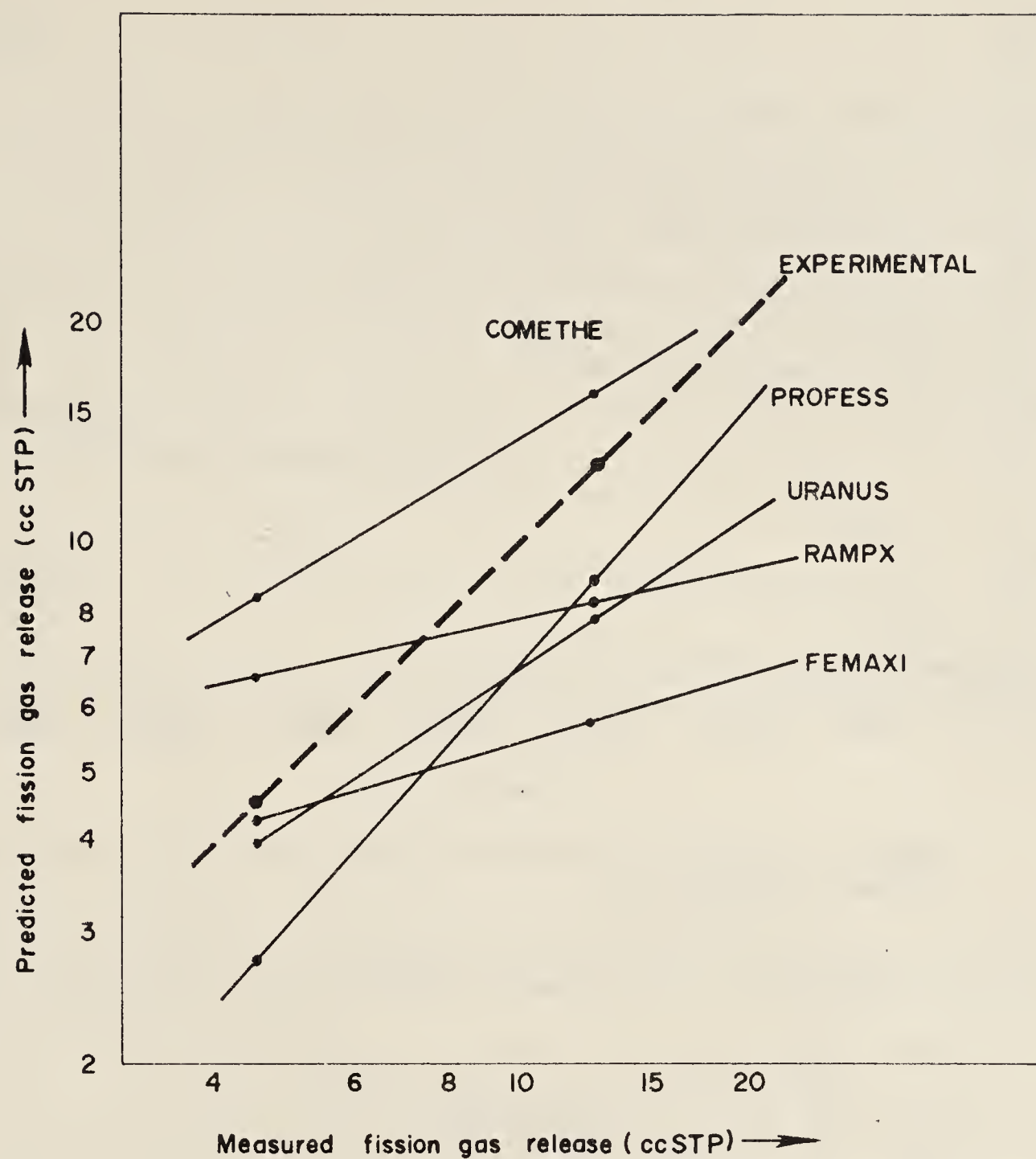


Figure 5. Comparison of the measured fission gas release in AG 11-9 and AG 11-10, with the prediction of some codes.

Table 3. Comparison of the grain growth prediction with experimental observation at the mid-stack location in the fuel elements

Fuel element	Fuel grain size at the centre (μm)		Size of grain growth region (fuel-fractional radius)	
	Predicted	Observed	Predicted	Observed
AG 11-8	No grain growth	No grain growth	0.00	0.00
AG 11-9	32.4	30	0.57	0.50
AG 11-10	24.2	Not measured	0.51	Not measured

agreement with metallographic observations (table 3). The calculations also revealed that the grain growth in AG 11-9 occurred during the initial period of irradiation (figure 7).

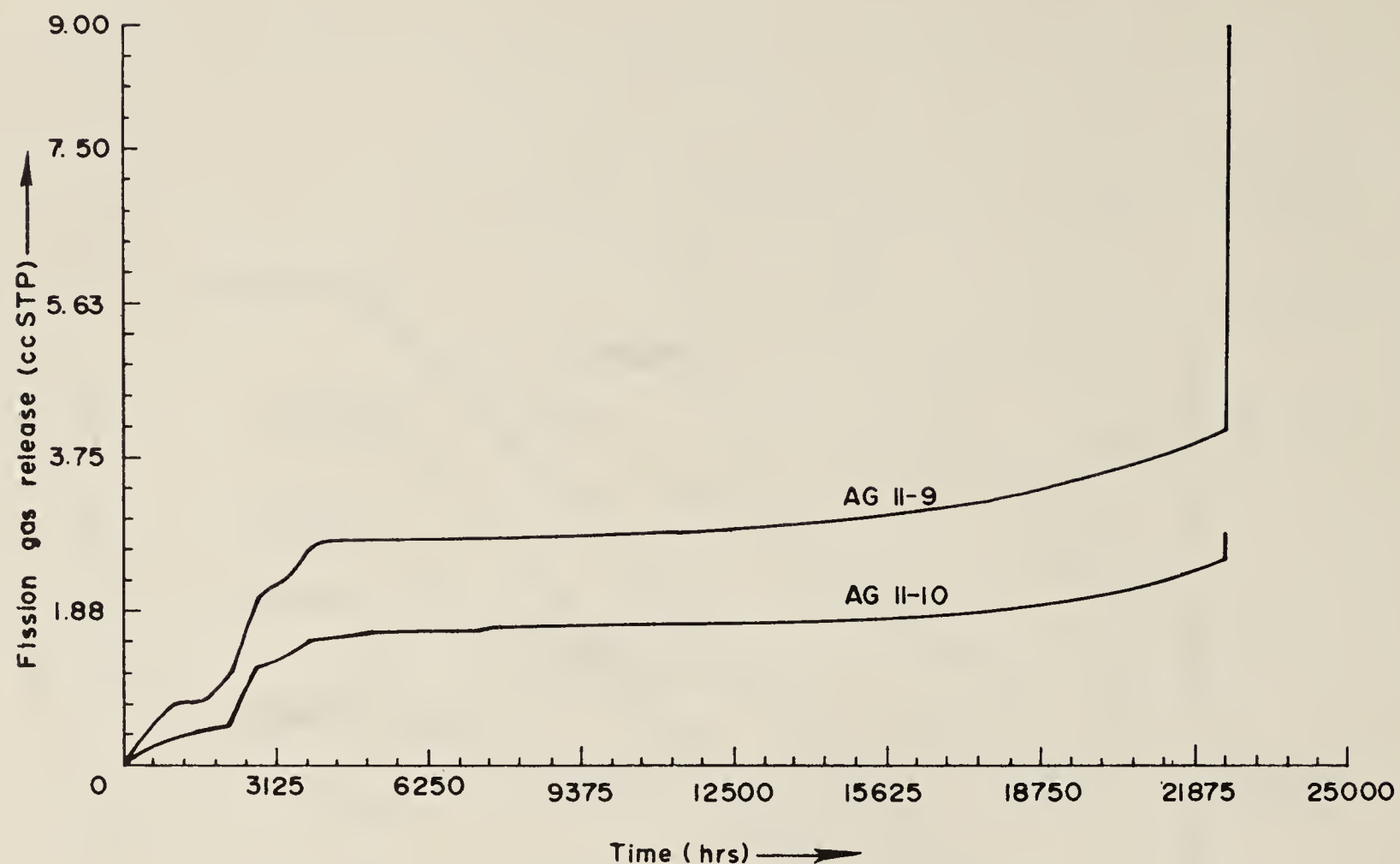


Figure 6. Predicted fission gas release in the fuel elements AG 11-9 and AG 11-10 as a function of irradiation time.

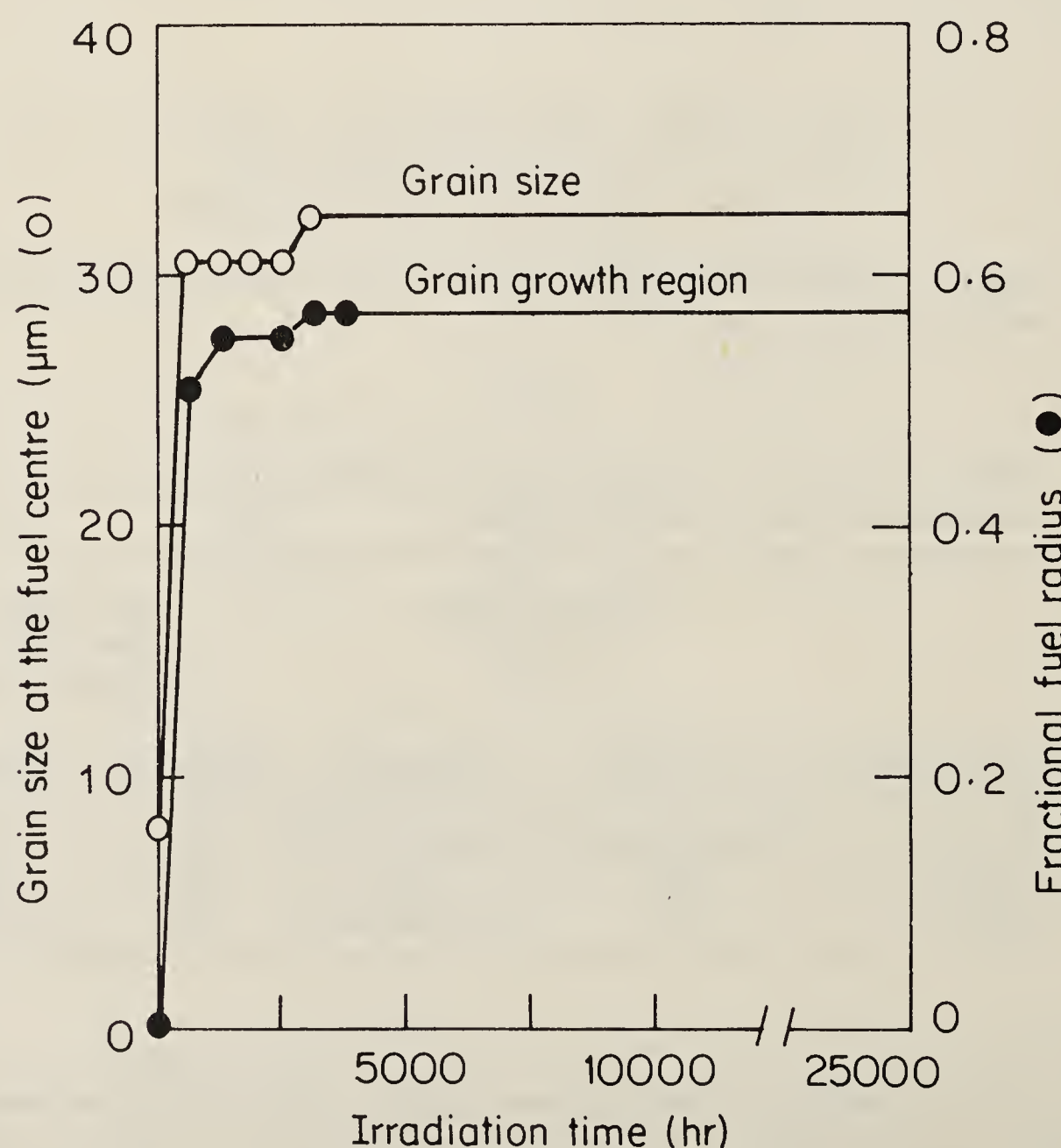


Figure 7. Predicted grain size at the fuel centre and the size of the grain growth region in the pellet cross-section for fuel elements AG 11-9, as a function of irradiation.

4. Conclusion

Computer code PROFESS was successfully used to calculate the performance parameters of the three fuel elements of an irradiation experiment commonly referred to as D-Com blind problem. The prediction of the fission gas release in the fuel elements and the fuel restructuring was found to be in reasonable agreement with experimental observations. The fuel-clad gap conductance model gives good simulation of the effect of fission gases and clearly revealed the occurrence of fuel-clad gap closure in the fuel elements during irradiation. It was noted, however, that there is a tendency for under-prediction of gas release during transient and better models may be required to represent the gas release in the fuel elements during transient conditions.

Acknowledgement

The authors wish to express their sincere thanks to Shri K S Sivaramakrishnan of PIE Section and Shri P R Roy, of Metallurgy Group for their keen interest in this work.

References

- Hilbert R F, Storhok V W, Chubb W and Keller D C 1971 *J. Nucl. Mater.* **38** 26
Hoppe N, Billaus M and Vliet J U 1982 Belgonuclair Report COMETHE III-L, Report No. BN 8201/-04
Misfeldt I 1982 Data for The D-Com blind problem on fission gas release, Report B-528, Metallurgy Dept., RISØ National Laboratory, Denmark
Misfeldt I 1983 *OECD-NEA-CSNI/IAEA Specialists meeting on Water Reactor Fuel Safety and Fission Gas release in off normal and Accident Condition, RISØ National Laboratory, Denmark*
Pati S R and Ritterbusch S E 1980 *Fission gas release during anticipated transient; IAEA Specialists Meeting on Water Reactor Fuel Element Performances Modelling, Blackpool, UK*
Pedersen N K 1978 *Proc. IAEA Specialists Meeting on Water Reactor Fuel Performance Computer Modelling, Blackpool, UK*
Ross A M and Stout R L 1962 Heat Transfer Coefficient between UO_2 and Zircaloy-2, Report AECL 1552.
Roy P R and Sah D N 1985 *Pramana (J. Phys.)* **24** 397
Sah D N, Venkatesh D and Sivaramakrishnan K S 1983 *Proc. Symp. on Irradiation Effects in Solids* (Bombay: BARC) p. 203
Sah D N, Venkatesh D and Ramadasan E 1984 *IAEA Specialists Meeting on Water Reactor Fuel Element Performance Modelling, Bowness on Windermere UK* (to be published).
Wood D S and Watkins B 1971 *J. Nucl. Mater.* **41** 327
Zimmermann H 1979 *IAEA Specialists Meeting on Behaviour of defected zirconium alloy clad ceramic fuel in water cooled reactors, Chalk River, Canada* p. 147

